DEVELOPMENT OF CARBON DOTS BASED MULTIFUNCTIONAL NANOMATERIALS FOR POTENTIAL APPLICATIONS

Ph.D. THESIS

by

ABHAY SACHDEV

CENTRE OF NANOTECHNOLOGY
INDIAN INSTITUTE OF TECHNOLOGY ROORKEE
ROORKEE-247667 (INDIA)
MAY, 2016

DEVELOPMENT OF CARBON DOTS BASED MULTIFUNCTIONAL NANOMATERIALS FOR POTENTIAL APPLICATIONS

A THESIS

Submitted in partial fulfilment of the requirements for the award of the degree

of

DOCTOR OF PHILOSOPHY

in

NANOTECHNOLOGY

by

ABHAY SACHDEV

CENTRE OF NANOTECHNOLOGY
INDIAN INSTITUTE OF TECHNOLOGY ROORKEE
ROORKEE-247667 (INDIA)
MAY, 2016

INDIAN INSTITUTE OF TECHNOLOGY ROORKEE
ROORKEE

CANDIDATE'S DECLARATION

I hereby certify that the work which is being presented in the thesis entitled **"DEVELOPMENT OF CARBON DOTS BASED MULTIFUNCTIONAL NANOMATERIALS FOR POTENTIAL APPLICATIONS"** in partial fulfilment of the requirements for the award of the Degree of Doctor of Philosophy and submitted in the Centre of Nanotechnology of the Indian Institute of Technology Roorkee, is an authentic record of my own work carried out during a period from July, 2013 to May, 2016 under the supervision of Dr. P.Gopinath, Associate Professor, Department of Biotechnology, Indian Institute of Technology Roorkee.

The matter presented in the thesis has not been submitted by me for the award of any other degree of this or any other Institute.

Signature of the Candidate

This is to certify that the above statement made by the candidate is correct to the best of my knowledge.

Date: **_____** **Signature of Supervisor**

The Ph. D. Viva-Voce Examination of **Mr. Abhay Sachdev**, Research Scholar, has been held on .....

Chairman, SRC **Signature of External Examiner**

This is to certify that the student has made all the corrections in the thesis.

Signature of Supervisor **Head of the Department**

Date:.....

Dedicated

to my Beloved Grandfather

and Parents

ACKNOWLEDGEMENTS

As I contemplate upon all the years in obtaining my Ph.D. degree, I would like to express my gratitude towards all those people who have contributed to my journey in different ways and made an everlasting impact on my life.

At this moment of accomplishment, first and foremost, I would like to convey my heartfelt thanks and appreciation to my supervisor, Dr. P. Gopinath who provided me a platform for pursuing Ph.D. He has been the guiding spirit for me since the day I started working under him as a postgraduate student. It was his cordial behaviour, continuous guidance and support that encouraged me to take up Ph.D. I was able to learn the intricacies of research from him. Under his guidance, I was able to overcome the tough times in my research. I can happily credit him for bringing out the best in me. He provided me the freedom and a conducive environment for work which helped me in achieving this feat in a short span of time. It was indeed an exciting and memorable experience working under him for all the years.

I offer my venerable thanks to the former and present Heads of Centre of Nanotechnology, Prof. Anil Kumar, Prof. Vijaya Agarwala, Prof. S.K. Nath and Prof. R. Jayaganthan for providing me the support and freedom for accessing various facilities in the centre. I would also like to thank student research committee (SRC) members of my thesis, Prof. R. P. Singh (Chairman, SRC), Prof. Vikas Pruthi (External Expert) and Dr. M. Sankar (Internal Expert) for their constructive criticism and precious suggestions which influenced my thought process. Acknowledgements are also due to the office staff of Centre of Nanotechnology, Mr. Rawan pal, Mr. Naresh, Mr. Vinod , Mr. Riyaz and Mr. Satinder for their timely help and guidance for all sorts of official work. My sincere thanks to the Head, Institute Instrumentation Centre and Department of Chemistry for allowing me to use the research facilities available in their respective departments.

I reserve this paragraph for my colleagues and friends at IIT Roorkee. I am grateful to my friends especially Ishita, Vijayesh, Rajesh, Deepika, Dr. Mini, Akshay and Raj Kumar for their research help in the form of experiment planning and execution, procurement of research related stuff, data interpretation and scientific discussions even at odd hours. They stood with me in good as well as bad times and never let me down. Their positive attitude, motivation and

continuous encouragement served as my pillers of strength in stressful times. It was a pleasure to have friends like them which made my stay at IIT Roorkee truly unforgettable. I wish them happiness and success for life. I also express my deep thanks to my lab colleagues, Uday, Bharat, Poornima, Shanid, Raj Kumar, Dr. Saba, Vinay and Vaibhavi who had a good understanding with me and helped me in troubleshooting the things with their valuable suggestions. I feel really privileged to have such lab colleagues who exuded positivity at the workplace with their jovial nature which enabled me to perform my research work in a healthy atmosphere. Dr. S. Chockalingam, who joined our Nanobiotechnology group as a post-doctoral fellow, deserves a special mention. During his short stay, he taught me the essential research related techniques which helped me prevail over the hurdles in my work.

Of course acknowledgements would be incomplete without thanking my parents. It was their dream to see me as a doctorate fellow. Their countless blessings and moral support made me sail through all the difficulties during my Ph.D.

The financial assistance provided by Ministry of Human Resource Development (MHRD) from July, 2013 to May, 2016 that made my research work very smooth and prompt, is gratefully acknowledged.

Last, but certainly not the least, I feel fortunate and harbor deep respect for my alma mater IIT Roorkee, for providing me the opportunity to prove my worth. Finally, I would like to thank Almighty, the God for endowing me with inner strength, self-confidence and patience throughout my Ph.D.

(Abhay Sachdev)

ABSTRACT

The discovery of fluorescent nanomaterials has been an important breakthrough in the ever expanding field of nanotechnology. With remarkable optical and chemical properties, fluorescent nanomaterials have been perceived as potential substitutes for organic dyes. Their exciting properties make them one of the most useful tools that chemistry has produced for biological purposes. Nanosized carbon dots (C-dots) have been the latest addition to the family of fluorescent nanomaterials which have enormous potential for application in diverse fields, ranging from analytical to biomedical. Besides, the versatile nature of C-dots can be exploited for creating multifunctional nanomaterials by combining them with drugs or nanoparticles. Such materials combine the therapeutic and imaging aspects in one entity for implementing multimodal functionality in biomedical applications. Hence, this thesis presents unique synthetic schemes for producing strongly fluorescent C-dots which have been further evaluated for their prospective applications. Furthermore, the development of C-dots based metal/hydrogel multimodal hybrid assemblies for anticancer and antioxidant applications has also been explored.

In Chapters 1-3, introduction, literature review and experimental procedures have been elucidated. In chapter 4, a unique approach has been devised, wherein, polyethylene glycol (PEG) and polyethyleneimine (PEI) passivated C-dots have been synthesized by one-step hydrothermal carbonization of chitosan. A comparative analysis of physicochemical and bioimaging properties of PEI based C-dots (CD-PEI) and PEG based C-dots (CD-PEG) was carried out. Further, the role of surface functionality was evaluated to gain an insight into the bioimaging efficiency of CD-PEI compared to CD-PEG.

In chapter 5, another interesting approach for synthesizing C-dots through green synthetic route was adopted. To this end, one-step hydrothermal treatment of coriander leaves was performed for preparing self passivated C-dots, without the aid of auxiliary passivating agent. These C-dots were further used as a fluorescence probe for sensitive and selective detection of Fe^{3+} ions. Eventually, the bioimaging and antioxidant potential of C-dots was evaluated through a variety of analytical assays. Therefore, the practicality of C-dots obtained from a herbal carbon source for versatile applications was validated.

In chapter 6, cerium oxide (CeO_2) based nanocomposite (NC) integrating fluorescent C-dots were synthesized by hydrothermal method. The antioxidant potency of CDs-CeO_2 NC was

evaluated in NIH3T3 fibroblast cells treated with H_2O_2, a major reactive oxygen species (ROS) responsible for oxidative stress. Tracking the intracellular fluorescence of CDs-CeO_2 NC by microscopy and flow cytometry made it possible to examine the capabilities of CeO_2 for abatement of H_2O_2-mediated oxidative stress, whilst monitoring their uptake.

C-dots based metal NCs constitute fascinating imaging and therapeutic tools for anticancer applications. In chapter 7, C-dots were integrated with silver@zinc oxide to form CD-Ag@ZnO NC. Accordingly, the ability of CD-Ag@ZnO NC in tracking the cellular uptake and mediating apoptotic effects was demonstrated against MCF-7 (breast cancer) and A549 (lung cancer) cells. By monitoring the green fluorescence emission of CDs, the cellular uptake and distribution of the CD-Ag@ZnO NC could be ascertained. Moreover, apoptosis induction in cancer cells treated with CD-Ag@ZnO NC was validated through morphological, biochemical and molecular studies.

Multifunctional hydrogels offer a seemingly efficient system for delivery of drugs and bioimaging modalities. In chapter 8, chitosan based hydrogel formulation composed of highly fluorescent C-dots and loaded with an anticancer drug, 5-Fluorouracil (5-FU) was realized to form 5-FU@CD-HY. Multifunctional aspects of 5-FU@CD-HY in monitoring the cellular uptake and inflicting apoptosis were revealed by *in vitro* studies on A549 cells. Green fluorescence of CDs in 5-FU@CD-HY aided the qualitative and quantitative assessment of cellular uptake. Additionally, the fluorescence of CDs could be used to detect apoptosis instigated by 5-FU. Induction of apoptosis in 5-FU@CD-HY treated cells was evidenced by changes in cell cycle distributions, visualization of characteristic apoptotic bodies through FE-SEM and apoptotic gene expression studies.

Keywords: C-dots, chitosan, hydrothermal, bioimaging, coriander, antioxidant, anticancer, nanocomposites, apoptosis, cerium oxide, reactive oxygen species, hydrogels.

LIST OF PUBLICATIONS

I. In Refereed Journals

1. **A. Sachdev,** I. Matai and P. Gopinath. Carbon Dots Incorporated Polymeric Hydrogels as Multifunctional Platform for Imaging and Induction of Apoptosis in Lung Cancer Cells. *Colloids and Surfaces B: Biointerfaces***,** 2016**,** 141, 242-252 *(Highlighted in Atlas of Science).*
2. **A. Sachdev** and P. Gopinath. Monitoring the Intracellular Distribution and ROS Scavenging Potential of Carbon dots-Cerium oxide Nanocomposites in Fibroblast Cells. *ChemNanoMat*, 2016, 2, 226-235.
3. **A. Sachdev** and P. Gopinath. Green Synthesis of Multifunctional Carbon Dots from Coriander Leaves and their Potential Application as Antioxidants, Sensors and Bioimaging agents. *Analyst*, 2015, 140, 4260-4269.
4. **A. Sachdev**, I. Matai and P. Gopinath. Dual-Functional Carbon Dots-Silver@Zinc Oxide Nanocomposite: *In Vitro* Evaluation of Cellular Uptake and Apoptosis Induction. *Journal of Materials Chemistry B*, 2015, 3, 1208-1220 *(Cover page of the issue).*
5. **A. Sachdev**, I. Matai and P. Gopinath. Implications of Surface Passivation on Physicochemical and Bioimaging Properties of Carbon Dots. *RSC Advances*, 2014, 4, 20915-20921.
6. I. Matai, **A. Sachdev** and P. Gopinath. Self-Assembled Hybrids of Fluorescent Carbon Dots and PAMAM Dendrimers for Epirubicin Delivery and Intracellular Imaging. *ACS Applied Materials & Interfaces*, 2015, 7, 11423-11435.
7. I. Matai, **A. Sachdev** and P. Gopinath. Multicomponent 5-Fluorouracil Loaded PAMAM Stabilized-Silver Nanocomposites Synergistically Induce Apoptosis in Human Cancer Cells. *Biomaterials Science*, 2015, 3, 457-468 *(Cover page of the issue).*
8. P. Dubey, I. Matai, S. Uday Kumar, **A. Sachdev**, B. Bhushan and P. Gopinath. Perturbation of Cellular Mechanistic System by Silver Nanoparticle Toxicity: Cytotoxic, Genotoxic and Epigenetic potentials. *Advances in Colloid and Interface Science*, 2015, 221, 4-21.
9. P. Dubey, B. Bhushan, **A. Sachdev**, I. Matai, S. Uday Kumar and P. Gopinath. Silver Nanoparticles Incorporated Composite Nanofiber for Potential Wound Dressing

Applications. *Journal of Applied Polymer Science*, 2015, 132, 42473 *(Cover page of the issue)*.

10. B. Bhushan, P. Dubey, S. Uday Kumar, **A. Sachdev**, I. Matai and P. Gopinath. Bionanotherapeutics: Niclosamide Encapsulated Albumin Nanoparticles as a Novel Drug Delivery System for Cancer Therapy. *RSC Advances*, 2015, 5, 12078-12086.
11. S. Uday Kumar, I. Matai, P. Dubey, B. Bhushan, **A. Sachdev** and P. Gopinath. Differentially Cross-linkable Core-shell Nanofibers for Tunable Delivery of Anticancer Drugs: Synthesis, Characterization and its Anticancer Efficacy. *RSC Advances*, 2014, 4, 38263-28272.
12. B. Bhushan, S. Uday Kumar, I. Matai, **A. Sachdev**, P. Dubey and P. Gopinath. Ferritin Nanocages: A Novel Platform for Biomedical Applications. *Journal of Biomedical Nanotechnology*, 2014, 10, 2950-2976.

II. Book

1. P. Gopinath, S.U. Kumar, I. Matai, B. Bhushan, D. Malwal, **A. Sachdev** and P. Dubey. Cancer Nanotheranostics, *Springer Briefs in Applied Science and Technology, Springer, Singapore* (2015), ISBN: 978-981-287-434-4, 1-93.

III. Conferences

1. **A. Sachdev**, I. Matai and P. Gopinath, "Synthesis of Carbon Dots-Ag/ZnO Nanocomposites for Theranostic Applications", poster presentation in *Tech Connect World Innovation Conference & Expo*, Washington DC, USA, 15-18 June, 2014.
2. **A. Sachdev**, I. Matai and P. Gopinath, "One-step Hydrothermal Synthesis of Water Soluble Green Luminescent Carbon Dots for Bioimaging", poster presentation in *International Conference on Nano Science and Technology (ICONSAT 2014)*, Mohali, India, 3-5 March, 2014.
3. I. Matai, **A. Sachdev** and P. Gopinath, "Chitosan as a Nanocarrier for Intracellular Delivery of Lysozyme", poster presentation in *International Conference on Nano Science and Technology (ICONSAT 2014)*, Mohali, India, 3-5 March, 2014.

CONTENTS

LIST OF FIGURES

LIST OF TABLES

ABBREVATIONS

% ……....	Percent
θ	Theta
λ_{ex} ……...	Excitation Wavelength
λ_{em} ……..	Emission Wavelength
µg ……...	Microgram
µm	Micrometre
µM …….....	Micromolar
µL	Microlitre
^{o}C	Degree Celsius
5-FU	5-Fluorouracil
5-FU@CD-HY	5-Fluorouracil loaded chitosan-C-dots hydrogels
Å ……....	Angstrom
a.u.	Arbitrary Unit
A549	Human Lung Adenocarcinoma Cells
AAS	Atomic Absorption Spectroscopy
Ag	Silver
Au	Gold
AO …….....	Acridine Orange
Bad	Bcl 2 Associated Death Promoter
Bax	Bcl 2 Associated X Protein
Bcl-2	B-cell Lymphoma 2
Bcl-xl	Basal Cell Lymphoma-Extra Large
BET	Brunauer-Emmett-Teller
BHK-21	Baby Hamster Kidney Cells
Caspases …….....	Cysteine-Aspartic Acid Proteases
cDNA …….....	Complementary Deoxyribonucleic Acid
C-dots/CDs	Carbon Dots
CD-PEI	PEI passivated C-dots
CD-PEG	PEG passivated C-dots
CD-Ag@ZnO	C-dots-silver@zinc oxide
CDs-CeO_2	C-dots-cerium oxide
Ce	Cerium

CeO_2	Cerium Oxide
Ch	Channel
cm …….....	Centimeter
cm^{-1}	Wavenumber
Cu	Copper
DCFH-DA	2',7'-dichlorofluorescin diacetate
DDS	Drug Delivery Systems
DLS	Dynamic Light Scattering
DMEM	Dulbecco's Modified Eagle's Medium
DMSO	Dimethyl Sulfoxide
DOX	Doxorubicin
DPPH	2,2-diphenyl-1-picrylhydrazyl
dsDNA …….....	Double Stranded DNA
EA …….....	Early Apoptosis
EB …….....	Ethidium Bromide
EC_{50}	Antioxidant Concentration for Decreasing the Concentration of Free Radicals by 50%
E.coli	*Escherichia coli*
EDTA	Ethylenediaminetetraacetic Acid
EE …….....	Entrapment Efficiency
EDS ……..	Energy Dispersive X-ray Spectrometry
FBS	Fetal Bovine Serum
FDA ...…….....	Food and Drug Administration
FE-SEM	Field Emission Scanning Electron Microscopy
FA	Folic Acid
FTIR	Fourier Transform Infrared Spectroscopy
g	Gram
GFP …….....	Green Fluorescent Protein
h	Hour
H_2O	Water
H_2O_2	Hydrogen Peroxide
HCl	Hydrochloric acid
HY.....	Hydrogels
IC_{50}	Half Maximal Inhibitory Concentration

ICP-MS	Inductively Coupled Plasma Mass Spectrometry
IFFT	Inverse Fast Fourier Transform
JCPDS ……..	Joint Committee on Powder Diffraction Standards
keV	Kiloelectron Volt
KBr	Potassium Bromide
LA …….....	Late Apoptosis
L-132	Human Normal Lung Epithelial Cells
M ……..	Molar
mg	Milligram
min	Minute
mL …….	Millilitre
mM	Millimolar
mm	Millimetre
MPa	Megapascal
mV	Millivolt
MCF-7	Human Breast Adenocarcinoma Cells
MRI	Magnetic Resonance Imaging
mRNA	Messenger RNA
MTT	3-(4,5-Dimethyl-2-thiazoyl)-2,5-diphenyltetrazolium bromide
N	Newton
NC	Nanocomposite
nm	Nanometer
NP ……...	Nanoparticle
ns	Nanosecond
NaCl …….....	Sodium Chloride
NaOH	Sodium Hydroxide
NIH3T3	Mouse Embryonic Fibroblast Cells
NIR	Near-infrared
pg	Picogram
pH	Potential of Hydrogen
PI	Propidium Iodide
ppm	Parts per million
PBS ……...	Phosphate Buffer Saline
PCR ……..	Polymerase Chain Reaction

PDT	Photodynamic Therapy
PEG ……...	Polyethylene Glycol
PEI	poly(ethyleneimine)
PPEI-EI	poly(propionylethylenimine-co-ethylenimine)
Q	Quantum Yield
QDs	Quantum Dots
ROS ..…….....	Reactive Oxygen Species
RNA	Ribonucleic Acid
RNase ……...	Ribonuclease
rpm	Revolutions Per Minute
RT-PCR …….....	Reverse Transcriptase-Polymerase Chain Reaction
s	Second
SAED …….....	Selected Area Electron Diffraction
S. aureus	*Staphylococcus aureus*
SDS-PAGE ……	Sodium dodecyl sulphate- polyacrylamide gel electrophoresis
SEM	Standard Error Mean
TEM	Transmission Electron Microscope
TGA …….....	Thermogravimetric Analysis
Tris-HCl	Tris (hydroxymethyl) aminomethane hydrochloride
TTDDA	4,7,10-trioxa-1,13-tridecanediamine
UV	Ultra Violet
V	Volts
v/v%	Volume Percent
wt%	Weight Percent
XRD	X-Ray Diffraction
Zn	Zinc
ZnO	Zinc Oxide

CHAPTER 1

INTRODUCTION

This chapter gives a brief introduction to the fluorescent nanoparticles theme that is primarily focussed on C-dots and their multimodal applications. The chapter also includes the objectives, significance and organization of the thesis.

CHAPTER 1

INTRODUCTION

Nanotechnology has been one of the cutting edge technologies in the last decade which adopts a pragmatic approach in designing nanomaterials for biomedical applications by combining physics, chemistry, materials science and biology. Intriguing size-dependent physical and chemical properties of nanoparticles have prompted the researchers to discover their prospective applications in various fields (Feynman, 1991). Nanoparticles ranging from a few to less than hundred nanometers with size comparable to DNA, protein, lipid and cell organelles have been fascinating because of their abilities to overcome cellular barriers and can easily penetrate into the cells (Salata, 2004, Silva, 2004 and Whitesides, 2005). Additionally, the interactions of nanomaterials with biological entities are critical from application point of view which requires understanding at both cellular and molecular levels, thus allowing the integration of nanotechnology and biology. In the field of medicine, nanomaterials have been used as effective tools to facilitate drug/gene delivery, fluorescence labelling, hyperthermia and magnetic resonance imaging (MRI) applications. Nanomaterials possess the desired competence to improve the current diagnosis and therapeutic schemes for a variety of human diseases. Numerous types of organic or inorganic nanomaterials such as carbon nanotubes, C_{60} fullerenes, graphene, iron oxide nanoparticles, gold nanoshells, quantum dots, polymers, liposomes, dendrimers have been actively pursued for a wide spectrum of biomedical applications (Corr et al., 2008, Gao et al., 2009, Bhardwaj et al., 2009, Koninti et al., 2014, Chaudhary et al., 2015 and Deka et al., 2016). Such nanoscale materials confer noteworthy advantages over conventional approaches in terms of improved cellular imaging, sensitivity and drug release kinetics (Parveen et al., 2012). With continued efforts in the field of nanomaterials synthesis and applications, a paradigm shift towards the development of multifunctional nanomaterials has been encountered. The strategy combines diagnostic tools (i.e. imaging) with therapeutic regimen (i.e. drug delivery) on a single platform to perform more than one function simultaneously (Kelkar et al., 2011). Consequently, these nanomaterials have revolutionized the field of healthcare applications, especially cancer diagnosis or therapy (Janib et al., 2010, Gopinath et al., 2014 and Gavvala et al., 2015). Engineering such multimodal systems can

enable real-time monitoring of cellular uptake, controlled release of drug and subsequent examination of cellular changes in response to drug (Ueno et al., 2011).

Fluorescence is a type of luminescence associated with fluorophores. In this process, a fluorophore absorbs light at a particular wavelength and subsequently emits light of longer wavelength having an energy corresponding to the difference in energy levels between ground and the excited states (Lakowicz, 1999). Fluorescent labels constitute one of the rapidly developing areas with applications in the field of biology and analytical chemistry (Dubertret et al., 2002, Frasco, 2009, Petryayeva et al., 2013, Hussain et al., 2015, Goutam et al., 2015 and Malik et al., 2015). Representative fluorescence parameters such as excitation/emission spectrum, quantum yield and fluorescence lifetime forms the basis of evaluating the spectral properties of the fluorophores in addition to interpreting small changes in their local environment (eg. pH, interacting ions, solvent polarity etc.). Fluorescence microscopy has been one of the powerful imaging techniques for studying a variety of phenomenon in cellular biology by monitoring the distribution of fluorophores. Fluorescence imaging has attracted significant interest because the technique is versatile, selective and has good contrast sensitivity (Wang et al., 2006). Imaging of biological matter using fluorescent labels is referred to as bioimaging which forms a realm of its own. Bioimaging based on fluorophores can be categorized into four types: (1) Fluorophores internalized in cellular compartments to make them fluorescent and hence image them. (2) Surface functionalization of fluorophores with receptors, ligands, proteins or oligomers for specific recognition, targeting and imaging of cellular components. (3) Utilization of fluorophores with sensing abilities for imaging non fluorescent biochemical species (eg. pH values, ions, free radicals in living cells). (4) Incorporation of fluorophores in multifunctional systems to track their uptake inside the cells under various physiological conditions, which is especially relevant for nanomedicine-based delivery systems (Wolfbeis, 2015).

Traditional classes of fluorescence labelling agents include organic dyes (fluorescein, cynein), fluorescent proteins and lanthanide chelates (Shimomura et al., 1962, Yu et al., 1994, Elbanowski et al., 1996, Chetia et al., 2014, Saha et al., 2014, Rurup et al., 2014 and Dar et al., 2015). However, these agents have some inherent drawbacks such as limited aqueous solubility, short stokes shift, low absorption coefficients, less photostability and poor photobleaching threshold. All these limitations reduce their sensitivity and hinder their use for long-term tracking. Fluorescence nanomaterials have been developed and primed to study fluorescence at nanoscale, with applications ranging from sensing to imaging (Wang et al.,

2006, Ruedas-Rama, et al. 2012 and Wolfbeis, 2015). As a new class of fluorescent labels, these nanoparticles have been gaining popularity in comparison to classical fluorescent agents on the basis of their superior properties. Nanometer size of the particles entails high signal to noise ratio, thereby improving the analytical sensitivity and accuracy. Additionally, their molecular size downplays the physical perturbation of living cells and renders high spatial resolution for imaging purposes. Moreover, fluorescent nanoparticles possess unique optical properties such as enhanced photostability, high brightness, size-dependent emission and large stokes shift.

Recent advances in the field of nanotechnology witnessed the design of significant numbers of fluorescent chemical and biological nanoprobes. In line with this, fluorescent nanoparticles were primarily used as substitutes for organic dyes intended for imaging cells, bacteria and cellular organelles (Chen et al., 2004, Nandi et al., 2015 and Ritenberg et al., 2016) or development of sensing systems (Pylaev et al., 2011, Kong et al., 2012 and Nie et al., 2014). Fluorescent nanoparticles that have been explored so far for their biomedical applications include quantum dots, aggregation-induced emission-based-fluorescent nanoparticles, silicon dots, carbogenic nanomaterials and metal nanoclusters (Ag, Au, Cu) (Warner et al., 2005, Sun et al., 2006, Zrazhevskiy et al., 2010, Zhang et al., 2014b, Wang et al., 2014f, Ghosh et al., 2015 and Khlebtsov et al., 2015). Few of such nanoparticles are already under clinical trials. Although efficient, some concerns have been voiced about the use of metal-based fluorescence nanoparticles. Discovery of Quantum dots (QDs) is considered one of the important milestones in the field of fluorescent nanoparticles. However, a good number of studies have demonstrated the potential hazards of heavy metal-based QDs. Toxicity of QDs depends on multiple factors: size, charge and surface capping materials (Hardman, 2006 and Yong et al., 2013). Release of heavy metal ions has been implicated for the toxicity of cadmium-based QDs. Similarly, the underlying toxicity mechanisms of QDs have been proposed in terms of generation of reactive oxygen species (ROS), reduction in cell number and induction of apoptosis (Chen et al., 2012b). Furthermore, several other factors like intricate synthesis, difficult surface conjugation and photo-oxidation limits their use. Further, carbogenic fluorescent nanoparticles such as carbon nanotubes (CNTs), carbon dots (C-dots) and graphene quantum dots (GQDs) having similar application prospects as QDs, but with lesser toxicological issues have been explored. Single-walled and multi-walled CNTs are fluorescent in the NIR range (800-1600 nm) but posses lower quantum yield. This emission wavelength is attractive for *in vivo* fluorescence imaging since it lies in the tissue-transparent region of the electromagnetic spectrum.

Genetically engineered multifunctional M13 phages were shown to assemble single-walled CNTs and ligands for targeted fluorescence imaging of tumors (Yi et al., 2012).

Ever since the discovery of C-dots in 2004, remarkable efforts have been done for exploring their synthetic modes and subsequent applications in diverse fields. In recent times, C-dots have been one of the forefront areas of nanotechnology owing to ease of synthesis, low cost of production, simple instrumentation and ample source availability. This provides an opportunity to create new and fundamentally different approaches for synthesizing C-dots, amenable to commercial production. Nevertheless, there is a need to build a rapid, economically effective and green synthetic route with precise control of size distributions to produce strongly fluorescent C-dots for practical applications. Similar to C-dots, GQDs have also attracted lot of interest on account of their fascinating optical and electronic properties. GQDs are zero dimensional nanomaterials which are obtained from one dimensional graphene sheets and exhibit pronounced quantum confinement and edge effects (Pan et al., 2010). GQDs consist of a large conjugated domain and regular structure, exhibiting excellent performance of graphene. Although GQDs are considered as a kind of C-dots, there are certain differences between the two. GQDs have graphitic lattice structure, whereas C-dots can exist in amorphous or crystalline state (Baker et al., 2010 and Li et al., 2013c). Besides, GQDs are composed of graphene sheets with lateral dimensions less than 100 nm in single-, double- and few- (3 to <10) layers, while C-dots are discrete, quasi-spherical carbon nanoparticles with sizes usually below 10 nm (Ponomarenko et al., 2008 and Lim et al., 2015). The unique features of C-dots such as excellent optical properties, ease of surface functionalization, good biocompatibility, high aqueous solubility and ultra small size endorse their candidature for a host of biomedical applications. In this perspective, C-dots have been employed for bioimaging, as a nanocarrier for drugs/genes/enzymes, biosensing and theranostics (Ding et al., 2014, Wang et al., 2014e, Zhang et al., 2015 and Zuo et al., 2016). C-dots mainly emit in green or blue spectral region, where autofluorescence of the biological tissues is significant, which limits its scope for imaging purposes. Recently, there have been few reports on production of C-dots which emit at longer wavelengths. Orange emissive C-dots were realized through conjugated sp2-domain controlling and surface charges engineering, while red emitting C-dots were synthesized through simple changes in the surface compositions rather than the particle size (Hu et al., 2015, Ding et al., 2016 and Qu et al., 2016). Alternatively, multicolour C-dots with excitation tunable fluorescence emission in the entire visible spectrum could be considered as apposite candidates for bioimaging (Liu et al., 2011, Wang et al., 2011, Luo et al., 2013, Li et al., 2013a

and Mehta et al., 2014). This provides the luxury of selecting the fluorescence emission colour of C-dots which seems to be tailor-made for their different biomedical applications.

Nanocomposites of C-dots with metal nanoparticles or polymeric systems have opened up new avenues for creating multifunctional C-dots-based materials. In fact, designing of such hybrid assemblies has enabled the exploitation of optical properties of C-dots beyond the conventional applications. The study of C-dots-based metal nanocomposites is a relatively new, yet exciting area of research. However, the luminescent properties of C-dots can be affected by the metal nanoparticles as a result of photo-induced electron transfer or aggregation of the C-dots (Li et al., 2011a, Luo et al., 2012 and Wang et al., 2014c). Therefore, the challenge is to combine C-dots with metal nanoparticles so that the nanocomposite retains the fluorescence. There are plenty of examples wherein nanocomposites of C-dots with various metals (Ag, Au, Fe) have been used for biomedical, catalytic, surface-enhanced Raman spectrometry and fluorescence-based sensing applications (Yu et al., 2012, Kleinauskas et al., 2013, Qin et al., 2013a, Mao et al., 2014, Mondal et al., 2014 and Bhunia 2016b). Currently the development of C-dots-based multifunctional materials is still in its infancy, necessitating intensive research for realizing their biomedical applications, in particular. In this thesis, facile synthetic regimes have been worked upon to produce strongly fluorescent C-dots for imaging and sensing applications. Further, C-dots-based hybrid assemblies have been formulated by combining them with therapeutic modalities through a holistic approach. Multifunctional aspects of such materials have been evaluated using appropriate *in vitro* model systems.

1.1 Objectives

The key objectives of the present work are as follows:

- Investigation of physicochemical and bioimaging properties of surface tailored C-dots.
- Development of a green synthetic approach for production of C-dots from natural molecular precursors for versatile applications.
- To synthesize C-dots-cerium oxide nanocomposite for synchronous bioimaging and antioxidant activity.
- Formulation of C-dots-silver@zinc oxide nanocomposite for *in situ* imaging and therapeutic purposes.
- To design C-dots integrated polymeric hydrogels as a nanocarrier for delivery of chemotherapeutic drug for cancer theranostic applications.

1.2 Significance of the present study

The salient features of the present study have been outlined below:

- A unique one-pot method for synthesizing surface functionalized C-dots using different polymeric passivating agents (PEI/PEG) by hydrothermal carbonization of chitosan.
- This is the first instance, wherein the effect of positive and negative charged surface passivation agents on bioimaging efficiencies of C-dots has been addressed using BHK-21 (normal) and A549 (cancer) cell lines.
- Green synthesis of self-passivated C-dots by one-step hydrothermal treatment of coriander leaves.
- Determination of antioxidant activity of as-synthesized C-dots.
- These C-dots were employed as fluorescence nanoprobes for sensitive and selective ion detection.
- Qualitative as well as quantitative analysis of bioimaging potential of C-dots through fluorescence microscopy and flow cytometry.
- A hydrothermal mediated approach for synthesis of C-dots-cerium oxide nanocomposites.
- Interaction of these nanocomposites with hydrogen peroxide (H_2O_2), a major reactive oxygen species responsible for oxidative stress has been studied by monitoring the change in fluorescence intensity.
- A distinctive approach based on sensing of fluorescence signal of C-dots in C-dots-cerium oxide nanocomposites by flow cytometry has been worked out to evaluate the H_2O_2 mediated oxidative stress in cells.
- Ability of C-dots-cerium oxide nanocomposites in preventing the H_2O_2 mediated oxidative stress in cells has also been elucidated.
- Novel, dual functional C-dots-silver@ zinc oxide nanocomposites were synthesized for monitoring the cellular uptake and induction of apoptosis in cancer cells.
- Comparative analysis of cellular uptake and apoptotic potential of C-dots-silver@ zinc oxide nanocomposite was performed using cancer cells such as A549 (lung cancer) and MCF-7 (breast cancer).
- C-dots were integrated to chitosan hydrogels and loaded with an anticancer drug, 5-Fluorouracil to formulate a multifunctional hybrid assembly (5-FU@CD-HY) for cancer theranostics.
- 5-FU@CD-HY exhibited superior functional properties such as intact fluorescence, higher surface area, good mechanical strength, swelling behaviour and pH dependent drug release.

- These hybrids themselves served as a nanotheranostic system to track the intracellular distribution and apoptotic effects of the anticancer drug such as 5-FU.
- Apoptosis evoking ability of the released 5-FU was examined through morphological, cell cycle and nuclear analysis.
- The apoptotic mechanism was then established through gene expression analysis.

1.3 Organisation of thesis

This thesis presents an organized compilation of the research work performed over the years. In this regard, the thesis has been divided into nine chapters. Chapter 1 presents an introduction to the fluorescent nanoparticles theme that is primarily focussed on C-dots and their multimodal applications, followed by precise objectives and significance of the work undertaken. Relevant to the work, an updated literature review on C-dots synthesis and its applications, metal-based nanoparticles and hydrogels has been summarized in chapter 2. a detailed account of experimental procedures has been provided in chapter 3. In chapter 4, a comparative analysis of the physicochemical and bioimaging properties of PEI/PEG surface functionalized C-dots has been done. Chapter 5 describes the green synthesis of C-dots from coriander leaves and their potential applications as antioxidants, sensors and bioimaging agents. Chapter 6 deals with the synthesis of C-dots-cerium oxide nanocomposites and their prospective application for monitoring as well as scavenging reactive oxygen species in fibroblast cells. Chapter 7 illustrates the formation of dual functional C-dots–silver@zinc oxide nanocomposites for simultaneous evaluation of cellular uptake and apoptosis induction in cancer cells. Chapter 8 elucidates the construction of a chitosan hydrogel-based hybrid assembly involving the inclusion of the synthesized C-dots and 5-Fluorouracil for cancer theranostics. Finally, the concluding remarks and the future scope of the present work have been discussed in chapter 9.

CHAPTER 2

LITERATURE REVIEW

This chapter provides an updated literature review on C-dots synthesis and its applications. The chapter also discusses various metal-based nanoparticles and hydrogels relevant to the thesis.

CHAPTER 2

LITERATURE REVIEW

2.1 Carbon dots (C-dots)

Carbon is generally a black material with low solubility and no fluorescence. As the size of the material decreases, the properties begin to change. Consequently, nanosized carbon has strikingly different properties compared to bulk carbon. The existence of C-dots came to light when researchers were trying to purify single-walled carbon nanotubes (SWCNTs) through preparative electrophoresis in 2004. Accidently, they observed a fast-moving band of highly luminescent carbonaceous material which was certainly not the SWCNTs (Xu et al., 2004). The first complete study regarding the origin and fluorescence of C-dots was provided by Sun's group (Sun et al. 2006). They employed oligomeric species for rendering effective passivation of the dot's surface, resulting in bright fluorescence emissions. C-dots are the newly discovered fluorescent, zero dimensional nanomaterials that constitute a class of nanocarbon family with quasispherical shape and sizes below 10 nm. They contain an amorphous or nanocrystalline cores with primarily sp^2 hybridized turbidostatic or graphitic carbon (Baker et al., 2010 and Li et al., 2012a). In addition to carbon, C-dots contain substantial fractions of oxygen and hydrogen due to which these are sometimes referred to as 'carbogenic dots' (Bourlinos et al., 2008 and Peng et al., 2009). With the advancements in the field of C-dots research, their fluorescence emission in particular has been generating interest for various applications. Semiconductor quantum dots (QDs) and C-dots share similar optical and physical properties with overlapping area of application (Zrazhevskiy et al., 2010 and Petryayeva et al., 2013). However, QDs have a heavy metal core (CdSe, CdTe) and are usually synthesized in organic-phase system by complex methodologies which limit their applicability on account of toxicity and high cost (Tagit et al., 2009, Blum et al., 2011, Stopel et al., 2013 and Chauhan et al., 2014). Contrastingly, C-dots exhibit some remarkable features in terms of being environmentally and biologically benign, high aqueous solubility, colloidal stability, chemical inertness and readily surface functionalization. What's more heartening is the fact that C-dots can be synthesized in a cost effective manner through numerous simple approaches with sufficiently high yield. Therefore, C-dots are gaining grounds for biological applications and emerging as the most sought after alternative to QDs for similar fluorescence related applications. In fact, the competitive performance of C-dots in comparison with QDs for

bioimaging applications has also been studied (Cao et al., 2012 and Fang et al., 2012). Typically, C-dots display some unique properties which have been outlined in **Fig. 2.1**. With their additional distinctive features such as ease of bioconjugation, resistance to photobleaching and stability under physiological conditions, C-dots have been utilized for a host of prospective biological applications including bioimaging, biosensing, photodynamic therapy and drug delivery (Luo et al., 2013 and Zhang et al., 2015). Moreover, the fluorescence of C-dots can be quenched by photoinduced electron transfer processes, enabling their use for different analytical applications (Zuo et al., 2016). Multifunctional features of C-dots enable their use for a host of prospective applications as illustrated in **Fig. 2.2**.

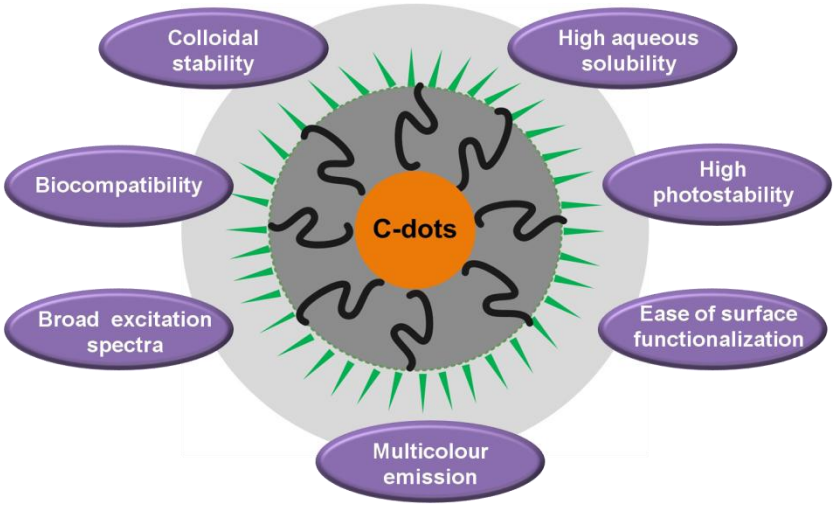

Figure 2.1 General properties of C-dots.

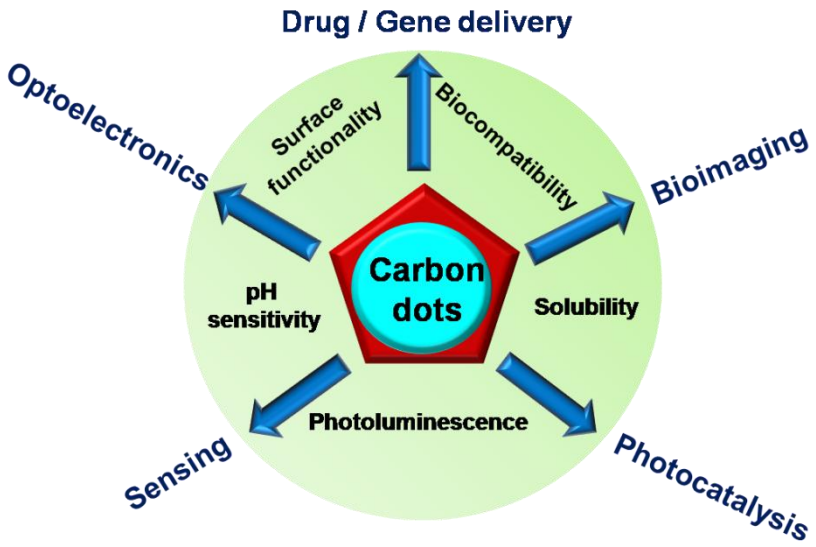

Figure 2.2 Potential areas of application for C-dots.

2.2 Synthetic methods for C-dots

The synthetic approaches for C-dots can be categorized into two main groups: top-down and bottom-up. Top-down approaches include arc discharge, electrochemical and laser ablation which involve the breakdown of chunks of carbon structure, which are quite complicated processes and require energy-consuming devices. In comparison, the bottom-up approaches are inexpensive and involve the synthesis of C-dots from molecular precursors by means of chemical reactions through microwave and combustion/chemical oxidation/thermal treatments (Baker et al., 2010).

2.2.1 Arc discharge

During the purification of SWCNTs derived from the arc discharge soot, Xu et al., 2004 discovered the C-dots for the first time. The arc-discharge soot was reacted with 3.3 N nitric acid for introduction of carboxyl groups to impart hydrophilicity. Sediment was then extracted with sodium hydroxide to obtain a black suspension which was further separated by gel electrophoresis. This resulted in fraction of C-dots with size dependent emission properties.

2.2.2 Electrochemical synthesis

Zhou et al., 2007 produced C-dots by electrochemical oxidation of multiwalled carbon nanotubes (MWCNTs) grown on carbon paper. An electrochemical cell consisting of MWCNTs as working electrode was immersed in an electrolyte solution of degassed acetonitrile containing 0.1M tetrabutylammonium perchlorate. Cycling applied potential resulted in change in colour of solution from yellow to dark brown, indicating the formation of C-dots. Various carbon nanomaterials, including C-dots were fabricated from high purity graphite rods by ionic liquid mediated exfoliation process. By changing the water/ionic liquid ratio, the C-dots production efficiency could be increased (Lu et. al., 2009). Zheng et al., 2009 demonstrated synthesis of C-dots by an electrochemical assembly consisting of graphite rod as working electrode with Pt mesh as counter electrode inserted in a phosphate buffer solution.

2.2.3 Laser ablation

This method of synthesis is based on laser assisted irradiation of carbon target in liquid. Sun et al., 2006 performed laser ablation of carbon target composed of a mixture of graphite powder and cement under the flow of argon gas. The obtained nanosized carbon aggregates were non-fluorescent. Further, the sample was refluxed with nitric acid solution for 12 h and finally surface passivated by diamine-terminated poly(ethylene glycol) (PEG1500N) or poly(propionylethylenimine-co-ethylenimine) (PPEI-EI) to produce strongly photoluminescent

C-dots. Hu et al., 2011 reported an efficient method for *in situ* synthesis and passivation of C-dots. In this method, graphitic flakes were dispersed in PEG 1500N by ultrasonication. A pulsed Nd:YAG laser mediated irradiation produced a black suspension which was subsequently centrifuged to obtain supernatant containing fluorescent C-dots. C-dots synthesized by laser irradiation usually have a broad size distribution and larger particles are washed away during subsequent processing steps. Hence, the yields of C-dots are generally low which hinders their utilization for various applications.

2.2.4 Microwave assisted synthesis

Microwave technique has been one of the most preferred processes for C-dots synthesis because of inherent advantages such as rapid heating and enhanced reaction rates. Several research groups have explored the formation of carbon dots from various carbonizable precursors through microwaves. Microwave assisted pyrolysis of PEG 200 and a saccharide (glucose or fructose) was done at 500 W for several minutes to synthesize C-dots (Zhu et al., 2009). In a follow-up study, a single step method for the synthesis of C-dots from carbohydrates (glycerol, glycol, glucose, sucrose) with the aid of an inorganic ion solution was reported, bypassing the use of surface passivation agent (Wang et al., 2011). The quantum yield of C-dots produced was less than 6%. In a similar attempt, blue fluorescent C-dots were produced by using 4,7,10-trioxa-1,13-tridecanediamine (TTDDA) as a passivating agent and glycerol as a carbon source by microwave irradiation with improved quantum yield values upto 15% (Liu et al., 2011). Following, Zhai et al., 2012 reported the plausibility of producing C-dots from a small molecule like citric acid in the presence of various amine molecules which serve as both N doped precursors and surface passivation agents. Polyethylenimine (PEI) functionalized carbon dots fabricated by microwave irradiation of a mixture of glycerol and branched PEI, wherein the latter being a nitrogen-rich compound was responsible for enhancing the fluorescence of C-dots. A rapid, one-step microwave mediated method for synthesizing C-dots using poly(ethylene glycol) (PEG) as a carbon source as well as a passivating agent was also been reported (Jaiswal et al., 2012). Water-soluble, green fluorescent phosphorous containing C-dots were produced using phytic acid by a similar approach (Wang et al., 2014d). Chowdhury et al., 2013 explored the possibility of obtaining C-dots from chitosan gel. C-dots demonstrating multicolour fluorescence were fabricated by carbohydrate carbonization approach using chitosan, a polysaccharide as a carbonaceous material and PEG 4000 for *in situ* surface passivation. Subsequently, highly fluorescent C-dots were obtained within minutes without any sort of post-synthetic treatment (Sachdev et al., 2013). Compared to other approaches, microwave mediated synthesis offers a simple, rapid and

economical means of synthesizing C-dots from organic precursors. Although efficient, the C-dots produced by this technique have low brightness which makes them unsuitable for biological applications. Moreover, the fumes produced during the carbonization process under microwave irradiation are often considered bad for human health and environment (Beyler et al., 1995).

2.2.5 Combustion/chemical oxidation/thermal routes

Combustion oxidation is one of the earliest reported methods of procuring C-dots from the soot obtained by the combustion of unscented candles or natural gas burners (Liu et al., 2007, Ray et al., 2009 and Tian et al., 2009). Mao and co-workers synthesized multicolour C-dots from the soot collected from a burning candle. Oxidative acid treatment of the soot introduced –OH and –COOH surface functionality. Obtained C-dots were further purified by polyacrylamide gel electrophoresis (PAGE) fractionation and hence resolved into discrete fluorescent bands. Electrophoretic mobility correlated with the observed fluorescence emission colour of C-dots, with the fast moving ones emitting at lower wavelength and vice versa (Liu et al., 2007). A similar approach was followed by Ray et al., 2009 in which size based separation of C-dots was carried in a solvent mixture of water/ethanol/chloroform in conjugation with high-speed, stepwise centrifugation. Recently, C-dots were extracted from pollutant diesel soot by a series of purification steps (Tripathi et al., 2014).

Chemical oxidation approach relies on the oxidative treatment of carbon sources to prepare C-dots. A simple aqueous route to obtain C-dots from carbohydrates was explored (Peng et al., 2009). Dehydration of carbohydrates by concentrated sulphuric acid produced sufficient carbonaceous material, which was further broken down into carbon nanoparticles via refluxing in nitric acid solution. Finally, surface passivation by TTDDA produced fluorescent C-dots. Similarly, Zhang et al., 2010 proposed a high-yield synthetic method for blue and green luminescent C-dots by controlled carbonization of sucrose and subsequent surface functionalization. An automatic chemical method for the synthesis of green fluorescent C-dots was demonstrated by simple mixing of acetic acid, water and diphosphorous pentoxide (P_2O_5) without any external heating. Here, acetic acid acted as a carbon precursor while P_2O_5 aided in catalyzing the carbonization reaction (Fang et al., 2012).

Thermal approaches like solvothermal and hydrothermal principally involve the pyrolysis of carbonaceous precursors under high temperature conditions to generate C-dots. These techniques have become increasing popular amongst various research groups owing to simple

equipment setup, low cost, eco-friendly and non-toxic production of C-dots from a variety of synthetic or natural organic sources (Komarneni, 2003). In this approach, the C-dot precursor solution is sealed inside a stainless steel vessel and reaction proceeds under high temperature (> 100°C) and pressure conditions. When water is used as a solvent, the above process is referred to as 'hydrothermal', while in case solvent other than water is used the process is considered as 'solvothermal'. Nitrogen doped C-dots were synthesized by a one-pot solvothermal route using carbon tetrachloride (CCl_4) and sodium amide ($NaNH_2$) mixture in methylbenzene (Ma et al., 2012). A green solvothermal route was adopted in which oxidative degradation of PEG 200 by a strong alkali was performed and further subjected to solvothermal heating at 160 °C for 24 h (Mitra et al., 2013). Hydrothermal route for C-dots synthesis is advantageous since it circumvents the multistep surface passivation problems and provides controlled reaction conditions. Generally, the hydrothermal synthesis of C-dots is accomplished by pyrolysis of a single precursor that acts as both carbon source and a passivating agent or by employing two components, that is, a passivating agent in addition to carbon precursor (Li et al., 2012a, Yang et al., 2012, Zhang et al., 2012, Sachdev et al., 2013,and Li et al., 2013a). In the recent past, a facile hydrothermal method for production of C-dots from glucose in the presence of monopotassium phosphate (KH_2PO_4) was reported (Yang et al., 2011). The formation and passivation proceeded simultaneously to produce intrinsically fluorescent C-dots, while the concentration of KH_2PO_4 dictated the fluorescence emission colour. Amino-functionalized C-dots were produced through the dehydration of chitosan saccharide structure without the aid of any strong acid solvent or surface passivation (Yang et al., 2012). Similarly, the hydrothermal treatment of several other carbohydrate moieties (maltose, lactose etc.) for C-dots production was also explored (Zhang et al., 2013 and Liu et al., 2014b). Yang et al. 2014a employed hydrothermal method to synthesize nitrogen-doped C-dots using ammonium citrate, serving as both carbon source as well as meeting the requirements of surface passivation. The groups on the surface of N-doped CDs acted as a self-passivation layer. Polyamine-functionalized C-dots were synthesized by carbonizing citric acid at a lower temperature (< 200°C) using bPEI as a functionalizing agent (Dong et al., 2012). Zhu et al., 2013c employed citric acid as a carbon source in combination with ethlenediamine as a separate nitrogenous passivation agent to obtain C-dots with higher quantum yields (upto 80%).

Green synthesis of C-dots is a highly attractive research topic, which exploits the use of natural, renewable carbon precursors. Nevertheless, it is always exciting to explore the green sources for C-dots because these are inexpensive, clean, nontoxic and easily accessible. A detailed

account of various methodologies for C-dots synthesis from natural carbonaceous green sources has been provided in **Table 2.1**.

Source	Synthesis method	Fluorescence emission	Reference
Orange juice	Hydrothermal	Green	Sahu et al. 2012
Pomelo peel	Hydrothermal	Blue	Lu et al. 2012
Soy milk	Hydrothermal	Blue	Zhu et al. 2012
Protein	Hydrothermal	Blue	Zhang et al. 2012
L-ascorbic acid	Solvothermal	Green	Wu et al. 2012
Egg shell	Microwave	Blue	Wang et al. 2012
Food caramels	Pyrolysis	Blue	Sk et al. 2012
Coffee grounds	Pyrolysis	Blue	Hsu et al. 2012
Grass	Hydrothermal	Blue	Liu et al. 2012
Watermelon peel	Pyrolysis	Blue	Zhou et al. 2012
Hair	Sulphuric acid carbonization and hair etching	Blue	Sun et al. 2013
Willow bark	Hydrothermal	Blue	Qin et al. 2013
Flour	Microwave	Blue	Qin et al. 2013
Plant leaves	Pyrolysis	Blue	Zhu et al. 2013
Grape juice	Hydrothermal	Blue	Huang et al. 2014
Milk	Hydrothermal	Blue	Wang et al. 2014
Potato	Hydrothermal	Blue, green and red	Mehta et al. 2014
Waste biomass	Ultrasonic	Blue	Park et al. 2014
Honey	Hydrothermal	Blue	Yang et al. 2014
Oats	Microwave	Blue	Shi et al. 2015
Lime juice	Hydrothermal	Green	Barati et al. 2015

Table 2.1 Synthetic scheme of C-dots from natural green sources by various methodologies.

However, the key challenge remains to produce C-dots with high quantum yields in ample amounts by using simple one-step methodologies. In the recent past, the hydrothermal preparative protocols for C-dots from biological materials have been well-documented.

Accordingly, the hydrothermal treatment of natural green sources orange juice (Sahu et al., 2012), grape juice (Huang et al., 2014), milk (Wang et al., 2014b), potato (Mehta et al., 2014), oats (Shi et al., 2015) and even waste biomass (Park et al., 2014) have been reported for C-dots. In the above investigations, the subsequent surface functionalization of CDs by various groups such as hydroxyl, carboxylic and amino was accomplished from the organic moieties present in the respective sources, thereby eliminating the need of auxiliary passivation agent. Hence, a green hydrothermal approach could be envisioned as an effective and economical means of producing highly fluorescent, water soluble C-dots on large scale for practical applications.

2.3 Fluorescence emission of C-dots

Fluorescence emission is one of the most exciting features of C-dots. Underlying the difficulty in predicting the exact fluorescence mechanism is the fact that the C-dots are prepared from numerous sources through diverse approaches and possess multiple complicated structures (Zhai et al., 2012, Nie at al., 2014, Hu et al., 2015 and Fu et al., 2015). In the available literature, wide discrepancies exist regarding the fluorescence origin in C-dots and are still debatable. Surface passivation is one of the phenomenon for inducing or improving the fluorescence emission from the dot surface **(Fig. 2.3)**. In one of the earlier studies it was found that the acid treated carbon nanoparticles could be made fluorescent only after surface passivation by diamine terminated oligomeric polymer (PEG 1500N) (Sun et al., 2006). This suggested the role of surface passivation for stabilization of surface energy traps for fluorescence emission. Apart from this, other nitrogen containing organic moieties such as polyethleneamine (PEI), poly(ethylenimide)-co-poly(ethyleneglycol)-co-poly(ethyl-enimide) (PPEI), ethylenediamine (EDA) and 4,7,10-trioxa-1,13-tridecanediamine (TTDDA) have been commonly employed for surface passivation (Cao et al., 2007, Liu et al., 2012a, Sachdev et al., 2013 and Ding et al., 2013). The attachment of nitrogenous groups onto the surface of C-dots has been found to generate stronger fluorescence emission in CDs. Also, various oxygen containing groups such as carboxyl, carbonyl, epoxy, hydroxyl have been implicated for fluorescence emissions. Candle soot derived C-dots contained abundant carbonyl groups and required no further passivation for fluorescence emission (Liu et al., 2007 and Tian et al., 2009). Besides, carboxylic groups on the surface of CDs have been held responsible for fluorescence (Hu et al. 2009). Another interesting scheme of improving the fluorescence emission of C-dots involves the doping of C-dots by inorganic salts or heteroatoms. For example, core carbon nanoparticle surface was doped with inorganic salts (ZnO, ZnS, or TiO2) along with the organic functionalization (Baker et al., 2010, Luo et al., 2013). The resulting C-dots (C_{ZnO}-dots, C_{ZnS}-dots, or C_{TiO2}-dots) exhibited much brighter fluorescence emissions

than their undoped counterparts. Dong et al. 2013 suggested strong fluorescence emission of C-dots as a result of surface-doped nitrogen or sulphur atoms. Additionally, mechanistic studies on fluorescence origin in C-dots suggest the synergistic effect of carbon nanoparticles core and surface functional groups in creating complex surface states (Zhu et al., 2013c). Investigation by ultrafast spectroscopy revealed the formation of special edge states consisting of carboxyl and carbonyl groups formed by the hybridization of carbon backbone with surface chemical groups give rise to green emission centres (Wang et al., 2014f).

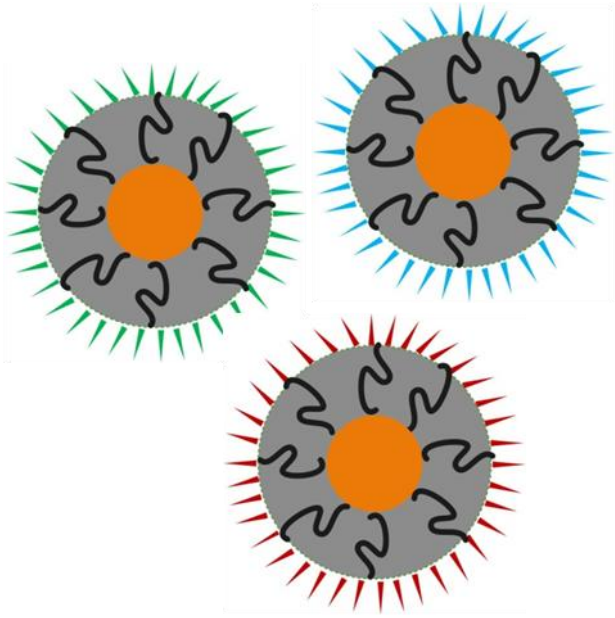

Figure 2.3 Fluorescent C-dots surface functionalized with organic, polymeric, inorganic or biological species.

Multicolour fluorescence in C-dots is another interesting feature which arises due to the presence of multiple emissive sites in a single particle or different sizes of the particle. The origin of excitation-dependent multicolour emission in C-dots was shown to be governed by the relative population of the emissive states rather than the different particle sizes or surface groups (Khan et al., 2015a). On the contrary, size dependent emission was found in C-dots fractioned according to size. C-dots emitted blue, green, yellow and orange fluorescence with an increase in size (Li et al., 2010b). Thus, it was demonstrated that the quantum confinement effects were responsible for the observed size dependent behaviour. Furthermore, surface passivation also influences multicolour fluorescence in C-dots. Surface passivated C-dots demonstrated excitation dependent fluorescence behaviour resulting in blue, green and red colour emission. Possibly, surface passivation causes the stabilization of various emission trap sites. These surface energy sites become emissive through effective radiative recombinations at different excitation wavelengths leading to multicolour emission (Sachdev et al., 2013).

Contrastingly, full spectrum tunable emitting C-dots were produced by controlling the oxygen and nitrogen contents in dots by tailoring the reagents during the synthetic process (Hu et al., 2015). Recently, Ding et al., 2016 reported C-dots with stable luminescence spanning the visible spectrum (blue to red) under single wavelength. C-dots were separated via silica column chromatography and differed with respect to surface states. Differences in surface states of the samples resulted from the varying degrees of oxidation which ultimately determined the fluorescence colour. Hence, the authors demonstrated that the surface energy bands were dependent on the surface groups and structures, rather than on the particle size.

2.4 C-dots as bioimaging agents

Ever since its inception, C-dots have been explored extensively for fluorescence based bioimaging applications. Owing to excellent fluorescence properties, low toxicity and aqueous solubility, C-dots fulfils the essential attributes of an ideal bioimaging agent (Luo et al., 2013 and Wang et al., 2014e). Of particular interest is the multicolour fluorescence and NIR emission of C-dots, which holds relevance for *in vitro* and *in vivo* imaging applications. Meanwhile, versatility of C-dots provides an opportunity for engineering C-dot based multifunctional platforms for various biomedical applications.

2.4.1 Cellular imaging *in vitro*

Sun et al., 2006 provided the first ever evidence of biolabelling by incubating *E. coli* bacteria with surface passivated C-dots and observed multicolour fluorescence by changing the excitation wavelength. Similarly, biolabeling mechanism of PEG passivated multicolour C-dots (CPs) was studied using Gram-positive *S. aureus* and Gram-negative recombinant green fluorescent protein (GFP)-expressing *E. coli* as model systems (Sachdev et al., 2013). CPs labelled GFP *E. coli* and *S. aureus* cells radiated light green, blue and red colour under various fluorescence microscopy filters. Time-dependent microscopy using GFP *E. Coli* bacteria further predicted optimal labelling time of 3 h for multicolour emission. Transmission electron microscopy (TEM) images provided evidence of cellular uptake of CPs inside bacterial cells at a concentration of 0.1 mg mL^{-1} without any bactericidal effects. Subsequently, C-dots were pursued for multiphoton bioimaging in mammalian cells such as MCF-7 cells. PPEI-EI passivated C-dots were found to be strongly emissive under fluorescence microscope following excitation by 800 nm laser. The cellular uptake of C-dots was restricted to the cell membrane and the cytoplasm of MCF-7 cells (Cao et al., 2007). Yet another study highlighted that L929 cells incubated with N doped photoluminescent C-dots emitted blue, green and red fluorescence under different excitation wavelength from the cytoplasmic area (Zhai et al.,

2012). So far, most of the available literature suggests that the C-dots without any specialized modifications localize mainly in the cytoplasmic areas via passive endocytosis, without any evidence of nuclear labelling. However, in a recent study HeLa cells incubated with C-dots showed nuclear uptake. The internalized C-dots were further able to selectively stain the nucleoli, thereby achieving organelle selection (Kong et al. 2014). Besides, bioconjugated C-dots have been used for specific targeting in various studies. For monitoring the pH changes in living cells, a C-dot based two-photon fluorescence probe was developed by covalent conjugation with a receptor molecule 4′-(aminomethylpheynl)-2′2′:6′,2′′-terpyridine (AE-TPY) (Kong et al., 2012). C-dots have also been used for specific targeting and imaging of cancer cells. An aptamer-conjugated imaging probe was developed for targeting cancers. Thiol-terminated C-dots (SH-gC-dots) were conjugated with maleimide-terminated TTA1 aptamer for targeting Tnc proteins (TTA1-C-dots). To study the possibility of targeting cancers using the TTA1-C-dots, HeLa (human cervical cancer cells), C6 (rat glioma cells) were selected as cancer cell lines, while CHO (Chinese hamster ovary cells) was used as non-cancerous model cell line. Compared with the SH-gC-dots, the targeting efficiency of the TTA1-C-Dots was higher in HeLa and C6 cells. The increase in fluorescence emission intensity for HeLa and C6 cell lines treated with the TTA1-C-dots correlated with enhanced targeting with respect to the SH-gC-Dots. However, in CHO cells, no detectable difference in fluorescence intensity was observed between TTA1-C-dots and SH-gC-dots (Lee et al., 2013b). There have been specific instances in which C-dots based folate receptor (FR) targeting in cancer cells was followed (Song et al., 2012, Wang et al., 2015 and Bhunia et al., 2016a). Folic acid (FA) conjugated fluorescent carbon nanodots (C-dots-FA) were synthesized which could be endocytosed by the overexpressed FR molecule (Song et al., 2012). The assembly was able to distinguish folate positive HeLa cancer cells from folate negative MCF-7 cancer cells. Additionally, HeLa cells produced bright fluorescence in comparison to normal NIH3T3 cells due to lower expression of FR receptor in normal cells, resulting in lesser uptake of C-dots-FA. This clearly indicated that the C-dots-FA system could discriminate FR-positive cancerous cells from normal cells. Likewise, C-dots loaded silica nanospheres were surface functionalized with folic acid for targeted bioimaging of cancer cells (Wang et al., 2015). Additionally, Ruan et al., 2014 demonstrated the potential of angiopep-2 (glioma targeting ligand) conjugated PEGylated C-dots for noninvasive glioma imaging. The above reported studies highlight that C-dots are amenable to various cell imaging applications without compromising their fluorescence properties.

2.4.2 *In vivo* imaging

The use of C-dots for *in vivo* mice imaging was first ever reported by Sun's group. C-dots were injected into the mice through three injection routes, namely subcutaneous, intradermal and intravenous. In all the cases, the C-dots remained strongly fluorescent post injection *in vivo* (Yang et al., 2009a). In yet another study, PEGylated C-dots were administered to mice in high doses. Histopathological analyses of liver, spleen and kidneys of mice were performed. The liver and spleen were excised from mice 6 h after intravenous exposure to C-dots. Liver and spleen had relatively higher amounts of C-dots. Further, no toxicity was observed in mice for extended periods of time (Yang et al., 2009b). Li et al., 2012b performed a similar bio distribution study of C-dots. Following tail vein injection, mice were harvested and frozen sections of different organs were obtained. Bright blue fluorescence of C-dots was visible in heart, liver, spleen, lung, kidney, intestine as well as in brain at 6, 16 and 24 h post injection. Out of these, spleen had the brightest blue fluorescence, indicating more uptake. Apart from biocompatibility, C-dots have exhibited the same or even better performances for *in vivo* imaging in mice models compared to commercially available CdSe–ZnS QDs (Cao et al., 2012). NIR fluorescence imaging potential of C-dots was also investigated in recent studies which is particularly noteworthy for *in vivo* imaging, because of lesser autofluorescence and tissue transparency in the NIR region (Tao et al., 2012 and Li et al., 2012a). Recently, angiopep modified PEGylated C-dots showed selective, significant glioma accumulation compared to their unmodified counterparts (Ruan et al., 2014).

2.4.3 C-dots based theranostics

Theranostics is a term generally used to refer to the incorporation of imaging and therapeutic modalities in a single platform (Kelkar et al., 2011 and Liu et al., 2014a). There have been several reports wherein C-dots directly serve as theranostic agents or employed for bioimaging purposes as part of a multifunctional theranostic system. C-dots have been shown to have cancer inhibition activity along with the bioimaging properties. As-prepared C-dots from green tea tend to inhibit growth of breast cancer cells such as MCF-7 and MDA-MB-231 in a dose dependent manner but showed less toxicity towards MCF-10A normal cells. The production of reactive oxygen species (ROS) was considered to be the main reason behind cancer inhibition effect of C-dots. With an increase in C-dots concentration, cellular levels of H_2O_2 increased and resulted in induction of apoptosis which ultimately led to the killing of cancer cells (Hsu et al. 2013). In yet another study, C-dots prepared from ginger juice were shown to have selective anticancer activity against HepG2 cancer cells and low cytotoxicity towards normal cells MCF-10A and FL83 B cells. IC_{50} value of C-dots on HepG2 cells was reported to be 0.35 mg mL^{-1}.

Western blot analysis revealed an up-regulation of tumor suppressor gene p53 in HepG2 cell line. Intracellular ROS production in C-dots treated HepG2 cells increased 18.2-fold with respect to normal cells ultimately leading to apoptosis (Li et al., 2014a). All the above instances signify the importance of the C-dot precursors in bestowing the requisite therapeutic response.

C-dots have also been examined as drug delivery systems (DDS). Hollow C-dots (HCDs) have been used for delivery of anticancer drug, doxorubicin (DOX). DOX-HCD complex displayed a pH-dependent release and performed the dual role of cell imaging and anticancer activity. The inherent green fluorescence of HCDs and red fluorescence of DOX formed a dual emission delivery system. Internalization of such a system was observed in A549 cancer cells by fluorescence microscopy. Green emission of HCDs in cytoplasm was observed after 24 h and red emission inside nucleus was due to the release of DOX from HCD and its entry inside the nucleus (Wang et al., 2013a). Similarly, FA capped C-dots modified with BSA have been used for the delivery of DOX to cancer cells. C-dots-FA-@DOX complex specifically targeted HeLa cancer cells by interaction with FR receptor and showed bright green coloured fluorescence, where as bare C-dots without FA depicted negligible fluorescence in HeLa cells. C-dots-FA-@DOX complex had an IC_{50} value of less than 0.04 mM, much lower than free DOX (0.08 mM) due to enhanced targeting and uptake by HeLa cells (Mewada et al., 2014). C-dots have also been integrated with Oxaliplatin (CD-Oxa) by means of condensation reaction between the amino groups on the surface of C-dots and the carboxyl group of Oxa(IV)-COOH. The theranostic complex CD-Oxa combines the bioimaging properties of C-dots and anticancer action of Oxaliplatin. This allows the tracking of drug molecules inside the cell by monitoring the fluorescence intensity of the complex. The activity of CD-Oxa complex was tested against HepG2 cancer cells. Upon incubation, the cells displayed multicolour emission due to internalization of CD-Oxa. Further, for *in vivo* studies mouse were injected with CD-Oxa (0.72 mg mL^{-1}) at the site of tumor. The fluorescence emission was detected readily, fluorescence area spreaded around the injection site to form a gradient density distribution. Fluorescence signal faded after 24 h and subsequent injections were done for repeated doses. With increasing time, tumor suppression was observed indicated by the flattening of tumor area (Zheng et al., 2014). For C-dot based photoresponsive theranostics, a quinoline phototrigger conjugated anticancer drug, 7-(3-bromopropoxy)-2-quinolylmethyl chlorambucil (Qucbl) was tethered onto the surface of C-dots (Qucbl-Cdots) for photoresponsive and regulated drug release. Activity and cellular uptake of the conjugate was studied using HeLa cancer cells. After 4 h incubation, cells exhibited bright green fluorescence in the cytoplasm and nucleus. Further, the cytotoxicity studies of Qucbl-Cdots on HeLa cells depicted decrease in cell viability with an

increase in chlorambucil concentration, while the viability remain unaffected for C-dots treated cells. Exposure to light caused the release of Qucbl from Qucbl-Cdots complex inside the cells ultimately leading to cell death. Optimal irradiation time for drug release to achieve the highest cytotoxicity was found to be 30 min, indicating the release of most of the tethered drug from Qucbl-Cdots complex (Karthik et al., 2013).

Gene delivery is perceived as a potential treatment for many disorders. Intrinsic biocompatibility and phenomenal fluorescence properties confer noteworthy advantages for the use of C dots as gene delivery agents. C-dots have the unique ability to sneak through the biological membranes with ease and deliver the desired therapeutic agent either directly or after some surface modification. C-dots passivated with a cationic polymer, PEI (CD-PEI) was complexed with plasmid DNA (pDNA) for executing gene transfection and subsequent expression. Confocal microscopy images revealed that CD-PEI were able to pDNA delivery to HeLa cells with transfection efficiency comparable to control PEI, but with lesser cytotoxic effects (Liu et al., 2012a). In a follow up study, a hybrid CD-PEI assembly was proposed for the real-time tracking of pDNA. CD-PEI was able to condense the pDNA in varying weight ratios and hence successfully transfected COS-7 and HeLa cells. Besides, the fluorescence of C-dots was used to monitor the association/dissociation of polymeric carrier/pDNA complex during transfection. The strategy involved the incorporation of PEI funcnationalized gold nanoparticles (PEI-Au) for tuning the fluorescence response of CD-PEI. Association of the whole complex with pDNA resulted in quenching of C-dots fluorescence. During transfection, at the post-endosomal step high salt concentrations cause the dissociation of the complex resulting in the release of pDNA and fluorescence recovery of C-dots, facilitating concomitant tracking of gene delivery (Kim et al., 2013). Lately, C-dots have also been exploited for siRNA delivery (Pierrat et al., 2015).

Photodynamic therapy (PDT) is one of the established cancer treatment modalities (Deng et al., 2015). Absorption of light of specific wavelength activates the photosensitizer (PS) to form ROS which ultimately cause the death of the cells in the vicinity. The use of C-dots for PDT based theranostics is relatively a newly discovered area. In one such approach, a photosensitizer, chlorin e6 was conjugated to C-dots (C-dots-Ce6) through conventional EDC–NHS chemistry for simultaneous fluorescence imaging and PDT under *in vitro* as well as *in vivo* conditions. The fluorescence emission of C-dots was found to overlap with the absorption of Ce6 which meant that C-dots could indirectly excite Ce6 by fluorescence resonance energy transfer (FRET). After 2 hours of incubation, red fluorescence was observed in the cytoplasm

of human MGC803 cells owing to localization of C-dots-Ce6. Further, C-dots-Ce6 incubated cells irradiated by laser depicted concentration-dependent cytotoxicity compared to non-irradiated controls. *In vivo* theranostics of C-dots-Ce6 was performed on nude mice with subcutaneous MGC803 gastric cancer xenograft. After sufficient growth of tumors, the mice were intravenously injected with C-dots-Ce6. Post injection, significant fluorescence emission was observed in the tumor area after 2-4 h which reached its plateau value between 4-8 h. Thus, PDT was realized after 8 h post injection by optimizing the fluorescence emission (Huang et al., 2012). On similar lines, a targeted C-dots based nanoprobe for PDT was developed by using zinc pthalocyanine as PS and FA as a targeting moiety (Choi et al., 2014). Recently, 5,10,15,20-tetrakis(1-methyl 4-pyridinio) porphyrins (TMPyP), a PS, was electrostatically conjugated to C-dots and used for two-photon (TP) excited PDT. Besides imaging capabilities, C-dots also tend to increase the water solubility of PS molecules through conjugation which generally have low solubility under aqueous conditions (Wang et al., 2014g).

2.5 Fluorescence sensing based on C-dots

Metal ion sensing is one of the most studied analytical applications of C-dots (Zuo et al., 2016 and Gupta et al., 2016a). Mercuric (Hg^{2+}) ion contamination poses serious threat to environment and is considered as a health hazard. Inspired by this challenge, C-dots based sensing of Hg^{2+} ions has been explored. Gonçalves et al., 2010 performed Hg^{2+} sensing based on static quenching due to formation of C-dots-Hg^{2+} complex. Yan et al., 2014 developed nitrogen doped C-dots (N-C-dots) and applied them for sensing of Hg^{2+} in river and mineral water. Further, N-C-dots were used for detection and imaging of Hg^{2+} inside living cells. Gupta et al., 2015 devised an efficient approach for detection of Hg^{2+} by nitrogen doped PEGylated C-dots which were further functionalized with dithiothreitol and used for detection of thiols. Recently, a cost-effective smart phone app was developed for real-time quantification of Hg^{2+} concentrations based on image analysis. Hg^{2+} concentrations were correlated with the brightness of C-dots which formed the basis of detection (Wang et al., 2016b). C-dots have been used as Fe^{3+} sensors as well. The work done by Zhu et al. 2013c demonstrated that the fluorescence of C-dots could be quenched by Fe^{3+} due to special coordination interaction between them. Fluorescence quenching mechanism was explained through time-correlated single photon counting (TCSPC), which predicted reduced lifetime of C-dots-Fe^{3+} complex compared to C-dots leading to dynamic quenching. C-dots synthesized by solid-phase approach were used as selective probe for detecting Fe^{3+} in living cells. This method was based on strong coordination between Fe^{3+} and oxygen groups of C-dots leading to non radiative electron transfer, presenting a fluorescence “turn off” means for Fe^{3+} determination (Zhang et al.,

2014a). A fluorescence turn "off-on" method for Fe^{3+} detection inside living cells was also proposed using C-dots derived from konjac fluor (Teng et al., 2014). Similar C-dots based label-free detection of Fe^{3+} was demonstrated in other studies as well (Wang et al., 2014a and Gong et al., 2015). Nevertheless, C-dots obtained through different synthetic schemes have been used for selective sensing of other metal ions such as Cu^{2+} (Zong et al., 2014), Pb^{2+} (Wee et al., 2013 and Gupta et al., 2016b), Co^{2+} (Li et al., 2015b), Sn^{2+} (Yazid et al., 2013) and Cr^{6+} (Zheng et al., 2013).

Endowed with intrinsic sensitivity and selectivity features, C-dots have been used for the detection of various molecules by monitoring the changes in their fluorescence emission behaviour. C-dots based silica aerogels were prepared for nitrogen dioxide (NO_2) gas sensing (Wang et al., 2013b). Similarly, a ratiometric probe based on blue emitting C-dots and red emitting CdTE QDs was developed for visual determination of NO_2 (Yan et al., 2015). C-dots have also been used as sensitive probes for detection of various biomolecules. For nucleic acid detection, dye-labeled single stranded DNA (ssDNA) was adsorbed onto the surface of C-dots resulting in fluorescence quenching of dye. This was followed by hybridization with complementary target ssDNA to form a hybrid double stranded DNA (dsDNA), which eventually gets detached from the C-dots surface leading to fluorescence recovery of dye. Additionally, the content of the target ssDNA could be determined by measuring the fluorescence intensity of the solution system before and after the addition of target DNA molecules (Li et al., 2011c). Boronic acid functionalized C-dots have successfully applied for non enzymatic blood glucose sensing and quantification (Shen et al., 2014). Dopamine (DOPA) is an important neurotransmitter whose deficiency is associated with many neurological disorders like schizophrenia, parkinson's and huntington's disease. A C-dots/tyrosine (C-dots/TYR) hybrid fluorescence probe was developed for dopamine detection. Oxidation of DOPA by TYR subsequently causes the fluorescence quenching of C-dots which forms the basis of detection. Moreover, the other guest molecules (metal ions, carbohydrates, phenols and cresols) showed negligible interference in DOPA detection (Li et al., 2014b). C-dots mediated detection of ROS has also been encountered. C-dots based ratiometric sensor for NO was realized through FRET process, where C-dots served as energy donor as well as anchor for NO recognition moiety (phenylenediamine containing naphthalimide). With an increase in concentration of NO, the fluorescence of CDs at 455 nm decreased, whereas a new emission band at 535 nm corresponding to fluorescence of energy acceptor- naphthalimide moiety appeared. Accordingly, the fluorescence emission of the solution turned from blue to green due to FRET process. The nanoprobe was able to track the exogenous NO levels in live cells as

well (Yu et al., 2013). A similar FRET based ratiometric probe was developed for mitochondrial H_2O_2 imaging by covalent linking a mitochondria-targeting ligand (triphenylphosphonium, TPP) in addition to H_2O_2 recognition element (PF l) onto C-dots (Du et al., 2014). For superoxide ($O_2^{\bullet-}$) anion sensing in living cells, C-dots acting as a reference fluorophore were hybridized to hydroethidine (HE), serving the dual role of recognition and response signal. Non fluorescent HE could recognize and react with $O_2^{\bullet-}$ and generated an emission peak at 610 nm upon 488 nm excitation wavelength, while the emission of C-dots at 525 nm under similar excitation remained unchanged, which formed the working principle for ratiometric detection of $O_2^{\bullet-}$ (Gao et al., 2014).

2.6 Antioxidant activity of C-dots

Very few, but sound evidence is available concerning the antioxidant potential of C-dots. In one of the earlier studies, free radicals generated chemically from an azo compound, 2,2-azodiisobutyramidine dihydrochloride (AAPH) were shown to be neutralized by C-dots and hence prevented the oxidation of the used radical probes dihydrorhodamine 123 (Dhr123) and Singlet Oxygen Sensor Green (SOSG). Moreover, the study suggested that the antioxidant effect was primarily targeted towards scavenging of singlet oxygen species (Christensen et al., 2011). Spent rapeseed meal derived C-dots were tested for their antioxidant potential via 2,2-diphenyl-1-picrylhydrazyl (DPPH) radical method. Antioxidant activity was detected on the basis of visual colour change of DPPH solution upon addition of C-dots. Probably, the quantum size effects and organic functionalities of C-dots enable the quenching of DPPH free radicals. The authors also formulated C-dot loaded protein nanocomposite films for packaging of oils, which were able to resist oxidation better than pristine protein sachet (Purkayastha et al., 2014). C-dots from date molasses demonstrated *in vitro* ROS scavenging potential. Nitro Blue Tetrazolium (NBT) assays confirmed the superoxide inhibition activity of C-dots inside the cells (Das et al., 2014). An increase in concentration of internalized C-dots caused the reduction in the number of black dotted (corresponding to NBT positive cells) MG-63 cells, thus relieving the oxidative stress inside the cells. Generally, the mechanisms for the antioxidant potential of C-dots are ambiguous and need further investigation.

2.7 Metal based nanoparticles

Over the years, the intrinsic properties of metallic nanoparticles (NPs) have been exploited for biomedical applications. These metal NPs exhibit exclusively different optical, electronic and chemical properties compared to bulk metal owing to quantum size effects (Schmid et al., 1999, Silva, 2004, Maksimova et al., 2008, Khlebtsov et al., 2008, Gill et al., 2013 and Liu et

al., 2015b). In addition, the NP based systems provide a platform for combining the properties of two or more different materials and enable their use as therapeutic agents for intended use (Mody et al., 2010, Panfilova et al., 2012 and Ravibabu et al., 2016). Thus, the prospective aspects of metal based NPs such as silver, zinc oxide and cerium oxide relevant to the thesis have been discussed below.

2.7.1 Silver nanoparticles

Silver nanoparticles (Ag NPs) are one of the much publicized nanoparticles which have been extensively applied for consumer and health-related applications. Antibacterial action of Ag NPs has been the subject of intense research contributing to their wide range of commercial applications such as water purification, food packaging, wound dressings, textile, cosmetics and paints (Mazurak et al., 2007, Gangadharan et al., 2010 and Dubey et al., 2015). Moreover, the therapeutic effects of Ag NPs on cancer cells have pharmaceutical implications. In a pioneering work, Asharani et al., 2009 reported the toxicity mechanism of Ag NPs using normal human lung fibroblast (IMR-90) and human glioblastoma (U251) cells. Possibly, the mitochondrial dysfunction initiated a cascade of events involving ROS production which triggered DNA damage, followed by cell cycle arrest at G2/M phase. A higher toxicity response was observed in U251 cells, highlighting the potential use of Ag NPs in cancer therapy. Gopinath et al., 2010 explored the apoptotic gene signalling pathway in Ag NPs treated human colon adenocarcinoma (HT29) cells. The findings suggested the occurrence of p53 dependent apoptotic pathway and mitochondrial DNA fragmentation leading to cell death. Similarly, Sanpui et al., 2011 loaded Ag NPs inside a chitosan nanocarrier for apoptosis induction using fairly low concentrations of Ag as an efficient approach compared to the use of free Ag NPs for similar purposes. Later, Ag NPs were co-delivered with an anticancer drug 5-Fluoruracil (5-FU) using a poly(amidoamine) (PAMAM) dendrimer as multifunctional nanocomposites for inducing synergistic antiproliferative effects in cancer cells (Matai et al., 2015). Thus, there is a need to develop combinatorial strategies for cancer therapy wherein Ag NPs could be used in minimal concentrations with other nanoparticles or chemotherapeutic drugs for mediating enhanced cytotoxic effects.

2.7.2 Zinc oxide nanoparticles

Metal oxide nanoparticles such as Zinc oxide (ZnO) nanoparticles often present themselves as versatile therapeutic agents. Bulk ZnO is considered as a ‘GRAS’ (generally recognized as safe) material by the FDA (Reddy et al., 2007). However, ZnO in the nano range has a relatively increased surface area, affecting the chemical reactivity and giving rise to unique

toxicity behaviour for specific biological applications. ZnO NPs share similar bactericidal and bacteriostatic mechanisms with Ag NPs, enabling their commercial use in food packaging materials. The incorporation of ZnO NPs in topical sunscreens and cosmetics largely due to their UV light absorption properties constitutes another vital application (Schilling et al., 2010 and Smijs et al., 2011). Due to widespread human exposure, the cytotoxicity mechanisms of ZnO NPs have been studied in detail in a wide array of organisms (Premanathan et al., 2011 and Sirelkhatim et al., 2015). The toxicity responses of ZnO NPs and the resultant cellular consequences upon uptake has been specifically studied in context of cancer cells (Rasmussen et al., 2010). Inherent preferential cytotoxic effect against cancer cell *in vitro* is one of the prime aspects observed for ZnO NPs (Hanley et al., 2008 and Wahab et al., 2014). The high degree of selective cancerous cell killing compared to normal ones was found to be dependent on the proliferation status of cells. Cancer cells with rapidly dividing capacities were obviously more susceptible. Moreover, ZnO NPs have displayed size dependent cytotoxicity in cancer cells, with the smaller ones being more toxic (Nair et al., 2009). Based on a body of evidence, ROS production leading to apoptosis has been elucidated as a decisive mechanism for cancer cell death (Moos et al., 2010, Wahab et al., 2014 and Sharma et al., 2012).

2.7.3 Cerium oxide nanoparticles

Cerium oxide nanoparticles (CeO NPs) have been synthesized through varied routes for numerous applications (Deori et al., 2013). In recent years, therapeutic applications of CeO NPs have been the matter of interest. CeO NPs have numerous surface defects due to oxygen vacancies together with high surface area to volume ratio, rendering catalytically active surface sites (Cassee et al., 2011 and Deori et al., 2015). The fascinating feature of CeO NPs to switch oxidation states between +3 (reduced) and +4 (oxidized) accounts for enzyme-mimetic activity, similar to biological antioxidants (Ratnam et al., 2006, Pirmohamed et al., 2010 and Xu et al., 2014). Specifically, redox state-dependent catalytic properties of CeO NPs have been explored (Deori et al., 2014). Higher Ce^{3+}/Ce^{4+} ratio in CeO NPs corresponds to superoxide dismutase (SOD) like activity which is beneficial for superoxide anions scavenging (Heckert et al., 2008). On the other hand, CeO NPs with lower Ce^{3+}/Ce^{4+} ratio demonstrated catalase mimetic activity by decomposing H_2O_2 to yield H_2O and O_2 (Pirmohamed et al., 2010). Such unique properties have prompted the use of CeO NPs as potential intracellular ROS scavengers (Karakoti et al., 2008, Lord et al., 2012, Ting et al., 2013 and Bhushan et al., 2015). Infact, CeO NPs have been shown to catalytically react with various ROS including hydroxyl radical ($OH^{\bullet}$), superoxide radical ($O_2^{\bullet -}$) and hydrogen peroxide (H_2O_2), depicting antioxidant properties (Korsvik et al., 2007, Asati et al., 2009 and Celardo et al., 2011). Accordingly, CeO NPs have been utilized as

antioxidant agents for the treatment of oxidative stress related diseases in cell as well as animal model systems. The therapeutic efforts were focussed on removal or prevention of ROS in a variety of disorders such as neurodegenerative, diabetes, retinal damage and cardiovascular diseases (Cedergren et al., 2007, Kumar at al., 2008 and Ray et al., 2012). Interestingly, CeO NPs have been reported to protect normal cells from ROS induced oxidative damage but not the cancer cells (Lin et al., 2006 and Perez et al., 2008). This selectivity in action can be attributed to pH dependent antioxidant activity of CeO NPs, due to loss of activity at low pH. Some recent reports have suggested that the uptake of CeO NPs in mammalian cells could induce cytotoxic effects, which discourages their potential applications (Park et al., 2008 and Hussain et al., 2012). Further, CeO NPs have been functionalized with dextran, heparin, PEG to improve the biocompatibility without compromising their therapeutic potential (Perez et al., 2008 and Ting et al., 2013). Efforts to develop safer formulations of CeO NPs along with better understanding of their biological interactions could pave the way for their clinical applications.

2.8 Hydrogels

Hydrogels are three-dimensional structures composed of cross-linked polymer networks. These networks are usually derived from water-soluble polymers, but resistant to dissolution due to the formation of chemical or physical bonds between the polymeric chains. Inherent water absorption of networks causes swelling, rendering the hydrogel its physical form (Peppas et al., 2000a). Depending on the bond formation and type of interactions hydrogels can be broadly classified as physical or chemical cross-linked hydrogels. In physically cross-linked hydrogels, the polymeric units are held together by secondary forces of interactions such as hydrogen bonding or ionic interactions. The interactions are reversible in nature, since the stability of these hydrogels depends on the external environmental conditions. On the contrary, chemically cross-linked hydrogels requires the addition of a cross-linker for covalent connection with various functional groups associated with polymeric backbone to form a stable, irreversible network (Peppas et al., 1976, Hoare et al., 2008 and Das et al., 2015). Physical cross-linking of hydrogels is advantageous owing to stimuli-responsiveness, *in situ* gelation, higher drug loading capacity and lesser toxicity (Kashyap et al., 2007, Tang et al., 2014 and Vashist et al., 2014). However, the selection of synthetic method for hydrogels is purely determined from the application point of view. Hydrophilic synthetic polymers such as PEG, PVA, PVP, PAA, PMA and PAM have been mostly utilized for formation of hydrogels (Hoffman, 2002, Bhattarai et al., 2010 and Baruah et al., 2016). Moreover, hydrogels exist in a variety of physical forms such as coatings, nanoparticles, microparticles, films and slabs. As a fascinating material, hydrogels are smart, compatible with biological systems and responsive to a variety of

environmental factors such as pH, light, temperature, ionic strength, solvent and electric field (Wang et al., 2016a, Huynh et al., 2009, Im et al., 2010 and Jin et al., 2013b). Hydrogels share some common properties with living tissues such as softness and low surface tension (Hamidi et al., 2008). Elasticity of hydrogels minimizes the risk of irritation to the adjacent tissues, while low interfacial tension reduces the chances of protein adsorption and cell adhesion preventing any undesired immunogenic responses. Consequently, hydrogels have been commonly employed for various biomedical applications including tissue engineering, diagnostics and implantable devices (Wichterle et al., 1960, Hoffman, 2002 and Das et al., 2015). In addition, unique characteristics of hydrogels have generated significant interest for their use as DDS. Porous nature of the hydrogels largely permits enhanced loading of drugs into the gel matrix and subsequent sustained release of drug for longer periods, maintaining the pharmacokinetics of the drug (Vashist et al., 2014 and Hoare et al., 2008). Mucoadhesive and bioadhesive characteristics of polymers used for hydrogel formulations can be advantageous for immobilization of hydrogels at non-horizontal surfaces of colon and nose (Peppas et al., 1996, 2000b). On account of distinct characteristics, biopolymer based hydrogels have been frequently used as DDS **(Fig. 2.4)**. Polysaccharides such as chondroitin sulphate, chitosan, agar, dextran, hyalouronan etc. have been used as biopolymers for hydrogel preparation (Payne et al., 2007, Stern et al., 2008 and Das et al., 2015). Tunable chemical structure, enzymatic degradability and external stimuli responsiveness of polysaccharides can be exploited for the synthesis of advanced modified hydrogels for multifunctional biomedical applications.

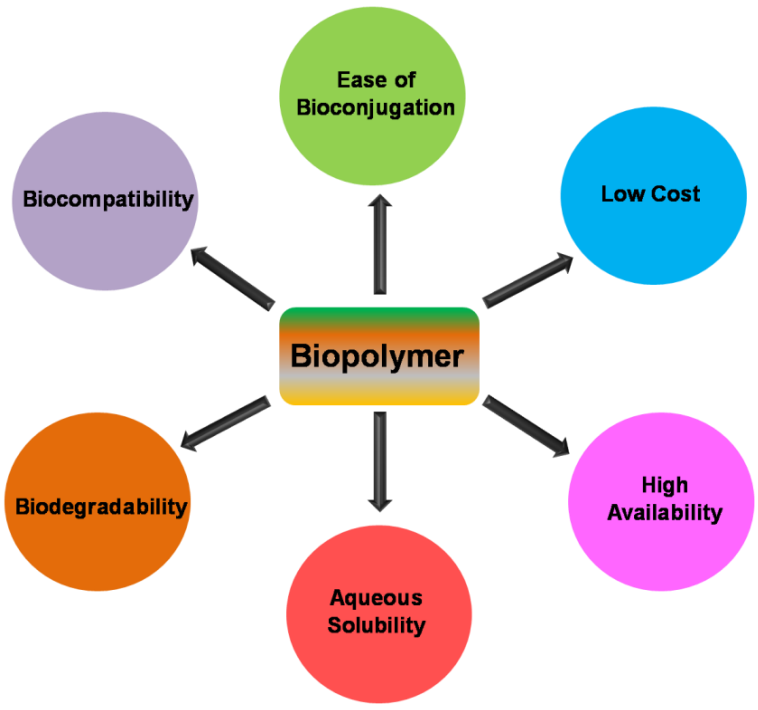

Figure 2.4 Advantages of biopolymer for preparation of hydrogels.

2.8.1 Chitosan hydrogels

Chitosan, a linear polysaccharide composed of β-(1-4)-linked D-glucosamine and N-acetyl-D-glucosamine units is obtained upon the deacetylation of chitin, which forms the exoskeleton of crustaceans and insects (Kumar et al., 2004). Lately, the chitosan has been known for its biocompatibility and biodegradability by human enzymes (lysozomal degradation etc.) (Muzzarelli, 1997). These along with other relevant traits such as hydrophilicity, bioadhesiveness, positive charge at physiological pH and reactive amino groups have inspired the development of chitosan based hydrogels for intended applications (Dwivedi et al., 2014). Generally, the synthesis of chitosan hydrogels is accomplished by covalent or ionic cross-linking of polymeric chains (Berger et al., 2004, Hoare et al., 2008 and Bhattarai et al., 2010). Covalently cross-linked chitosan hydrogels can be classified into three types on the basis of their structure: interlinking of chitosan chains, hybrid polymer networks (HPNs) and interpenetrating polymer networks (IPNs) (Wang et al., 2001). In case of HPNs and IPNs, additional polymers are added along with a covalent cross-linker for preparation of the gel network eg. Gelatin has been used as a hybrid polymer for HPNs while PEO has been used to form an entangled network in IPNs (Yin et al., 2000). Covalent cross-linking of chitosan has been performed using small molecules like glutaraldehyde, glyoxals, diacrylate and diisocyanate (Hennink et al., 2002). Out of these, glutaraldehyde has been used most frequently. The aldehyde groups of glutaraldehyde react with amino groups of chitosan to form imine bonds via Schiff reaction (Monteiro et al., 1999). However, glutaraldehyde is generally considered toxic to human body (Sung et al., 1999). On the other hand, ionic cross-linking is a simple and mild technique, eliminating the need of auxiliary catalysts. In addition, most of the ionic cross-linkers employed in the synthetic process are biocompatible. This procedure involves the solubilisation or dispersion of cross-linker in the aqueous acidic medium of chitosan (Moura et al., 2011 and Zhou et al., 2015). Ionic interactions between the positively charged amino groups of chitosan and negatively charged groups of cross-linker constitute the main interactions inside the network. The nature of the interactions is determined by the type of cross-linker. Metallic anions like Pt (II) and Pd (II) interact through the formation of coordinate-covalent bonds, while anionic molecules of sulphates, citrates and phosphates mediate cross-linking by electrostatic interactions (Shu et al., 2001). Phosphate-bearing anionic molecules such as sodium tripolyphosphate and β-glycerophosphate have been commonly employed (Schütz et al., 2011 and Zhou et al., 2015). However, ionic cross-linked hydrogels have certain drawbacks such as low mechanical strength and high degradation rate (Berger et al., 2004). Moreover, chitosan hydrogels have been prepared by coupling covalent and ionic cross-linking to combine the advantages of both types of cross-linking (Moura et al., 2011). In

the process, genipin was used as a covalent cross-linker, which was added to a solution of chitosan containing glycerol phosphate (ionic-cross linker) to improve the extent of cross-linking, degradability and morphology of the hydrogels. From the perspective of drug delivery, ionically-cross-linked chitosan hydrogels are preferred since these are well-tolerated and exhibit pH sensitive swelling which enables the controlled release of drugs from the gel matrix. Chitosan based *in situ* gelling systems have been used for controlled delivery of various anticancer chemotherapeutic drugs. Localized chemotherapeutic approach provides high local drug concentration at the target site in addition to reducing the systemic toxicity of drugs. Thermoresponsive chitosan-glycerophosphate hydrogel formulation loaded with paclitaxel was assessed for its antitumoral activity against EMT6 tumors implanted Balb/c mice *in vivo* and found to be more effective than the commercially available Taxol drug with lesser side effects (Ruel-Gariépy et al., 2004). Chitosan/dipotassium orthophosphate hydrogels were developed for delivery of DOX for osteosarcoma manangement. The formulation not only induced the reduction of primary and secondary osteocarcinoma, but also reduced the additional toxic effects associated with the administration of free DOX (Ta et al., 2009). Similarly, chitosan-gold hybrid hydrogels were used as a controlled DDS for DOX (Chen et al., 2012a). Thermosensitive co-crosslinked chitosan were developed for delivery of cisplatin which were effective against melanoma cells (Moura et al., 2013).

In summary, the literature review elaborated the basic properties and fluorescence mechanism of C-dots. The various synthetic routes for C-dots along with their limitations and advantages were also discussed. Hence, there is a necessity for exploring new synthetic schemes which can produce C-dots with superior fluorescence properties. Further, C-dots can be exploited for prospective biological and analytical applications. Metal based nanoparticles exhibit distinct therapeutic effects and can be combined with C-dots to form nanocomposites which can serve as dual-modality systems. Besides, the formation principles of chitosan hydrogels were elucidated in detail, but their application for cancer theranostics remain unexplored. With these observations and understanding from the literature, the scope for further research was identified and worked upon. The experimental approaches, analysis and inferences drawn to achieve the objectives are mentioned in detail in the subsequent chapters.

CHAPTER 3

MATERIALS AND METHODS

In this chapter, synthetic strategies have been described in detail. The various characterization techniques and experimental assays performed have also been described.

CHAPTER 3

MATERIALS AND METHODS

3.1 Materials

All the chemicals were of analytical/molecular grade and used directly without any purification. Ultra pure water (18 MΩ cm) was used for all the preparations.

Materials	Company and catalogue no.
• Chitosan (low molecular weight, M_w = 50-190 kDa, degree of deacetylation = 75-85 %)	Sigma-Aldrich, 448869
• Polyethylene glycol (PEG-4000)	SRL, 1647131
• Branched poly(ethyleneimine) (bPEI) (M_w = 25 kDa)	Sigma-Aldrich, 408727
• Glacial Acetic acid	SRL, 0129168
• Fresh coriander leaves	Local grocery shop
• Zinc nitrate hexahydrate	Himedia, RM691
• Silver nitrate	Merck, 1.93200.0027
• Citric acid monohydrate	SDFCL, 20081
• Ammonium cerium (IV) nitrate	Sigma-Aldrich, V800040
• Sodium acetate anhydrous	Sigma-Aldrich, V800363
• Glycerol (M_w = 92.09 g mol^{-1})	SRL, 62417
• 5-Fluorouracil (5-FU), (purity > 99 %)	Sigma-Aldrich, F6627
• Ferric chloride anhydrous	Himedia, GRM1379
• Sodium hydroxide (NaOH)	SRL, 1949181
• Hydrochloric acid (HCl)	Rankem, H0080

- N-dimethylformamide (DMF) — Rankem, D0130
- Methanol — SDFCL, 20158
- Dimethylsulfoxide (DMSO) — Himedia, TC185
- Nitric acid — Rankem, N0060
- Ethanol — Amresco, E193
- Potassium bromide (KBr) — Merck, 1.04907.100
- Glutaraldehyde, 25 % — Sigma-Aldrich, 340855
- Phosphate buffer saline (PBS) — Himedia, RM7385
- Phosphotungstic acid hydrate — Sigma-Aldrich, P4006
- Quinine sulphate — Loba Chemie, 055390025
- 2,2-diphenyl-1-picrylhydrazyl (DPPH) — Himedia, RM2798
- Hydrogen peroxide (H_2O_2), 30 % w/v — Thermo Fisher Scientific, 18755
- Dulbecco's modified eagle medium (DMEM) — Himedia, AT007
- Fetal bovine serum (FBS) — Gibco Life Technologies, 10270-106
- Penicillin-streptomycin — Gibco Life Technologies, 10378-016
- Dulbecco's phosphate buffer saline, Ca^{2+} and Mg^{2+} free (DPBS) — Sigma-Aldrich, D5652
- Trypsin-EDTA, 0.25 % — Gibco Life Technologies, 25200-072
- 3-(4,5-Dimethyl-2-thiazoyl)-2,5-diphenyltetrazolium bromide (MTT) — Amresco, 0793
- Acridine orange (AO) — Himedia, TC262
- Ethidium bromide (EtBr) — SRL, 054817
- Bis Benzimide H 33342 trihydrochloride (Hoechst 33342) — Sigma-Aldrich, 14533
- 2',7'-dichlorofluorescin diacetate (DCFH-DA) — Sigma-Aldrich, D6883
- Lysotracker Red — Life Technologies, L7528

- 3,8-diamino-5-[3-(diethylmethylammonio)propyl]-6-phenylphenanthridinium diiodide (PI) — Sigma-Aldrich, P4170
- Tri reagent — Sigma-Aldrich, T9424
- Triton X-100 — Merck, RM845
- Agarose — SRL, 83404
- Tris buffer — SRL, 2044122
- Ethylenediaminetetraacetic Acid (EDTA) — SRL, 054448

3.2 Synthetic procedures

3.2.1 Synthesis of PEI passivated C-dots and PEG passivated C-dots

Firstly, 400 mg of bPEI was added to 60 mL of ultrapure water and stirred for 30 min. To this, 300 µL of acetic acid was added for dissolution of 400 mg of chitosan and the resultant mixture was magnetically stirred for 3 h. Then the solution was transferred to a hydrothermal reactor and sealed. The mixture was heated at a constant temperature of 200 °C for 8 h in a nitrifying atmosphere (pressure - 15 kg/cm^2g). When cooled to room temperature, the solution was collected and centrifuged (Beckman Coulter Allegra X-22R) at 7400 *g* for 20 min to disentangle the large, insoluble black carbonaceous precipitates. Finally, the dark-brown supernatant was collected which was referred to as CD-PEI. The supernatant solution was further reconstituted to obtain CD-PEI at a concentration of 1.3 mg mL^{-1}.

Similarly, CD-PEG was synthesized by following a similar procedure as described above, except 400 mg of PEG-4000 was used instead of bPEI as a surface passivating agent. In this case a yellow coloured solution was obtained which was referred to as CD-PEG.

3.2.2 Synthesis of C-dots from coriander leaves

Briefly, 5 g of coriander leaves were chopped very finely and dissolved in 40 mL of distilled water. The solution was then transferred to 80 mL vessel and subjected hydrothermal treatment for 4 h at 240 °C. The solution was allowed to cool naturally and the large black insoluble carbonaceous particles were removed by filtration through a 0.22 µm filter membrane. Finally, the volume of the solution was adjusted with water to obtain C-dots at a concentration of 10 mg mL^{-1} for further characterization and use.

3.2.3 Synthesis of C-dots-cerium oxide nanocomposite (CDs-CeO_2 NC)

C-dots were synthesized by a similar methodology which has been discussed in section 3.2.1 using chitosan as a carbon source and bPEI as a surface passivating agent.

CeO_2 nanoparticles were prepared according to a previously reported method (Liu et al., 2012c). 2.74 g (0.07 M) of ammonium cerium (IV) nitrate was mixed with 10 g of sodium acetate in 70 mL of ultrapure water. Then 10 mL of acetic acid was added and the solution was stirred for another 2 h. The as-formed greenish-yellow solution was subjected to hydrothermal treatment at 220 °C for 12 h. Finally, brown precipitates were collected by centrifugation of the solution at 7400 *g* for 10 min. These precipitates were then washed with water and ethanol several times and kept for drying at 60 °C overnight. The precipitates were grinded to obtain a fine brown coloured CeO_2 nanopowder.

In order to synthesize CDs-CeO_2 NC, 200 mg each of chitosan and bPEI was dissolved in 30 mL of deionized water containing 150 µL of acetic acid under stirring conditions. Subsequently, 300 mg of as-synthesized CeO_2 nanoparticles were dispersed in above-mentioned chitosan-bPEI solution by bath sonication. The mixed suspension was transferred to hydrothermal reactor vessel and maintained at 200 °C for 8 h. After cooling to room temperature, the solution was filtered through a 0.22 µm filter membrane to remove the black insoluble carbonaceous precipitates. Finally, a brownish-yellow coloured solution was obtained which was referred to as CDs-CeO_2 NC.

3.2.4 Synthesis of C-dots-silver@zinc oxide nanocomposite (CD-Ag@ZnO NC)

PEG-passivated C-dots were synthesized by following a similar procedure which has been elucidated section 3.2.1.

Ag@ZnO was synthesized according to a previously reported method (Matai et al., 2014). Equimolar amounts of zinc nitrate and silver nitrate were added to an 8 % aqueous citric acid solution with stirring. The transparent solution obtained was heated at 80 °C for 30 min until a gel was formed. Microwave treatment of the obtained gel for 5-25 cycles (each cycle consisted of 30 s on/30 s off to prevent excessive boiling of the solvent) resulted in brownish fluffy solids. The reaction product was washed with absolute ethanol and dried at 100 °C for 20 min. The resulting powder was further calcined at 500 °C for 2 h in a muffle furnace to obtain a dark brown Ag@ZnO nanopowder as the final product.

For synthesizing CD-Ag@ZnO NC, a stock solution of 1 mg mL^{-1} of Ag@ZnO was prepared in ultrapure water by sonication for 15 min. Under continuous magnetic stirring, a 500 µL aliquot of Ag@ZnO stock solution was mixed with 500 µL of an aqueous solution of pre-synthesized C-dots (1.3 mg mL^{-1}). The reaction was allowed to proceed for 24 h at room temperature. The product was then centrifuged at 18 000 rpm for 20 min to remove the excess unreacted C-dots. The CD-Ag@ZnO NC was collected as pellets and was reconstituted to a final volume of 1 mL using ultrapure water.

3.2.5 Synthesis of chitosan-based hydrogel formulations

C-dots were synthesized by following a similar protocol explained in section a section 3.2.1. Herein, Chitosan was used as the carbon source in conjugation with bPEI as a surface passivating agent.

Chitosan hydrogels (HY) were synthesized according to pre-existing scheme with slight modifications (Konwar et al., 2015). Briefly, 0.1 g of chitosan powder was added to a 6 mL aqueous solution (1 % v/v) of acetic acid containing 300 µL of glycerol and magnetically stirred for 3 h. Here, glycerol acts as an ionic cross-linker for chitosan chains. After complete chitosan dissolution, 5 N NaOH solution (1.5 mL) was added drop-wise to the above mixture. White precipitate formation takes place instantaneously upon the addition of NaOH due to gelation. The resultant precipitates were washed several times with water to remove excess reactants. Finally, the product was lyophilized (Delvac Mini Lyodel, India) at -80 °C (0.080 mbar) for 4 h to obtain white, freeze-dried hydrogels.

Similarly, for synthesis of chitosan-C-dots (CD-HY), chitosan-5-FU (5-FU@HY) and 5-FU loaded chitosan-C-dots hydrogels (5-FU@CD-HY), aqueous solution of pre-synthesized C-dots (1.3 mg mL^{-1}) and 5-FU (3 mg mL^{-1}) were added to chitosan-glycerol mixture before gelation.

3.3 Characterization techniques

3.3.1 UV–visible spectroscopy

Absorption spectra of the samples (200‑700 nm) were recorded using Lasany LI-2800 double-beam spectrophotometer.

3.3.2 Fluorescence spectroscopy

Fluorescence spectral measurements were carried out using a Hitachi F-4600 fluorescence spectrophotometer and a Biotek, Cytation 3 multi-mode microplate reader, respectively.

3.3.3 Field-emission scanning electron microscopy (FE-SEM)

Morphological examination and elemental analysis of the as-prepared samples was carried out by Ultra plus-Carl Zeiss microscope equipped with energy dispersive X-ray spectrometry (EDS). FE-SEM sample was prepared by depositing a drop of solution on a silicon substrate which was then air-dried and mounted on aluminium stubs. The sample was then sputter coated with gold using Denton gold sputter unit to minimize charging during imaging, before analyzing under FE-SEM.

3.3.4 Transmission electron microscopy (TEM)

Suitable dilutions of the samples were drop-cast onto the carbon-supported copper grids (200 mesh, Icon Analytical) and air dried. Images were acquired with a FEI Technai G2 TEM operating at 200 keV. Particle size analysis was performed using Image J software (http://rsb.info.nih.gov/ij/download.html). High resolution TEM (HRTEM) images were processed using Gatan Digital Micrograph software to obtain Inverse Fast Fourier Transform (IFFT) images.

In case of chitosan-based hydrogel formulations, negative staining was done with 2 % phosphotungstic acid for contrast enhancement and improvement of image quality. EDS accessory was used for performing elemental analysis.

3.3.5 Zeta potential and dynamic light scattering (DLS) measurements

Appropriate aqueous dilution of the sample was taken in a folded capillary cell supported with platinum electrodes and inserted in the sample holder of the Malvern Zetasizer Nano ZS90 (25 °C) for analysis. Zeta potential values and hydrodynamic sizes were calculated by a built-in Dispersion Technology Software of the zetasizer.

3.3.6 X-ray diffraction (XRD)

XRD patterns were obtained using a using a Bruker AXS D8 advance powder X-ray diffractometer ($Cu_{K\alpha}$ radiation, $\lambda = 1.5406$ Å) in the range of 10°–90° at a scan rate of 1° min^{-1}. PANalytical X'pert High Score Plus software was used for the analysis and refinement of XRD profiles of the samples.

3.3.7 Fourier transform infrared (FTIR) spectroscopy

FTIR spectrum of the samples was obtained by Thermo Nicolet spectrometer in the range 4000-400 cm^{-1} by using the KBr disc method.

3.3.8 CHNS analyzer

Elemental analysis was carried out on an Elementar Analysensysteme GmbH variomicro CHNS.

3.3.9 Thermogravimetric analysis (TGA)

Thermal stability of the samples was interpreted from the thermograms obtained from TG/DTA SII 6300 EXSTAR thermal analyzer. Approximately, 10 mg of the respective sample was heated at a constant rate of 10 °C/min under the flow of nitrogen gas and weight loss at various stages was recorded.

3.3.10 Fluorescence lifetime measurements

A Horiba Jobin Yvon Fluoro Cube Fluorescence Lifetime System equipped with a Nano LED (635 nm) source was used for recording the fluorescence decay curves. IBH decay analysis v 6.1 software was used for fluorescence decay and lifetime analysis.

Average lifetime (τ_{av}) was calculated by using the following equation:

$$\boldsymbol{\tau_{av} = a_1\tau_1 + a_2\tau_2 + a_3\tau_3}$$

where τ_1, τ_2 ,τ_3 were the first, second and third component of the decay time of the sample and a_1, a_2 , a_3 were the corresponding relative weightings (emission %) of these components, respectively.

3.3.11 Surface area analysis

Nitrogen adsorption-desorption isotherms of freeze-dried samples were recorded on Quantachrome NOVA 2200e high speed automated surface area analyzer. The samples were degassed at 150 °C for 2 h. Specific surface area and pore volume was determined by Brunauer-Emmett-Teller (BET) method using the Nova Win software.

3.3.12 Fluorescence microscopy

An EVOS FL Color, AMEFC 4300 fluorescent inverted microscope was used to obtain microscopic images at various magnifications under bright-field, DAPI (excitation 360 nm, emission 447 nm), GFP (excitation 470 nm, emission 525 nm) and RFP (excitation 530 nm, emission 593 nm) light cubes, respectively.

3.4 Quantum yield measurements

Quinine sulphate was chosen as a reference fluorophore having a quantum yield of 0.54 at 360 nm. Fluorescence quantum yield of the samples in water was calculated according to the following equation:

$$Q = Q_R \times \frac{I}{I_R} \times \frac{A_R}{A} \times \frac{\eta^2}{\eta_R^2}$$

where, Q is the quantum yield of desired sample, I is the measured integrated emission intensity (area under the curve), refractive index being η and A means the optical density. Subscript R denotes the reference fluorophore of known quantum yield. To eliminate the

chances of re-absorption effects, the absorption in 10 mm cuvette was always kept under 0.1 at the excitation wavelength. The emission range of the samples was kept between 375-700 nm.

3.5 Photostability test

The stability in emission was evaluated by continuous excitation of the samples kept in a 10 mm cuvette inside a fluorescence spectrophotometer (Hitachi F-4600) equipped with Xenon arc lamp. The emission of the samples was monitored within a time scan of 9000 s (2.5 h).

3.6 SDS-PAGE (Sodium dodecyl sulphate- polyacrylamide gel electrophoresis)

Samples were loaded to a 12 % denaturing gel and electrophoresis was performed at 120 V for 1 h using Biorad Mini-Protean electrophoresis unit. After electrophoresis, the fluorescent bands were excised and visualized under different excitation filters using inverted microscope (EVOS FL® Color, AMEFC 4300).

3.7 pK_a value estimation

The excited state pK_a value of the samples was calculated according to the following equation:

$$pK_a^* = pH_x + \lg [(I_B - I_x)/ (I_x - I_{HB+})]$$

where I_B represents the fluorescence intensity at absolute base form, I_x is the fluorescence intensity at the pH chosen and I_{HB+} is the fluorescence intensity of absolute acid form, respectively.

3.8 Determination of antioxidant activity of C-dots derived from coriander leaves

Antioxidant potential was measured by 2, 2-diphenyl-1-picrylhydrazyl (DPPH) free radical assay with few modifications (Pyrzynska et al., 2013, Das et al., 2014 and Purkayastha et al., 2014). Precisely, different concentrations of C-dots were added to 0.5 mL of 50 µM methanolic solution of DPPH. Final volume of all the solutions was adjusted to 0.6 mL. The samples along with appropriate controls were incubated for 30 minutes in dark environment. 0.1 mL aliquots of all the samples were added to 96- well plate. Change in absorbance of DPPH was measured at 517 nm using a multi-mode microplate reader (Biotek, Cytation 3). Percentage radical scavenging activity of C-dots was calculated using the following formula:

$$\% \text{ Scavenging activity} = (AD_{517} - AS_{517}/ AD_{517}) \times 100$$

where, AD and AS are the absorbance of the DPPH solution (without C-dots) and sample solution (with C-dots), respectively.

3.9 Procedure for ion sensing by C-dots derived from coriander leaves

All the metal ion stock solutions were prepared from their respective salts. Aqueous solutions of these metal ions were further diluted with deionized water to obtain a final concentration of 60 µM. Each of the metal ion solution was mixed with C-dots (10 µL, 0.1 mg mL^{-1}), stirred and incubated for 15 min at room temperature. Aliquots were transferred to 96-well black plate and fluorescence measurements were done. For Fe^{3+} sensing, similar steps were followed. In a typical assay, 10 µL of C-dots solution was added to 1 mL Fe^{3+} salt solutions of different concentrations. The fluorescence intensity and spectra were recorded at an excitation wavelength of 320 nm.

3.10 Fluorescence measurements in aqueous medium

The effect of H_2O_2 on fluorescence of CDs and CDs-CeO_2 NC was studied as follows: In a typical assay, PBS buffer solutions (pH 7.4) containing various concentrations of H_2O_2 were mixed with a dispersion of CDs or CDs-CeO_2 NC (each used at a final concentration of 0.5 mg mL^{-1}). Final volume of the solutions was adjusted to 1 mL. The resulting solutions were incubated further for 30 min at room temperature. 100 µL of each solution was transferred to the respective wells of a 96-well black plate. The fluorescence spectrum was recorded for each well at an excitation wavelength of 360 nm within an emission range of 390-700 nm.

3.11 Swelling studies

A known amount of freeze-dried hydrogel formulations was immersed in 2 mL of phosphate buffer saline (PBS, pH 7.4) and kept at room temperature for 24 h. These samples were taken out from the PBS solution, wiped carefully with tissue paper to remove surface droplets and weighed in swollen state. % Swelling was expressed using the following equation:

$$\% \text{ Swelling} = \frac{W2 - W1}{W1} \times 100$$

where, W1 is the weight of dried sample and W2 is the weight of the sample in swollen state after 24 h.

3.12 Mechanical testing

Mechanical properties were studied using small scale mechanical tensile tester machine (Bose ElectroForce 3230 Series III). The tensile testing was done on a 450 N load cell at a speed of 0.1 N/s using a maximum load of 200 N. For this specific purpose, the hydrogel solutions were dried at 45 ºC overnight to yield hydrogel films (thickness ~ 0.8 mm). Rectangular strips of the samples having dimensions 8.5 × 3.2 × 0.8 mm were cut and clamped vertically. The signals of load and displacement were recorded throughout the experiment.

Stress was computed by dividing the force produced through extension by the initial cross-sectional area, whereas strain was calculated by dividing the extended length by original length. Stress-strain curves were then plotted for working out the tensile strength (TS) and percent elongation at break for the samples.

3.13 Entrapment of 5-FU

Entrapment efficiency (EE) of 5-FU in 5-FU@CD-HY was estimated by centrifuging the formulation at 10 000 rpm for 15 min. The supernatant containing free 5-FU was collected and absorbance was recorded at 266 nm using UV-vis spectrophotometer. Accordingly, the concentration of free drug was calculated from the concentration-absorption curve of 5-FU (using the regression equation: $y = 0.0478x + 0.02$, $R^2 = 0.9995$). The EE was calculated as follows:

$$\text{EE\%} = \frac{\text{weight of } 5-\text{FU added} \quad - \text{weight of free } 5-\text{FU in supernatant}}{\text{weight of } 5-\text{FU added}} \times 100$$

3.14 *In vitro* release profile of 5-FU

50 mg of freeze dried 5-FU@CD-HY was separately dispersed in 4 mL of PBS (pH 7.4) and acetate buffer (pH 5.5) and incubated for 48 h in a 37 ºC thermostatically-controlled oven under mild agitation (100 rpm). At each specific time point, namely, 3, 6, 9, 12, 24, 36 and 48 h, sample was centrifuged at 10 000 rpm for 10 min and supernatant was collected. The absorbance of the released 5-FU from 5-FU@CD-HY in the collected buffer solution was measured spectrophotometrically at 266 nm. Next, the concentration of 5-FU at each time point was determined from the concentration-absorption curve of 5-FU. The percentage of 5-FU released was calculated by using the following equation:

$$\text{Cumulative release \%} = \frac{\text{Amount of 5-FU released in the supernatant}}{\text{Total amount of 5-FU loaded in 5-FU@CD-HY}} \times 100$$

3.15 Cell culture

A549 (human lung adenocarcinoma), BHK-21 (Baby hamster kidney fibroblast), MCF-7 (breast adenocarcinoma), L-132 (human normal lung epithelial) and NIH3T3 (mouse embryonic fibroblast cells) were procured from National Centre for Cell Sciences (NCCS) Pune, India. These cell lines were cultured in DMEM supplemented with 10 % (v/v) FBS and 1% penicillin-streptomycin solution. The cells were maintained at 37 °C in a 5 % CO_2 incubator under humidified conditions. Cells were subcultured as and when required for various assays.

3.15.1 MTT assay

Cellular viability upon exposure to varying concentrations of test samples was assessed by colorimetric MTT assay. This method is based on the measurement of mitochondrial activity of live cells to transform a yellow MTT solution to a purple formazan product. Typically, 10^4cells/well were seeded in 96-well cell culture plates (Corning, Costar) and allowed to attach for 12 h. The cells were then treated with medium (DMEM) containing different concentrations of test samples for specific periods of time. Following incubation, medium from each well was discarded and cells were briefly washed with PBS. Fresh medium (100 µL) containing 10 µL of MTT reagent (5 mg mL^{-1} in PBS) was added to each well. After 4 h, the MTT containing medium was aspirated again and 150 µL of dimethyl sulfoxide (DMSO) was added to dissolve the formazan crystals in each well. The absorbance of the purple formazan crystals (570 nm) in each well was quantitated using multi-mode plate reader (Biotek, Cytation 3). Cells without any sample treatment (in DMEM) were used as control. Relative cell viability [mean (%) ± SEM, n=3] was estimated as follows:

$$\text{Cell viability (\%)} = \frac{(\text{A570} - \text{A690}) \text{ for treated cells}}{(\text{A570} - \text{A690}) \text{ for control cells}} \times 100$$

MTT assay for various chitosan-based hydrogel formulations was performed with slight modifications. Cells were seeded in 24-well cell culture plates (Eppendorf) at a density of 2 × 10^4 cells/well. After 24 h, sterile pieces of corresponding hydrogel formulations of uniform weight (0.5-2 mg) containing different amounts of 5-FU and CDs were added to the cell culture medium and incubated for 48 h. The successive steps were similar to those elucidated above.

3.15.2 Evaluation of bioimaging potential of CD-PEI and CD-PEG

In order to explore the bioimaging efficiencies of CD-PEI and CD-PEG, A549 and BHK-21 cells were seeded in 35 mm cell culture plate (Eppendorf) containing 2 mL of DMEM. After appropriate growth of the cells, equal concentration of 0.22 µm filtered sterilized aqueous suspension of CD-PEI and CD-PEG (5 mg mL^{-1}) were added to respective dishes under similar conditions. After an incubation of 1 h, the medium containing CD-PEI and CD-PEG was removed. The cells were then washed twice with PBS to remove any media traces left over. The cells were retained in PBS during optical imaging. Bioimaging efficiencies of CD-PEI and CD-PEG were assessed by examining the labelled A549 and BHK-21 cells under inverted fluorescent microscope (EVOS FL Color, AMEFC 4300).

For quantitative analysis of bioimaging, 10^5 A549 cells were seeded in 35 mm cell culture plates. After 12 h, equal concentration of CD-PEI and CD-PEG (5 mg mL^{-1}) were added to appropriate plates and further incubated for 1 h. Cells were then trypsinized, collected and washed briefly with PBS to remove unbound CDs. Fluorescence spectroscopy and quantum yield measurements for CDs labelled cells were performed by preparing equivalent dilutions for comparative purposes.

3.15.3 Bioimaging and cellular distribution of C-dots derived from coriander leaves

For exploring the bioimaging potential of C-dots, A549 and L-132 cells were seeded at a density of 2×10^5 in 2 mL DMEM in 35 mm cell culture plates. Consequently, fresh medium containing 0.5 mg mL^{-1} filter sterilized C-dots were added to the respective plates and incubated for 12 h. After washing with PBS twice, the cells were imaged using a fluorescence inverted microscope. Cellular distribution of C-dots was studied in a similar manner, except that the cells were stained with 3 µL of Hoechst 33342 (working concentration-10 mg mL^{-1}) and incubated for 15 min before imaging the cells under fluorescence microscope. For flow cytometry, C-dots treated and untreated A549 and L-132 cells were trypsinized, collected and resuspended in PBS for analysis. The cell suspension was then analyzed using a flow cytometer (Amnis Flowsight) under 488 nm excitation laser by recording 10 000 events in the appropriate channel. Collected data was analyzed using Amnis Ideas software.

3.15.4 Protective effect of CDs-CeO_2 NC against ROS *in vitro*

Cells were seeded in 96-well cell culture plates and exposed to varying concentrations of CDs-CeO_2 NC for 24 h before H_2O_2 treatment. Medium from each well was discarded and fresh medium containing 750 µM H_2O_2 was added. After 4 h incubation, the viability of the cells was determined by the MTT assay.

3.15.5 Inductively coupled plasma mass spectrometry (ICP-MS)

NIH3T3 cells were seeded at a density of 2×10^5 cells on individual 35 mm cell culture dishes and treated with 10 µg mL^{-1} CDs-CeO_2 NC for different time spans. At each time point, medium was removed and cells were washed twice with PBS to remove excess of nanocomposites. Digestion of the cells was performed by adding 1 mL of concentrated nitric acid solution (16 M). The digested solution was then harvested, diluted with deionized water and analyzed by ICP-MS to determine the cellular concentration of cerium. Duplicate readings were analyzed for each sample. Results were expressed as mean amount of cerium in pg/cell.

3.15.6 Cellular uptake and flow cytometeric evaluation of CDs-CeO_2 NC

The uptake of CDs-CeO_2 NCs or blank CDs was monitored qualitatively by fluorescence microscope. Precisely, NIH3T3 cells (2×10^5 cells/well) were seeded on 6-well cell culture plates and allowed to attach for 6 h. For time-dependent uptake, cells were incubated with CDs-CeO_2 NC or blank CDs (50 µg mL^{-1}) for different periods of time. In order to visualize co-localization, cells were counterstained with 1 µL of Lysotracker Red (stock-100 µM) at specific points and incubated further for 10 min. A brief PBS wash was given and cell images were acquired under DAPI (for CDs-CeO_2 NC) and RFP (for Lysotracker Red) filters of fluorescence microscope.

Intracellular fluorescence intensity of cells treated with CDs or CDs-CeO_2 NC in absence and presence of H_2O_2 was measured through flow cytometry. In these experiments, 2×10^5 cells were plated in individual 35 mm cell culture dishes and treated with the respective samples. After incubation, the cells were further treated with 750 µM of H_2O_2 and kept for 4 h. Untreated cells were used as control. Subsequently, cells were trypsinized and suspended in PBS (200 µL) for flow analysis. Plot of normalized frequency % in channel 3 was recorded by using a 488 nm laser. Collected data (10 000 gated events) was analyzed by Amnis ideas software.

3.15.7 Acridine orange/ethidium bromide (AO/EB) staining

To distinguish between live, apoptotic and necrotic cells, the cells were stained with 10 µL of the dual-dye mixture AO/EB (working concentration-10 µg mL^{-1}). Cells were grown in 6-well tissue culture plates (Eppendorf) and treated with different concentrations of the test samples. After the specified incubation time, the culture media was removed. Cells were then washed twice with PBS and stained with AO/EB in PBS. Images were captured under GFP and RFP filters of fluorescence microscope.

3.15.8 Cellular characterization via FE-SEM

For morphological analysis by FE-SEM, cells were cultured till 70-80 % confluency on glass cover slips on a 35 mm cell culture dish and then treated with certain concentration of test sample for 12 h. Untreated cells were cultured in DMEM and were used as reference. Afterwards, treated as well as untreated cells were washed with PBS and fixed with 2 % glutaraldehyde solution for 15 min on cover slips. Traces of glutaraldehyde were removed by ethanol/water gradient treatment. Cover slips with attached cells were air-dried, gold coated prior to examination by FE-SEM (Ultra plus-Carl Zeiss).

3.15.9 Determination of reactive oxygen species (ROS)

Intracellular ROS levels in the cells were investigated by DCFH-DA dye based assay. Upon cellular uptake the non-fluorescent DCFH-DA compound gets oxidized to highly fluorescent, dichlorofluorescein (DCF) by the action of intracellular esterases which forms the basis of ROS detection. For this purpose, NIH3T3 cells (2×10^5) were plated in individual 35 mm cell culture dishes and incubated with different concentrations of CDs-CeO_2 NC or CeO_2 nanoparticles for 24 h prior to H_2O_2 exposure. Untreated cells were used as control to determine the normal level of ROS in cells. Thereafter, cells were washed with PBS and exposed to 750 µM of H_2O_2 for 4 h. Cells were resuspended in PBS containing DCFH-DA dye (working concentration- 20 µM) and incubated for 30 min at 37 ºC for dye diffusion. Images were taken using the GFP filter of the fluorescence microscope. Quantitative assessment of ROS was carried out through flow cytometer in a similar manner. A similar treatment regime was followed as mentioned above. For flow analysis, cells were trypsinized and cell suspended in PBS. The fluorescence intensity of the oxidized product, DCF was measured using 488 nm excitation laser of flow cytometry. For each sample, Amnis ideas software was used to analyze 10 000 gated events acquired in channel 2 and ROS generation was expressed in terms of percentage of cells expressing green (DCF) fluorescence.

Additionally, the determination of ROS production in MCF-7 and A549 cells treated with CD-Ag@ZnO NC was done through flow cytometry. In this case, cells were seeded in 6-well tissue culture plate (2×10^5 cells/well) and treated with varied concentrations of CD-Ag@ZnO NC or Ag@ZnO for 3 h. After twice PBS wash, 1 mL of DMEM containing 20 µM DCFH-DA, dye was added and incubated for 15 min at 37 °C. Subsequent steps for flow cytometeric analysis were similar as described above.

3.15.10 Cellular uptake studies of CD-Ag@ZnO NC

3.15.10.1 Qualitative and quantitative cellular uptake

Cellular uptake was monitored qualitatively through fluorescence microscopy. MCF-7 and A549 cells were seeded on 6-well cell culture plates at a density of 2×10^5 cells/well. After 12 h, different concentrations of the test samples were added to the wells. At the end of incubation, the medium was removed and the cells were washed twice with PBS to remove the unbound sample. The cells were then observed under fluorescence microscopy. For the quantitative determination of cellular uptake, 10^4 cells/well (100 µL) were seeded into 96-well black cell culture plates and incubated overnight for cell attachment. Different concentrations of CD-Ag@ZnO NC were added into the wells and incubated for different periods of time. At

the end of the incubation, the cells were washed twice to remove the unbound dead cells. Next, 100 µL of 0.5 % Triton X-100 in 0.2 M NaOH solution was added for cell lysis. A multi-mode microplate reader was used to quantify the fluorescence intensity from the released CD-Ag@ZnO NC inside the wells at excitation and emission wavelengths of 320 and 400 nm, respectively.

3.15.10.2 Hoechst 33342 staining

Real-time nuclear uptake was monitored by incubating MCF-7 and A549 cells in 6-well cell culture plates with similar concentrations of CD-Ag@ZnO NC for specified periods of time. After specific time spans, the cells were stained with 3 µL of Hoechst 33342 (working concentration-10 mg mL^{-1}) and incubated for 15 min. Finally, the cells were given a brief wash with PBS and stored in PBS for imaging. An overlay of cell images was obtained by capturing images under the DAPI and GFP filters of the fluorescence microscope.

3.15.10.3 Atomic absorption spectroscopic analysis

MCF-7 and A549 cells were seeded in 6-well cell culture plates (2×10^5 cells/well) and exposed to different concentrations of CD-Ag@ZnO NC in duplicate for 3 h. The cells were thoroughly washed and counted after exposure. The cells were then harvested by adding 1 mL of lysis solution (0.5 % Triton X-100 in 0.2 M NaOH solution). The uptake of Ag and Zn by the A549 and MCF-7 cells was assessed quantitatively by graphite furnace AAS (Avanta M, GBC Scientific Equipment). Calibration standards for Ag and Zn at concentrations of 2, 3 and 4 ppm and 0.5, 1 and 1.5 ppm, respectively, were prepared from commercially available standards. The results were expressed as the cellular dose of Ag or Zn in pg/cell.

3.15.11 Release of Ag and Zn ions in DMEM

To examine the dissolution of CD-Ag@ZnO and Ag@ZnO in DMEM, the concentrations of Ag and Zn ions released from CD-Ag@ZnO and Ag@ZnO after incubation at various time points were measured. At each time point, the samples were centrifuged at 14000 g for 20 min and the supernatant was collected. Appropriate dilutions of the samples were digested with nitric acid (final concentration 1 %) before analysis. Finally, the resulting Zn and Ag ion concentrations were determined by graphite furnace AAS using pure Ag (2, 3 and 4 ppm) and pure Zn (0.5, 1 and 1.5 ppm) standards as reference.

3.15.12 Qualitative and quantitative assessment of cellular uptake of 5-FU@CD-HY

A549 cells were seeded on 6-well cell culture plates at a density of 2×10^5 cells/well and

allowed to attach overnight. Following attachment, different concentrations of CD-HY and 5-FU@CD-HY were added in the respective wells. After 48 h incubation, media was removed from each well and replaced with 1 mL PBS containing 3 µL Hoechst 33342 (working concentration-10 mg mL^{-1}) for nuclear staining. Real-time monitoring of cellular uptake and morphological changes were observed through fluorescence microscope equipped with DAPI (for Hoechst 33342) and GFP (for CDs) filters. For time-dependent uptake studies, the cells were incubated with 5-FU@CD-HY for different periods of time to observe co-localization. At each specified time point, the cells were co-stained with 1 µL of Lysotracker Red (stock-100 µM) and incubated for 10 min. After incubation, the excess dye was removed by washing with PBS. Cell images were then captured and processed using GFP (for CDs) and RFP (for Lysotracker Red) filters of fluorescence microscope.

Quantitative cellular uptake studies of CD-HY and 5-FU@CD-HY treated A549 cells were carried out through flow cytometry. In these experiments, the green fluorescence of CDs was used to distinguish between treated and untreated cells. Cells (2×10^5) were plated in 35 mm cell culture plates and left for attachment overnight. CD-HY and 5-FU@CD-HY with equivalent weight concentration were added to cells. Untreated cells were used as control. Cells were then trypsinized, collected and suspended in PBS (200 µL) for flow analysis. A 488 nm laser was used to excite CDs in hydrogel formulations and plot of normalized frequency % in channel 2 was acquired by collecting 10000 events for each sample.

3.15.13 Cell cycle analysis

Cells were grown in 6-well cell culture plates and incubated with appropriate concentrations of CD-HY, 5-FU@CD-HY and equivalent concentration of free 5-FU (6.4 µg mL^{-1}) for 48 h. Floating as well as adherent cells were harvested by trypsinization, suspended in PBS and fixed with 70 % ethanol solution in ice for 15 min. Fixed cells were then subjected to standard propidium iodide (PI) staining (50 µg mL^{-1} PI, 1 mg mL^{-1}, RNase A and 0.05 % triton X-100) and kept at 37 °C for 45 min in dark. Cell cycle distribution of cells was analyzed using flow cytometer by collecting 10 000 events for each sample. Cell debris and fixation artefacts were eliminated by appropriate gating of cell population. The amount of PI-labelled DNA in each phase of cell cycle was quantified by recording the red fluorescence of PI in channel 4.

3.15.14 Semi-quantitative reverse transcription polymerase chain reaction (RT-PCR)

For gene expression studies, cells were treated with respective concentration of test samples and incubated for specific time spans. Untreated cells were used as reference. Afterwards, total

RNA isolation was done using Tri reagent method. cDNA synthesis was done by reverse transcription reaction of total RNA using Super Script II Reverse Transcriptase. cDNA product was further used for gene specific amplification of apoptotic genes by RT‑PCR (Veriti, Applied Biosystems, Thermo Fisher Scientific). The cycling steps (35 cycles) involved an initial denaturation at 94 °C for 3 min followed by PCR denaturation at 94 °C for 30 s, annealing at 60 °C for 30 s, extension at 72 °C for 1 min and final extension at 72 °C for 10 min. The amplified PCR products were finally resolved on EtBr stained 1.2 % agarose gel and visualized under UV light inside a gel documentation system (Bio-Rad). The fold difference in expression was computed using Image lab 4.0 software. The pro-apoptotic set of genes utilized for gene expression studies included p53, bax, bad, c-myc, caspase 3, while the anti-apoptotic genes considered were bcl-2 and bcl-xl. The housekeeping gene β-actin was selected as internal control. The forward and reverse primer sequences for all the primers used in the study are mentioned in Table 3.1.

3.15.15 Statistical analysis

Statistical data for individual experiments were expressed as mean ± standard error mean (SEM) of three or more independent events. Data analysis was done via two-way ANOVA and student's t-test (wherever applicable) using GraphPad Prism 6.0.

Gene	Primers
Beta-actin	Forward: 5’ CTGTCTGGCGGCACCACCAT 3’ Reverse : 5’ GCAACTAAGTCATAGTCCGC 3’
p53	Forward: 5’ TGGCCCCTCCTCAGCATCTTAT 3’ Reverse : 5’ GTTGGGCAGTGCTCGCTTAGTG 3’
Caspase 3	Forward : 5’ TTCAGAGGGGATCGTTGTAGAAGTC 3’ Reverse : 5’ CAAGCTTGTCGGCATACTGTTTCAG 3’
C-myc	Forward : 5’ CCAGGACTGTATGTGGAGCG 3’ Reverse : 5’ CTTGAGGACCAGTGGGCTGT 3’
Bax	Forward : 5’ AAGCTGAGCGAGTGTCTCAAGCGC 3’ Reverse : 5’ TCCCGCCACAAAGATGGTCACG 3’
Bad	Forward : 5’ CCTTTAAGAAGGGACTTCCTCGCC 3’ Reverse : 5’ACTTCCGATGGGACCAAGCCTTCC 3’
Bcl-xl	Forward : 5’ATGGCAGCAGTAAAGCAAGC 3’ Reverse : 5’ CGGAAGAGTTCATTCACTACCTGT 3’
Bcl-2	Forward : 5’ TCCGCATCAGGAAGGCTAGA 3’ Reverse : 5’ AGGACCAGGCCTCCAAGCT 3’

Table 3.1 Forward and reverse primer sequences for various apoptotic signalling genes.

CHAPTER 4

Investigation of Physicochemical and Bioimaging Properties of Surface Tailored C-Dots

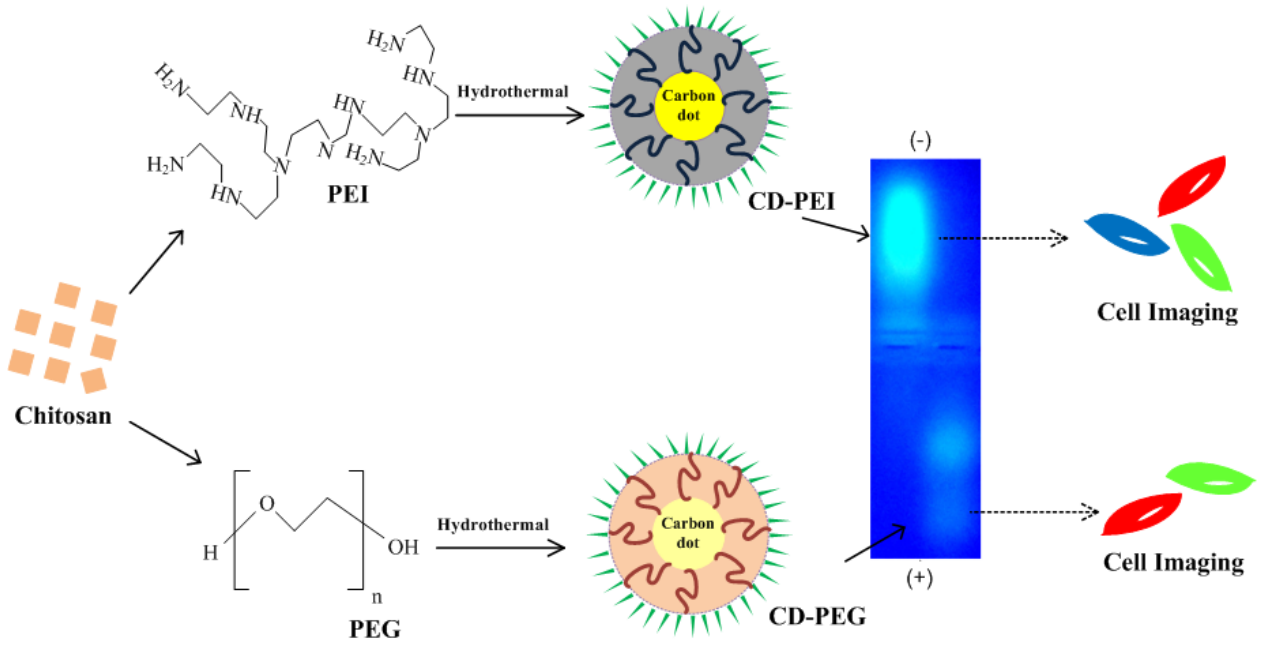

CHAPTER 4

INVESTIGATION OF PHYSICOCHEMICAL AND BIOIMAGING PROPERTIES OF SURFACE TAILORED C-DOTS

4.1 Overview

Luminescent C-dots are a new addition to the world of quantum-sized fluorescent nanomaterials and have shown enormous potential for bio-applications (Li et al., 2012a and Luo et al., 2013). Microwave mediated synthesis has been used most frequently for synthesizing C-dots in a rapid and facile way. However, the technique is associated with some disadvantages, such as low quantum yield and low brightness of C-dots (Sachdev et al., 2013). To alleviate these problems, surface passivation in conjugation with hydrothermal synthesis route can be adopted (Liu et al., 2011 and Liu et al., 2012a). By this method brighter C-dots can be produced in a single step with higher quantum yields without any post-synthetic treatments. Bioimaging applications of functionalized C-dots have become one of the hot topics of research ever since its inception. Conversely, the effect of positive and negative charged surface passivation agents on bioimaging efficiencies of C-dots have not been addressed as yet. Most of the available reports till date suggest the fluorescence emission of C-dots in blue or green spectral region. Multicolour emitting C-dots that can be excited even at longer wavelengths for red fluorescence emission could be advantageous for bioimaging purposes, thereby circumventing the problem of tissue autofluorescence. In view of the above issues, the present study reports one-pot hydrothermal synthesis of surface functionalized C-dots from chitosan. The surface functionality of the C-dots has been tailored by using polymeric passivating agents of different nature (PEI/PEG) under identical reaction conditions. The rationale behind the study is to evaluate the optical performance and bioimaging competence of different surface functionalized C-dots (CD-PEI/CD-PEG). Further, the study investigates their potential as biocompatible imaging agents using BHK-21 (normal) and A549 (cancer) cell lines.

4.2 RESULTS AND DISCUSSION

4.2.1 Synthesis and characterization of CD-PEI/CD-PEG

Hydrothermal based carbonization is a convenient and rapid approach for formation of CD-PEI and CD-PEG. Chitosan has a low carbonization temperature, while PEI and PEG can passivate the surface of C-dots due to their respective polyamine and polyhydroxyl structures (Sun et al., 2006, Li et al., 2010a, Dong et al., 2012, Liu et al., 2012a, Kim et al., 2013 and Sachdev et al., 2013). Under similar hydrothermal conditions, high temperature and pressure caused the carbonization of chitosan along with simultaneous *in situ* passivation by PEI and PEG to yield CD-PEI and CD-PEG. To eliminate the ambiguity of stability and also to rule out the speculation regarding PEI and PEG being carbonized, both were subjected to hydrothermal treatments under similar conditions in separate experiments. The colour of the solutions remained unchanged and no emission was observed. Based on our investigation, we propose the formation scheme for CD-PEI and CD-PEG **(Fig. 4.0)**. The aqueous solutions of CD-PEI and CD-PEG exhibit significant bright green luminescence when irradiated with UV light **(inset in Fig. 4.1 (A))** (Sahu et al., 2012). CD-PEI and CD-PEG were also examined for their optical properties. As shown in **Fig. 4.1 (A)** CD-PEI depicts two absorption bands at 288 nm (π-π^* transition) and 334 nm (n-π^* transition), while CD-PEG shows a single absorption band at 248 nm (π-π^* transition) (De et al., 2013). The fluorescence spectra of CD-PEI and CD-PEG depict an excitation dependent emission phenomenon, as illustrated in **Fig. 4.1 (B) and (C)**. For CD-PEI, the increase in excitation wavelength from 320 nm to 520 nm resulted in shifting of maximum emission from 445 nm to 554 nm, with a concurrent decrease in emission intensity. The phenomenon of progressive red shift in emission spectra was also observed for CD-PEG, affecting a shift in its maximum emission from 400 nm to 490 nm. It is worth mentioning that shift in emission peak of C-dots is an indication of multicolour fluorescence. However, CD-PEI tends to have stronger emission intensity than CD-PEG under similar excitation wavelengths. The maximum emission for CD-PEI and CD-PEG was recorded at an excitation wavelength of 360 nm and 320 nm, respectively. The origin of emission in C-dots can be attributed to surface effects contributing to complexity of excited states along with the size dependent effects, as reported previously (Cao et al., 2007 and De et al., 2013). The quantum yield of CD-PEI and CD-PEG was measured using quinine sulphate as a standard and found to be 13.15 % and 7.01 %, respectively **(Table 4.1)**, which was adequately bright for bioimaging as well as higher than our earlier reported values (Sachdev et al., 2013). The fluorescence lifetime decay curve of CD-PEI and CD-PEG and their average lifetime data have been given in **Fig. 4.2** and **Table 4.2**. For both the samples, the decay curves can be fitted to a triple exponential function (Liang et al., 2013b and Bhunia et al., 2013). The mean lifetime for

CD-PEI and CD-PEG was calculated to be 6.193 ns and 4.825 ns, respectively. Such shorter lifetimes indicate radiative recombination of excitations (Zhu et al., 2009). Conclusively, enhanced quantum yield and average lifetime of CD-PEI could be due to the incorporation of N heteroatoms (Zhai et al., 2012 and Park et al., 2016). TEM images of CD-PEI **(Fig. 4.3 (A))** and CD-PEG **(Fig. 4.3 (B))** reveal a pattern of uniform dark dots with near spherical morphology. The average size of CD-PEI and CD-PEG was determined to be 3.4 ± 0.46 nm and 3.9 ± 0.48 nm, respectively from the particle size distributions **(insets in Fig. 4.3)**. Dynamic light scattering (DLS) measurements predict that CD-PEI and CD-PEG **(Fig. 4.4)** have an average diameter around 4.10 nm and 7.85 nm, respectively. In general, the hydrodynamic diameter is slightly larger than dried-state diameter. Similarly, the hydrodynamic diameter in both the cases was bigger than that estimated by TEM, which might be due to polymeric surface passivation of C-dots (Yin et al., 2013).

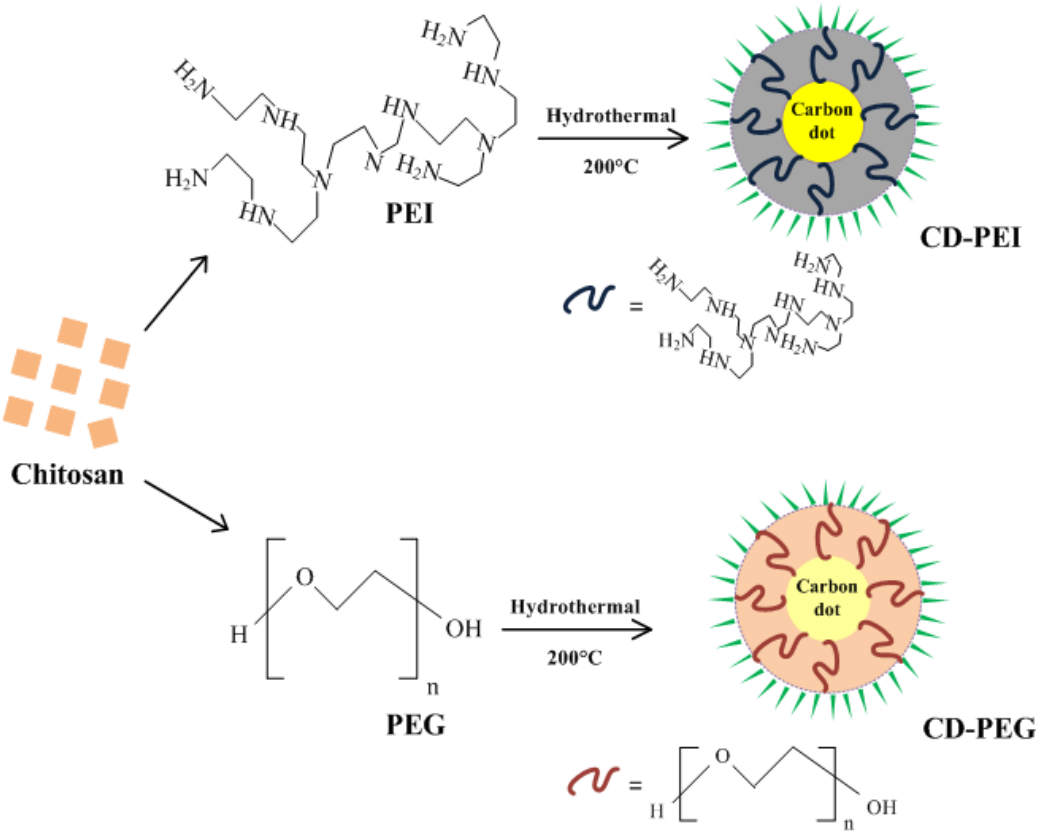

Figure 4.0 Schematic diagram depicting one-pot hydrothermal synthesis of CD-PEI and CD-PEG.

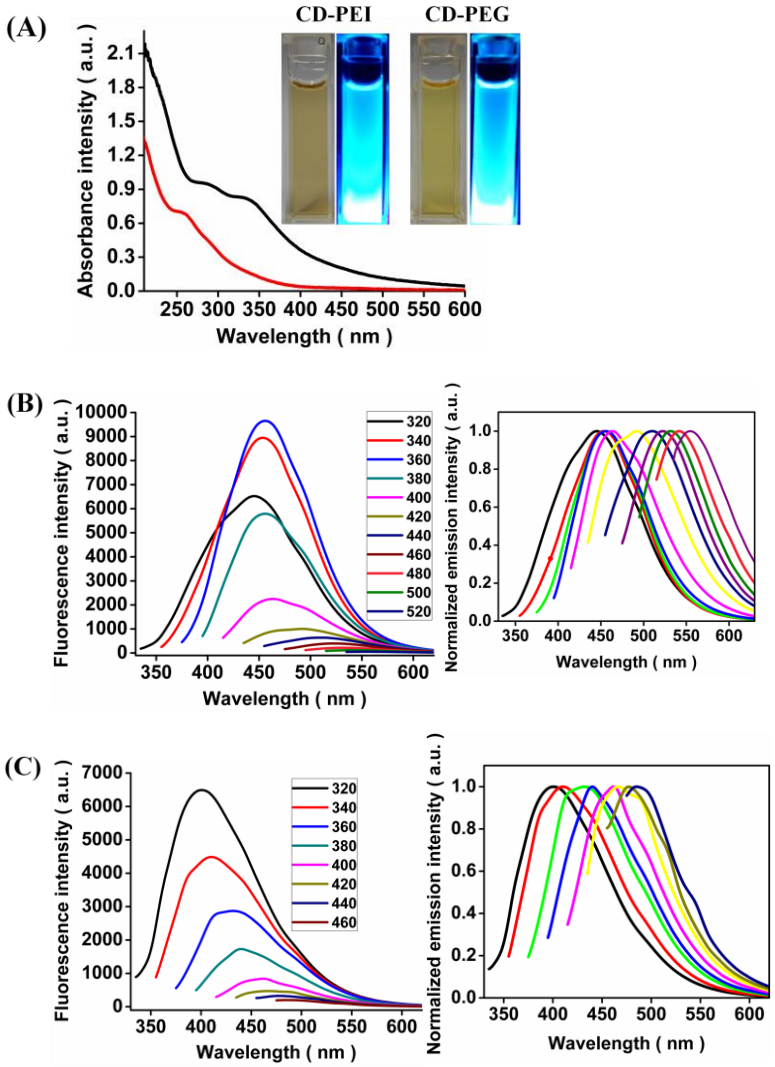

Figure 4.1 (A) UV-vis absorption spectra of CD-PEI (black) and CD-PEG (red).The insets are the diluted aqueous solution of as-prepared CD-PEI and CD-PEG in ambient light(left) and UV-light (right).(B) Fluorescence emission spectra of CD-PEI at different excitation wavelengths (inset: normalized emission spectra). (C) Fluorescence emission spectra of CD-PEG at different excitation wavelengths (inset: normalized emission spectra).

Sample	**Integrated emission intensity (*I*)**	**Absorbance at 360 nm (*A*)**	**Refractive index of solvent (*η*)**	**Quantum yield at 360 nm (*Q*)**
Quinine sulphate	796366	0.0860	1.33	0.54 (known)
CD-PEG	127103	0.1057	1.33	0.0701
CD-PEI	241753	0.1072	1.33	0.1315

Table 4.1 Quantum yield calculation of C-dots.

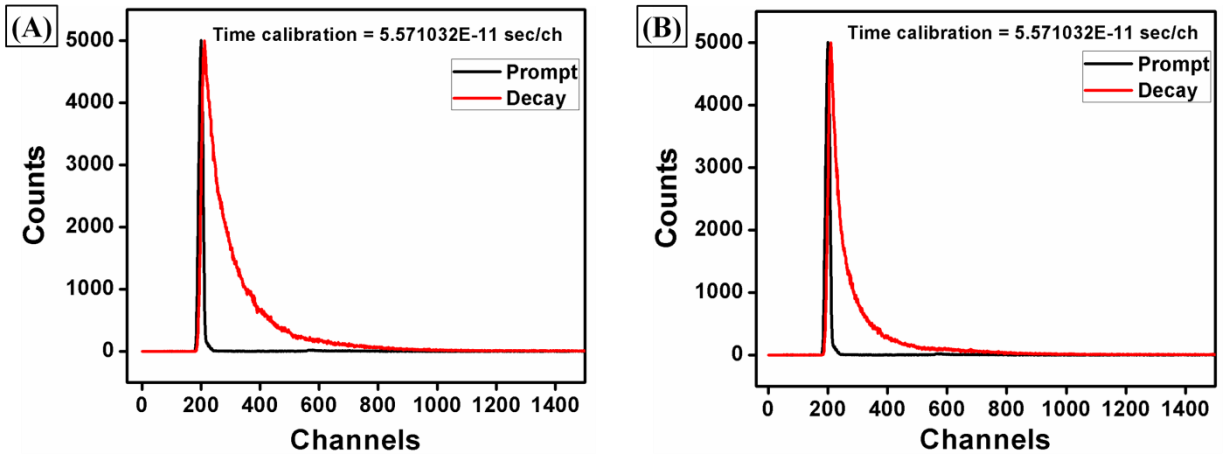

Figure 4.2 Fluorescence decay curve of (A) CD-PEI (λ_{ex} = 360 nm; λ_{em} = 460 nm) and (B) CD-PEG (λ_{ex} = 320 nm; λ_{em} = 400 nm).

Sample	a_1	τ_1(ns)	a_2	τ_2(ns)	a_3	τ_3(ns)	τ_{av}(ns)	χ^2
CD-PEI	0.0912	1.221	0.6174	4.979	0.2913	10.326	6.193	1.173
CD-PEG	0.5002	3.316	0.2125	0.746	0.2873	10.470	4.825	1.219

Table 4.2 Tabular representation of fluorescence lifetime calculation of CDs.

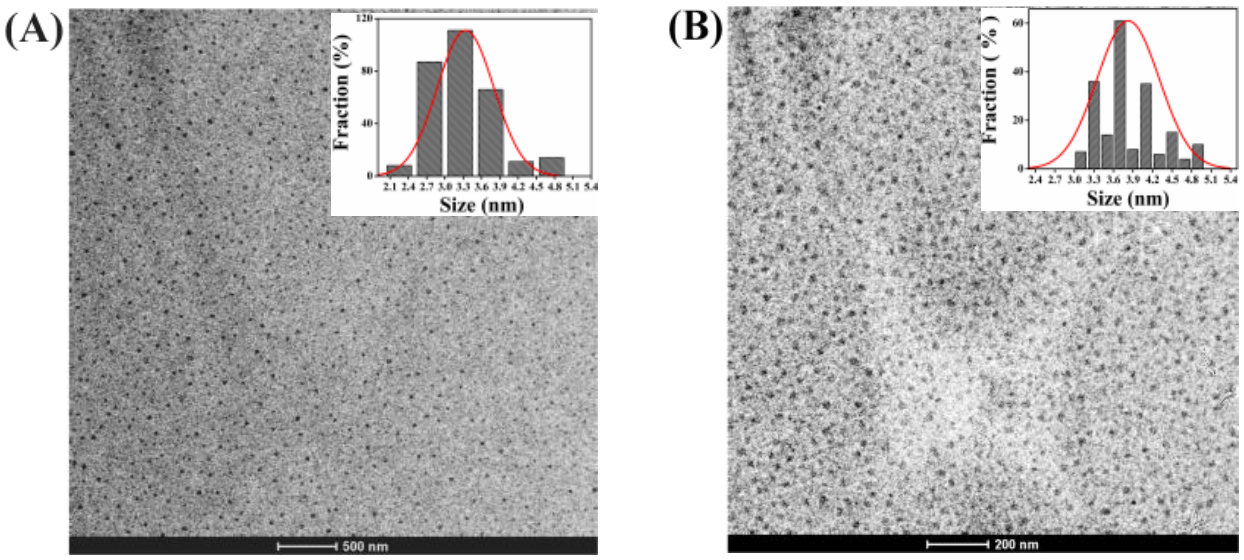

Figure 4.3 TEM images of C-dots. (A) CD-PEI and (B) CD-PEG. The insets are the size distribution histograms of C-dots.

Fig. 4.5 represents the EDAX spectrum of CD-PEI and CD-PEG, signifying the presence of carbon, oxygen and nitrogen elements. From the results, it can be seen that the CDs are predominantly composed of carbon. Their composition was mainly dictated by the nature of passivating agent. Higher nitrogen content in CD-PEI probably suggested the presence of amino groups, while higher oxygen content indicated the presence of hydroxyl groups in CD-PEG. XRD patterns of CD-PEI and CD-PEG **(Fig. 4.6 (A))** display a broad peak at 2θ values of 26.84° and 22.63° respectively, corresponding to (002) plane of nanocarbon. CD-PEI shows an additional weak peak at 2θ = 42.03°, which is attributed to (101) plane. The obtained patterns confirm the amorphous nature of CDs (Zhu et al., 2013c and Pandey et al., 2013). The presence of various functional groups was further explained through FTIR to establish the exact chemical nature of CD-PEI and CD-PEG. Notably, the FTIR spectra of CD-PEG shows peaks at 3432 cm^{-1} ,1638 cm^{-1} ,1406 cm^{-1} and 1091 cm^{-1} corresponding to O-H, C=O , C-N and C-O-C groups **(Fig. 4.6 (B))** in compliance with our previous study (Sachdev et al., 2013). Furthermore, it is known that chitosan can be carbonized under hydrothermal conditions and pyrolysis results in loss of characteristic vibrations of chitosan saccharide structure (Yang et al., 2012). As seen in FTIR spectra of CD-PEI (Fig. 4.6 (B)), the characteristic absorption peaks of chitosan disappear which indicates carbonization. CD-PEI shares many characteristic peaks of PEI such as N-H at 3432 cm^{-1} and 1562 cm^{-1}, C-N at 1309 cm^{-1} (Fig. 4.6 (B)) (Dong et al., 2012, Liu et al., 2012a and Hu et al., 2014). These results reveal that while chitosan got carbonized during pyrolysis, PEI remained stable. Lately, PEI has been reported to be stable up to 200 °C, which is in agreement with the obtained results (Dong et al., 2012 and Yin et al., 2013). However, a noticeable difference between PEI and CD-PEI lies in the peak at 1638 cm^{-1} (C=O stretching vibration), due to hydrothermal treatment the, C=O peak became sharp and strong for CD-PEI. At the same time, CD-PEI showed less intense N-H peak at 1562 cm^{-1} compared to PEI. These surface functional groups impart hydrophilicity and stability to CDs. No precipitation or aggregation was observed in aqueous solution of CDs for several months.

Agarose gel mobility assay **(Fig. 4.7 (A))** was performed to study the surface charge dependent mobility of CDs under electric field. Smear fluorescent bands of CD-PEI and CD-PEG were seen in opposite directions.CD-PEG and DNA migrated towards the positive terminal, while CD-PEI migrated in opposite direction, indicative of the fact that CD-PEI is positively charged and CD-PEG is negatively charged. Sodium dodecyl sulphate- polyacrylamide gel electrophoresis (SDS-PAGE) was done for preliminary investigation of multicolor fluorescence of CDs. CD-PEI shows a single, resolved band **(Fig. 4.7 (B))**. This underscores the fact that as-prepared CD-PEI was pure.

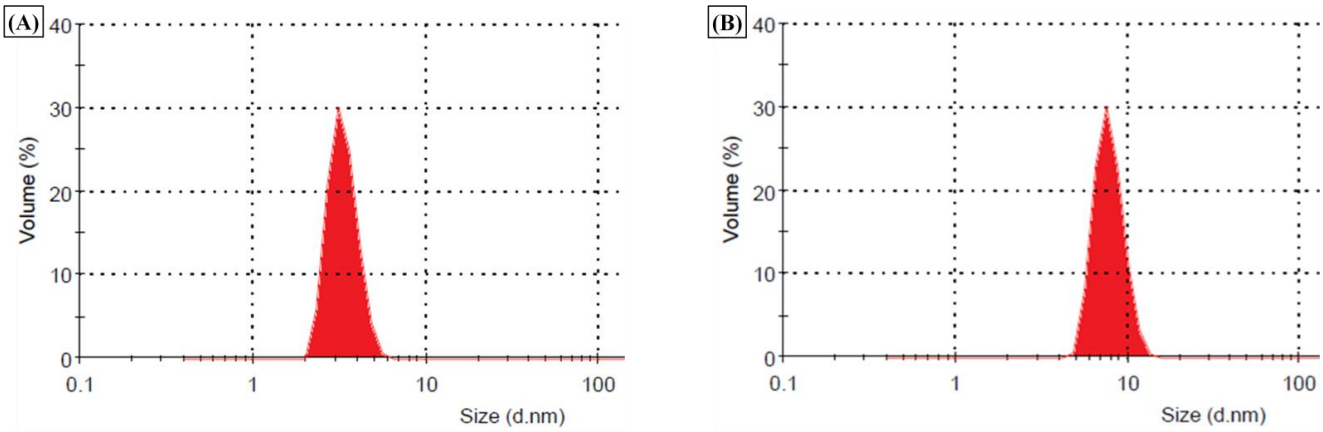

Figure 4.4 DLS spectrum of (A) CD-PEI and (B) CD-PEG representing size distribution by volume.

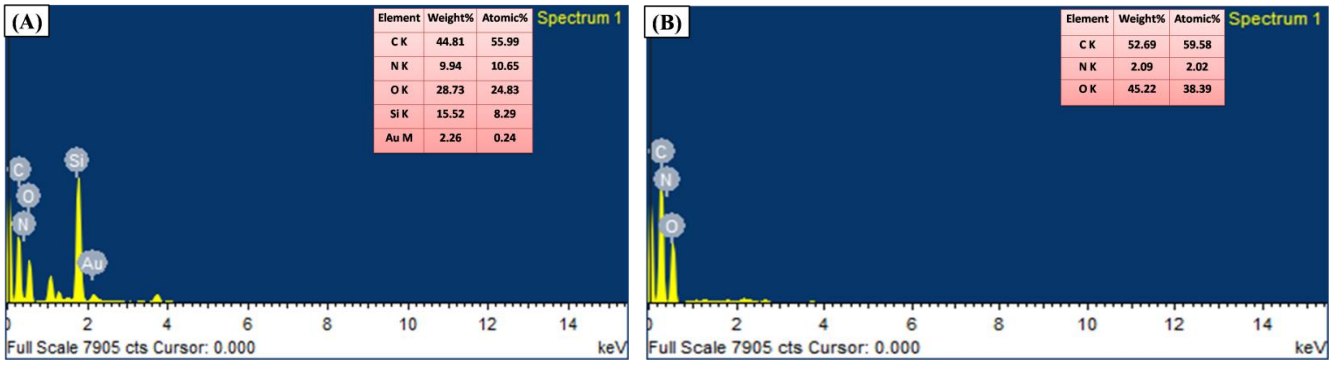

Figure 4.5 EDAX spectrum and elemental composition of (A) CD-PEI and (B) CD-PEG.

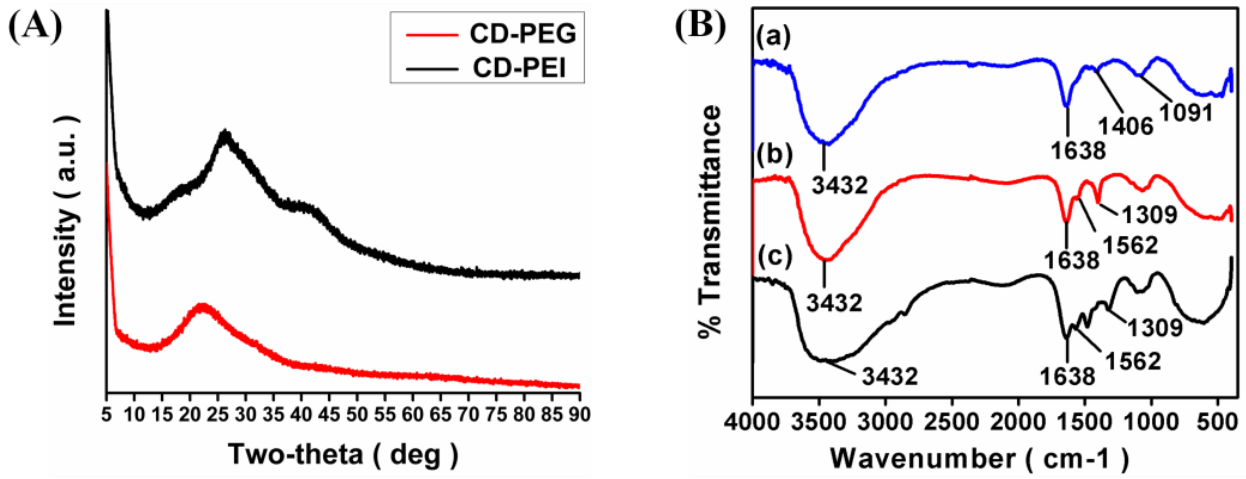

Figure 4.6 (A) XRD patterns of C-dots. (B) FTIR spectrum of (a) CD-PEG, (b) CD-PEI and (c) PEI.

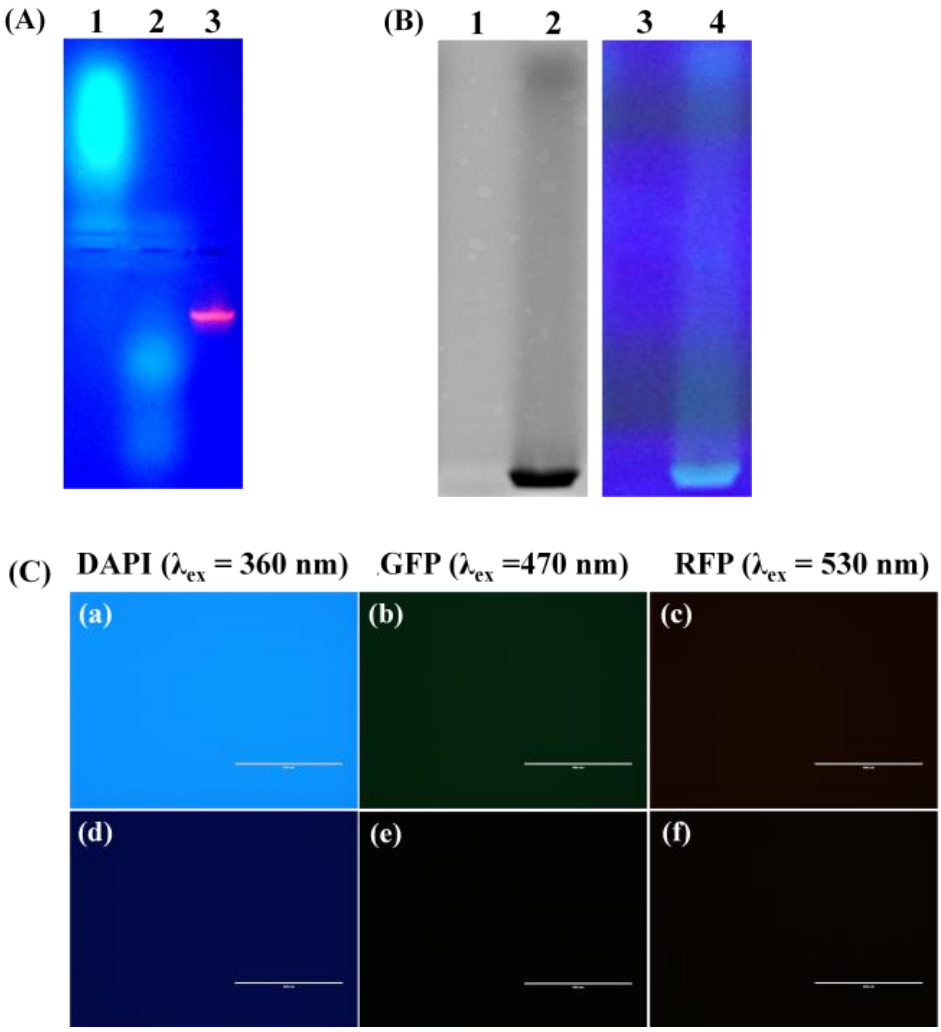

Figure 4.7 (A) Agarose gel electrophoretic mobility of CD-PEI (lane 1), CD-PEG (lane 2) and ethidium bromide stained DNA (lane 3) under UV light (λ_{ex} = 365 nm). (B) SDS- PAGE electrophoresis pattern of CD-PEG (lane 1 & 3) and CD-PEI (lane 2 & 4) observed under normal light (left) and UV light (right). (C) Fluorescence microscopic images taken under various excitation filters. Excised gel band of CD-PEI representing multicolor fluorescence (a-c). Excised gel band of CD-PEG (d-f). Scale bar: 400 μm.

Even more encouraging is the fact that CD-PEI (at such low concentration) was amenable to SDS-PAGE applications (Liu et al., 2007). No fluorescent band was observed in case of CD-PEG at concentration equivalent to CD-PEI, owing to its lesser brightness **(Fig. 4.7 (C))**. The excised CD-PEI band depicts multicolor fluorescence, whereas no fluorescence was observed from excised piece of gel (CD-PEG) and blue color was primarily due to background noise.

4.2.2 pH sensitivity and stability of CD-PEI and CD-PEG

pH sensitive feature of C-dots is one of the interesting phenomenon studied over the years (Jia et al., 2012 and Nie et al., 2014). Therefore, fluorescence response of CD-PEI and CD-PEG

was investigated at different pH values by adjusting the pH by 0.1 N solutions of HCl and NaOH under constant ionic strengths conditions. The fluorescence intensity of CD-PEI was found to be pH dependent **(Fig. 4.8 (A))**. There was a steady increase in fluorescence intensity in the pH range of 3-7, with maximum intensity at pH 7.0. Shift in pH from acidic to basic caused a notable reduction in fluorescence intensity of CD-PEI. The minimum in fluorescence intensity was recorded at pH 12.0. Such pH dependent behavior is due to surface amino groups of PEI, owing to their protonation in acidic condition and deprotonation under alkaline environments (Hu et al., 2014). The colloidal stability of CD-PEI over a wide range of pH values was conducted by zeta potential measurements **(Fig. 4.8 (B))**. The isoelectric point of CD-PEI was found to be pH 9.0 (Dong et al., 2012). Zeta potential increased dramatically and reached its maximum value (27.7 mV) at pH 7.0, but became very low at pH values above 7.0, with minimum stability at pH 12.0. The excited state pKa (pKa*) of CD-PEI was calculated to be 5.04 ± 0.11 based on the change in fluorescence intensity with pH spectra at 460 nm **(Fig. 4.9)** (Zhou et al., 2013b). Conversely, for CD-PEG, fluorescence intensity was less under acidic conditions (pH 3-6). An apparent increase in fluorescence intensity was evident in the pH range of 7-12 **(Fig. 4.10 (A))**. Unlike CD-PEI, a shift in fluorescence emission was observed for CD-PEG from pH 10.0 onwards. The change in surface state brought about by the ionization of surface hydroxyl groups influences the electronic transitions in CD-PEG, giving rise to such pH dependent behaviour. Isoelectric point in case of CD-PEG was approximated to be pH 6.0. Contrary to CD-PEI, the zeta potential of CD-PEG was low at pH ≤ 7.0 **(Fig. 4.10 (B))**. There was a marked increase in zeta potential when pH shifted to alkaline. Highly negative zeta potential (29.6 mV) at pH 12.0 explains the higher stability of CD-PEG under basic conditions. The estimation of highest zeta potential values for CD-PEI and CD-PEG to effect stable particle dispersions are in concurrence with the maximum emission observed at specific pH values (Chandra et al., 2013). The effect of varying ionic strengths on the fluorescence intensity of C-dots was studied. There were no considerable changes in fluorescence characteristics of CD-PEI **(Fig. 4.11 (A))** and CD-PEG **(Fig. 4.11 (B))** as NaCl concentration increased from 0.2 to 1.0 M, which is imperative for C-dots to withstand high salt concentrations encountered during biological applications (Zhu et al., 2013c). Moreover, no photobleaching effects were observed for CD-PEI **(Fig. 4.11 (C))** and CD-PEG **(Fig. 4.11 (D))** under continuous irradiation for 2 h. Fluorescence intensity decreased marginally for both CD-PEI (7.94 %) and CD-PEG (4.68 %), portraying fairly good photostability. Resistance to photobleaching along with resilience to ionic strength conceive the possibility of using C-dots as potential candidates for bioimaging applications compared to organic chromophores.

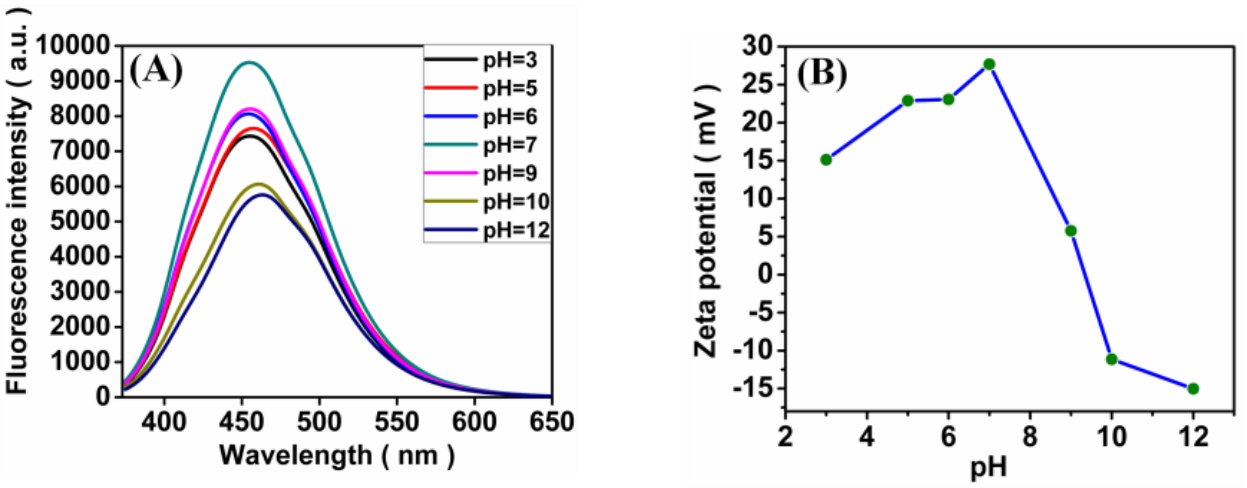

Figure 4.8 (A) pH-dependent fluorescence emission spectra of CD-PEI (λ_{ex} = 360 nm). (B) Zeta potential of CD-PEI as a function of pH.

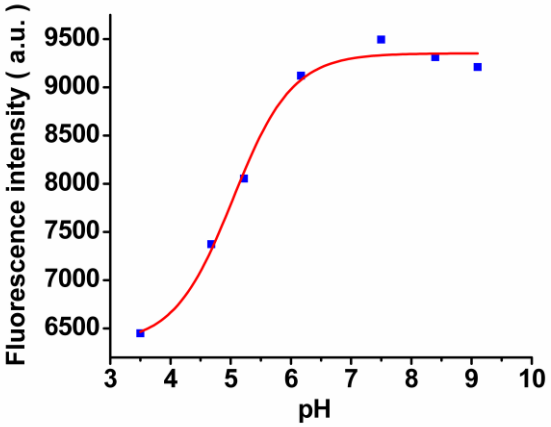

Figure 4.9 Change in fluorescence intensity of CD-PEI at 460 nm (λ_{ex} = 360 nm) as a function of pH. The solid line is fit to emission intensity from pH 3.5-9.0.

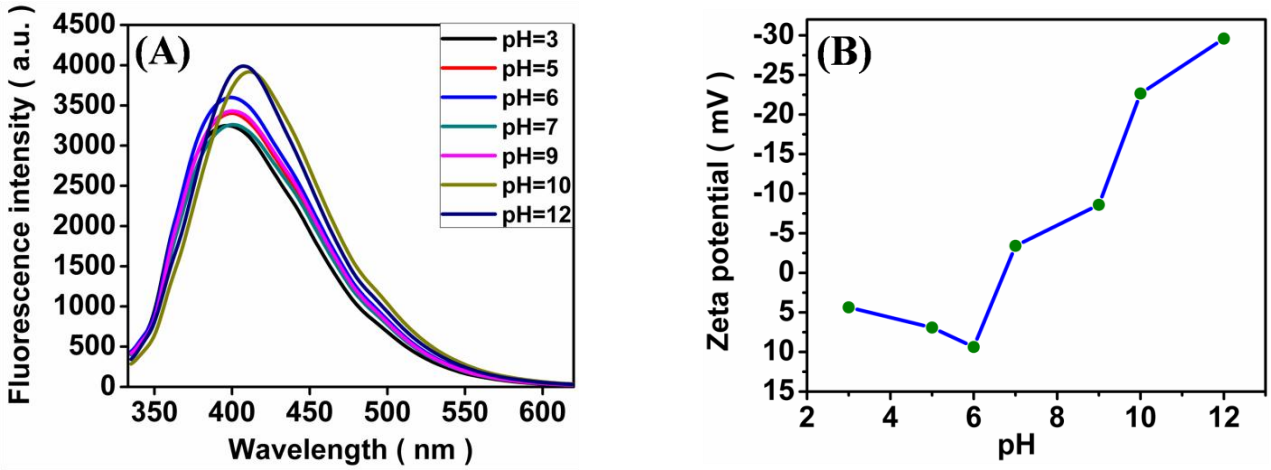

Figure 4.10 (A) pH-dependent fluorescence emission spectra of CD-PEG (λ_{ex} = 320 nm). (B) Zeta potential of CD-PEG as a function of pH.

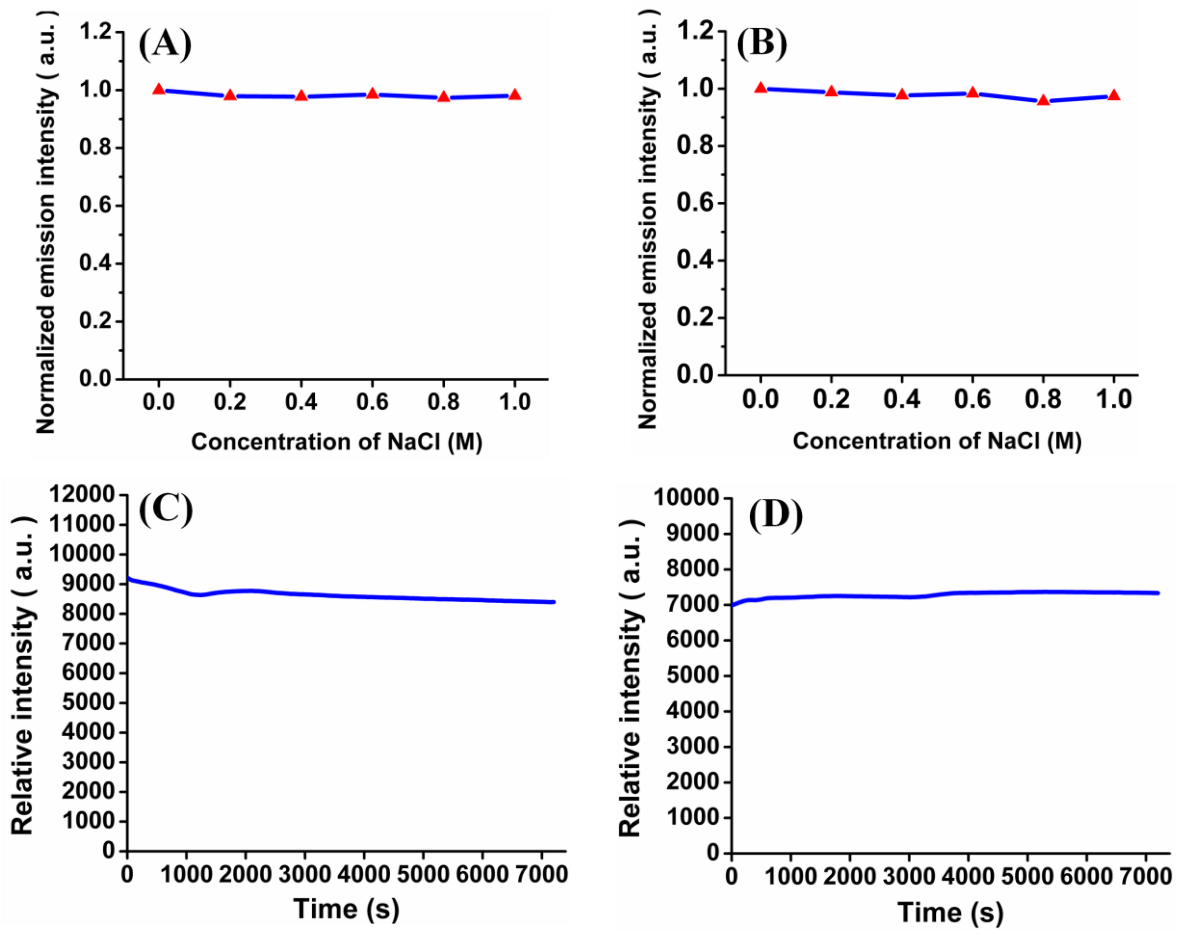

Figure 4.11 Plot of normalized emission intensity versus different ionic strength for (A) CD-PEI and (B) CD-PEG. Dependence of fluorescence emission intensity against time showing photostability profile of (C) CD-PEI (λ_{ex} = 360 nm; λ_{em} = 456 nm) and (D) CD-PEG λ_{ex} = 320 nm; λ_{em} = 400 nm).

4.2.3 Bioimaging efficiencies of CD-PEI and CD-PEG

CD-PEI and CD-PEG were evaluated for bioimaging under *in vitro* conditions. We have chosen A549 and BHK-21 cell lines as model systems for bioimaging based on the following considerations. First, A549 cells are lung adenocarcinoma cells which is most prevalent and fatal type of cancer, whereas BHK-21 are normal cells. These provide a platform to examine the bioimaging efficiencies of CDs in both cancer and normal cells. Second, BHK-21 cells differ from A549 cells in terms of morphology; that is, BHK-21 cells are relatively elongated and have a fibroblastic appearance, while A549 cells are epithelial like cells that possess polygonal morphology. **Fig. 4.12 (a-d)** shows the fluorescence microscopic images of A549 cells labelled with CD-PEI and CD-PEG. A distinct fluorescence imaging pattern was observed for the two types of C-dots. CD-PEI can be clearly seen in the cells depicting blue, green and red colour fluorescence, owing to its excitation dependent behaviour.

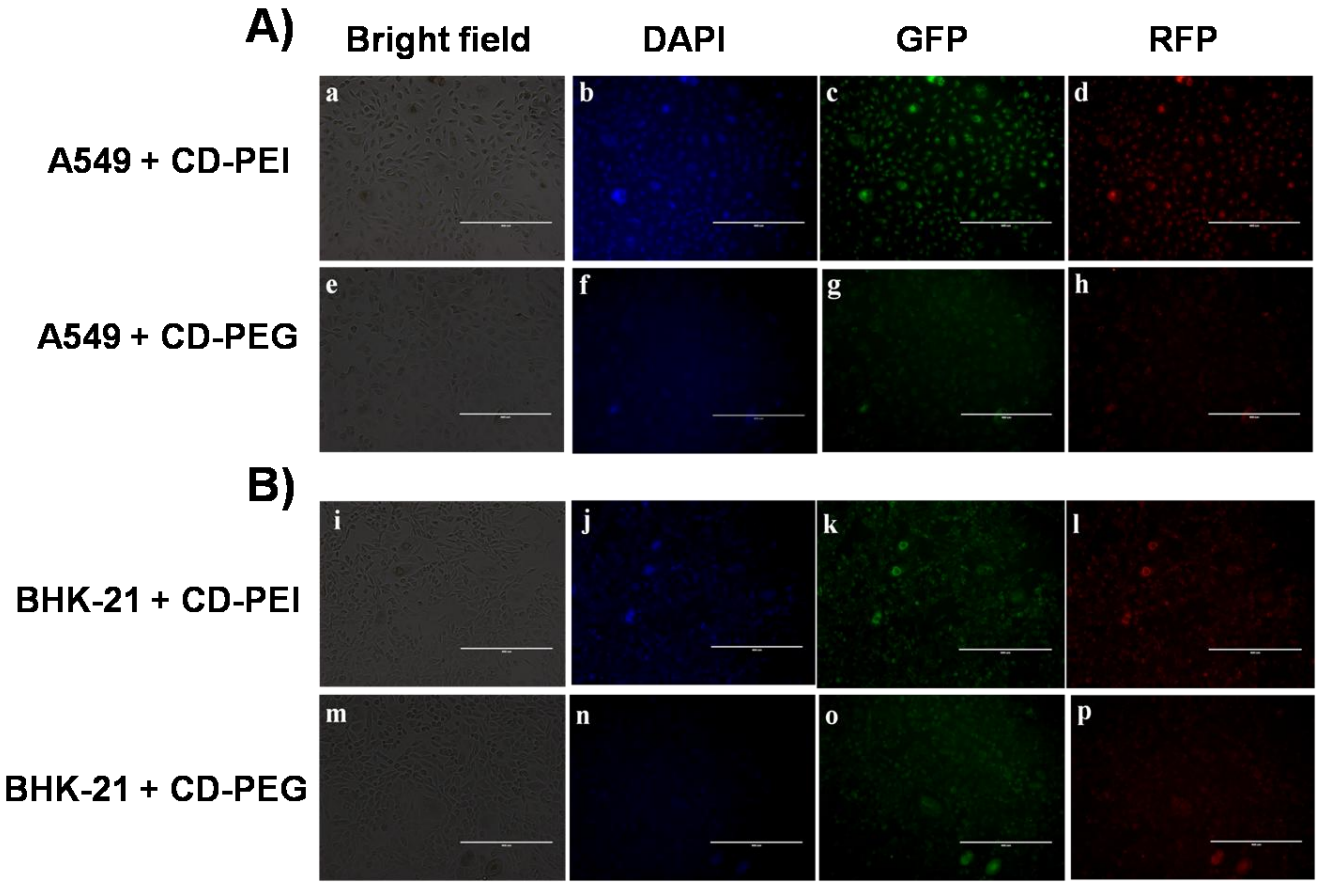

Figure 4.12 (A) Comparison of fluorescence microscopic images of A549 cells incubated with CD-PEI (a-d) and CD-PEG (e-h).(B) Comparison of fluorescence microscopic images of BHK-21 cells incubated with CD-PEI(i-l) and CD-PEG (m-p). Scale bar: 400 µm. Filters: DAPI (λ_{ex} = 360 nm, λ_{em} = 447 nm)**;** GFP (λ_{ex} = 470 nm; λ_{em} = 525 nm); RFP (λ_{ex} = 530 nm; λ_{em} = 593 nm).

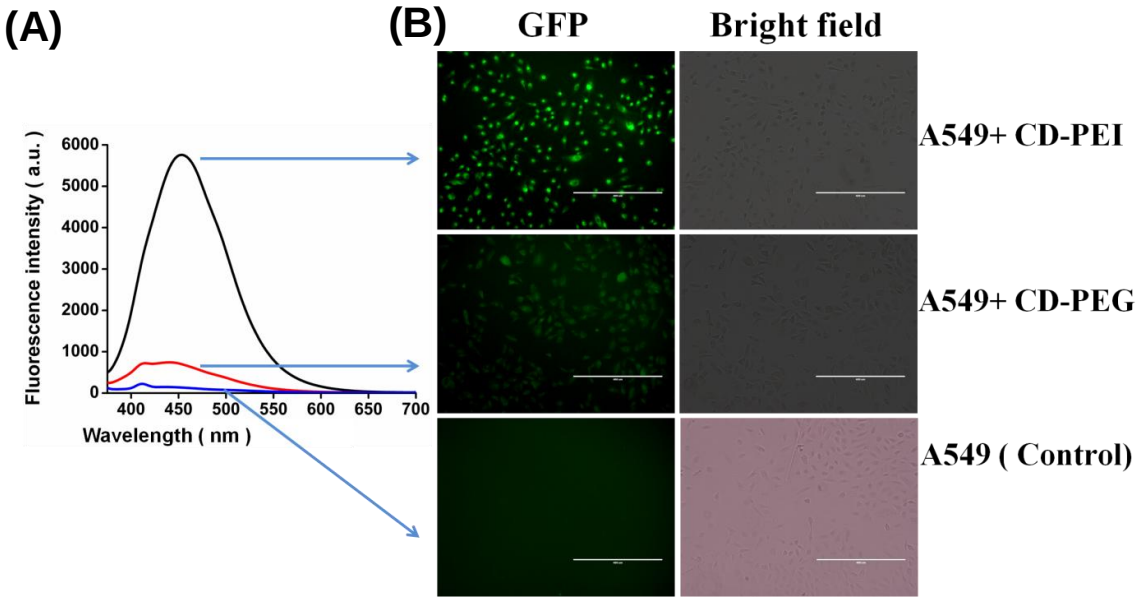

Figure 4.13 (A) Fluorescence spectra of A549 cells (blue), A549 + CD-PEG (red) and A549 + CD-PEI (black). (B) Fluorescence microscopic images of A549 cells labeled with C-dots.

Sample	Integrated emission intensity *(I)*	Absorbance at 360 nm *(A)*	Refractive index of solvent (η)	Quantum yield at 360 nm *(Q)*
Quinine sulphate	627215	0.0831	1.33	0.54
A549 + CD-PEI	85996	0.0939	1.33	0.0655
A549 + CD-PEG	50046	0.1024	1.33	0.0349

Table 4.3 Quantum yield measurements of CDs labeled A549 cells.

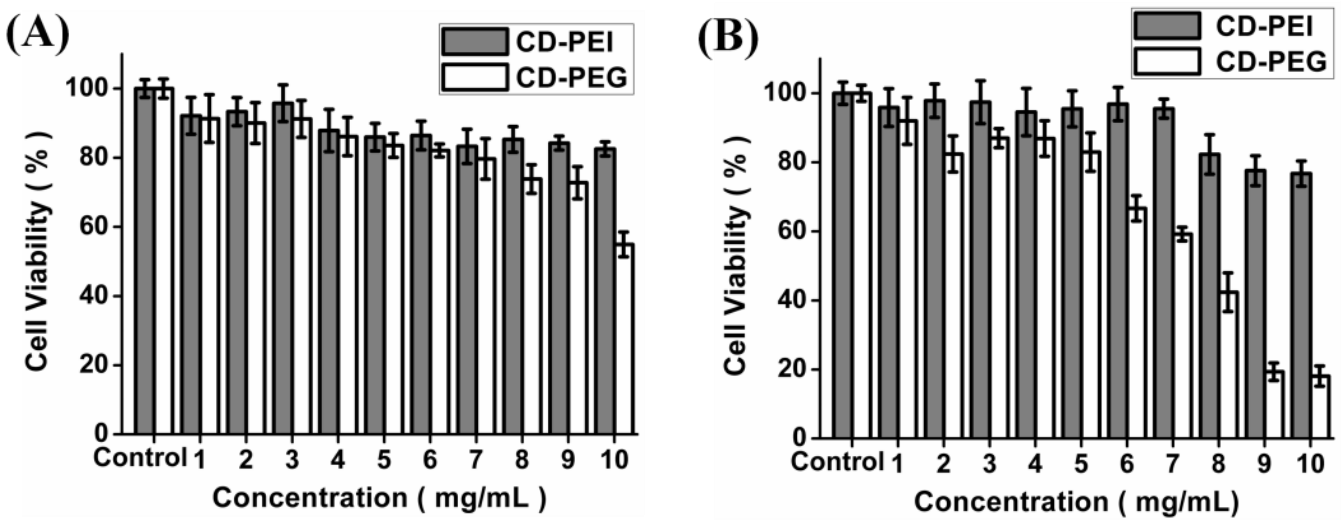

Figure 4.14 MTT based cytotoxicity assay of C-dots against (A) A549 cells and (B) BHK-21 cells. The percentage cell viability is assumed to be 100 % for control in each case.

However, CD-PEG labelled A549 cells **(Fig. 4.12 (e-h))** showed only green and red fluorescent images under similar parameters. BHK-21 cells labelled with CD-PEI **(Fig. 4.12 (i-l))** and CD-PEG **(Fig. 4.12 (m-p))** demonstrated similar fluorescence profiles. Besides, CD-PEG labelled A549 and BHK-21 cells barely depict any blue colour fluorescence under similar microscopic parameters. On closer examination two phenomena are evident: (1) labelled A549 cells exhibit bright fluorescence images than labelled BHK-21. This could be due to enhanced cellular uptake of C-dots by cancer cells compared to normal cells. (2) Fluorescence microscopic images of CD-PEI and CD-PEG labelled cells testify the excellent bioimaging characteristics of former compared to latter. This outcome seems perfectly rational in terms of physical and chemical properties of C-dots. CD-PEI is positively charged due to the presence of amine groups on its surface which was confirmed through zeta potential **(Fig. 4.8)** and electrophoresis studies **(Fig. 4.7 (A))**. Hence, CD-PEI is more capable of binding to the cell membrane through electrostatic interactions. On the other hand, the overall surface charge of CD-PEG is negative due to presence of PEG chains impeding its interaction with cell membrane. The above investigations clearly acknowledge the fact that the surface functionality to a greater extent influences the bioimaging efficiency of C-dots. Meanwhile, one can see ubiquitous distribution of C-dots inside the cells. Wide distribution of CDs in the cytoplasm contrary to nucleus (relatively weak fluorescence) was observed due to lesser penetration of C-dots, similar to previous published reports (Cao et al., 2007, Liang et al., 2013b and Ding et al., 2013).

Quantitative assessment of bioimaging efficiency of C-dots was performed by fluorescence spectroscopy and quantum yield measurements. The fluorescence characteristics of C-dots labelled A549 cells have been shown in **Fig. 4.13**. CD-PEI labelled cells had more fluorescence intensity than CD-PEG labelled cells. The obtained fluorescence microscopic images corroborate well with the fluorescence spectroscopic measurements. Additionally, the fluorescence of C-dots labelled cells was quantitated through quantum yield measurements. The quantum yield of CD-PEI and CD-PEG labelled cells were 6.55 % and 3.49 %, respectively **(Table 4.3)**. A major concern for bioimaging is the cytotoxicity of fluorescent nanoparticles which limits their applicability. MTT assay was performed in order to determine the optimal concentration of C-dots to eliminate the possibility of cell death and detrimental morphological changes during bioimaging. From the results shown in **Fig. 4.14 (A)**, it is clear that about 94 % of A549 cells were viable up to 3 mg $mL^{-1}$of CD-PEI. When the concentration of CD-PEI was increased to 10 mg mL^{-1}, cell viability subsequently declined to 83 %. Likewise, A549 cells incubated with CD-PEG showed nearly 90 % cell viability up to

3 mg mL^{-1}, while severe decline in cell viability was observed beyond mg mL^{-1}. MTT plot of BHK-21 cells **(Fig. 4.14 (B))** depict that around 95 % cells were viable in the presence of 5 mg mL^{-1} of CD-PEI and above 82 % of the cells remained viable up to 5 mg mL^{-1} concentration of CD-PEG. Previous investigations have shown that CD-PEI is less toxic than PEI for cell based applications due to comparatively lower cationic charge density (Hu et al., 2014). Essentially, the maximum concentrations of CD-PEI and CD-PEG estimated through MTT assay were much higher than necessary for bioimaging applications.

In summary, PEI and PEG surface passivated C-dots were synthesized through a one-step hydrothermal method. Physicochemical properties of CDs were influenced by the nature of the passivating polymer. CD-PEI demonstrated superior fluorescent characteristics compared to CD-PEG. The proposed study also validated the differential labelling capacity of C-dots based on surface charge by competitive experiments as well as comparative study on cancer and normal cells. Importantly, both types of C-dots were found to be biocompatible at concentrations optimal for bioimaging. Designing C-dots that are stable in the biological milieu can facilitate the creation of fluorescent nanoprobes for potential biomedical applications.

CHAPTER 5

Development of a Green Synthetic Approach for Production of C-dots from Natural Molecular Precursors for Versatile Applications

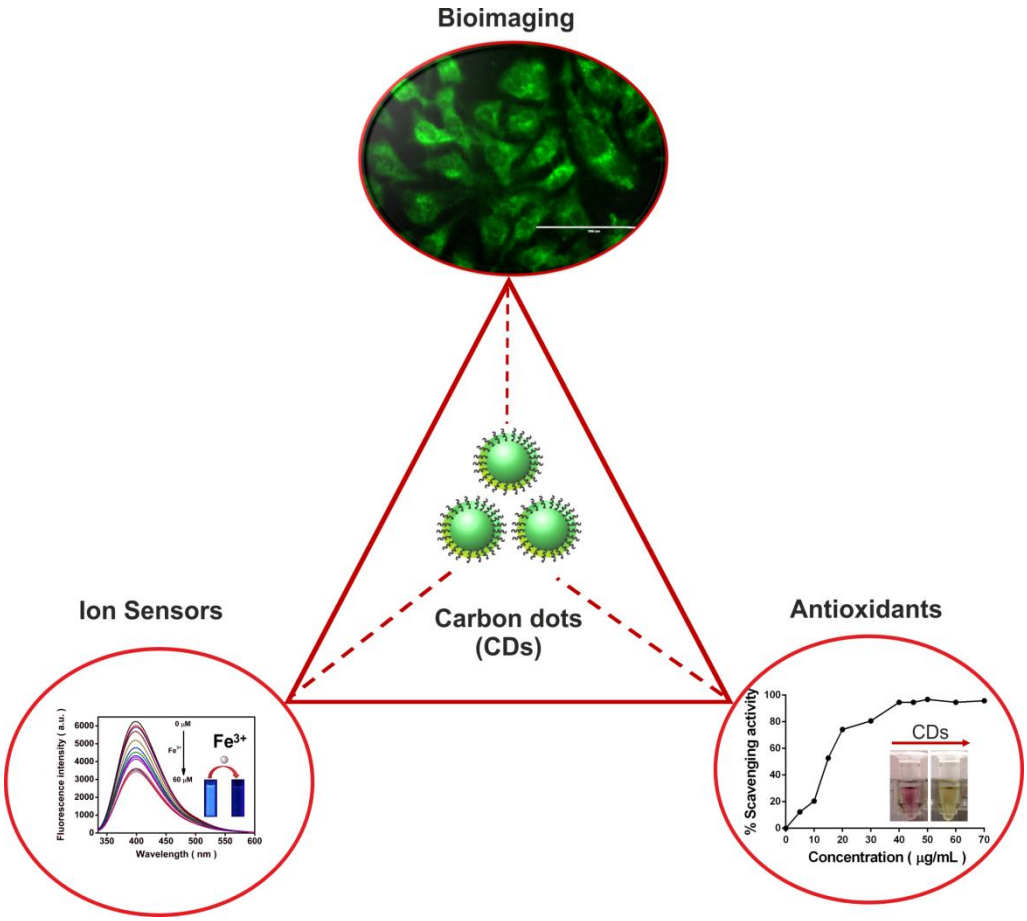

CHAPTER 5

DEVELOPMENT OF A GREEN SYNTHETIC APPROACH FOR PRODUCTION OF C-DOTS FROM NATURAL MOLECULAR PRECURSORS FOR VERSATILE APPLICATIONS

5.1 Overview

In recent years, one-step hydrothermal approach for C-dots synthesis has gained immense popularity because of higher consistency, controlled reaction conditions and economic viability. Despite several benefits, use of toxic precursors and passivating agents in the hydrothermal process often complicate their biological applications. Green synthesis of C-dots is a highly attractive research topic, which exploits the use of natural, renewable carbon precursors. Additionally, the functional groups associated with complex organic moieties in the natural precursors would take care of the surface passivation processes to improve fluorescence and water solubility of the as-synthesized C-dots. Nevertheless, it is always exciting to explore the green sources for C-dots because these are inexpensive, clean, nontoxic and easily accessible. However, the key challenge remains to produce C-dots with high quantum yields in ample amounts by using simple one-step methodologies. In the quest of exploring natural precursors C-dots synthesis, herein a simple green synthetic approach for synthesizing C-dots from coriander leaves by one-step hydrothermal mediated synthesis has been reported. This methodology is cost-effective, less time-consuming and uses water as a solvent. Importantly, no additional surface passivation agent was required and coriander leaves solely served as the carbon source and the passivation agent for C-dots. Coriander leaves are edible and naturally contain carbohydrate and proteins which are abundant in carbon, nitrogen and oxygen elements. Consequently, the formation of C-dots may involve dehydration and carbonization of the coriander leaves followed by *in situ* surface passivation under high temperature and pressure during the hydrothermal treatment (Huang et al., 2014 and Park et al., 2014). Fortunately, the as-prepared C-dots have sufficient quantum yield, favourable for exploring their applications. Besides, a detailed analysis of the optical and physicochemical properties of C-dots has been presented. Apart from this, our study encompasses the multifunctional aspects

of C-dots such as potential antioxidants and selective ion detection probes. To demonstrate the bioimaging potential of C-dots *in vitro,* A549 (human lung adenocarcinoma) and L-132 (human normal lung epithelial) cells have been selected as model systems, since lung cancer is the second-most prevalent type of cancer in the world (Kumar et al., 2013).

5.2 RESULTS AND DISCUSSION

5.2.1 Synthesis and characterization of C-dots from coriander leaves

Coriander is a natural herb which is commonly being used around the world as a condiment, abundant in carbon, oxygen and nitrogen elements. Moreover, coriander leaves can act as an excellent green and natural precursor material for the synthesis of C-dots without the aid of any additional passivating agent. The successful preparation of such C-dots has been carried out by a one-step hydrothermal treatment, which produced a yellow or light brown aqueous solution, indicating successful carbonization of the coriander leaves. Bright green luminescence under UV light further implied the formation of C-dots **(Fig. 5.1 (A))**. The aqueous solution of C-dots shows two absorption peaks at 273 nm and 320 nm which were attributed to π-π^* transition of C=C bonds and n-π^* transition of C=O bonds in C-dots **(Fig. 5.1 (B))** (Sachdev et al., 2013, Sachdev et al., 2014 and Park et al., 2014). On the other hand, fluorescence spectra depicted an excitation dependent behaviour. With an increase in excitation wavelength from 320 nm to 480 nm, the maximum emission shifted from 400 nm to 510 nm along with a concurrent decrease in emission intensity **(Fig. 5.1 (C))**. The quantum yield of C-dots was determined to be 6.48 % using quinine sulphate as a reference **(Table 5.1)**. TEM images revealed uniform black dots with near-spherical morphology **(Fig. 5.2 (A))**. The average mean diameter of the C-dots was 2.387 with size distribution ranging from 1.5 to 2.98 nm, as estimated from statistical distributions **(Fig. 5.2 (B))**. Due to small size, low contrast and amorphous nature of C-dots, high resolution TEM images could not be obtained. The aqueous suspension of C-dots had an average hydrodynamic diameter of 4.158 nm, slightly more than the mean dried-state diameter as illustrated by TEM results **(Fig. 5.2 (C))**. EDS elemental mapping distributions further indicated the presence of carbon (C), nitrogen (N) and oxygen (O) elements in CDs **(Fig. 5.2 (D))**. These correspond to the distribution of the functional groups formed on the surface of C-dots. SAED pattern of the C-dots showed diffused rings, suggesting an amorphous carbon phase **(Fig. 5.3)**.

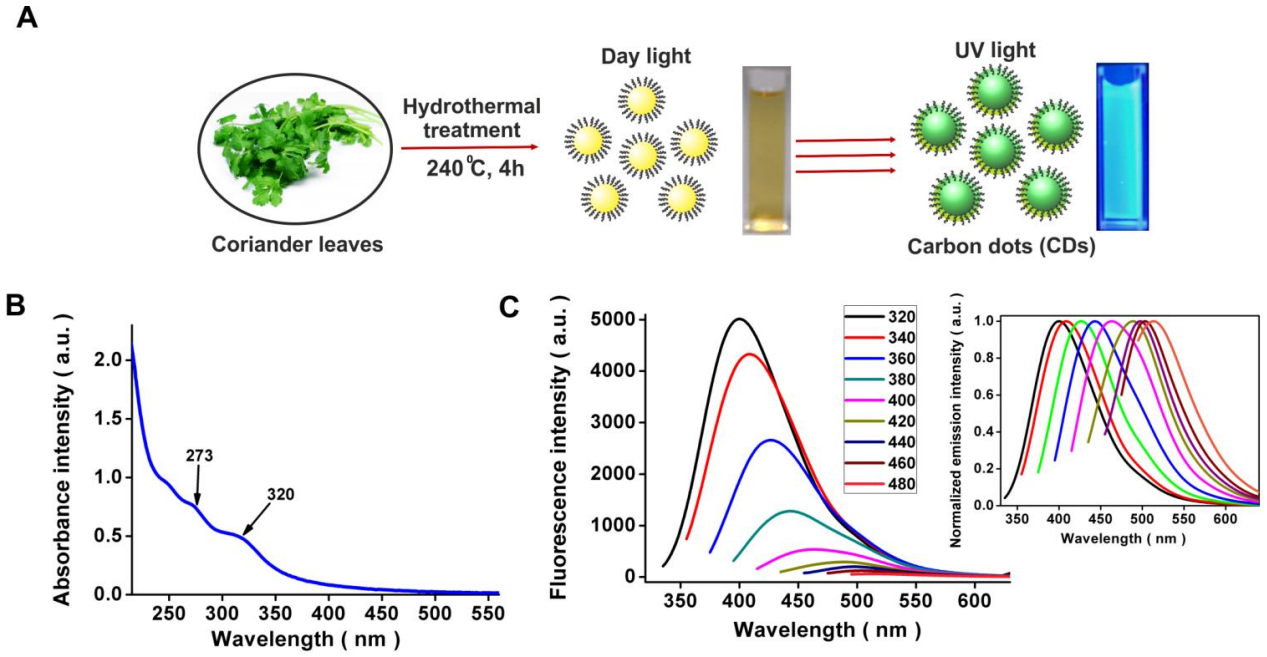

Figure 5.1 (A) Schematic illustration depicting one-step synthesis of C-dots from coriander leaves. (B) UV-vis absorption spectrum of C-dots. (C) Fluorescence emission spectra of C-dots at different excitation wavelengths ranging from 320 nm to 480 nm with increments of 20 nm (inset: normalized emission intensity).

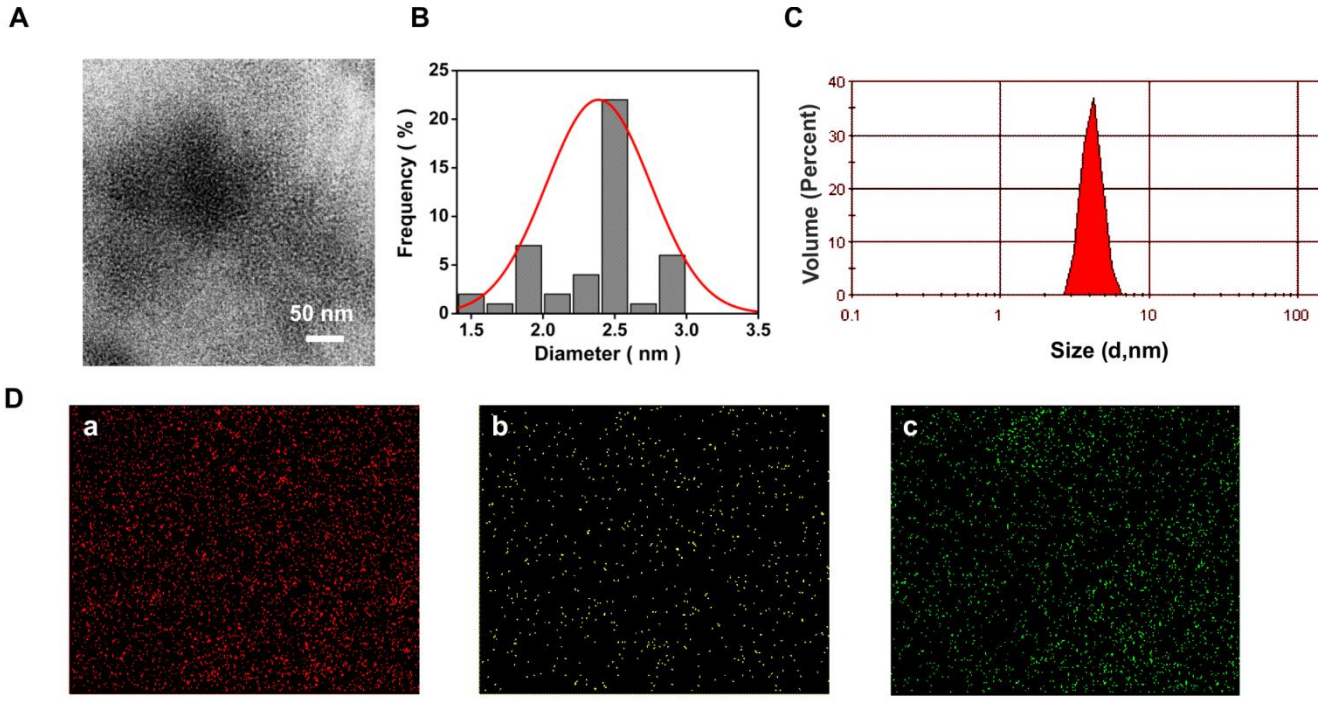

Figure 5.2 (A) TEM image of C-dots. (B) Size distribution histogram of C-dots as determined by TEM. (C) DLS spectrum (size distribution by volume) of aqueous suspension of C-dots. (D) Elemental mapping of C-dots. (a–c) Individual elemental distribution (red for carbon, yellow for nitrogen and green for oxygen).

Sample	**Integrated emission intensity *(I)***	**Absorbance at 360 nm *(A)***	**Refractive index of solvent (η)**	**Quantum yield at 360 nm *(Q)***
Quinine sulphate	542308	0.1320	1.33	0.54 (known)
C-dots	85962	0.1742	1.33	0.0648

Table 5.1 Quantum yield calculation of C-dots.

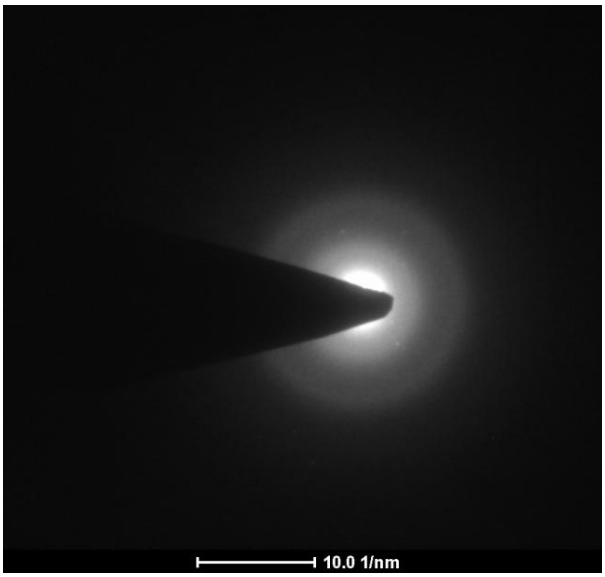

Figure 5.3 SAED pattern of C-dots.

In addition, XRD pattern depicted a broad amorphous hump at 2θ = 21.5° along with a weak peak at 2θ = 38.5° corresponding to (002) and (101) planes of amorphous carbon in accordance with the SAED results **(Fig. 5.4 (A))** (Mewada et al., 2013). FTIR spectrum was further recorded to ascertain the exact chemical composition of C-dots **(Fig. 5.4 (B))**. Overlapping O–H/N–H stretching bands were detected at 3432 cm^{-1}, whereas peaks at 2837 cm^{-1} and 804 cm^{-1} corresponded to C–H stretching and bending vibrations (Mehta et al., 2014 and Park et al., 2014). Peaks at 2359 cm^{-1} and 2341 cm^{-1} represented C–N stretching, while N–H deformation vibration was observed at 1558 cm^{-1} (Zhu et al., 2013b and Mehta et al., 2014). Furthermore, peaks at 1706 cm^{-1} and 1640 cm^{-1} corresponded to C=O and C=C stretch of carbon backbone of C-dots. Notably, the peaks at 1377 cm^{-1}, 1333 cm^{-1} and 1020 cm^{-1}

indicated asymmetric and symmetric vibrations of C–O–C, while peaks at 1124 cm^{-1} and 1050 cm^{-1} represented stretching and bending vibrations of C–O bonds in carboxyl groups (Mehta et al., 2014). The above investigations suggested that C-dots were functionalized with hydroxyl, carboxylic, carbonyl and amino groups, derived from organic moieties in coriander leaves under hydrothermal conditions. These groups endow the C-dots with excellent water solubility, with no signs of aggregation or loss of fluorescence after several months. The zeta potential of C-dots was negative (-24.9 mV), due to the abundance of hydroxyl and carboxylic groups on the surface **(Fig. 5.4 (C))**, in accordance with the FTIR data (Zhu et al., 2013b and Liang et al., 2014). The thermal stability of C-dots was demonstrated by the TGA curve **(Fig. 5.4 (D))**. The thermogram exhibited a three-step degradation pattern, with an initial weight loss of 3 % at 100 °C due to elimination of water molecules or the moisture associated with C-dots. A slight weight loss (7 %) occurred between 100 and 200 °C, indicating thermal stability of C-dots up to 200 °C. The final degradation step resulted in a significant weight loss (93 %) in the range of 200-435 °C due to the gradual degradation of the surface functional groups of C-dots. Beyond 435 °C the curve levelled off (Wang et al., 2013a and Mewada et al., 2013). Elemental composition of C-dots was elucidated by CHN analyzer, confirming the presence of 50.8 % C, 5.3 % H, 4.07 % N and 39.83 % O (calculated). Higher C and O content and lesser N content indicated that these particles were predominantly composed of carbon and oxygen containing functional groups along with few nitrogen containing groups, which corroborates well with the EDS data **(Table 5.2)**. Fluorescence spectra of C-dots were recorded at different pH values by adjusting the pH by 0.1 N solutions of HCl and NaOH. With an increase in pH in the range of 3-12, a steady increase in fluorescence intensity was recorded, with a maximum intensity at pH 12.0, beyond which no significant changes were found **(Fig. 5.5 (A))**. Such pH dependent behaviour could be due to changes in the surface state of C-dots due to the ionization of the carboxyl and hydroxyl groups as observed earlier (Sachdev et al., 2014). The colloidal stability of C-dots was studied in terms of changes in the zeta potential as a function of pH **(Fig. 5.5 (B))**. The zeta potential value changed from 19.03 mV to -22.2 mV with an increase in pH. Higher zeta potential value favoured stable particle dispersion which is in accordance with the maximum emission observed at pH 12.0. The effect of the solvent on the solubility and fluorescence intensity of C-dots was investigated **(Fig. 5.6 (A))**. C-dots were found to be soluble in organic solvents such as N-dimethylformamide (DMF), dimethylsulfoxide (DMSO) and methanol. Further, it was observed that C-dots had the highest fluorescence intensity in water, followed by methanol, DMSO and DMF, without any shift in the emission peaks. Due to high polarity of water compared to other organic solvents, C-dots demonstrated superior fluorescence intensity in water.

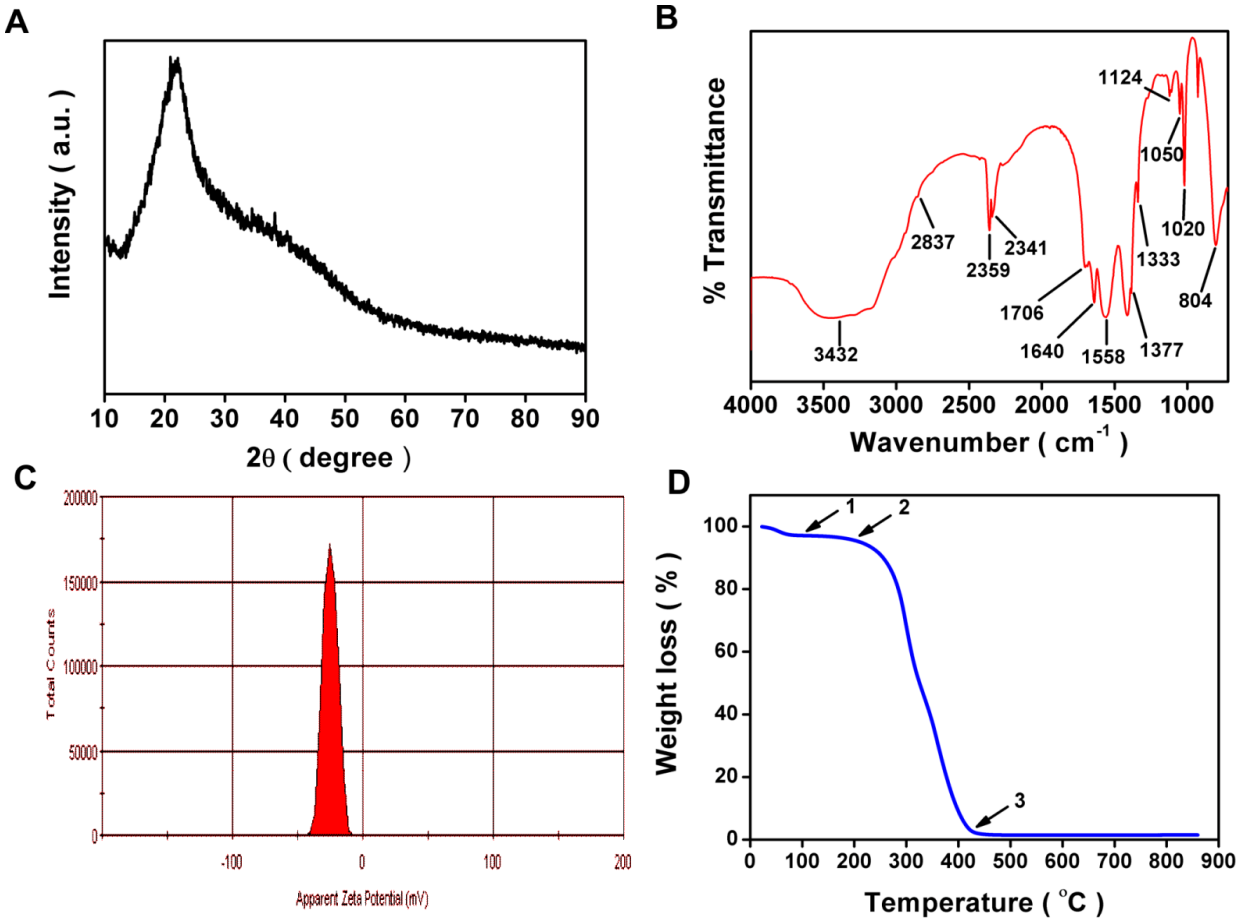

Figure 5.4 (A) XRD pattern, (B) FTIR spectrum, (C) Zeta potential and (D) TGA analysis of C-dots.

	C (%)	H (%)	N (%)	O (%) (Calculated)	Composition
C-dots	50.8	5.3	4.07	39.83	$C_{4.0}H_{5.0}O_{2.5}N_{0.3}$

Table 5.2 Elemental analysis of as-prepared C-dots through CHNS analyzer.

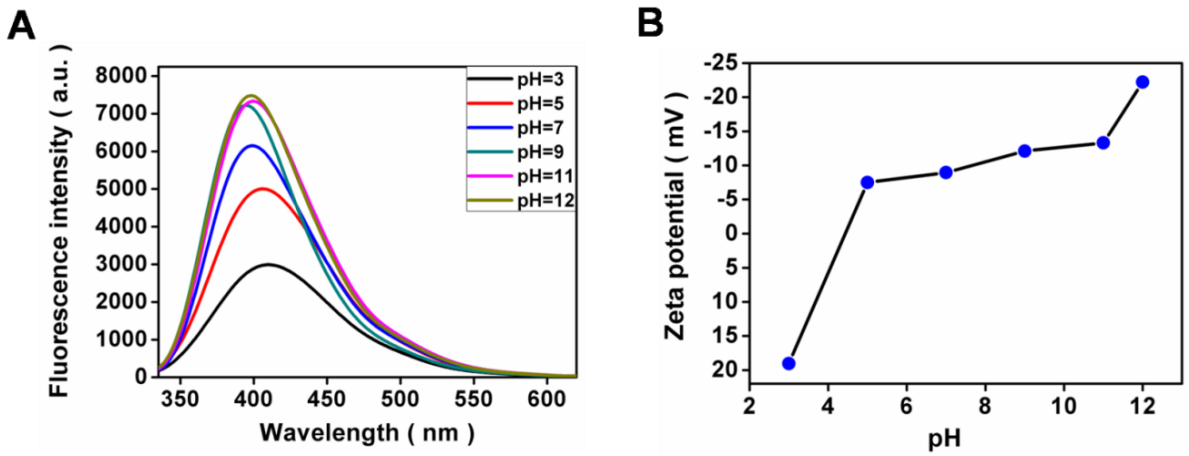

Figure 5.5 (A) Dependence of fluorescence emission of C-dots on pH (λ_{ex} = 320 nm). (B) Variation in zeta potential of C-dots as a function of pH.

This multisolvent solubility could be attributed to the polar functional groups such as carboxyl and hydroxyl on the surface of C-dots. Nonetheless, photostability studies indicate that C-dots had a stable emission even after 2.5 h of continuous excitation. Fluorescence intensity decreased slightly (2.87 %), representing a fairly good photostability **(Fig. 5.6 (B))**.

5.2.2 Antioxidant activity

Antioxidant activity is a commonly used parameter to assess the ability of a material to scavenge or neutralize free radicals. There have been quite a few reports on the antioxidant activity of C-dots (Das et al., 2014 and Purkayastha et al., 2014). DPPH based assay is one of the most commonly employed method to evaluate the antioxidant activity (Pyrzynska et al., 2013). DPPH is a long-lived, nitrogen containing free radical which is deep purple in colour, which turns yellow as soon as it interacts with an antioxidant. Different concentrations of C-dots were added to 50 µM methanolic DPPH solution. Decrease in absorbance at 517 nm was detected within minutes of incubation. From the results shown in **Fig. 5.7 (A)**, the radical scavenging activity of C-dots was found to increase in a dose-dependent manner. As the concentration of C-dots increased from 5 to 70 µg mL^{-1}, there was a subsequent increase in the scavenging activity from 12 to 94 %. From the curve the EC_{50} value (amount of antioxidant required to decrease the concentration of DPPH by 50 %) of C-dots was estimated to be 15 µg mL^{-1}. Interestingly, the DPPH solution turned colourless to yellow with an increase in the concentrations of C-dots **(Fig. 5.7(B))**.

5.2.3 Ion sensing

In recent years, the development of fluorescence based sensors for selective and sensitive detection of metal ions has been pursued by various research groups (Sivaraman et al., 2012, Sivaraman et al., 2013, Sivaraman et al., 2014a and Kamali et al., 2015). In order to evaluate the ability of C-dots obtained from coriander leaves for analytical purposes, their fluorescence intensity in the presence of different metal ions was monitored. **Fig. 5.8 (A)** shows the relative change in the fluorescence intensity of C-dots (0.1 mg mL^{-1}) in the presence of various metal ions (each at a concentration of 60 µM). Out of the 12 kinds of metal ions, Ag^{+}, Cu^{2+}, Hg^{2+} and Fe^{2+} caused slight reduction in the fluorescence intensity. This may be due to non-specific interactions between the functional groups and metal ions. In contrast, Fe^{3+} ions caused the strongest fluorescence quenching effect on C-dots, thereby depicting higher selectivity towards Fe^{3+} ions than other metal ions (Bao et al., 2014, Geng et al., 2014, En et al., 2014 and Sivaraman et al., 2014b).

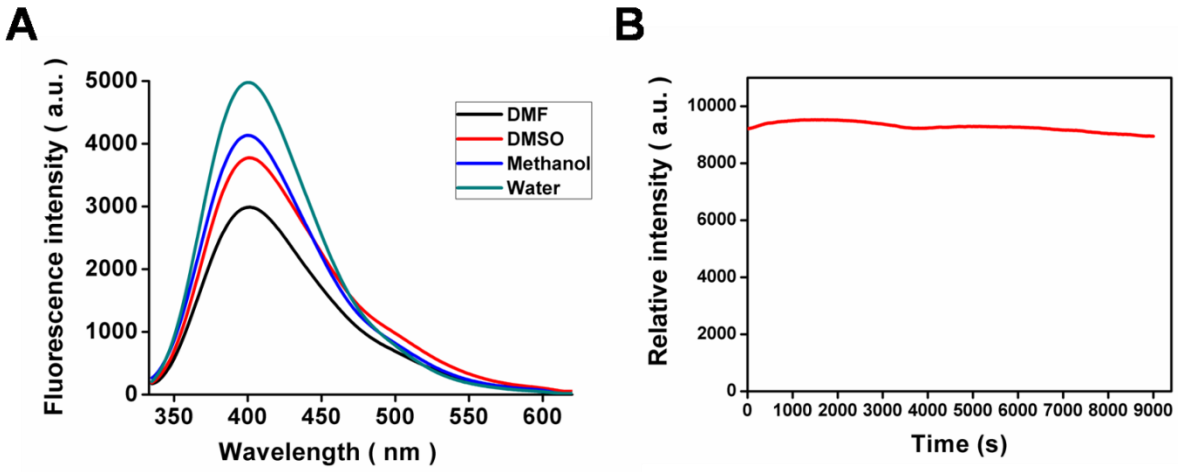

Figure 5.6 (A) Effect of solvents on fluorescence intensity of C-dots (λ_{ex} = 320 nm). (B) Dependence of fluorescence emission intensity against time depicting photostability of C-dots (λ_{ex} = 320 nm; λ_{em} = 400 nm).

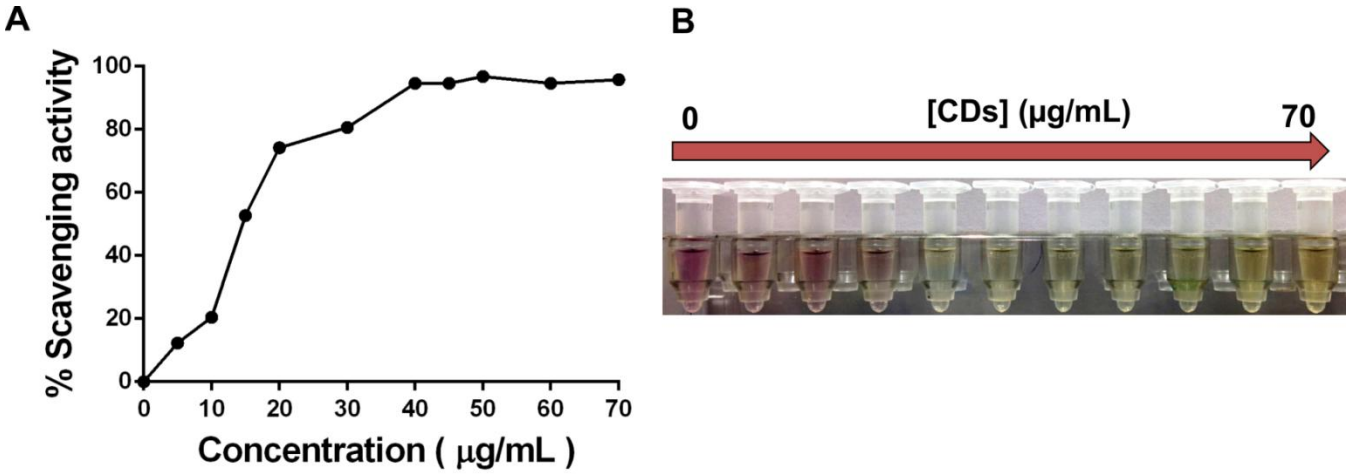

Figure 5.7 (A) DPPH free radical scavenging activity of C-dots. (B) Photographic representation of bleaching of DPPH solution with a progressive increase in concentration of C-dots.

This discrimination effect for Fe^{3+} ions originates due to exceptional coordination between Fe^{3+} ions and hydroxyl groups of C-dots, similar to previous reports (Wang et al., 2014a, Teng et al., 2014 and Gong et al., 2015). To explore the sensitivity of C-dots towards Fe^{3+} ions, different concentrations of Fe^{3+} ions in the range of 0-60 µM were added in the C-dots solution (0.1 mg mL^{-1}). **Fig. 5.8 (B)** shows a steady decline in fluorescence intensity with increasing Fe^{3+} concentration. **Fig. 5.8 (C)** further represents the relative fluorescence response of C-dots (F_0/F) as a function of Fe^{3+} concentration. The fluorescence quenching efficiency can further be described by the Stern-Volmer plot depicting a perfect linear behaviour (linear correlation coefficient of 0.9874) in the concentration range 0-6 µM **(inset in Fig. 5.8 (C))**.
The equation for the same is as follows:

$$\mathbf{F_0/F = 0.07590X + 0.9780}$$

where F_0 and F are the fluorescence intensities of C-dots in the absence and presence of Fe^{3+} and X represents the concentration of Fe^{3+}. On the basis of the above equation, the quenching constant, K_{sv} (slope of the linear fit) was calculated to be 7.590×10^4 mol^{-1} dm^{-3}. Likewise, the limit of detection was determined to be 0.4 µM based on the equation $3\sigma/m$, where σ is the standard deviation of blank signal (n = 4) and m is the slope of the linear fit. The detection limit is comparable to other reported values for Fe^{3+} detection by C-dots (Zhu et al., 2013 and Teng et al., 2014). Notably, this value is much lower than the maximum permissible level (5.36 µM) for Fe^{3+} in drinking water as per the guidelines laid down by World Health Organization (WHO, 2011). Finally, fluorescence decay curve analysis was done to gain an insight into the fluorescence quenching mechanism of C-dots **(Fig. 5.8 (D))**. Decay curves of C-dots and C-dots–Fe^{3+} overlapped suggesting negligible change in the fluorescence lifetime of C-dots in the presence of Fe^{3+}. In addition, the average lifetime of C-dots and C-dots-Fe^{3+} complex was calculated to be 5.94 ns and 5.90 ns, respectively which consisted of three lifetime components **(Table 5.3)**. The reduced lifetime of C-dots indicates the occurrence of dynamic quenching, thereby suggesting the possibility of electron transfer from hydroxyl group of C-dots in the excited state to the d orbital of Fe^{3+} (Zhu et al., 2013c and Zhai et al., 2014). EDS mapping further shows the distribution of Fe^{3+} in C-dots-Fe^{3+} complex **(Fig. 5.9)**. Elemental maps depicted the presence of Fe^{3+} along with the major constituent elements of C-dots. This suggests the uniform distribution of C, O and N with Fe^{3+} concentrated in specific areas. Since, C-dots demonstrate a pH dependent response, the quenching effect of Fe^{3+} on C-dots was explored at various pH values. **Fig. 5.10** shows the pH dependent fluorescence response of the C-dots-Fe^{3+} complex.

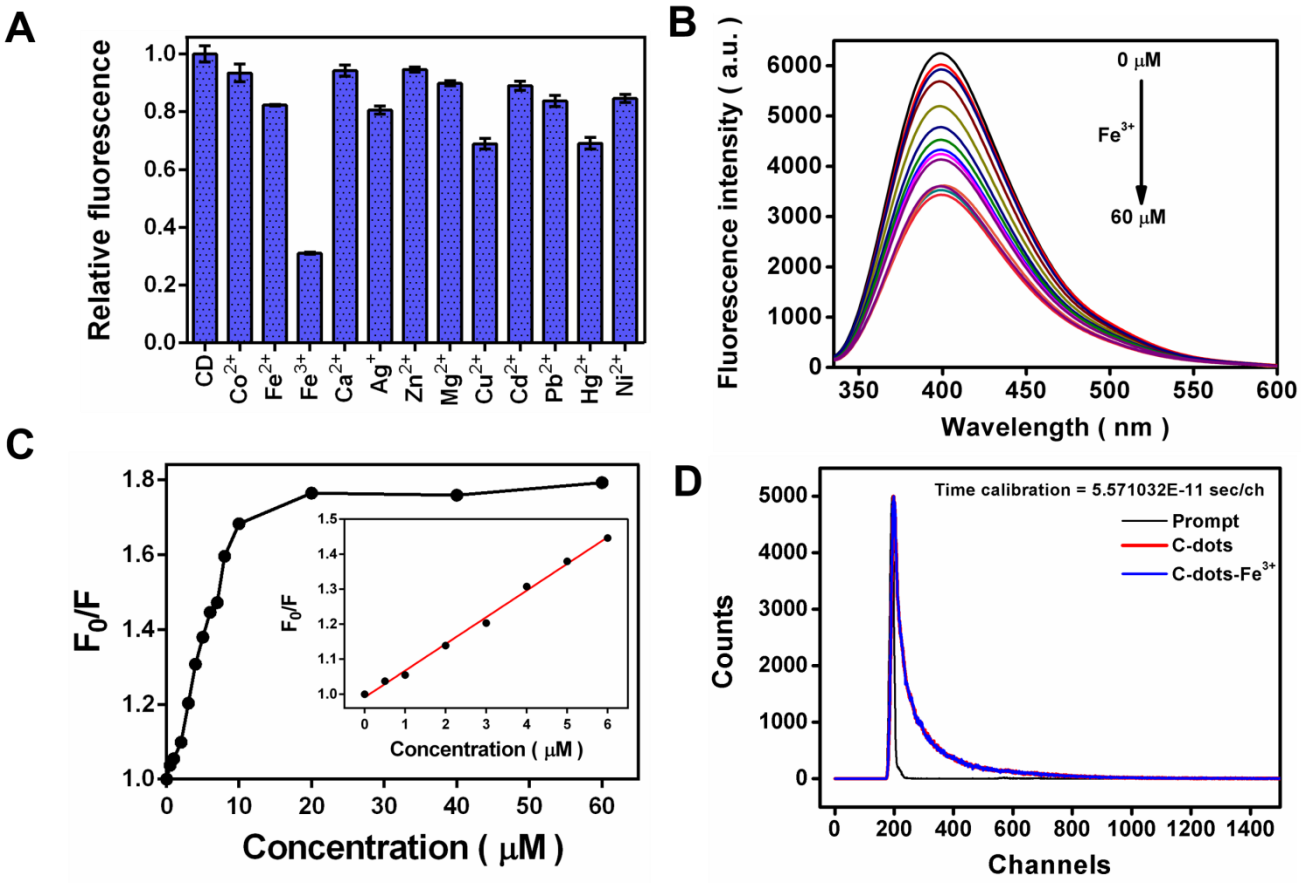

Figure 5.8 (A) Fluorescence response of C-dots in the presence of different metal ions in aqueous solution. (B) Fluorescence spectral quenching of C-dots upon addition of various concentrations of Fe^{3+} (C) Relative fluorescence response of C-dots (F_0/F) versus concentration of Fe^{3+} from 0 to 60 μM. Inset is the linear region from 0 to 6 μM. F_0 and F are the fluorescence intensities of C-dots at 400 nm in the absence and presence of Fe^{3+}, respectively. (D) Fluorescence decay curve of C-dots in the absence and presence of Fe^{3+} (λ_{ex} = 320 nm; λ_{em} = 400 nm).

Sample	a_1	τ_1(ns)	a_2	τ_2(ns)	a_3	τ_3(ns)	τ_{av}(ns)	χ^2
C-dots	0.3677	3.211	0.1881	0.521	0.4442	10.503	5.943	1.121
C-dots-Fe^{3+}	0.3579	3.071	0.1876	0.525	0.4545	10.360	5.906	1.149

Table 5.3 Fluorescence lifetime calculation of C-dots in presence and absence of Fe^{3+}.

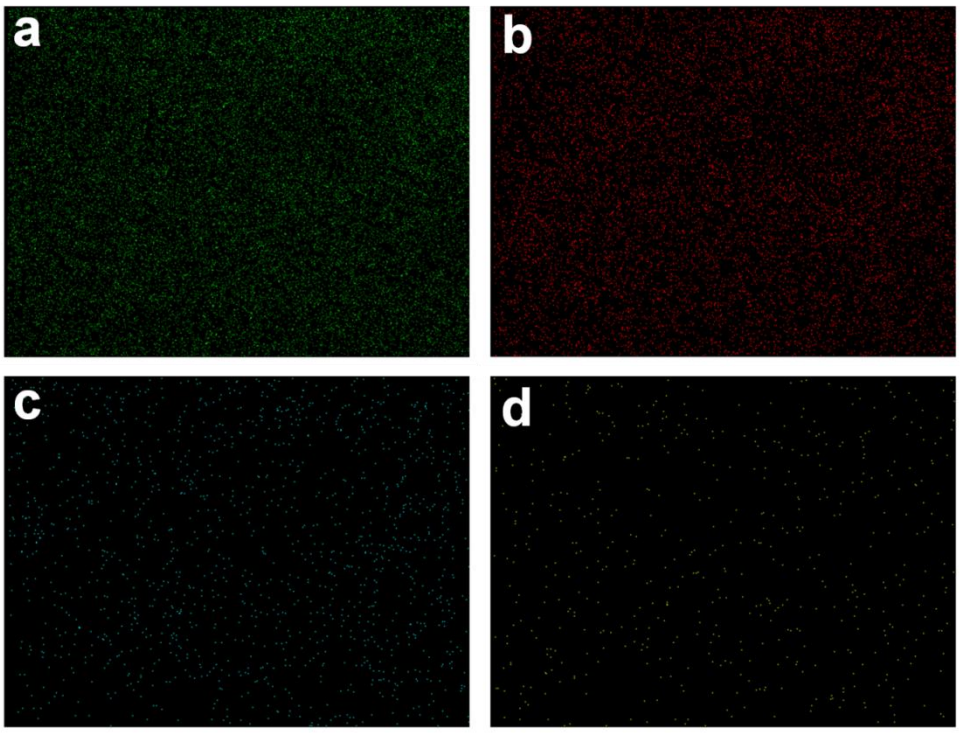

Figure 5.9 EDS elemental mapping of C-dots-Fe^{3+}. (a-d) Individual elemental distribution (red for carbon, green for oxygen, cyan for nitrogen and yellow for iron).

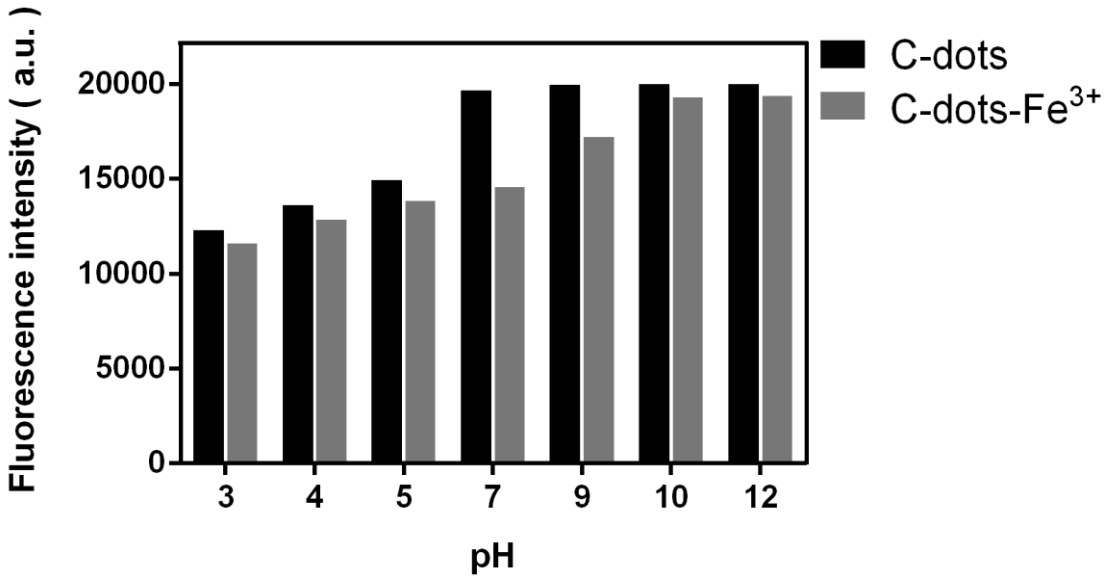

Figure 5.10 Fluorescence response of C-dots in the absence (black) and presence (grey) of 60 μM Fe^{3+}at different pH values. (λ_{ex} = 320 nm; λ_{em} = 400 nm).

Under acidic conditions, low quenching efficiency was observed, due to protonation of surface carboxylic groups, resulting in weaker interactions in the C-dots-Fe^{3+} complex. In the pH range 7-9, a substantial decrease in fluorescence intensity (higher quenching efficiency) was observed owing to the deprotonation of surface carboxylic groups, thereby strengthening the interaction between Fe^{3+} and C-dots. Conversely, at higher pH values lower quenching efficiency was observed again, which could be due to the complexation of Fe^{3+} by OH^- instead of C-dots (Yan et al., 2014 and Huang et al., 2014). The above outcomes highlight the competence of C-dots as a Fe^{3+} nanosensor.

5.2.4 Biocompatibility and bioimaging

Cytotoxic effects during imaging of cells play a key role in determining the applicability of nanoparticles as fluorescence imaging agents. Hence, it becomes imperative to assess the cytotoxicity of C-dots before employing them for bioimaging. In this regard, the MTT assay was performed and the results are presented in **Fig. 5.11 (A)**. A549 cells did not show any decline in cell viability when the concentration of C-dots was increased to 0.3 mg mL^{-1} with respect to control. Afterwards, a marginal decrease in cell viability was observed with increasing concentration of C-dots. The survival rate was around 86 % even at a high concentration of 1 mg mL^{-1}. Similarly, L-132 cells accounted for more than 85 % cell viability at all the tested doses of C-dots ranging from 0.1 to 1 mg mL^{-1}. Overall, the exposure of varied concentrations of C-dots did not induce any serious cytotoxic effect in both A549 and L-132 cells. Essentially, the results portray the biocompatibility of C-dots for bioimaging. As a proof-of-concept, A549 and L-132 cells were stained with C-dots **(Fig. 5.11 (B))**. Distinct green fluorescence inside the cells was observed upon subsequent cellular uptake of C-dots **(Fig. 5.11 (b,d))**. In addition, the bright field images of C-dots treated cells indicate normal morphology of cells, endorsing their biocompatibility **(Fig. 5.11 (a,c))**. For cellular uptake studies, Hoechst 33342 dye was used as a marker for nucleus and the cellular distribution of C-dots was tracked in A549 and L-132 cell lines. As can be seen in **Fig. 5.12**, CDs were ubiquitously distributed in the cytoplasm of cells, evident from the green fluorescence emanating around the nucleus. However, no co-localization of blue (Hoechst 33342) and green fluorescence (C-dots) was observed, which underscores the fact that C-dots were not able to penetrate inside the cell nucleus (Shi et al., 2015 and Sachdev et al., 2015b). The quantification of cellular uptake of C-dots in A549 and L-132 cells was done by determining the percentage of fluorescent cells using a flow cytometer with reference to control cells **(Fig. 5.13)**.

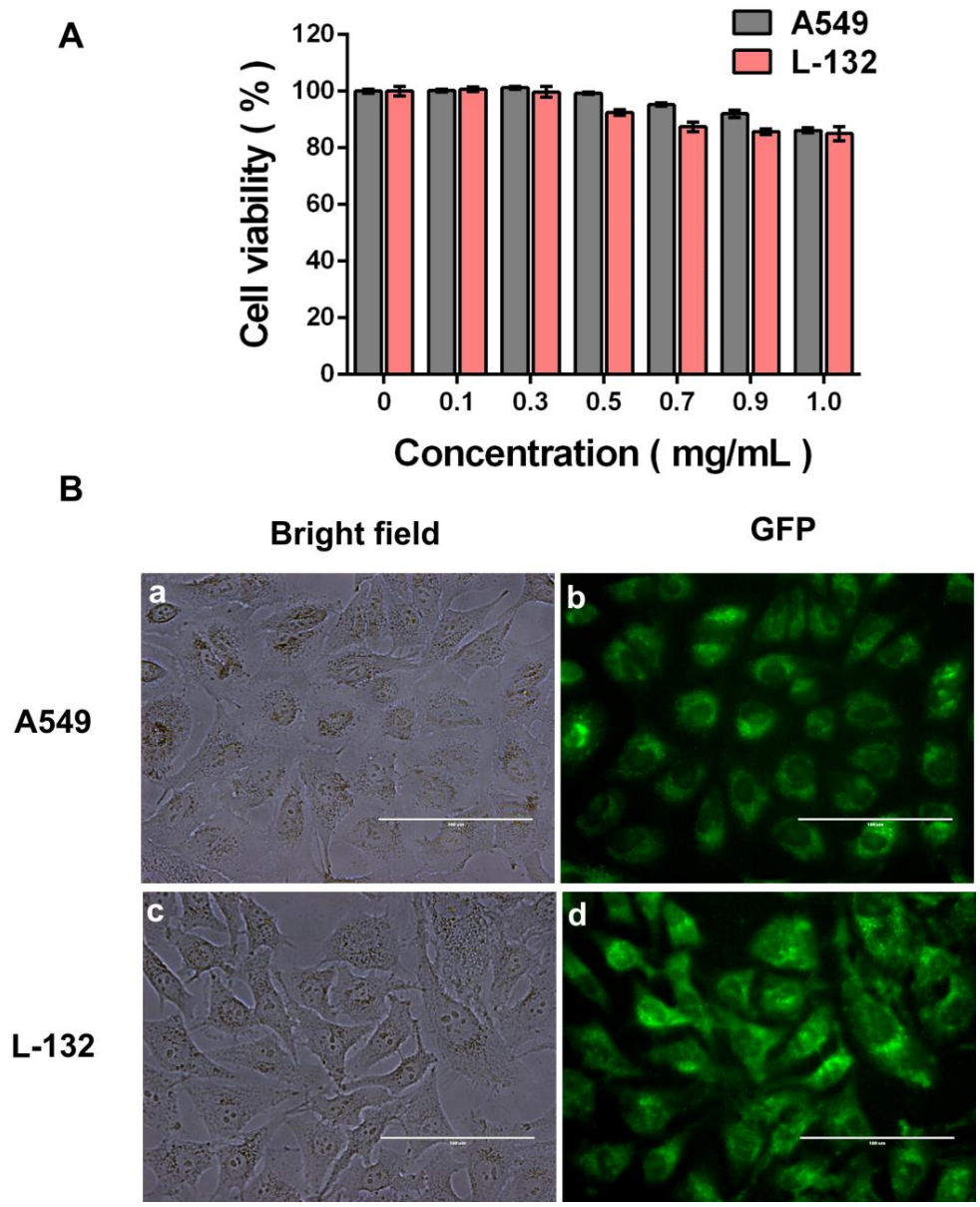

Figure 5.11 (A) *In vitro* cell viability of A549 and L-132 cells treated with various concentrations of C-dots as estimated by the MTT assay. The error bars represent mean ± S.E.M. of three individual experiments. (B) Representative fluorescence microscopic images of A549 (a and b) and L-132 (c and d) cells incubated with 0.5 mg mL^{-1} C-dots. Scale bar: 100 μm. GFP Filter (λ_{ex} = 470 nm; λ_{em} = 525 nm).

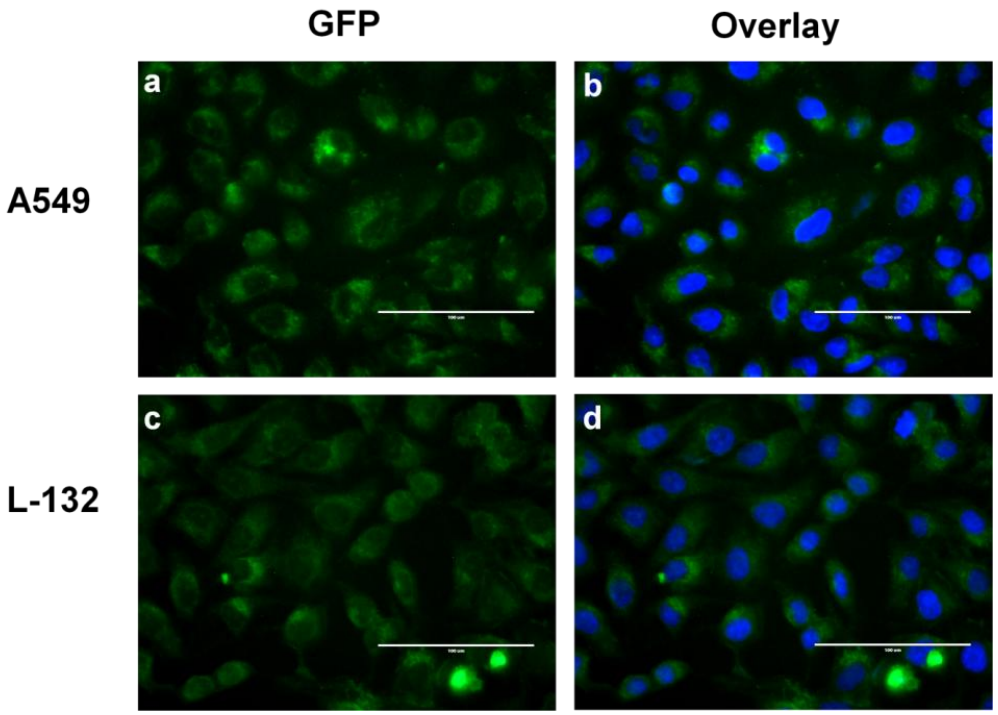

Figure 5.12 Cellular distribution micrographs of A549 and L-132 cells treated with 0.5 mg mL^{-1} of C-dots and stained with Hoechst 33342. The overlay images were acquired using a combination of DAPI (for Hoechst 33342) and GFP (for C-dots) filters. Scale bar: 100 µm.

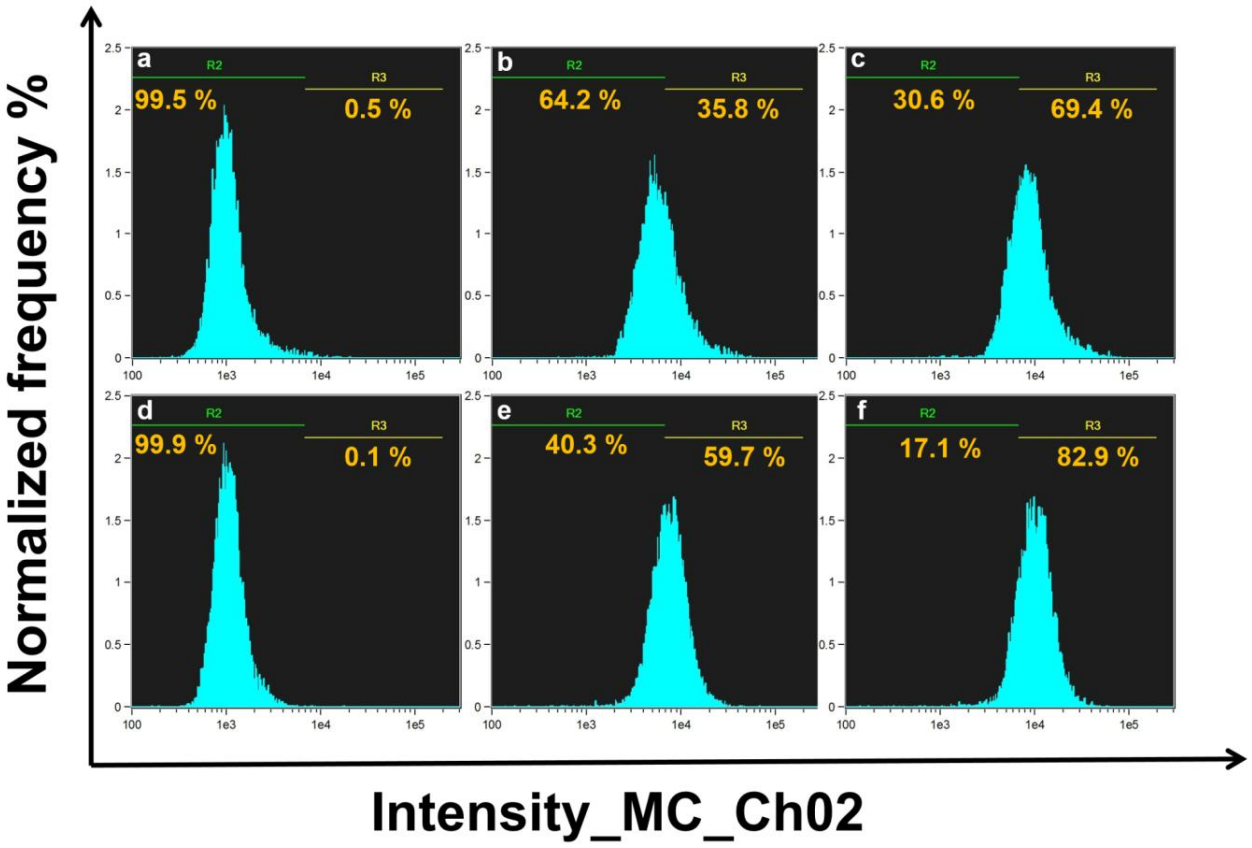

Figure 5.13 Flow cytometric analysis of cellular uptake of C-dots in A549 and L-132 cells. Upper panel: (a) untreated and (b) 0.3 mg mL^{-1}, (c) 0.5 mg mL^{-1} C-dots treated A549 cells. Lower panel: (d) untreated and (e) 0.3 mg mL^{-1}, (f) 0.5 mg mL^{-1} C-dots treated L-132 cells.

The fluorescence signal originating from C-dots stained cells was strong enough to be detected by flow cytometer, while the cells not treated with C-dots with insignificant background fluorescence were used as control. On closer inspection, an increase in the intracellular fluorescence intensity of C-dots (percentage of fluorescent cells) was observed in both the cell types with an increase in concentration of C-dots, thereby indicating concentration dependent cellular uptake. For the A549 treated cells, the percentage of fluorescent cells increased from 35.8 % to 69.4 % with an increase in the concentration of C-dots **(Fig. 5.13 (b-c))**. On the other hand, the percentage of fluorescent cells in L-132 treated cells also increased correspondingly from 59.7 % to 82.9 % in a dose-dependent manner **(Fig. 5.13 (e-f))**. Evidently, there were marked differences in cellular uptake between the two cell types at equivalent cell numbers.
L-132 cells had higher cellular uptake of C-dots than A549 cells at similar test doses, under same conditions.

In summary, coriander leaves were successfully utilized for C-dots synthesis. These C-dots were characterized through various analytical techniques. The functional groups associated with organic moieties in coriander leaves took care of the surface passivation of C-dots. C-dots exhibited DPPH radical scavenging activity at very low concentrations which suggested their antioxidant potential. Besides, a detailed mechanism for detection of Fe^{3+} ions by C-dots was elucidated. These C-dots also demonstrated bioimaging potential as evident from fluorescence microscopy and flow cytometeric analysis. Detection of fluorescence signal from the C-dots stained cells by flow cytometer predicted subtle differences in cellular uptake between different cell types, which are generally not detected by fluorescence microscopy.

CHAPTER 6

Synthesis of C-dots-Cerium Oxide Nanocomposite for Synchronous Bioimaging and Antioxidant Activity

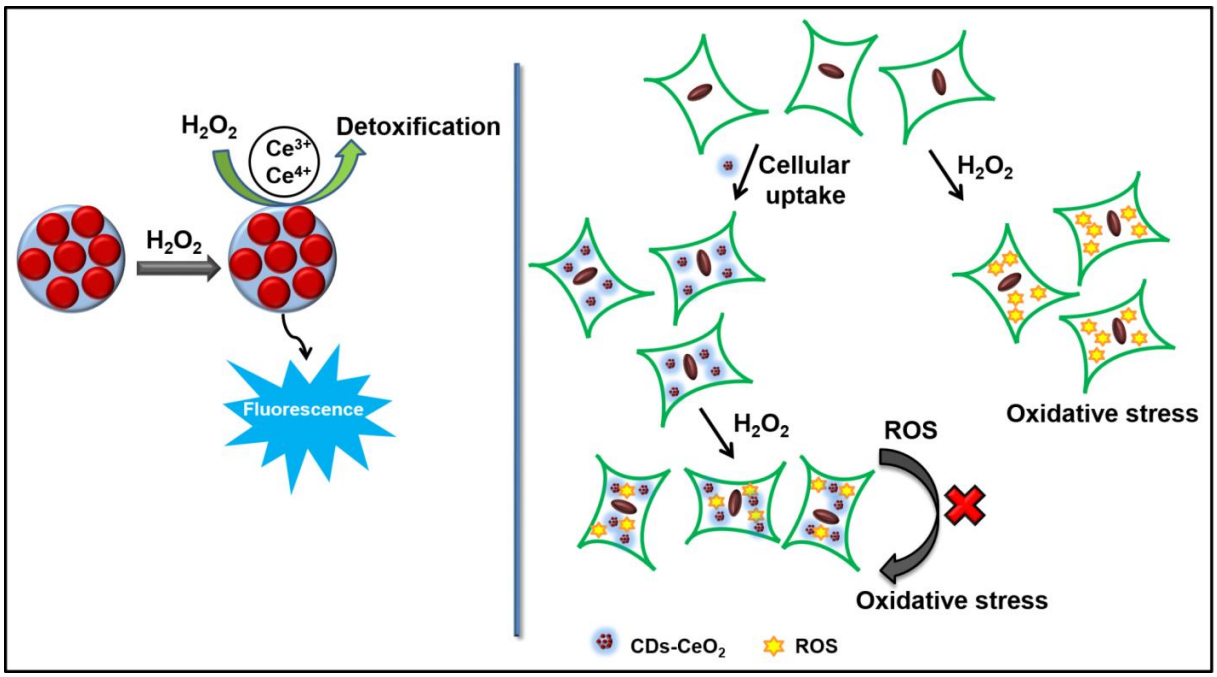

CHAPTER 6

SYNTHESIS OF C-DOTS-CERIUM OXIDE NANOCOMPOSITE FOR SYNCHRONOUS BIOIMAGING AND ANTIOXIDANT ACTIVITY

6.1 Overview

The development of nanoparticles for therapeutic purposes has been the subject of intense research over the years. Advances in engineering and the applications of such therapeutic nanoparticles require understanding of their interactions at the cellular level. Incorporating fluorescence probes can make it possible to monitor the interactions and cellular uptake, because of their high sensitivity (Ueno, 2011). The key challenge, though, remains to develop nanoparticles having low toxicity with therapeutic as well as imaging properties for concurrent disease detection and therapy (Babu et al., 2010 and Parveen et al., 2012). Reactive oxygen species (ROS) are produced at low levels inside the cells upon aerobic respiration and subsequently removed by antioxidant defence systems in cells. Under excessively high ROS levels, the cells' inherent antioxidant enzymes become inefficient and lead to oxidative stress (Cadenas et al., 2000). Hydrogen peroxide (H_2O_2) is a major ROS species, whose increased levels (>0.7 μM) are considered detrimental for human health (Wijeratne et al., 2005 and Coyle et al., 2006). Thus, it of prime significance to develop strategies to monitor and ameliorate H_2O_2 levels for normal cell functions. Cerium oxide (CeO_2) nanoparticles serve as excellent intracellular ROS scavengers and their mechanism of action has been elucidated lately. However, visualization of the interaction of CeO_2 nanoparticles with ROS species and hence the evaluation of their antioxidant activity remains underexplored. This underscores the need to combine them with fluorescence probes. In the present work, C-dots with strong blue fluorescence have been used as a fluorescence probe in association with CeO_2 nanoparticles with antioxidant potential to construct dual functional CDs-CeO_2 nanocomposite (NC) by a facile hydrothermal method. Recent findings have suggested that the fluorescence signal of CDs is also sensitive to varying concentrations of H_2O_2 (Wei et al., 2014 and Lan et al., 2015). It is anticipated that the interaction of H_2O_2 with CDs would also result in fluorescence quenching under biological conditions as well. Conversely, CDs-CeO_2 NC can interact and

neutralize H_2O_2 due to the catalytic effect of CeO_2, thus preventing the fluorescence quenching of CDs in the NC. As a proof of concept, *in vitro* evaluation of bioimaging and antioxidant potential of the as-synthesized CDs-CeO_2 NC was conducted successfully on NIH3T3 fibroblast cells. The motive behind the conjugation of CDs was, on one hand, to evaluate the cellular uptake of CDs-CeO_2 NC and, on the other hand, to correlate their fluorescence signal emanating from the cells with ROS scavenging. Hence, this work envisages CDs-CeO_2 NC as a versatile tool for synchronized cellular uptake and ROS scavenging antioxidant activity.

6.2 RESULTS AND DISCUSSION

6.2.1 Synthesis and characterization of CDs-CeO_2 NC

CDs-CeO_2 NC was synthesized via a facile hydrothermal method as depicted in **Fig. 6.1**. Hydrothermally synthesized CeO_2 nanoparticles upon subsequent integration with chitosan-bPEI served as the template for the formation of NC. In the synthetic process, *in situ* formation of bright fluorescent CDs from chitosan-bPEI by carbonization and passivation processes in the presence of CeO_2 nanoparticles under hydrothermal conditions (high temperature and pressure) yielded CDs-CeO_2 NC. The use of chitosan-bPEI is a recently discovered approach to synthesize CDs, wherein chitosan acts as a low-temperature (< 250 °C) carbonizable source while the polyamine structure of bPEI mediates surface functionalization and passivation in a single step, amenable to the development of NC involving CDs (Yang et al., 2012, Dong et al., 2012 and Sachdev et al., 2014). TEM analysis was performed to characterize the as-formed CDs-CeO_2 NC **(Fig. 6.2 (A))**. Numerous small dots on the surface of the particles with relatively dark contrast represented CDs. This demonstrated the successful transformation of chitosan-bPEI to CDs, which were distributed on the surfaces of CeO_2 in the NC. The structure of CDs-CeO_2 NC was further investigated by HRTEM **(Fig. 6.2 (B))**. The lattice fringes in the HRTEM image were separated by masking techniques of Gatan Digital Micrograph software to generate the inverse fast Fourier transform (IFFT) image **(inset in Fig. 6.2 (B))**. A distinctive set of separated lattice planes with spacings of 0.31 and 0.27 nm could be visualized, and corresponded to (111) and (200) planes of CeO_2, respectively. CDs could not contribute to the lattice pattern due to their amorphous nature. Morphological and elemental examinations were carried out through FE-SEM **(Fig. 6.2 (C))**. Nearly spherical, agglomerated particles of CDs-CeO_2 NC can be seen in high-magnification FE-SEM image, which is very similar to TEM observations. Further, EDS elemental mapping detected the presence of characteristic elements such as Ce, O and C on the entire surface.

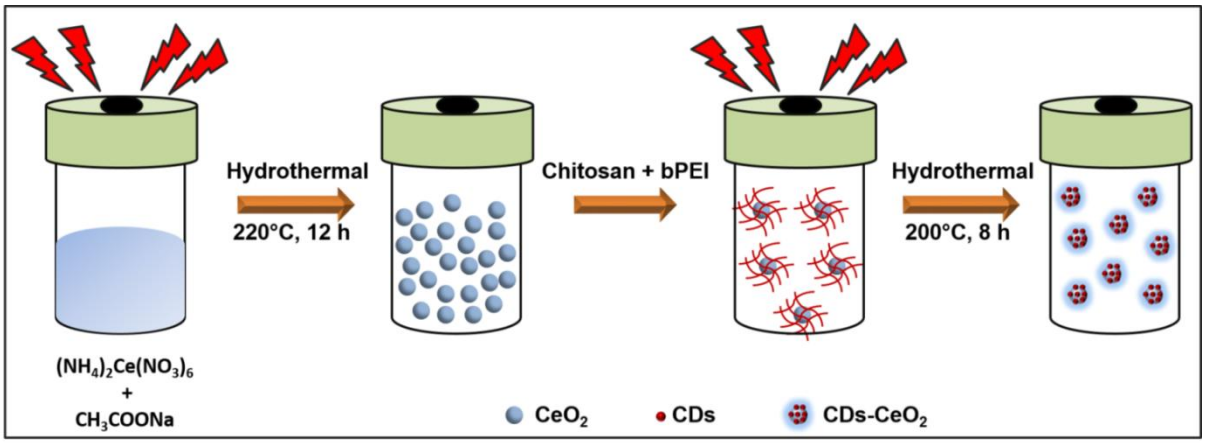

Figure 6.1 Schematic representation for the synthesis of CDs-CeO_2 NC.

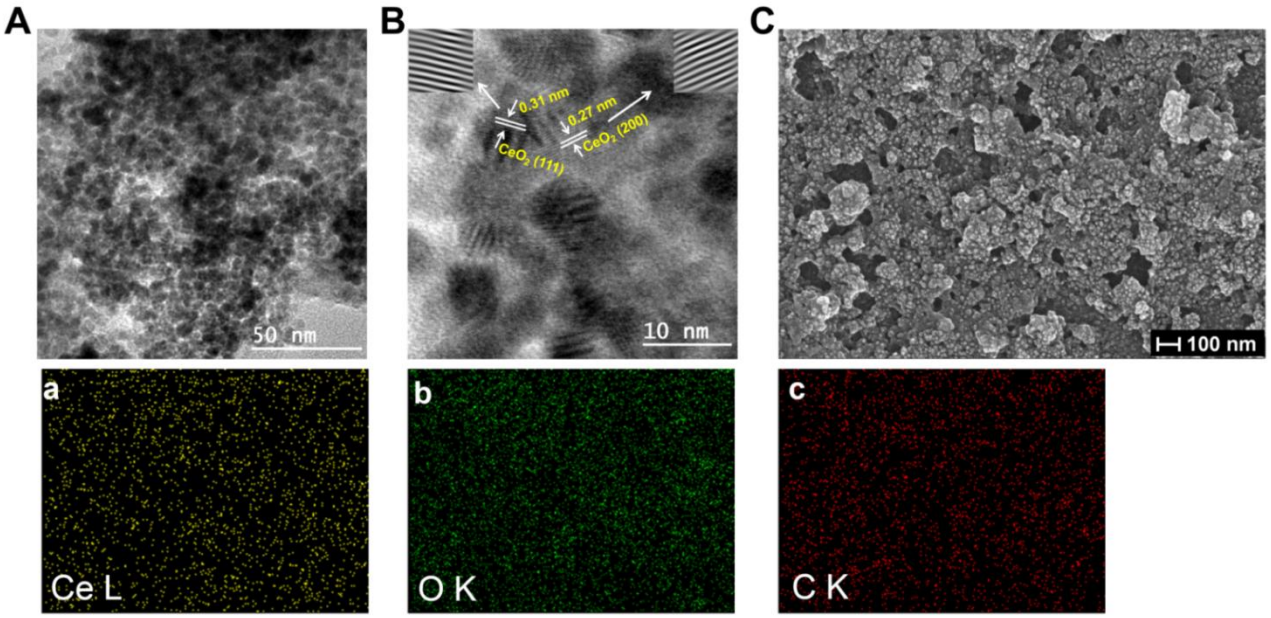

Figure 6.2 (A) TEM and (B) HRTEM micrograph of CDs-CeO_2 NC. Insets in fig. 2(B) are the inverse FFT images of the selected regions corresponding to CeO_2 of CDs-CeO_2 NC. (C) FE-SEM image of CDs-CeO_2 NC. (a-c) Colour coded SEM-EDS dot maps depicting the distribution of individual elements in CDs-CeO_2 NC.

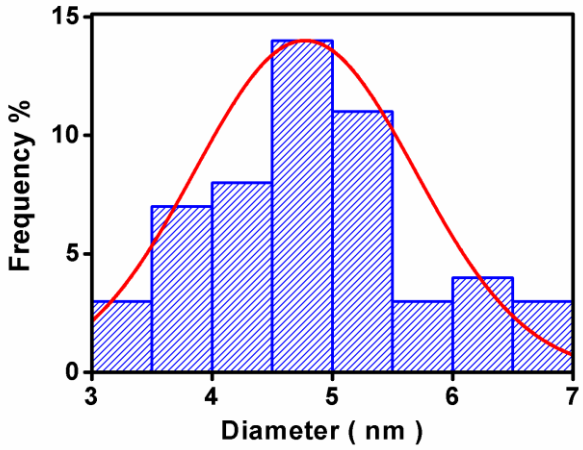

Figure 6.3 Particle size distribution curve of CDs-CeO_2 NC.

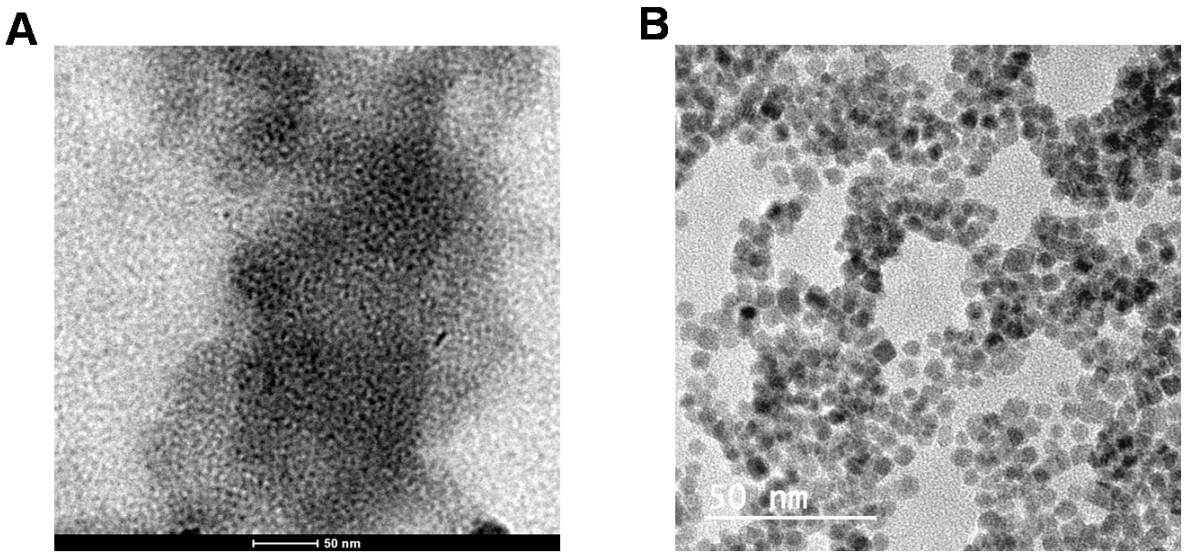

Figure 6.4 TEM image of (A) CDs and (B) CeO_2 nanoparticles.

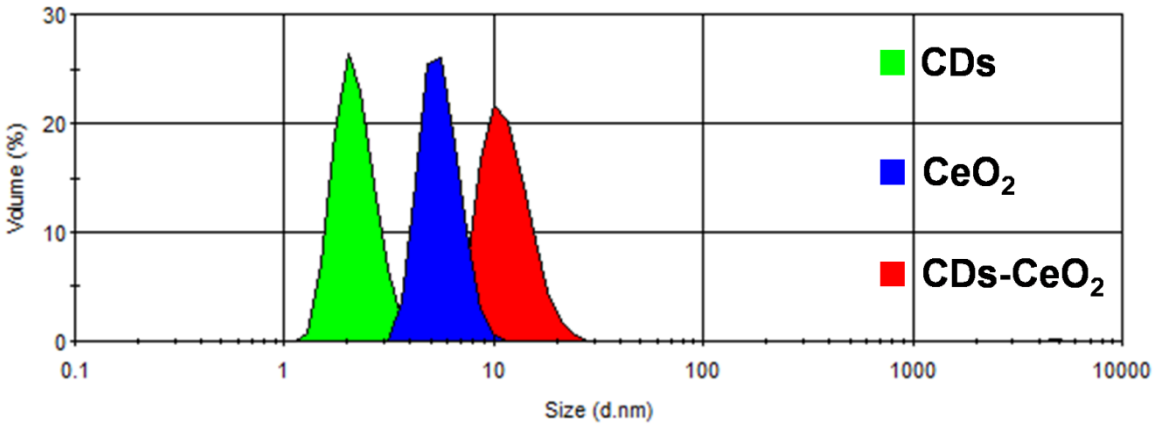

Figure 6.5 Size distribution by volume for aqueous dispersions of samples estimated through DLS.

The size of CDs-CeO_2 NC particles was in the range of 3 to 7 nm, as estimated from the size-distribution histogram **(Fig. 6.3)**. The as-synthesized blank CDs appeared as uniformly distributed dots with an average size of 2.81 ± 0.593 nm **(Fig. 6.4 (A))**. Pure CeO_2 nanoparticles displayed a discrete, spherical morphology with an average size of 5.39 ± 0.768 nm **(Fig. 6.4 (B))** (Liu et al., 2012c). It is important to note that no significant difference between the sizes of CDs-CeO_2 NC and CeO_2 nanoparticles was observed. However, the surface of CDs-CeO_2 NC appeared comparatively rougher (due to distribution of CDs) than that of the CeO_2 nanoparticles, which provides indirect an evidence for the formation of CDs-CeO_2 NC. In addition, the average hydrodynamic size of CDs-CeO_2 NC predicted by dynamic light scattering (DLS) was 10.10 nm, whereas the same for blank CDs and CeO_2 nanoparticles was found to be 2.01 and 5.61 nm, respectively **(Fig. 6.5)**. The estimated hydrodynamic sizes are in accordance with the TEM size observations.

The phase structure of the CDs-CeO_2 NC was explored by XRD **(Fig. 6.6 (A))**. For CeO_2, the characteristic diffraction peaks at 28.18°, 32.84°, 47.42°, 56.29°, 59° and 70° were indexed to (111), (200), (220), (311), (222), and (400) planes of cubic fluorite structure of CeO_2 crystal structure (JCPDS card:43-1002). The XRD pattern of CDs-CeO_2 NC exhibited characteristic peaks of CeO_2 phase, in agreement with HRTEM analysis. Additionally, broad peaks at 22.5° and 39.3° were also noted, which could be assigned to (002) and (101) planes of amorphous CDs (Sachdev et al., 2014, Zhai et al., 2014 and Sachdev et al., 2015a). This clearly indicated the incorporation of CDs in the NC. Chemical functionalization of CeO_2 with CDs was verified by FTIR **(Fig. 6.6 (B))**. In the FTIR spectrum of pure CeO_2, absorption bands in the low frequency region at 875 cm^{-1}, 668 cm^{-1} and 534 cm^{-1} were attributed to stretching vibrations of Ce-O (Srivastava et al., 2013). Moreover, the strong peaks in the region 1400-1600 cm^{-1} could be indexed to symmetric and asymmetric stretching of organic moieties associated with CeO_2 nanoparticles (Yu et al., 2012 and Bhushan et al., 2015). Stretching and bending vibration of O-H groups at 3414 cm^{-1} and 1635 cm^{-1} were observed, which may arise due to the moisture in the sample. The FTIR spectra of CDs-CeO_2 NC showed characteristic absorption bands of CDs besides CeO_2. Appearance of a sharp and strong peak at 1640 cm^{-1} signified C=O stretch of the carbon backbone of CDs. Notably, amine I and II C–N peaks originating from the surface of CDs were also detected at 1387 cm^{-1} and 1270 cm^{-1}. Additionally, peaks at 1093 cm^{-1} and 1020 cm^{-1} corresponded to C–O–C asymmetric and symmetric vibrations in CDs (Mehta et al., 2014 and Sachdev et al., 2015a). A minor red-shift in vibration peak of Ce-O from 534 cm^{-1} to 516 cm^{-1} indicates the interaction between CDs and CeO_2 in the nanocomposite. The formation of CDs-CeO_2 NC was also studied by UV-visible spectrometry **(Fig. 6.6 (C))**. UV-vis spectra of

CDs showed two absorption bands owing to π electron transitions. Absorption peak at 274 nm was due to π-π* transition, while the broad absorption peak at 324 nm corresponded to n-π* transition, in agreement with the previous reports on CDs (Tang et al., 2012, Wang et al., 2014d, Wang et al., 2014e and Kwon et al., 2015). Pure CeO_2 nanoparticles had a characteristic absorption maximum at 290 nm. As for CDs-CeO_2 NC spectrum, distinctive absorption peaks due to CDs and CeO_2 were visible. The combined observation of decrease in intensity of peak at 290 nm (CeO_2) and shift in the absorption peak to longer wavelength at 330 nm (CDs) indicated that the CDs interacted and covered the surface of CeO_2, typical of NC spectra (Khan et al., 2014 and Bhaisare et al., 2016). In addition, the appearance of emission peak of CDs at 410 nm in fluorescence spectrum of CDs-CeO_2 NC further testify the anchoring of CDs at the surface of CeO_2 **(Fig. 6.6 (D))**.The slight drop in the fluorescence intensity of the CDs-CeO_2 NC compared to blank CDs (equivalent concentration) could be a result of photoinduced electron transfer between CDs and CeO_2, which is commonly observed in metal-CDs NC (Luo et al., 2012, Wang et al., 2014c and Yang et al., 2015). From the triple exponential fluorescence decay curves of CDs and CDs-CeO_2 NC, their average lifetime was calculated **(Fig. 6.7 and Table 6.1)**. A marginal reduction in the mean fluorescence lifetime of CDs-CeO_2 NC (5.035 ns) compared to blank CDs (5.204 ns) further signifies that the interaction between CDs and CeO_2 in the NC did not cause fluorescence quenching of CDs. The quantum yields for CDs and CDs-CeO_2 NC were calculated to be 16.49 % and 11.23 %, respectively under similar conditions **(Table 6.2)**. All these investigations revealed that CeO_2 slightly influenced the fluorescence features of CDs in the NC form without hampering their overall brightness, pertinent for bioimaging applications. The stability and changes in the surface charge of CeO_2 after the incorporation of CDs was also evaluated, which is of prime significance for their biological application **(Fig. 6.8)**. The average zeta potential value of blank CeO_2 nanoparticles and CDs was calculated to be 39.6 and 10.9 mV under physiological conditions (PBS, pH 7.4). Accordingly, the zeta potential value of CDs-CeO_2 NC (35.6 mV) was between that of CDs and CeO_2, explaining the appreciable stability and dispersion of the composite particles.

6.2.2 Effect of H_2O_2 on the fluorescence intensity

The fluorescence response of CDs and CDs-CeO_2 NC in the presence of H_2O_2 was monitored. A steady decline in fluorescence intensity of CDs was evident with an increase in H_2O_2 concentration **(Fig. 6.9 (A))**. Accordingly, the fluorescence quenching efficiency showed successive increase with respect to concentration of H_2O_2 (Fig. 6.9 (B)). CDs exhibited a strong blue emission under UV light, whereas H_2O_2-CDs solution manifested a faint emission indicative of a stronger quenching effect **(inset in Fig. 6.9 (B))**.

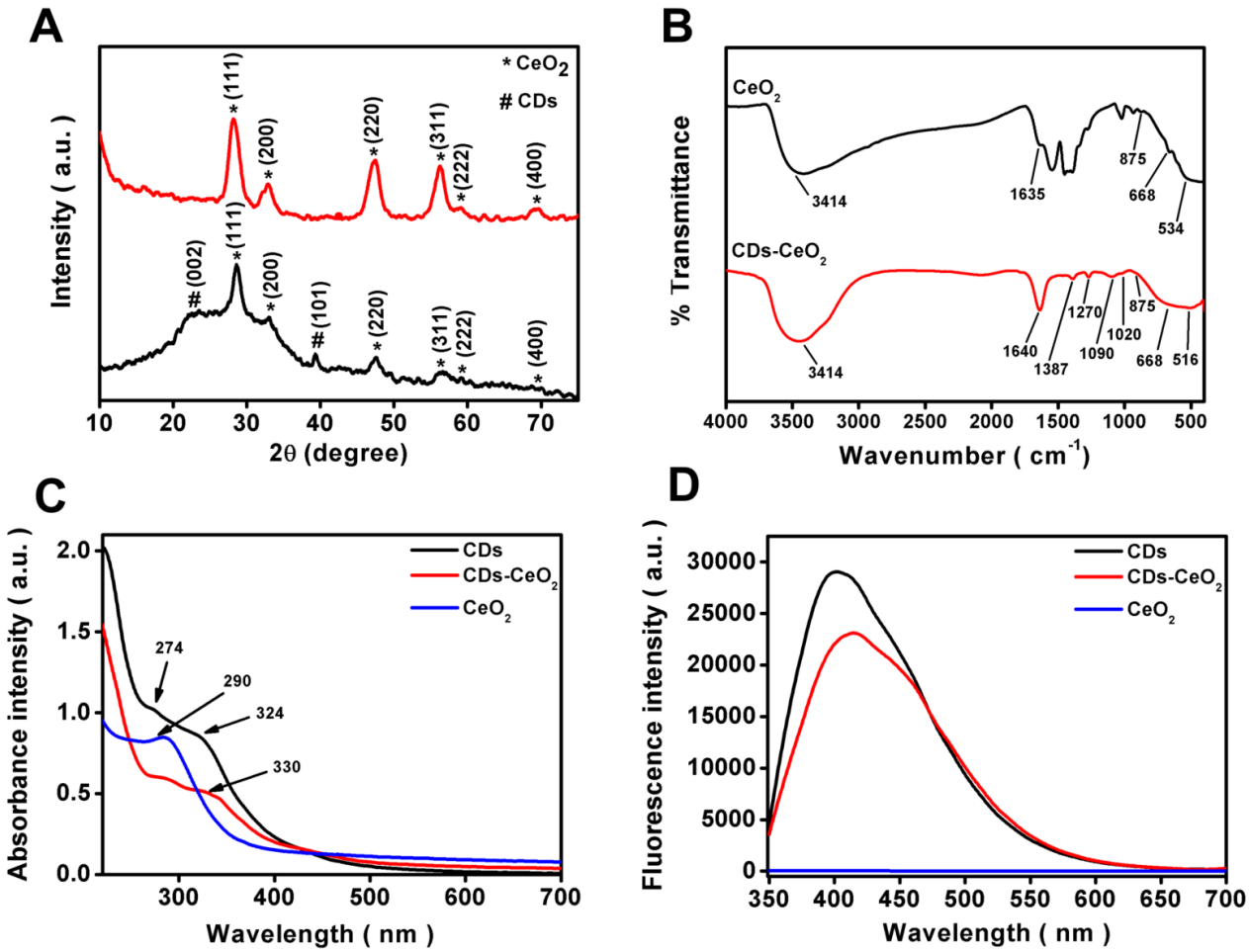

Figure 6.6 (A) XRD plots of CeO_2 (red) and CDs-CeO_2 NC (black). (B) FTIR spectrum. (C) UV-visible absorption spectra with characteristic peaks indicated by black arrows. (D) Fluorescence emission spectra.

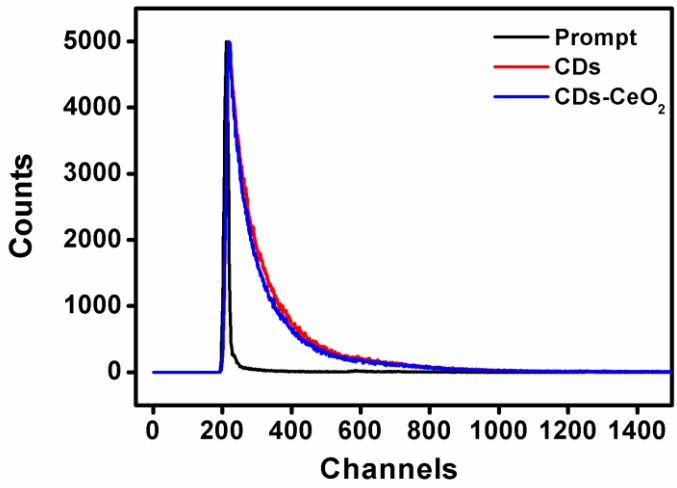

Figure 6.7 Fluorescence decay curve of CDs and CDs-CeO_2 NC (λ_{ex} = 360 nm; λ_{em} = 450 nm).

Sample	a_1	τ_1(ns)	a_2	τ_2(ns)	a_3	τ_3(ns)	τ_{av}(ns)	χ^2
CDs	0.856	0.795	0.5852	4.281	0.3292	10.180	6.537	1.169
CDs-CeO_2	0.1090	0.791	0.5861	3.993	0.3049	10.690	5.685	1.076

Table 6.1 Tabular representation of fluorescence lifetime calculation from the decay curves.

Sample	Integrated emission intensity *(I)*	Absorbance at 360 nm *(A)*	Refractive index of solvent (η)	Percent Quantum yield at 360 nm *(Q)*
Quinine sulphate	620706	0.1317	1.33	54 (known)
CDs	86549	0.0601	1.33	16.49
CDs-CeO_2	69297	0.0707	1.33	11.23

Table 6.2 Tabular representation for the quantum yield calculations.

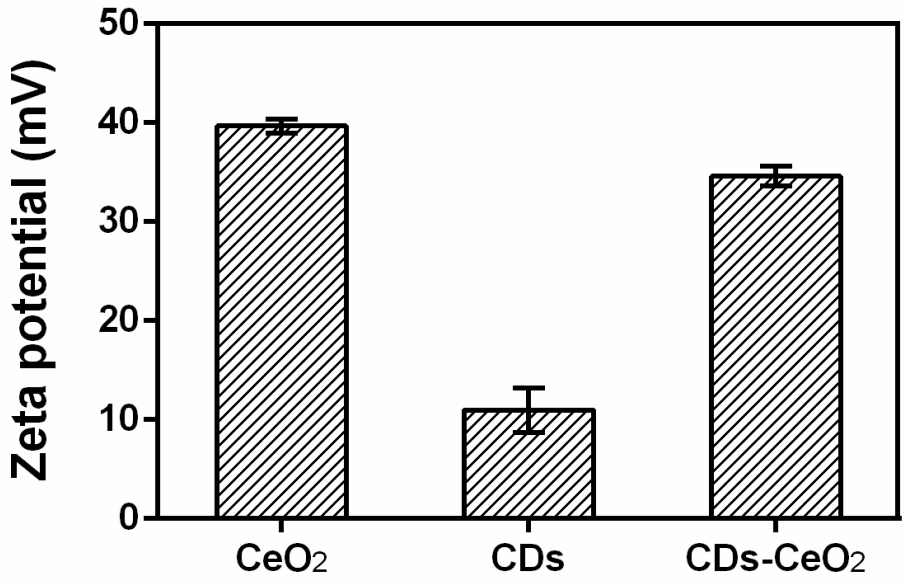

Figure 6.8 Zeta potential measurements for CeO_2, CDs and CDs-CeO_2 NC.

The electron transfer between the amine or hydroxyl groups of CDs and H_2O_2 leads to fluorescence quenching. Such effect arises due to the tendency of H_2O_2 to donate electrons, resulting in the formation of special coordination bonds, in agreement with the previous reports (Shan et al., 2014 and Lan et al., 2015). Interestingly, the fluorescence intensity of CDs-CeO_2 NC in the presence of different concentrations of H_2O_2 changed only slightly **(Fig. 6.9 (C))**. Consequently, a lower fluorescence quenching efficiency was observed with incremental H_2O_2 concentrations, confirmed by an intact fluorescence emission **(Fig. 6.9 (D))**. Perhaps owing to the catalase mimetic activity of CeO_2 via Fenton type reaction, H_2O_2 is converted into H_2O and O_2 (Pirmohamed et al., 2010 and Lee et al., 2013a). Over and above, CeO_2 could be capped by H_2O_2 credited to a higher affinity between them, as described by various mechanistic studies, which may perhaps contribute to fluorescence maintenance of CDs in the NC upon H_2O_2 addition (Ornatska et al., 2011 and Liu et al., 2015a). Based on the above outcomes, it can be deduced that the antioxidant activity as well as higher sensitivity of CeO_2 resulted in neutralization of H_2O_2 and hence prevented the fluorescence quenching of CDs in CDs-CeO_2 NC.

6.2.3 Cytotoxicity

In order to utilize CDs-CeO_2 NC for biological applications, the MTT assay was first performed to assess the dose-dependent cytotoxic effects **(Fig. 6.10 (A))**. NIH3T3 cells incubated with CeO_2 or CDs alone did not exhibit cytotoxic effects. Likewise, CDs-CeO_2 NC treated cells maintained an appreciable viability (> 75 %) under similar concentrations. Thus, the obtained results illustrated the low toxicity of the NC. Next, the protective effect of CDs-CeO_2 NC in NIH3T3 cells against oxidative stress induced by H_2O_2 was investigated **(Fig. 6.10 (B))**. Noticeably, most of the cells died when exposed to H_2O_2. In contrast, the cells preincubated with different concentrations of CeO_2 or CDs-CeO_2 NC before H_2O_2 treatment had higher cellular viability. Importantly, the incorporation of CDs in the NC did not make any difference, such that both CeO_2 and CDs-CeO_2 NC exercised the protective effect in the same concentration range (10-500 µg mL^{-1}). In order to further validate the protective effect of CDs-CeO_2 NC, apoptotic staining assay was carried out. To this end, cells were dyed with acridine orange (AO) and ethidium bromide (EB) to label the intact and apoptotic cells and examined under fluorescence inverted microscope **(Fig. 6.11)**. AO dye can label the nucleus of intact as well as apoptotic cells and emits green fluorescence, whereas EB can selectively stain the nucleus of apoptotic cells to produce orange fluorescence.

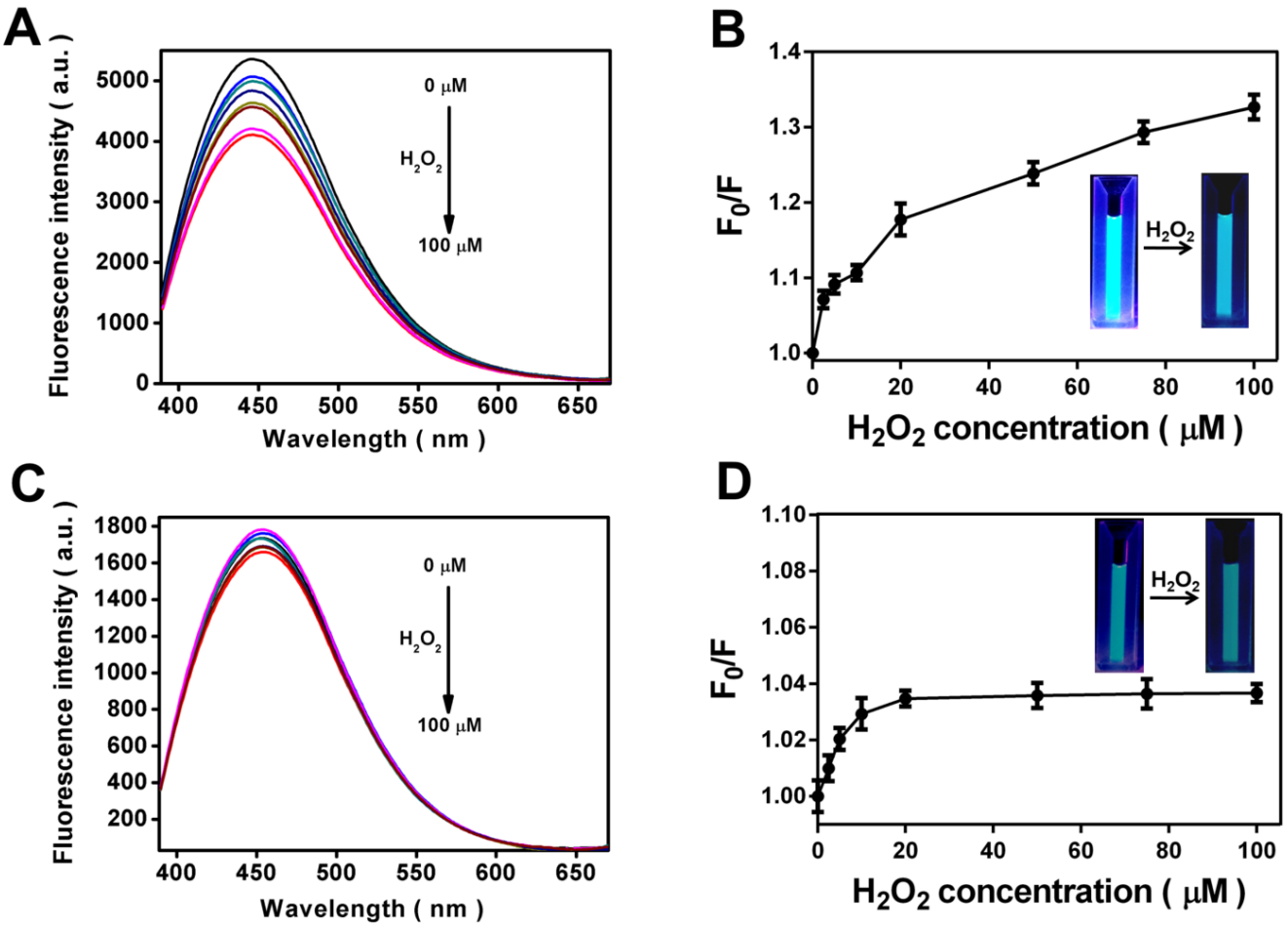

Figure 6.9 Fluorescence spectra of (A) CDs and (C) CDs-CeO_2 NC in presence of various concentrations of H_2O_2. Relative fluorescence response (F_0/F) of (B) CDs and (D) CDs-CeO_2 NC as a function of H_2O_2 concentration in PBS buffer solutions (pH 7.0). Insets in fig. 4(B,D) are the images taken under UV illumination for aqueous dispersions of CDs and CDs-CeO_2 NC before and after the addition of H_2O_2, respectively.

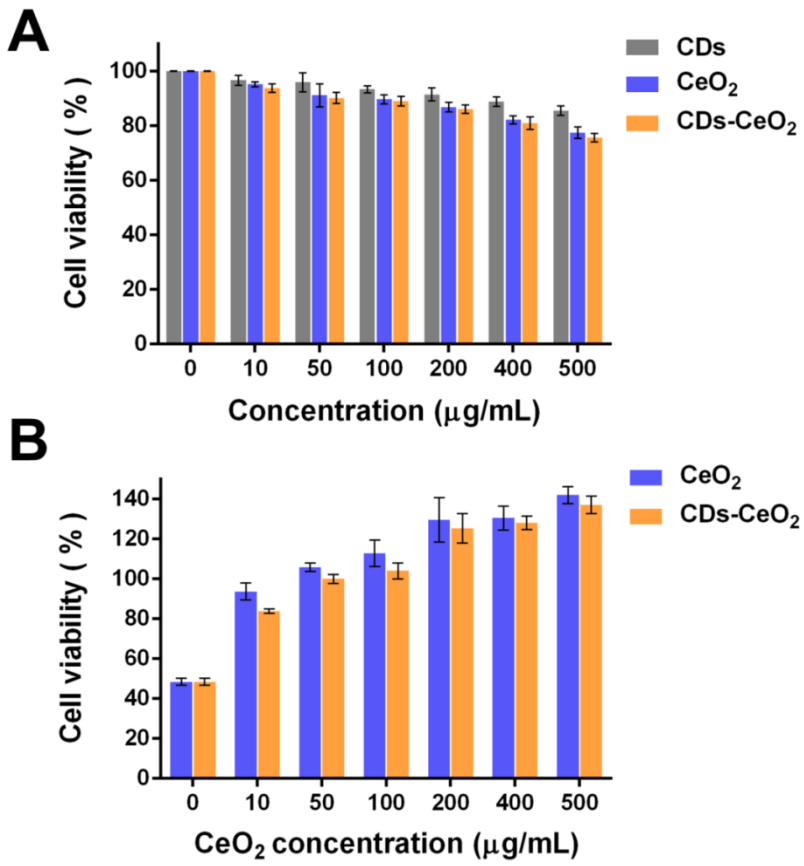

Figure 6.10 (A) MTT based cell viability plot of NIH3T3 cells. (B) Protective effect of CeO_2 and CDs-CeO_2 NC at equivalent concentrations on NIH3T3 cells against oxidative stress caused by treatment with 750 µM H_2O_2.

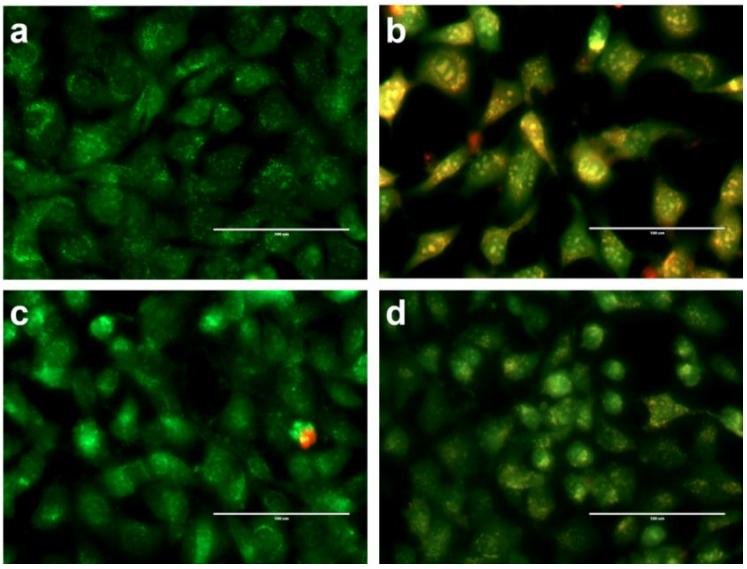

Figure 6.11 AO/EB dual staining images of (a) untreated cells (b) H_2O_2 treated cells (c) CDs-CeO_2 NC treated cells and (d) H_2O_2 treated cells pre-incubated with CDs-CeO_2 NC. Scale bar: 100 µm.

As expected, the untreated and CDs-CeO_2 NC treated cells appeared green in colour indicating an intact morphology. H_2O_2 treated cells were greenish-yellow in colour, suggesting the onset of apoptosis. Cells preincubated with CDs-CeO_2 NC upon H_2O_2 exposure remained green in colour, suggesting the possible role of CDs-CeO_2 NC in preventing oxidative-stress-mediated apoptosis.

6.2.4 Cellular uptake

Cellular uptake and distribution of CDs-CeO_2 NC was evaluated qualitatively by fluorescence microscopy. For this, the cells were incubated with CDs-CeO_2 NC for 2, 4 and 6 h and counterstained with Lysotracker red **(Fig. 6.12)**. Perceptible blue fluorescence (due to emission of CDs) and red fluorescence (due to emission of Lysotracker red) was observed in the cells under different filters. Moreover, an increase in the blue fluorescence inside the cells signifies time dependent increase in intracellular concentration of CDs-CeO_2 NC. Closer examination of micrographs at each time point ascertained overlapping positions of bright blue and red fluorescence spots, endorsing co-localization. The merged fluorescence images further reveal lysosomes as the cellular target of CDs-CeO_2 NC. For comparison, the cellular uptake of blank CDs inside the cells at same concentration was also followed **(Fig. 6.13)**. CDs essentially localized inside the lysosomes with time, similar to CDs-CeO_2 NC. FE-SEM analysis was performed for morphological and elemental analysis of CDs-CeO_2 NC treated NIH3T3 cells **(Fig. 6.14 (A))**. As can be seen from the images, the cells were spindle-shaped and well-attached, which typifies an intact morphology. Also, the detection of distinctive element (Ce) by EDS elemental mapping confirmed the internalization of CDs-CeO_2 NC by the cells. Cellular uptake was quantified by measuring the cellular dose of cerium using ICP-MS **(Fig. 6.14 (B))**. In the stipulated time frame, average cerium concentration per cell increased from 4.1 to12.11 pg. When the data was expressed in terms of uptake from the total added cerium, the percentage cerium internalized by cells was in the range of 8.2-24.2 %. The obtained results predicted time-dependent internalization of CDs-CeO_2 NC, which is in concurrence with the findings by fluorescence microscopic imaging.

6.2.5 Intracellular bioimaging in presence of ROS

To investigate the competence of CDs-CeO_2 NC in imaging and protecting the cells from H_2O_2 mediated oxidative stress, qualitative and quantitative evaluation of fluorescence signal emanating from the cells was done.

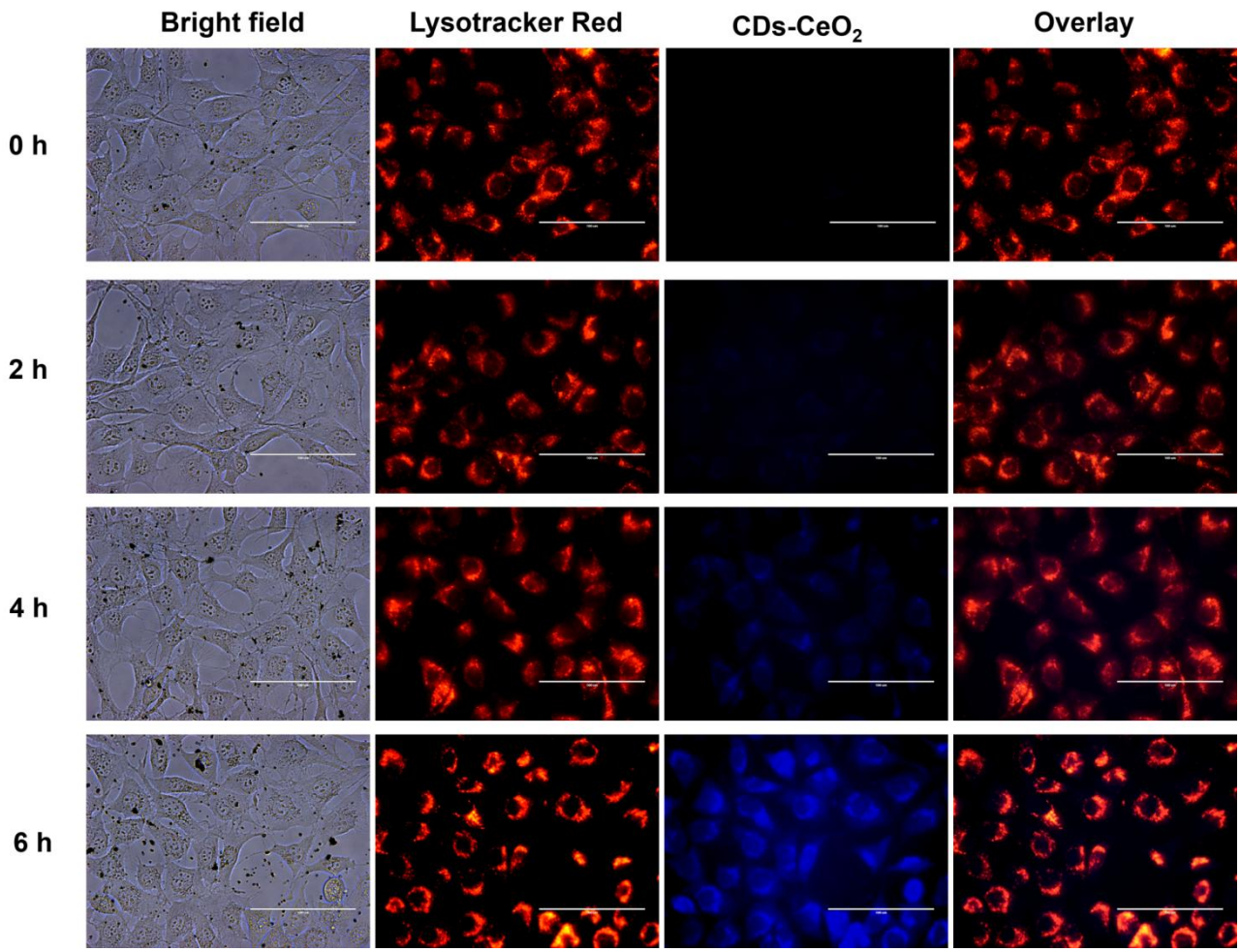

Figure 6.12 Time-dependent cellular uptake and co-localization of CDs-CeO_2 NC (blue fluorescence) and lysosomes (red fluorescence) in NIH3T3 cells. The overlay images were generated by via RFP (lysotracker red) and DAPI (CDs) filters of fluorescence microscope. Scale bar: 100 µm.

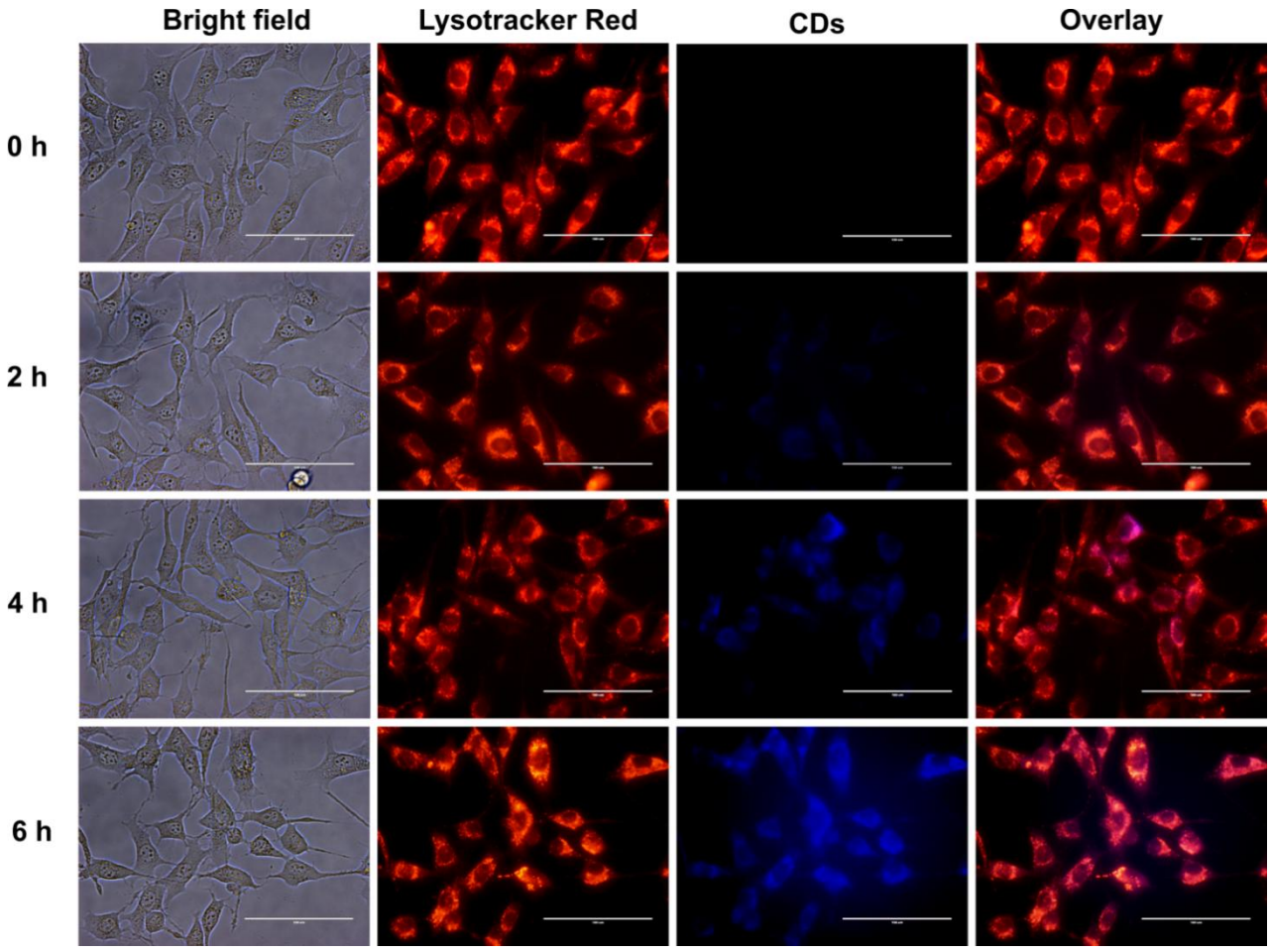

Figure 6.13 Time-dependent cellular uptake and co-localization of CDs (blue fluorescence) and lysosomes (red fluorescence) in NIH3T3 cells. The overlay images were generated by via RFP (lysotracker red) and DAPI (CDs) filters of fluorescence microscope. Scale bar: 100 µm.

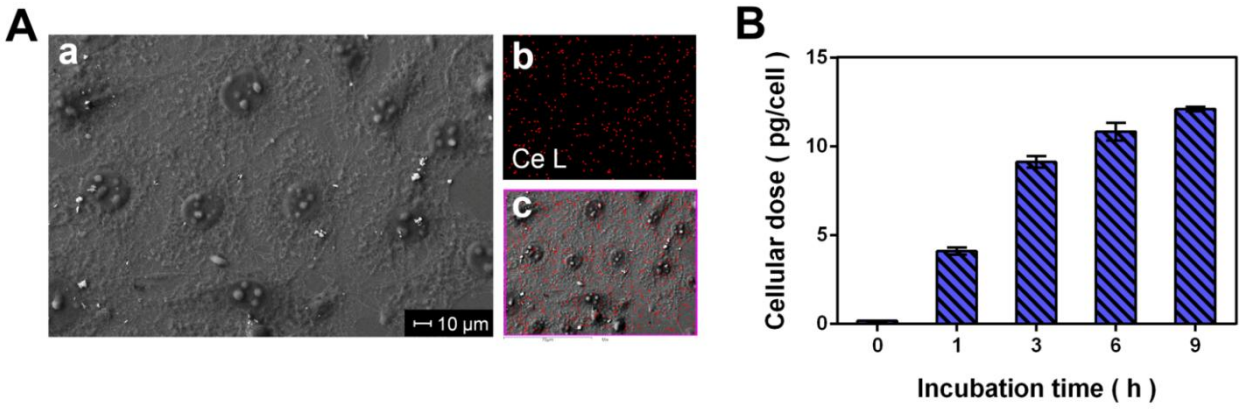

Figure 6.14 (A) FE-SEM image of (a) NIH3T3 cells incubated with 50 µg mL^{-1} CDs-CeO_2 NC. (b) Colour coded EDS dot maps depicting the distribution of cerium inside the cells. (c) Overlay FE-SEM image generated by combination of (a) and (b). (B) ICP-MS analysis for the quantification of cerium internalized by NIH3T3 cells with increasing time. Results are expressed as mean ± standard deviation of two replicates.

When the cells were treated with CDs alone, strong blue fluorescence was observed in the cytoplasm of the cells **(Fig. 6.15 (b))**. Conversely, when CDs pretreated cells were exposed to H_2O_2, a marked decrease in blue fluorescence of the cells was apparent **(Fig. 6.15 (e))**. Similarly, the fluorescence intensity of H_2O_2 treated cells was found to be on the lower side compared to non H_2O_2 treated cells in the flow cytometeric analysis, which validates the above observations **(Fig. 6.15 (c,f))**. Therefore, the fluorescence intensity of CDs could be used as an indicator of oxidative stress in cells. CDs-CeO_2 NC penetrated and labelled the cells in a similar manner. However, upon H_2O_2 exposure, the CDs-CeO_2 NC treated cells maintained the blue fluorescence emission inside the cells, suggesting non induction of oxidative stress **(Fig. 6.15 (h,k))**. As a matter of fact, flow cytometry graphs portrayed only a comparatively mild decrease in fluorescence signal of H_2O_2 treated cells **(Fig. 6.15 (i,l))**. Thus, treatment of cells with the fluorescent CDs-CeO_2 NC would lead to the inactivation of H_2O_2 by CeO_2 along with the concomitant monitoring of oxidative stress by fluorescence signal of CDs.

6.2.6 ROS scavenging

The ROS scavenging potential of CDs-CeO_2 NC was demonstrated in NIH3T3 cells subjected to H_2O_2 mediated oxidative stress. Microscopic analysis of ROS levels in treated and untreated cells was done by DCFH-DA assay **(Fig. 6.16 (a1-d1))**. H_2O_2 treated cells exhibited strong green fluorescence compared to untreated cells due to higher ROS levels. Subsequently, the fluorescence of cells pretreated with either 50 or 100 μg mL^{-1} of CDs-CeO_2 NC was significantly reduced, implying efficient reduction in ROS levels. Quantitative analysis of intracellular ROS levels was undertaken by flow cytometry and reported as the percentage of gated cells expressing DCF signal with reference to control cells **(Fig. 6.16 (a2-d2))**. A bimodal distribution of DCF fluorescence intensity profiles of H_2O_2 treated cells was observed. CDs-CeO_2 NC were effective in reducing intracellular ROS as evident by shifts in the cell population from a region of higher oxidative stress (fluorescence intensity $>10^4$) to a region of lower oxidative stress (fluorescence intensity range: $10\text{-}10^4$) compared with cells exposed to H_2O_2 only. Consequently, the percentage of cells with elevated ROS levels decreased from 30.1 to 20 % with an increase in concentration of CDs-CeO_2 NC. For comparison, we also determined the percentage reduction in ROS levels for cells treated with bare CeO_2 at identical concentrations **(Fig. 6.17)**. Accordingly, ROS levels decreased in a dose-dependent manner from 24.2 to 16.5 %, which is almost comparable to CDs-CeO_2 NC treated cells. Hence, the above examinations confirm the antioxidant potential of CDs-CeO_2 NC to mitigate the ROS levels following their uptake inside the cells.

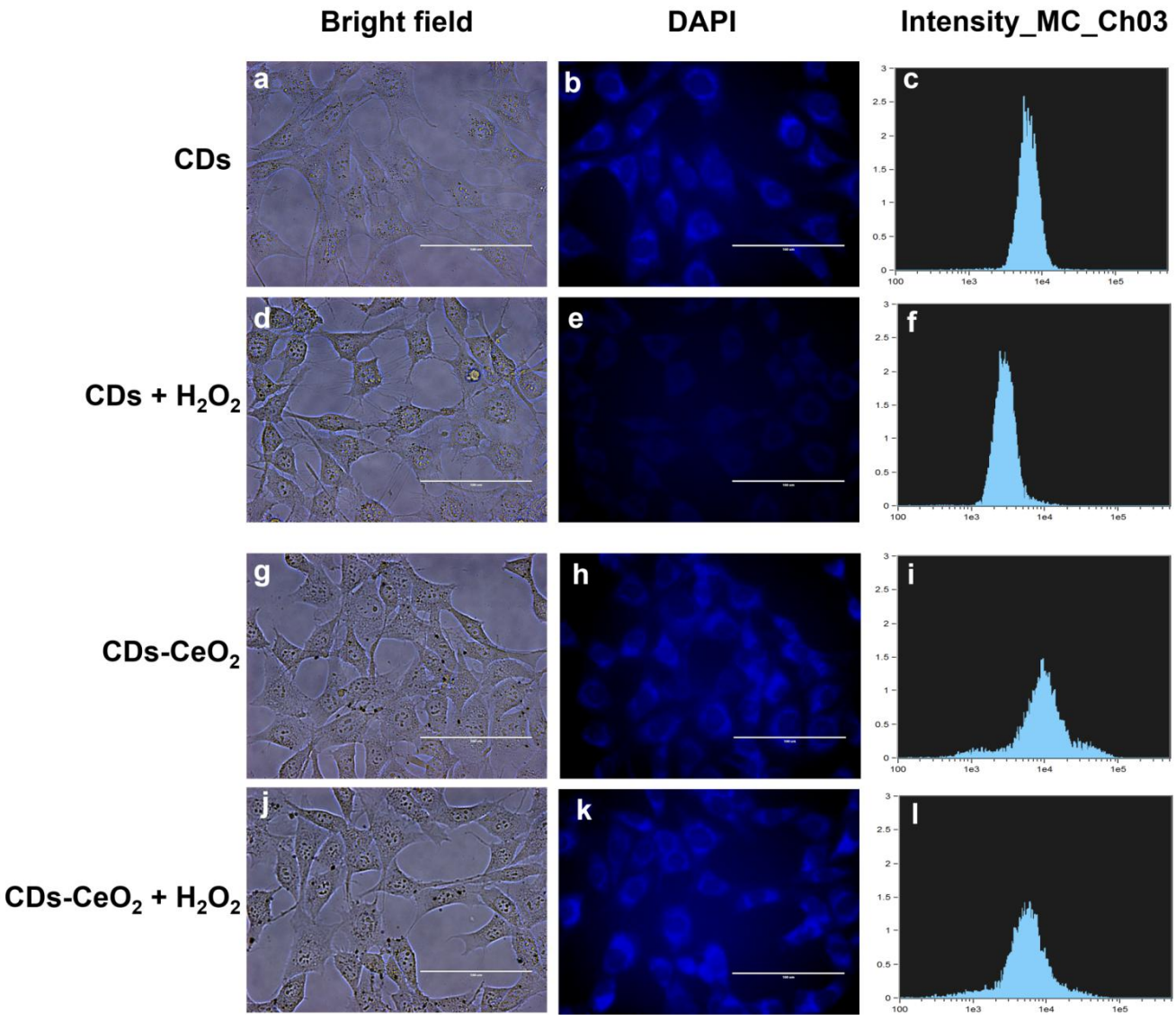

Figure 6.15 Representative microscopic and flow cytometeric analysis of cells upon treatment with equal concentration of CDs and CDs-CeO_2 NC (100 µg mL^{-1}) for 12 h in absence or presence of H_2O_2 (750 µM). Left and middle panel represents the microscopic images acquired under bright field and DAPI filters. Scale bar: 100 µm. Right panel corresponds to the fluorescence intensity of the respective samples recorded by a flow cytometer.

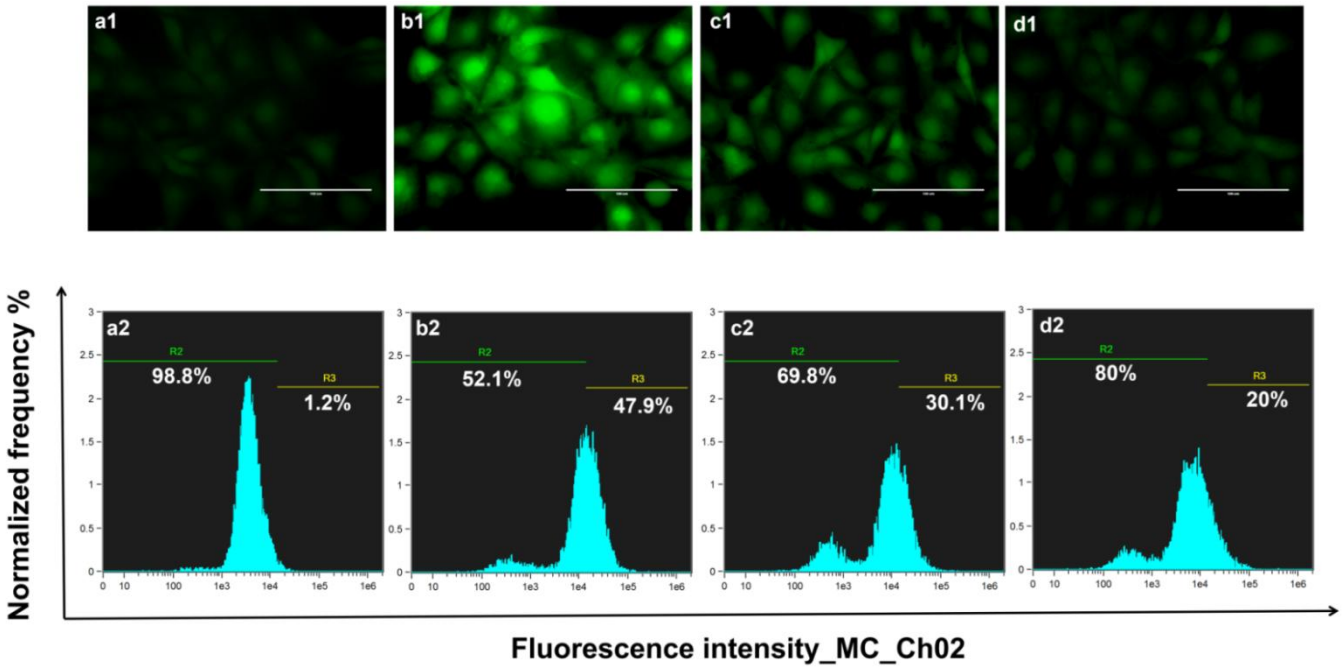

Figure 6.16 Microscopic and flow cytometeric analysis of intracellular ROS levels in (a1,a2) untreated cells, H_2O_2 treated cells pre-incubated without (b1,b2) and with (c1,c2) 50 µg mL^{-1} and (d1,d2) 100 µg mL^{-1} of CDs-CeO_2 NC. Upper panel: microscopic images of DCF fluorescence. Scale bar: 100 µm. Lower panel: the corresponding flow cytometeric quantitation of the same.

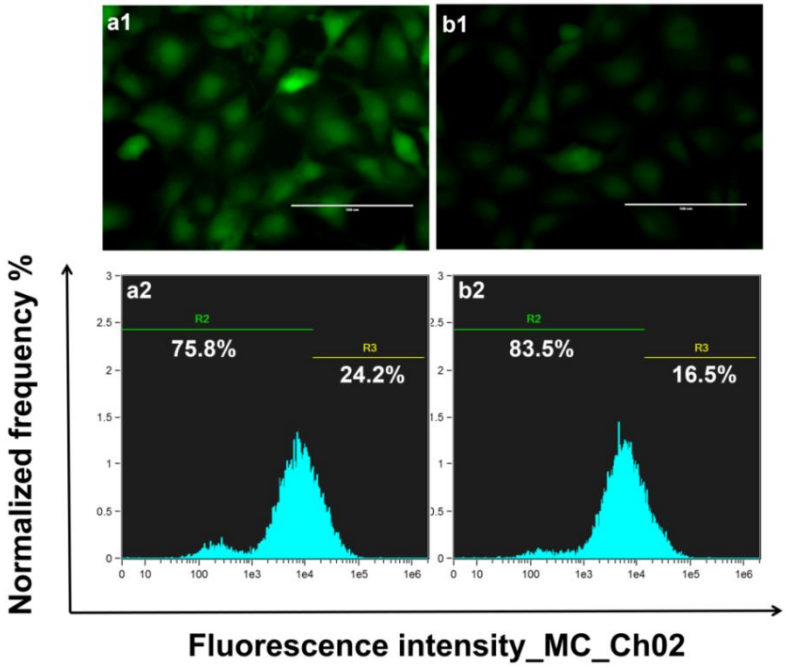

Figure 6.17 Microscopic and flow cytometeric analysis of intracellular ROS levels in H_2O_2 exposed cells pre-incubated with (a1,a2) 50 µg mL^{-1} and (b1,b2) 100 µg mL^{-1} of CeO_2 nanoparticles. Upper panel: microscopic images of DCF fluorescence. Scale bar: 100 µm. Lower panel: the corresponding flow cytometeric quantitation of the same.

In summary, dual-modal CDs-CeO_2 NC was synthesized by a hydrothermal approach for monitoring the intracellular distribution and ROS scavenging. Fluorescence spectroscopic studies confirmed that the CDs-CeO_2 NC maintained their fluorescence emission in the presence of relatively higher H_2O_2 concentrations. Cells pre-incubated with CDs-CeO_2 NC exhibited concentration dependent protective effects upon exposure to H_2O_2. Additionally, CDs-CeO_2 NC was able to prevent H_2O_2 mediated apoptotic effects. The intracellular distribution of CDs-CeO_2 NC was discerned by its inherent blue fluorescence emission. The fluorescence signal of CDs-CeO_2 NC inside the cells changed slightly in comparison to cells treated with CDs alone upon H_2O_2 incubation which can be attributed to the ability of CeO_2 in preventing oxidative stress.

CHAPTER 7

Preparation of C-dots-Silver@Zinc Oxide Nanocomposite for *In Situ* Imaging and Therapeutic Purposes

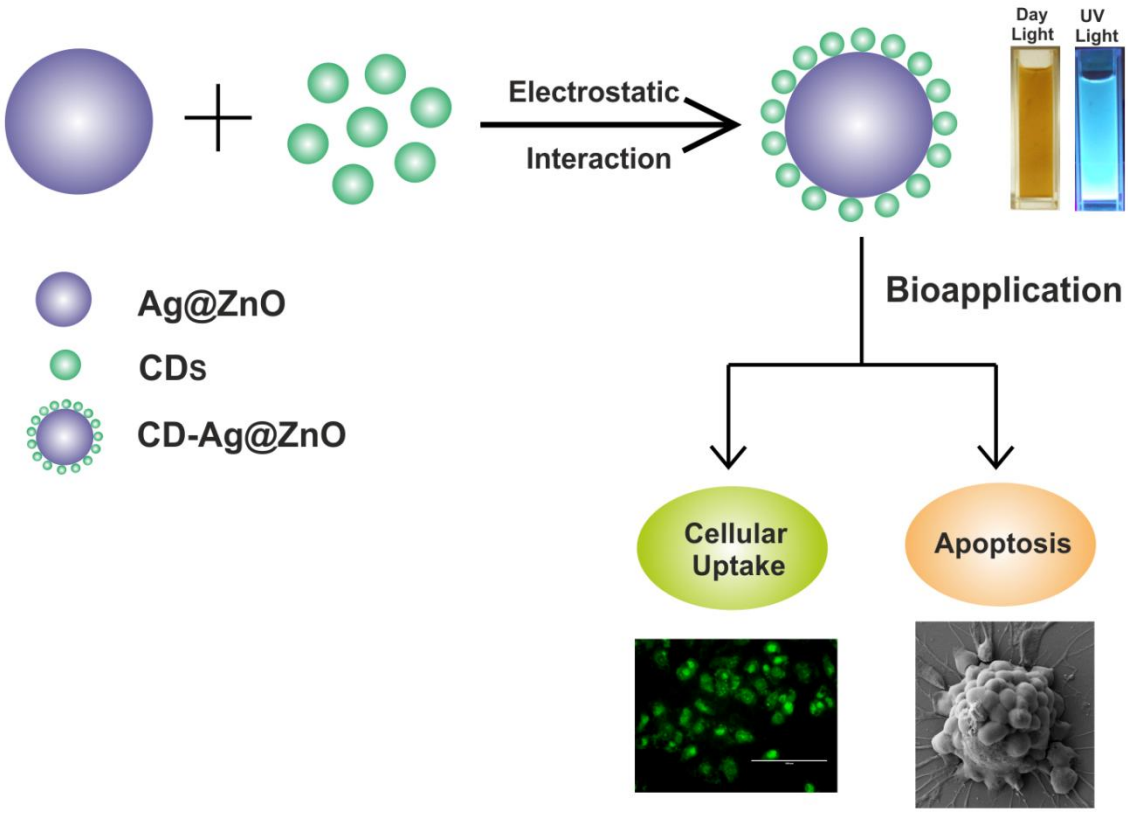

CHAPTER 7

PREPARATION OF C-DOTS–SILVER @ZINC OXIDE NANOCOMPOSITE FOR *IN SITU* IMAGING AND THERAPEUTIC PURPOSES

7.1 Overview

C-dots have raised high expectations in biology as a result of their intrinsic biocompatibility and remarkable fluorescence characteristics. Generally, organic dyes have been incorporated into multifunctional nanocomposite (NC) systems to evaluate cellular uptake. For example, coumarin-6 has been used as a fluorescent marker to evaluate the intracellular uptake of nanoparticles (Liu et al., 2012b, Gao et al., 2013, Huang et al., 2013b and Tao et al., 2014). However, coumarin-6 has certain disadvantages, such as water insolubility and cytotoxicity, which discourages its use in intracellular studies. C-dots, on the other hand, are able to circumvent these issues and could be useful candidates in monitoring cellular uptake. Metal-based nanoparticles have been extensively applied in consumer-related applications. As a result of their widespread use and our increased exposure to these nanoparticles, their cytotoxicity has been studied in detail. Accordingly, Ag and ZnO nanoparticles have attracted much attention as potential apoptotic agents for anticancer treatment, which has been confirmed through various mechanistic studies (Gopinath et al., 2010, Sharma et al., 2012 and Wahab et al., 2014). Conversely, most reported studies do not give a clear idea about the cellular uptake of Ag and ZnO. With this motivation, an endeavour has been made to combine C-dots with Ag@ZnO to form CD-Ag@ZnO NC with dual functionality. Consequently, PEG was used as a surface passivation agent for generating CDs in a one-pot synthesis. The negatively charged PEG passivation layer of CDs has the ability to form a hybrid assembly with the positively charged Ag@ZnO by electrostatic interactions. Further, the rationale behind the study is to investigate the multifunctional aspects of the CD-Ag@ZnO NC, exploiting the ability of the Ag@ZnO component to evoke apoptosis, while simultaneously using CDs as a fluorescence imaging probe. To the best of our knowledge, this is the first report of the use of CDs to examine the cellular uptake of metal-based NC systems. MCF-7 (breast cancer) and A549 (lung cancer) cell lines have been selected as model systems for the study because these are the most prevalent types of cancer in humans. To elucidate the multiple origins of

apoptosis, the levels of reactive oxygen species (ROS) were measured and apoptotic gene expression studies have been performed.

7.2 RESULTS AND DISCUSSION

7.2.1 Synthesis and characterization of CD-Ag@ZnO NC

A simple method has been demonstrated for synthesizing CD-Ag@ZnO NC by combining negatively charged CDs with positively charged Ag@ZnO through electrostatic interactions **(Fig. 7.1 (A))**. The optical properties and formation of CD-Ag@ZnO NC were studied using various spectroscopic and microscopic techniques. The aqueous solutions of the as-prepared CDs and Ag@ZnO showed a single absorption band at 257 (π-π^* transition) and 372 nm, respectively, whereas CD-Ag@ZnO NC showed two absorption bands at 251 and 348 nm **(Fig. 7.1 (B))**. The fluorescence intensity of CDs in the CD-Ag@ZnO NC decreased slightly with respect to that of the blank CDs **(Fig. 7.1 (C))**. This may be a result of photo-induced electron transfer between the Ag@ZnO and CD components. The fluorescence quantum yield of CD-Ag@ZnO NC was calculated to be 6.42 %, which was comparable with that of the CDs (6.74 %) measured under similar parameters **(Table 7.1)**. Similarly, the fluorescence lifetime decay curves for the CDs and CD-Ag@ZnO NC clearly show triple exponential decay and their average lifetimes were calculated **(Fig. 7.2 and Table 7.2)**. The mean lifetime of the CD-Ag@ZnO NC was estimated to be 5.035 ns, slightly less than that of the CDs (5.204 ns). The quantum yield and fluorescence lifetime measurements prove that Ag@ZnO did not completely quench the fluorescence of the CDs, in contrast with previous reports (Luo et al., 2012 and Wang et al., 2014c). Consequently, the electrostatic interactions of CDs with Ag@ZnO pursued in this work provide several advantages, such as the ability to retain the fluorescent properties without any reduction in quantum yield and a minor reduction in the fluorescence intensity of the NC with respect to CDs, which suggests their potential for cell imaging (Datta et al., 2014). The TEM images of CD-Ag@ZnO NC provide direct evidence of the distribution of the CDs on the surfaces of Ag@ZnO **(Fig. 7.3 (A))**. The average size of the NC was estimated to be 37.5 ± 3.2 nm. Zeta potential measurements were carried out to examine the surface properties of the CD-Ag@ZnO NC **(Fig. 7.3 (B))**. The surface of the CDs was negatively charged (zeta potential = -21.5 mV), whereas the Ag@ZnO surface was positively charged (zeta potential = +22.3 mV). However, the zeta potential of CD-Ag@ZnO NC was +10.8 mV, which implied that the Ag@ZnO was capped by CDs.

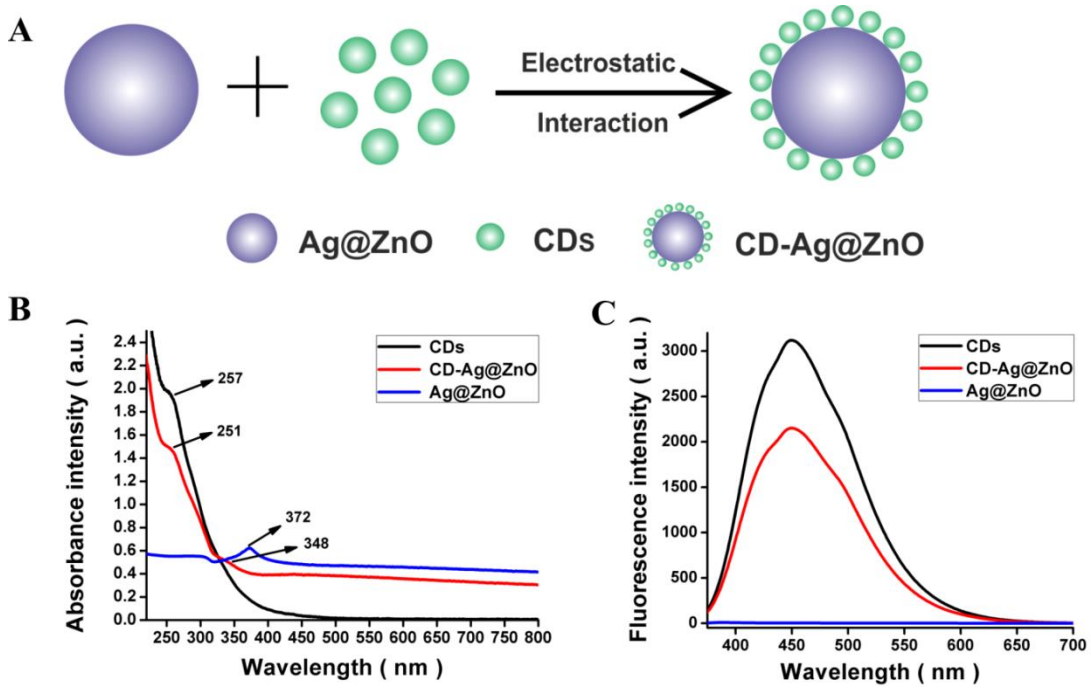

Figure 7.1 (A) Schematic illustration of the synthesis of the CD-Ag@ZnO NC. (B) UV-visible absorption spectra. (C) Fluorescence emission spectra (λ_{ex} = 320 nm; λ_{em} = 400 nm).

Sample	Integrated emission intensity *(I)*	Absorbance at 360 nm *(A)*	Refractive index of solvent (η)	Quantum yield at 360 nm *(Q)*
Quinine sulphate	658172	0.0728	1.33	0.54 (known)
CDs	92856	0.0823	1.33	0.0674
CD-Ag@ZnO	88239	0.0821	1.33	0.0642

Table 7.1 Quantum yield measurements.

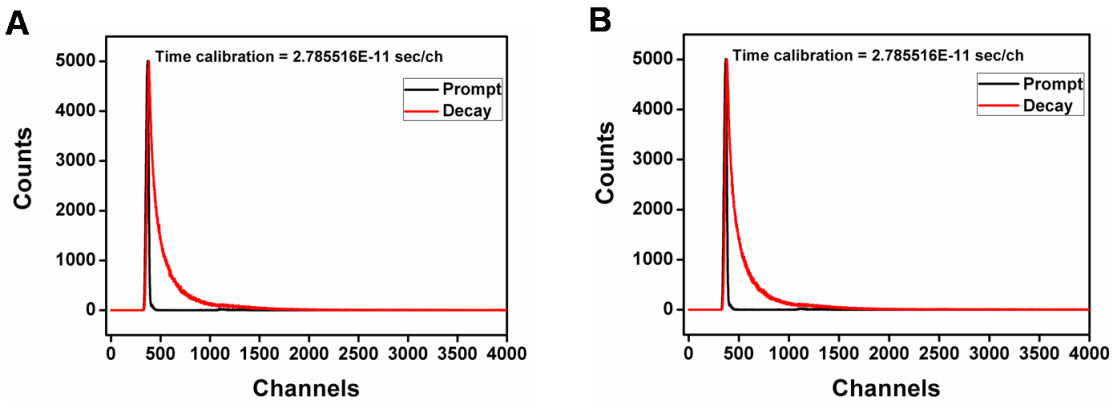

Figure 7.2 Fluorescence decay curve of (A) CDs and (B) CD-Ag@ZnO (λ_{ex} = 320 nm; λ_{em} = 400 nm).

Sample	a_1	τ_1(ns)	a_2	τ_2(ns)	a_3	τ_3(ns)	τ_{av}(ns)	χ^2
CD	0.5409	3.306	0.1521	0.590	0.3070	10.833	5.204	1.169
CD-Ag@ZnO	0.5323	3.334	0.1634	0.644	0.3043	10.369	5.035	1.157

Table 7.2 Tabular representation of fluorescence lifetime calculation.

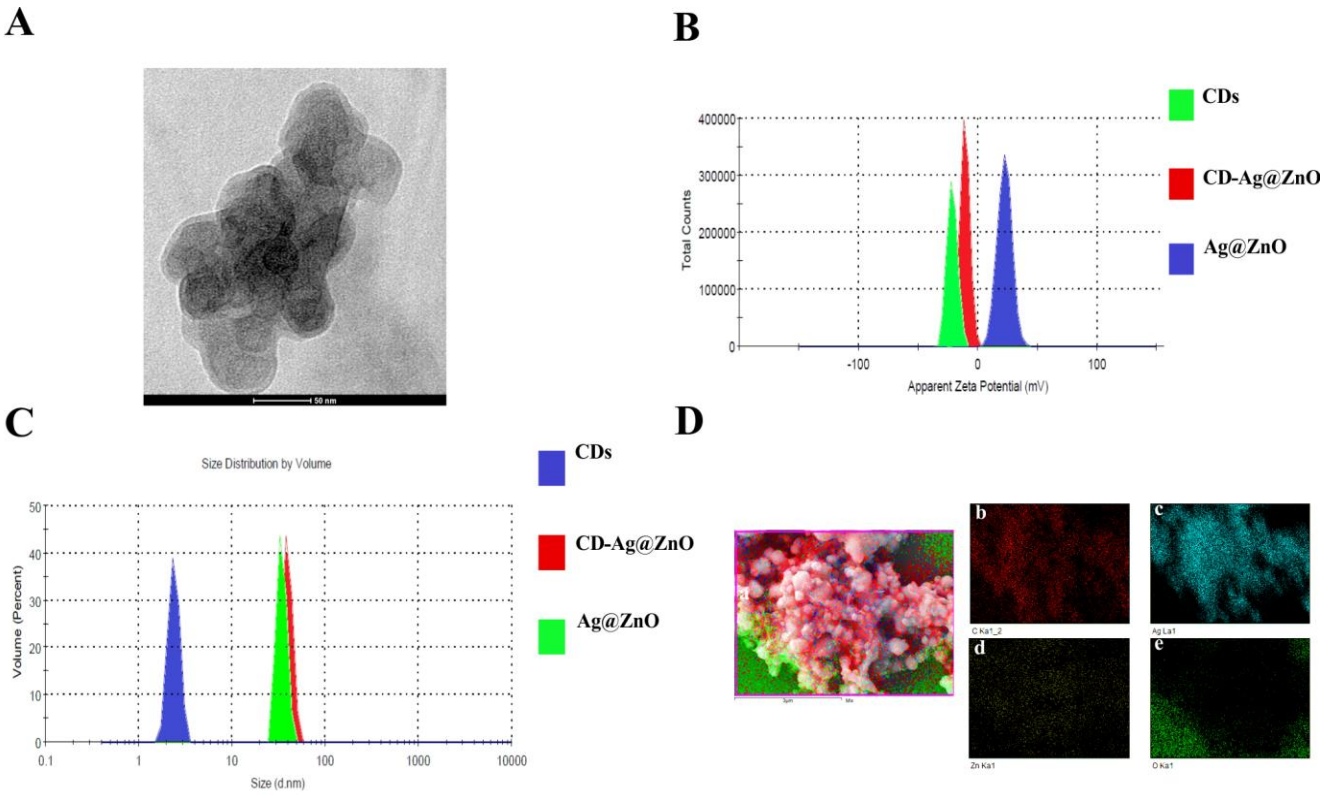

Figure 7.3 (A) Representative TEM image of CD-Ag@ZnO NC. (B) Zeta potential and (C) size distribution of aqueous solutions of CDs, CD-Ag@ZnO and Ag@ZnO at pH 7.0. (D) FE-SEM image of CD-Ag@ZnO NC and colour-coded SEM/EDX dot maps. (a) Overlay FE-SEM image showing elemental distributions in CD-Ag@ZnO NC. (b-e) Individual elemental distribution maps (red = C, cyan = Ag, yellow = Zn and green = oxygen).

As shown in **Fig. 7.3 (C)**, the average hydrodynamic diameter of the CDs was 2.4 nm. After successful loading of the CDs, the hydrodynamic diameter of the CD-Ag@ZnO NC (39.58 nm) was slightly larger than that of the corresponding Ag@ZnO (34.16 nm). To further verify the presence of CDs and Ag@ZnO in the NC, elemental analysis was carried out using low magnification FE-SEM **(Fig. 7.3 (D))**. The energy-dispersive X-ray spectrometry (EDS) elemental mapping distributions indicated the presence of C, Ag, Zn and O evenly distributed in the CD-Ag@ZnO NC. The overlay SEM image further showed the presence of carbon on the surface, with the core consisting of Ag, Zn and O in agreement with the TEM and zeta potential measurements.

Moreover, the EDAX spectrum revealed the relative percentage elemental composition of CD-Ag@ZnO NC to be 14.84 % C, 56.11 % Ag, 19.05 % Zn and 10 % O **(Fig. 7.4)**. N_2 adsorption-desorption isotherms **(Fig. 7.5 (A))** were recorded to determine the porous nature of Ag@ZnO. Calculations based on the adsorption data using the BJH model indicated that Ag@ZnO had a specific surface area of 6.560 m^2 g^{-1}, a pore volume of 0.010 cm^3 g^{-1} and an average pore diameter of 1.49 nm. The TEM results **(Fig. 7.5 (B))** show that the CDs were mostly spherical and had an average diameter of about 2.1 nm, which implies that the CDs cannot penetrate the 1.49 nm pores of Ag@ZnO in the CD-Ag@ZnO NC (Wang et al., 2013a and Zhou et al., 2013a). This observation is consistent with the TEM and zeta potential measurements. The phase structure of the CD-Ag@ZnO NC was also explored. The XRD pattern shows a broad, amorphous peak at 22.63°, which corresponds to the (002) plane of the CDs, whereas the highly crystalline diffraction peaks match well with the typical wurtzite ZnO (JCPDS card # 36-1451) and face-centred cubic Ag (JCPDS card #04-0783) phases, respectively **(Fig. 7.6 (A))**. Characteristic peaks obtained for the CDs and Ag@ZnO clearly agree with previously reported results (Yu et al., 2012, Sachdev et al., 2014 and Matai et al., 2014). The FTIR spectra show specific functional groups present in the CD-Ag@ZnO NC **(Fig. 7.6 (B))**. The peaks at 3432, 1638 and 1403 cm^{-1} were due to the O–H, C=O and C–N groups of the CDs. The passivating agent, PEG, imparts O–H functionality to the CDs. In addition, the peaks at 1090, 804 and 708 cm^{-1} corresponded to the Zn–O–Zn, Zn–O–H and Zn–O–Zn stretching and bending frequencies, respectively. The absorption bands at 476 and 652 cm^{-1} were attributed to the stretching vibrations of the Zn–O and Ag–ZnO bonds (Matai et al., 2014). Notably, no C–Ag nor C–Zn bond was found. This indicated that the negatively charged O–H functionalized CDs were electrostatically adsorbed on the surface of the Ag@ZnO component (Li et al., 2011a and Bian et al., 2014).

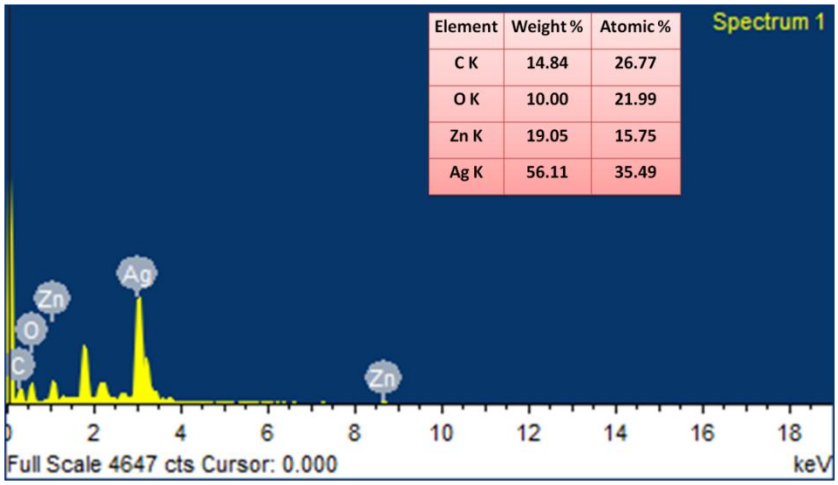

Figure 7.4 EDAX spectrum and elemental composition of CD-Ag@ZnO NC.

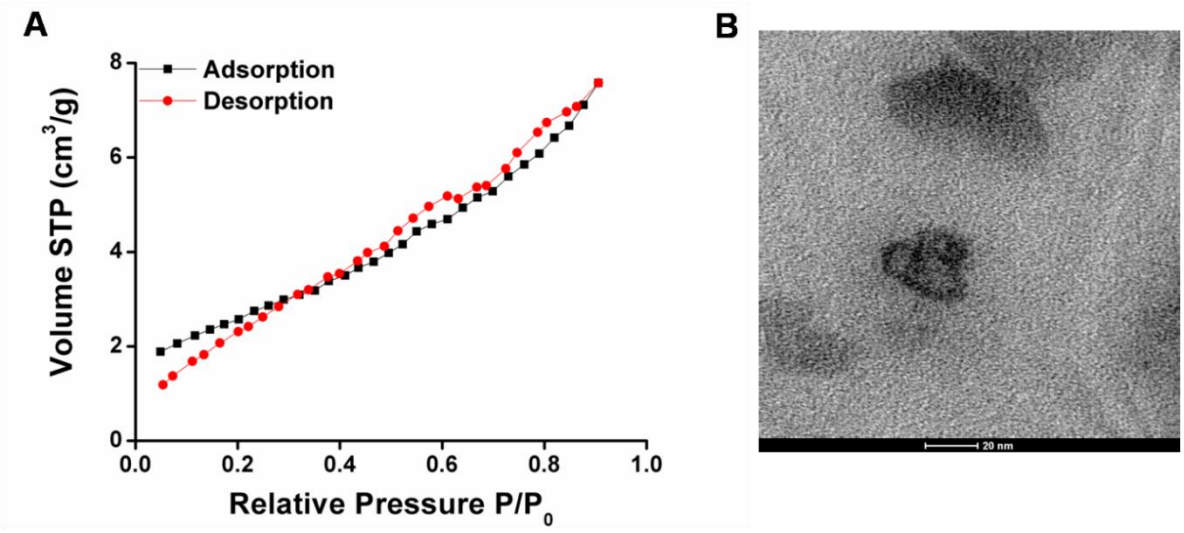

Figure 7.5 (A) N_2 adsorption–desorption isotherms for Ag@ZnO. (B) TEM image of CDs.

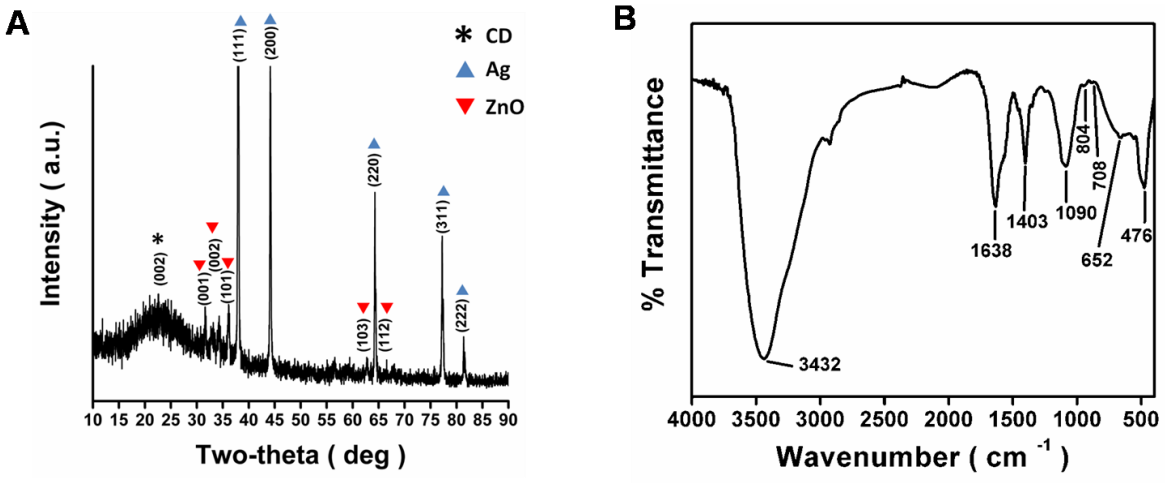

Figure 7.6 (A) XRD spectra of CD-Ag@ZnO NC. (B) FTIR spectra of CD-Ag@ZnO NC.

7.2.2 *In vitro* cytotoxicity

The percentage cell viability was determined quantitatively by MTT assay. MCF-7, A549 and L-132 cells were exposed to varying concentrations of the CD-Ag@ZnO NC (10-90 µg mL^{-1}). The obtained results show a significant reduction in the viability of both cancer cell lines in a dose-dependent manner. The IC_{50} values (at which 50 % of cells are dead) of CD-Ag@ZnO against MCF-7 and A549 cells were 50 and 70 µg mL^{-1}, respectively **(Fig. 7.7 (A) and (B))**. The MCF-7 and A549 cells treated with blank Ag@ZnO showed a severe decrease in cell viability at similar concentrations. For example, the IC_{50} values for Ag@ZnO treated MCF-7 and A549 cells were 20 and 50 µg mL^{-1}, respectively which are far lower than those estimated for CD-Ag@ZnO. However, the CD-Ag@ZnO NC showed mild cytotoxicity towards normal L-132 cells compared with cancer cells in the same concentration range **(Fig. 7.7 (C))**. Moreover, the probable reason for the lower cytotoxicity of the CD-Ag@ZnO NC compared with the blank Ag@ZnO may be the presence of the CDs on the surface, which prevents the premature interaction of the NC with the cells. Hence, the chances of aggregation of CD-Ag@ZnO NC in cell culture media are minimized resulting in controlled cell death. The biocompatibility of the CDs was clearly established as the cells treated with CDs had higher cell viability (nearly 97 %), even at a high concentration of 3 mg mL^{-1}, compared with cells treated with CD-Ag@ZnO NC and Ag@ZnO **(Fig. 7.7 (D))**. To further validate the differential toxic effect of CD-Ag@ZnO NC, the morphology of the cancer and normal cells treated at similar concentrations was examined by an inverted microscope under bright-field conditions. The A549 and MCF-7 cells treated with 50 µg $mL^{-1}$of the CD-Ag@ZnO NC appeared rounded and had shrunk in size. At a similar concentration, the treated L-132 cells showed a predominantly healthy and normal morphology to that of untreated control cells, with few rounded cells **(Fig. 7.8)**. These results indicate that the reduction in cell viability is primarily due to the action of the Ag@ZnO component in the CD-Ag@ZnO NC.

7.2.3 Cellular uptake

Cellular uptake is an important factor contributing to the action and cytotoxic effects of nanoparticles (Liu et al., 2012b, Gao et al., 2013 and Gliga et al., 2014). MCF-7 and A549 cells were selected as models to evaluate the cellular uptake of the CD-Ag@ZnO NC inside cancer cells. The cells were incubated with different concentrations of the CD-Ag@ZnO NC and their uptake was monitored qualitatively by fluorescence microscopy **(Fig. 7.9)**.

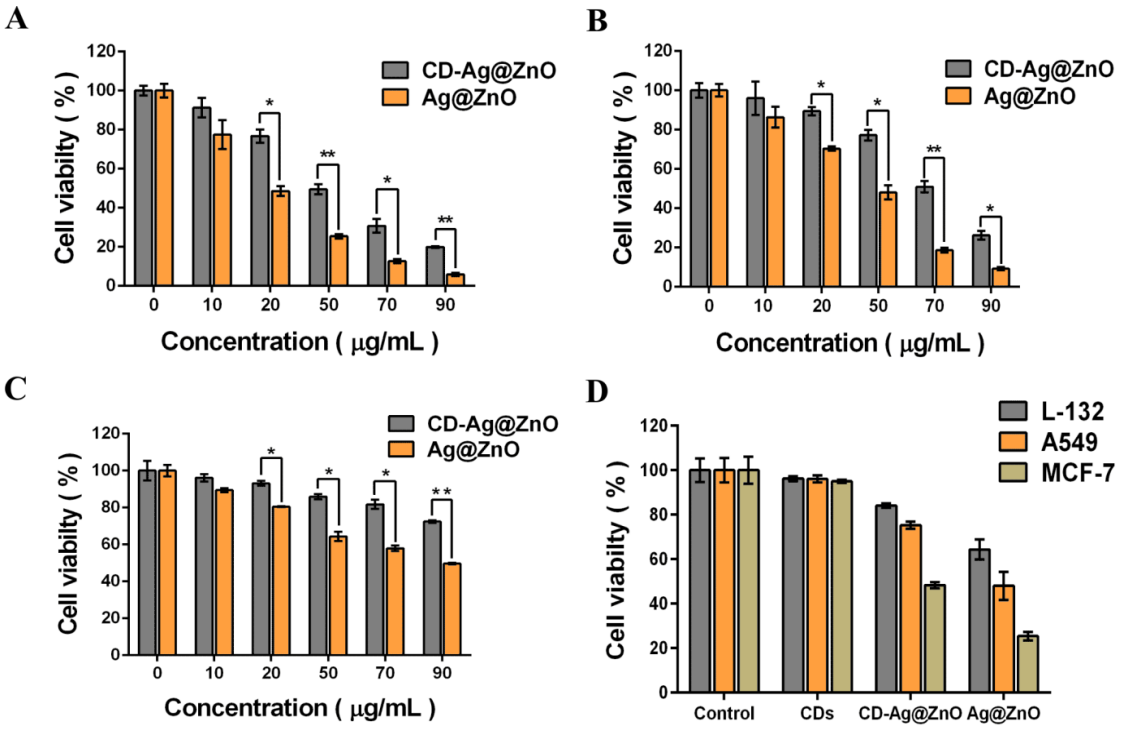

Figure 7.7 Cell viability of (A) MCF-7, (B) A549 and (C) L-132 cells estimated from the MTT assay. (D) Comparative cytotoxicity analysis of CDs (3 mg mL^{-1}), CD-Ag@ZnO (50 μg mL^{-1}) and Ag@ZnO (50 μg mL^{-1}). The data are presented as mean ± SEM values of three individual experiments. The statistical significance between the samples treated with the CD-Ag@ZnO NC and the blank Ag@ZnO is denoted by *($p < 0.05$) and **($p < 0.001$).

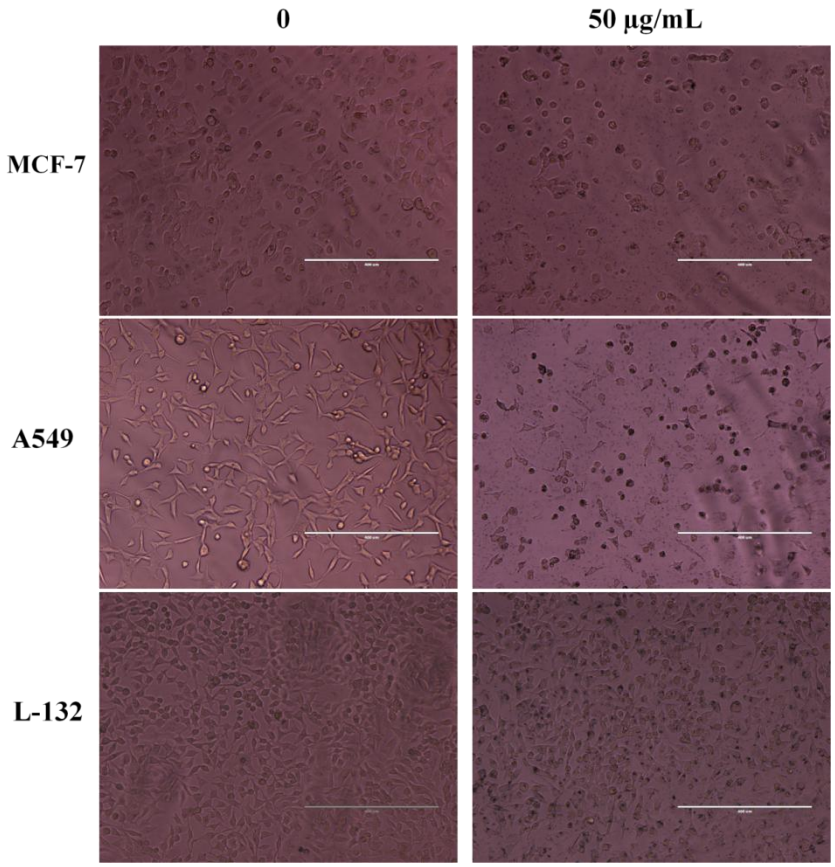

Figure 7.8 Bright field microscopic images. Scale bar: 400 μm.

The fluorescence emitted from the CDs in the CD-Ag@ZnO NC was used to track the cellular localization of the CDs. Blank CDs were internalized in the cytoplasm of the cells, but could not enter the nucleus **(Fig. 7.9 e and m)** (Sachdev et al., 2014). However, in case of CD-Ag@ZnO NC treated cancer cells, cytoplasmic as well as nuclear localization was observed in a dose-dependent manner. At lower concentrations (20 µg mL^{-1}), the CD-Ag@ZnO NC were mostly distributed in the cytoplasm **(Fig. 7.9 f and n)**. Nevertheless, at higher concentrations (50 and 70 µg mL^{-1}), along with the cytoplasmic internalization, bright green fluorescence was also observed in the nucleus of MCF-7 and A549 cells **(Fig. 7.9 g, h, o and p)**. A plausible explanation for nuclear uptake could be rupturing of the nuclear membrane at higher concentrations, resulting in enhanced permeability to the NC. Using Hoechst 33342 as a marker of the nucleus, the cellular uptake of the CD-Ag@ZnO NC was tracked (Wang et al., 2013a and Zhao et al., 2014). The onset of cellular uptake was observed after 0.5 h of treatment, followed by a continuous increase up to 3 h **(Fig. 7.10)**. In both cancer cell types, a green fluorescence was initially observed around the cell nuclei. With increasing time, we observed the co-localization of blue (Hoechst 33342) and green fluorescence (CD-Ag@ZnO NC), suggesting nuclear internalization. Cytoplasmic constriction was also observed with time. We used L-132 cells to examine the cellular uptake of CD-Ag@ZnO NC in normal cells. Interestingly, the normal cells exhibited efficient cellular uptake without any substantial cytotoxic effects at similar concentrations **(Fig. 7.11)** (Mukherjee et al., 2014). However, no nuclear uptake was observed in normal cells, in contrast with cancer cells. These results suggest a differential uptake pattern of CD-Ag@ZnO NC in human cancer and normal cells. The cellular uptake of CD-Ag@ZnO NC was both concentration- and time-dependent **(Fig. 7.12)**. As the concentration of NC increased, the fluorescence intensity and hence the uptake of NC increased in both MCF-7 and A549 cells **(Fig. 7.12 (A))**. Likewise, an enhanced uptake of CD-Ag@ZnO NC was observed with increasing incubation time up to 3 h in both the cancer cell lines **(Fig. 7.12 (B))**. As is evident from these investigations, the cellular uptake differed between the two cancer cell lines. At equal concentrations and similar time points, CD-Ag@ZnO NC was taken up by the MCF-7 cells at higher levels than the A549 cells. AAS was further used to quantify the cellular doses of Ag^{+} and Zn^{2+} at different concentrations of CD-Ag@ZnO (Fig. 7.12 (C) and (D)) (Gliga et al., 2014). The average Ag^{+} concentration per cell was in the range 6-10.4 pg for MCF-7 cells and 5.2-9.25 pg for A549 cells. Correspondingly, the average Zn^{2+} content per cell was in the range 4.67-12.39 pg (MCF-7) and 3.53-9.71 pg (A549). From the results obtained, it was apparent that the MCF-7 cells had higher intracellular doses of Ag and Zn than the A549 cells.

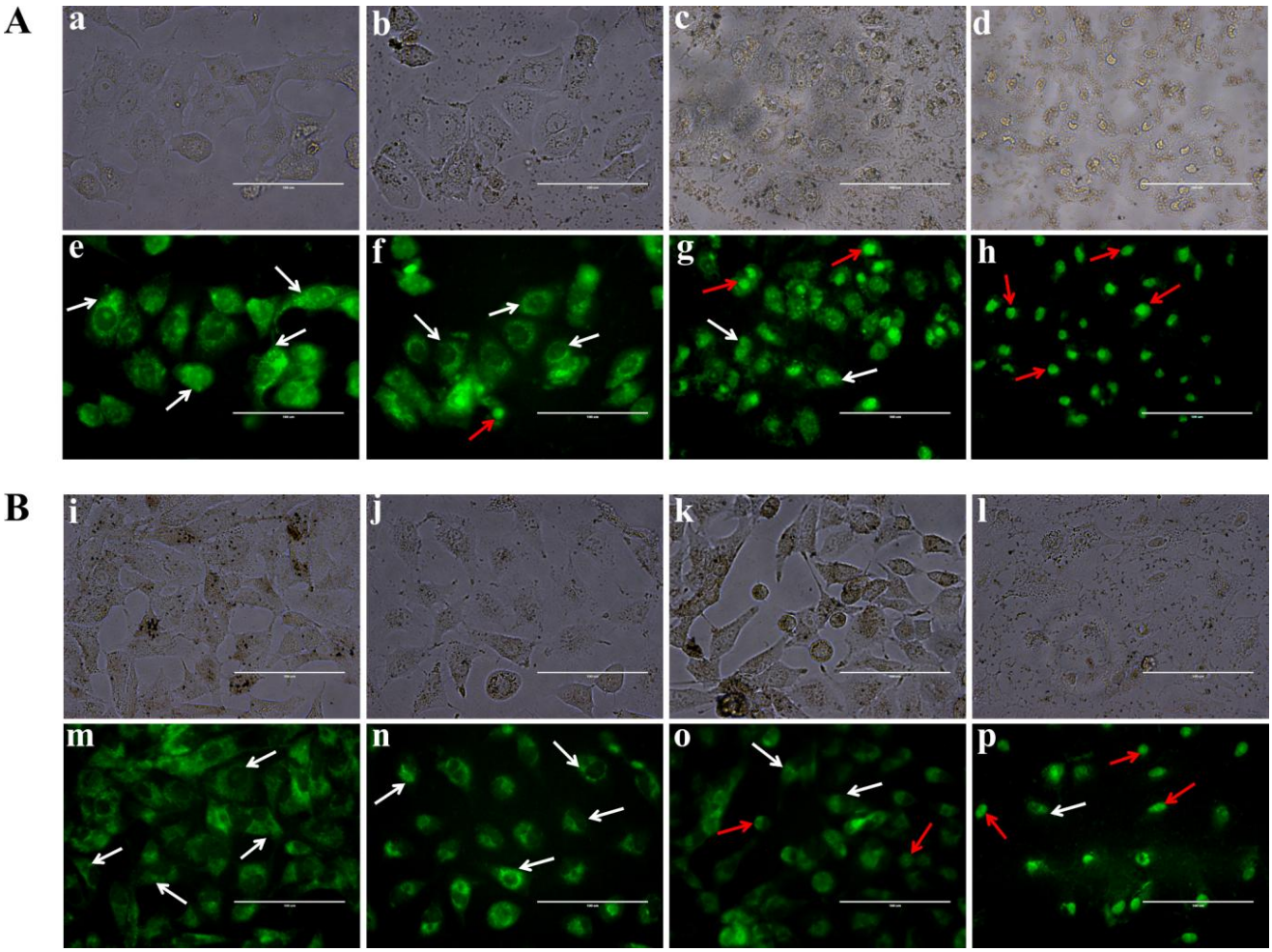

Figure 7.9 Fluorescence microscopic images showing the cellular uptake in (A) MCF-7 and (B) A549 cells. Upper panel: MCF-7 cells treated with (a and e) CDs and (b and f) 20 µg mL^{-1}, (c and g) 50 µg $mL^{-1}$and (d and h) 70 µg mL^{-1}CD-Ag@ZnO NC. Lower panel: A549 cells treated with (i and m) CDs and (j and n) 20 µg mL^{-1}, (k and o) 50 µg mL^{-1}, (l and p) 70 µg mL^{-1} CD-Ag@ZnO NC. The images in (a-d) and (i-l) are the corresponding bright-field images. The white and red arrows represent the cytoplasm and nuclear localization, respectively.
Scale bar: 100 µm.

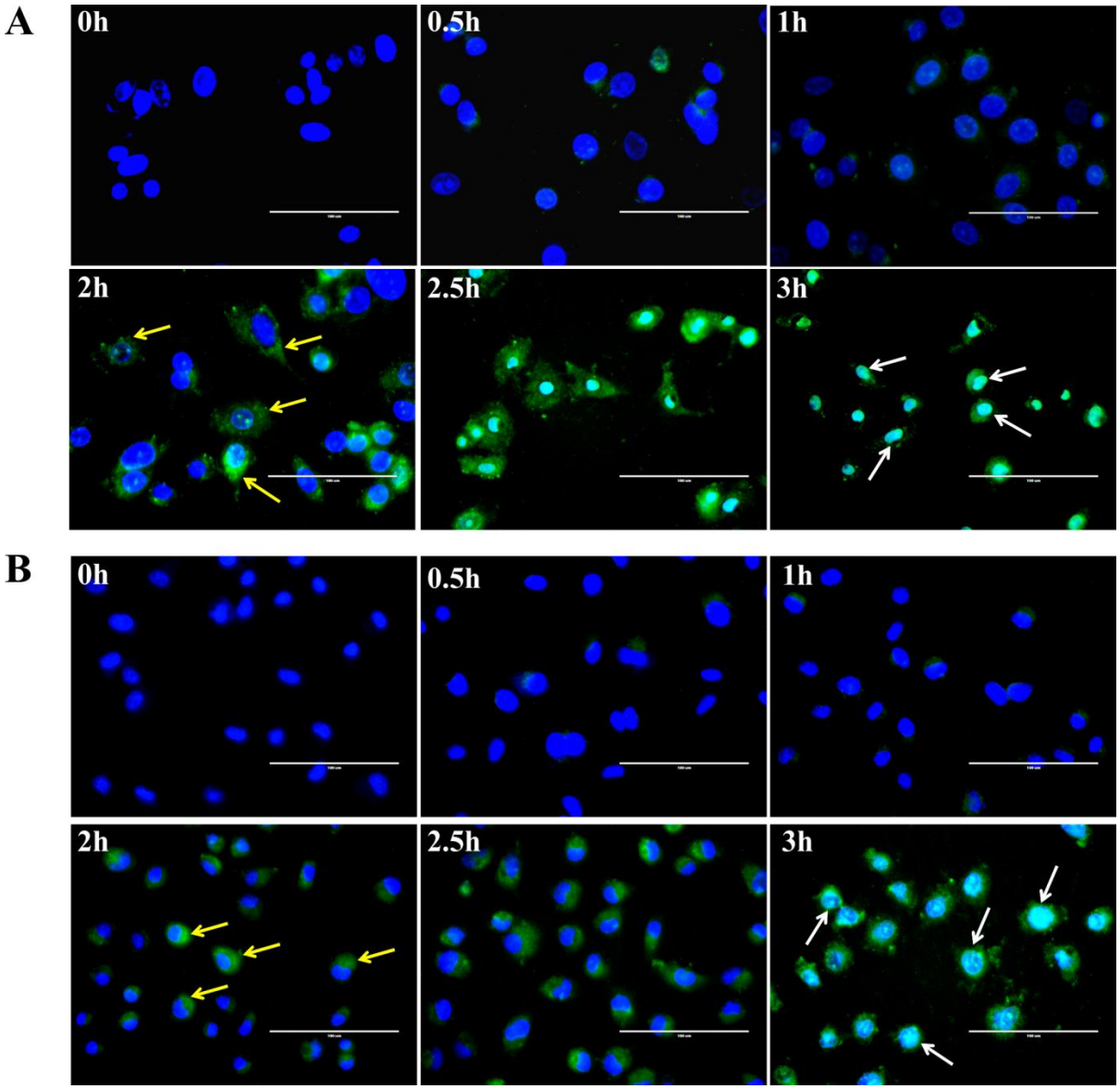

Figure 7.10 Time-dependent overlay images of (A) MCF-7 and (B) A549 cells treated with 50 µg mL^{-1} CD-Ag@ZnO NC and stained with Hoechst 33342.Yellow and white arrows represent cytoplasm and nuclear localization, respectively. Overlay images have been acquired using a combination of DAPI (for Hoechst 33342) and GFP (for CD-Ag@ZnO NC) filters. Scale bar: 100 µm.

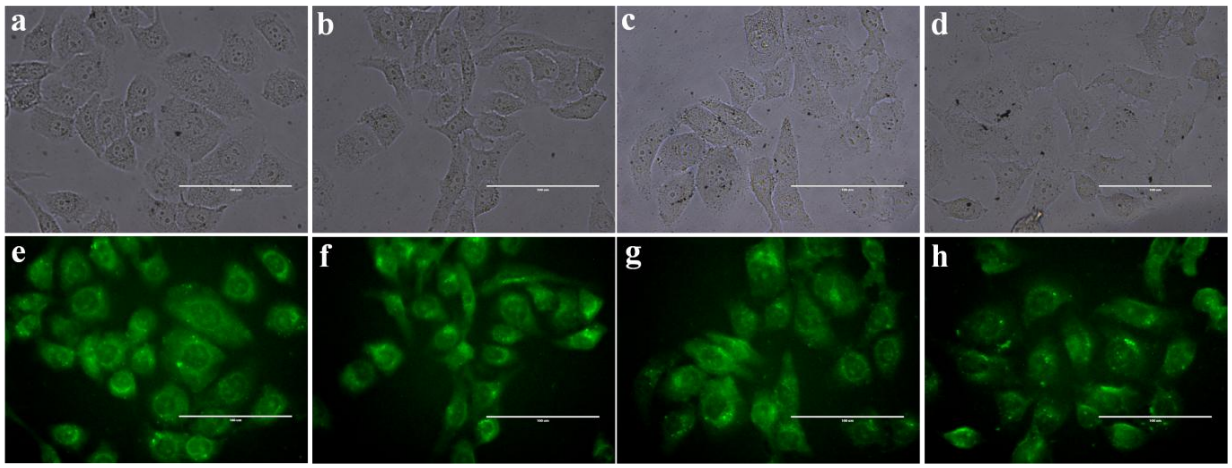

Figure 7.11 Fluorescence microscopic images depicting the cellular uptake in L-132 cells. a,e) CDs and b,f) 20 µg mL^{-1}, c,g) 50 µg mL^{-1}, d,h) 70 µg mL^{-1} CD-Ag@ZnO NC treated L-132 cells. The images in the upper panel are corresponding bright field images.

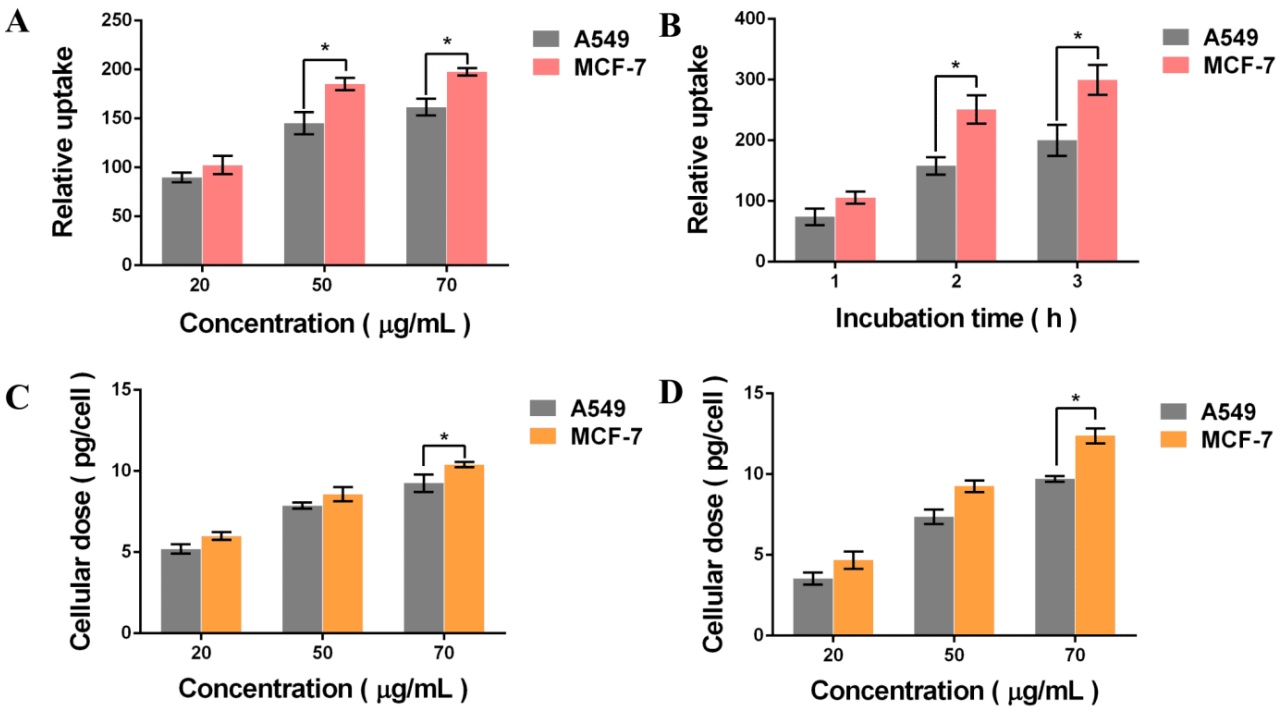

Figure 7.12 Quantitative cellular uptake of CD-Ag@ZnO NC.(A) Cellular uptake of different concentrations of CD-Ag@ZnO NC for 2 h (B) Cellular uptake of 50 µg mL^{-1} CD-Ag@ZnO NC for different times. Quantitative cellular doses of (C) Ag and (D) Zn treated with different concentrations of CD-Ag@ZnO NC for 3 h. The values are represented as mean ± S.E.M. of two individual experiments. Statistical significance between MCF-7 and A549 cells treated with CD-Ag@ZnO NC is denoted by * *($p < 0.05$)*.

7.2.4 Cell death and cell morphology

The apoptosis-inducing ability of Ag and ZnO is one of the most widely studied mechanisms in cancer cells (Gopinath et al., 2010, Rasmussen et al., 2010, Sanpui et al., 2011, Hsiao et al., 2011 and Akhtar et al., 2012). To distinguish between live, apoptotic and necrotic cells in MCF-7 and A549 cells treated with CD-Ag@ZnO NC, DNA intercalating AO/EB dual-dye staining was performed (Sharma et al., 2014). The AO dye can permeate the cell nucleus of both viable and apoptotic cells and emits green fluorescence on binding to double-stranded DNA and red fluorescence when bound to single-stranded DNA or RNA. Conversely, EB can only enter cells with a disrupted plasma membrane and emits an orange fluorescence on intercalation into DNA. Early apoptotic (EA) cells have an intact cell membrane and show bright green granules, indicating nuclear fragmentation. Late apoptotic (LA) cells have a compromised nuclear membrane with more permeability to EB and their nucleus appears orange in colour. The emission from the CDs was not considered here because of the relatively weak fluorescence of bare CDs compared with the fluorescent dye (Wang et al., 2013a). As can be seen in **Fig. 7.13 a and e**, the untreated MCF-7 and A549 cells appeared green, indicating healthy viable cells. However, the MCF-7 cells treated with lower concentrations (20 µg mL^{-1}) of CD-Ag@ZnO NC displayed more EA and fewer LA cells **(Fig. 7.13 b)**, whereas only EA cells were seen at similar concentrations in A549 cells **(Fig. 7.13 f)**. In contrast, with increasing concentrations of NC (50 and 70 µg mL^{-1}), the LA cells outnumbered the EA cells **(Fig. 7.13 c, d, g and h)**. FE-SEM studies were performed to study the morphological changes associated with apoptosis in cancer cells exposed to CD-Ag@ZnO NC. **Fig. 7.13 C** shows that the control cells were spindle-shaped, well-attached to the surface and had an intact membrane morphology. In contrast, the IC_{50} treated cells shrunk in size, became rounded, loosely attached and exhibited membrane blebbing, which are the hallmarks of apoptotic cell death (Gopinath et al., 2010 and Sanpui et al., 2011). The apoptotic effects of CD-Ag@ZnO NC were more pronounced in MCF-7 cells than in A549 cells, clearly endorsing the higher cellular uptake of NC in MCF-7 cells.

7.2.5 ROS production and expression of apoptotic genes

It is a well-known fact that increased levels of ROS can result in oxidative stress, ultimately leading to apoptosis in cancer cells. Earlier studies have implicated excessive ROS production on exposure to Ag and ZnO as leading to cellular oxidative stresses (Rasmussen et al., 2010, Sanpui et al., 2011, Wahab et al., 2014 and Mukherjee et al., 2014).

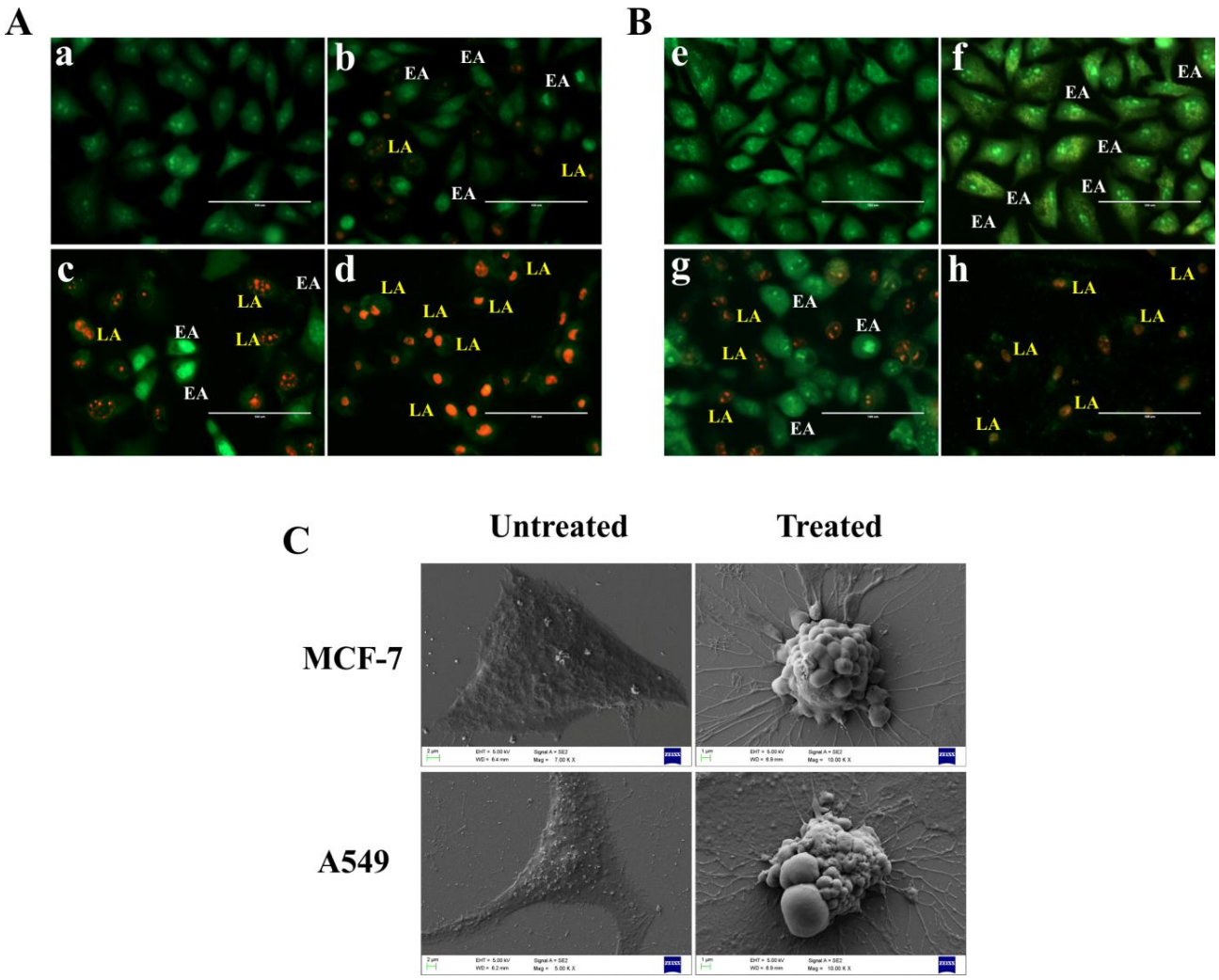

Figure 7.13 Fluorescence microscopic images of AO/EB stained cells of (A) MCF-7 and (B) A549 cells. (a,e) untreated and (b,f) 20 µg mL^{-1}, (c,g) 50 µg mL^{-1}, (d,h) 70 µg mL^{-1} CD-Ag@ZnO NC treated cells. EA and LA represent early apoptotic and late apoptotic cells respectively. Scale bar: 100 µm. (C) Representative FE-SEM images of untreated and CD-Ag@ZnO NC treated cells. Scale bar: 2 µm (untreated) and 1 µm (treated).

Under such circumstances, the efficiency of the cellular antioxidant mechanisms is reduced, resulting in mitochondrial dysfunction and DNA damage (Yu et al., 2014). Therefore, we evaluated the role of oxidative stress in cytotoxicity mediated by CD-Ag@ZnO NC using a DCFH-DA dye based assay. This assay is based on the passive uptake of the non-fluorescent DCFH-DA dye, which reacts with the ROS inside the cells and is subsequently converted to highly fluorescent DCFH by the action of intracellular esterases. The ROS levels were quantified by determining the percentage of fluorescent cells using a flow cytometer **(Fig. 7.14)**. The fluorescent signal of the CDs showed little interference with the fluorescence signal of DCF during the flow measurements as a result of the relatively weak brightness of the CDs compared with DCF. From these results it was clear that the CD-Ag@ZnO NC treated cells showed more ROS production than the untreated cells. For the MCF-7 treated cells, the percentage of cells with elevated ROS increased from 14.4 to 47.6 % with an increase in the concentration of NC **(Fig. 7.14 a-d)**. The treated A549 cells also showed increased generation of ROS in a dose-dependent manner from 5.3 to 28 % **(Fig. 7.14 e-h)**. At similar treatment concentrations, intracellular ROS production was increased in the MCF-7 cells compared with the A549 cells. For comparison, we also determined the percentage induction of ROS in cancer cells treated with Ag@ZnO at identical concentrations. The intracellular ROS production increased from 24.1 to 81.6 % for the MCF-7 cells and 14.7 to 69.4 % in the A549 cells, respectively **(Fig. 7.15)**, which is much higher than in the CD-Ag@ZnO treated cancer cells. The dissolution of Ag@ZnO and CD-Ag@ZnO NC in DMEM cell culture medium was analysed by AAS (Fig. 7.16). Ag@ZnO released more Ag^{+} and Zn^{2+} ions than CD-Ag@ZnO NC at all lengths of time (3, 6 and 12 h) and at all concentrations (20, 50 and 70 ppm). Nevertheless, the concentrations of ions released from the NC have been implicated in the production of ROS (Hsiao et al., 2011 and Turney et al., 2012). Comparatively lower ROS production in CD-Ag@ZnO NC treated cancer cells was perhaps a result of the lower release rate of Ag^{+} and Zn^{2+} ions from Ag@ZnO cores. All these findings correlate perfectly with the cytotoxicity and cellular uptake studies, in which the MCF-7 cells were found to be more sensitive than the A549 cells under similar treatment regimens. Based on these outcomes, it was favourable to use MCF-7 cells to explain the apoptotic gene expression in cells exposed to CD-Ag@ZnO NC with reference to untreated cells. In this regard, semi-quantitative RT-PCR was used to analyse the levels of expression of pro-apoptotic genes (p53, caspase 3, bax, bad and c-myc), anti-apoptotic genes (bcl-2, bcl-xl) and the housekeeping gene β-actin in MCF-7 cells.

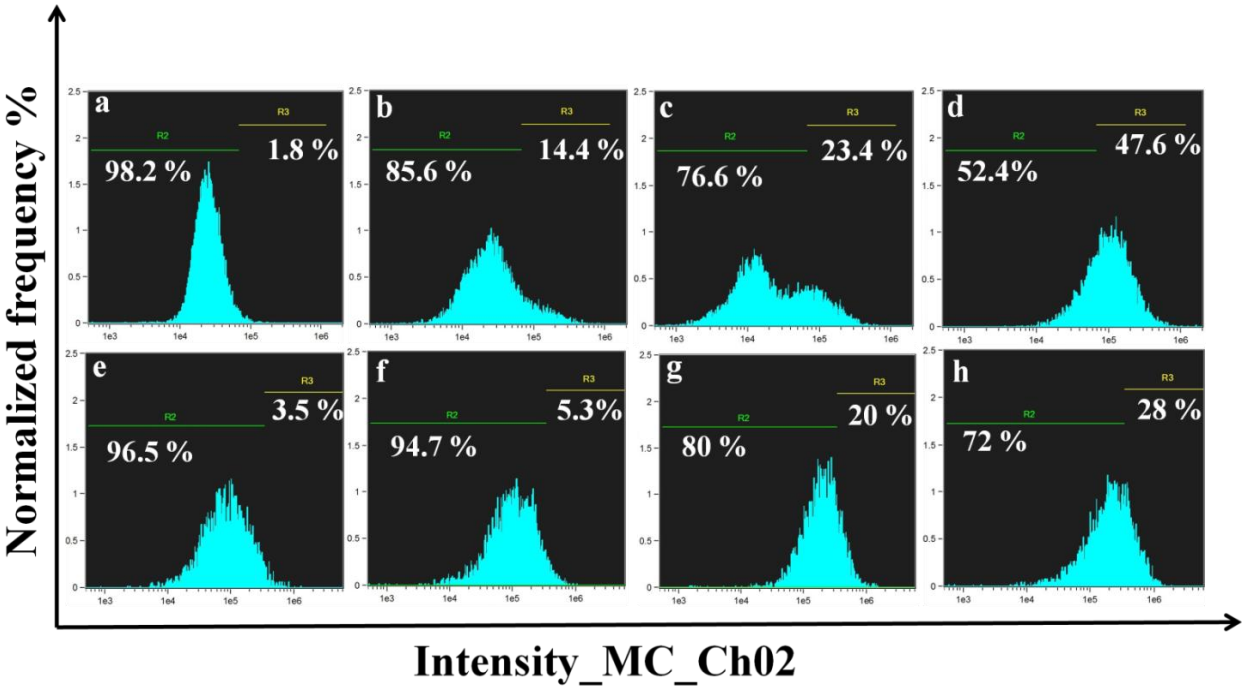

Figure 7.14 Flow cytometeric analysis of ROS production in MCF-7 and A549 cells. Upper panel: (a) untreated and (b) 20 µg mL^{-1}, (c) 50 µg mL^{-1}, (d) 70 µg mL^{-1} CD-Ag@ZnO NC treated MCF-7 cells. Lower panel: (e) untreated and (f) 20 µg mL^{-1}, (g) 50 µg mL^{-1}, (h) 70 µg mL^{-1} CD-Ag@ZnO NC treated A549 cells.

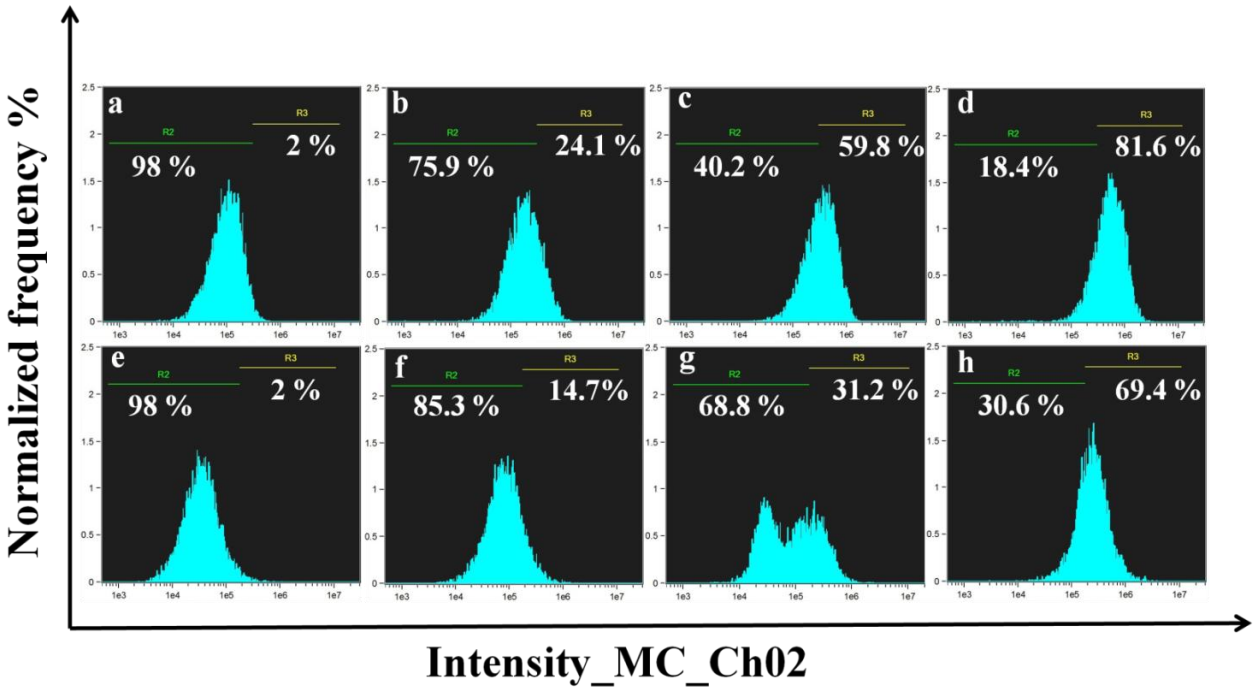

Figure 7.15 Flow cytometeric analysis of ROS production in MCF-7 and A549 cells. Upper panel: (a) untreated and (b) 20 µg mL^{-1}, (c) 50 µg mL^{-1}, (d) 70 µg mL^{-1} Ag@ZnO treated MCF-7 cells. Lower panel: (e) untreated and (f) 20 µg mL^{-1}, (g) 50 µg mL^{-1}, (h) 70 µg mL^{-1} Ag@ZnO treated A549 cells.

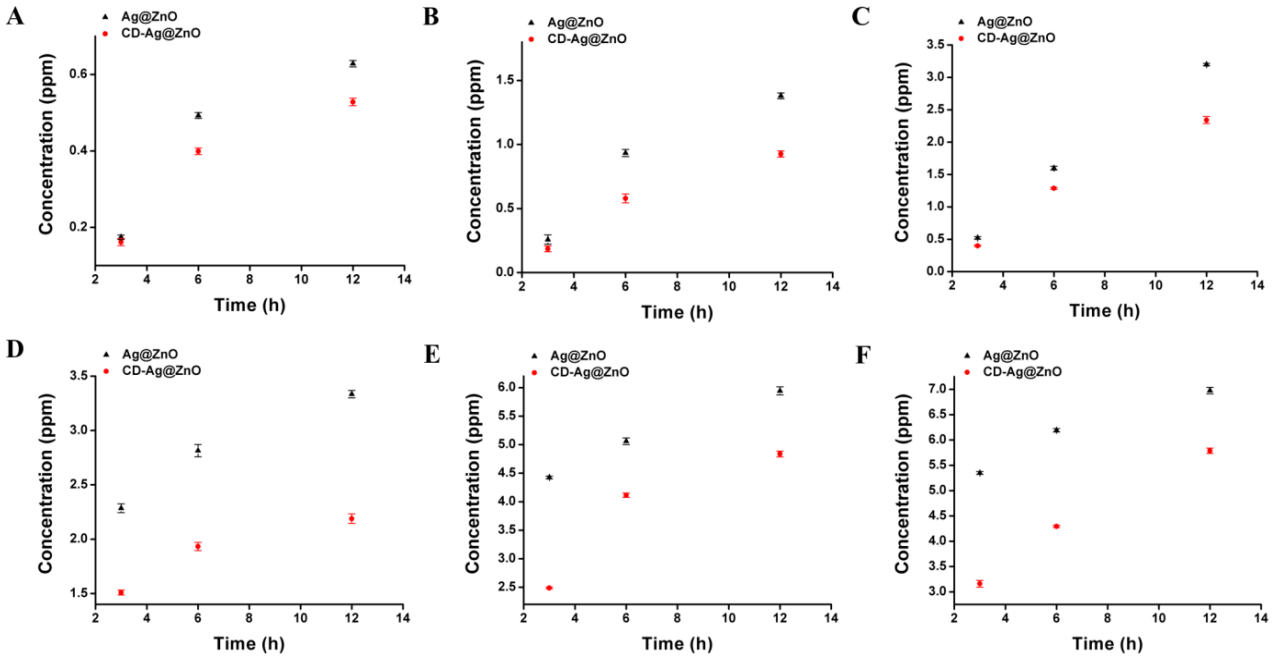

Figure 7.16 AAS analyses of silver (A-C) and zinc (D-F) ions released from Ag@ZnO and CD-Ag@ZnO NC after 3, 6, and 12 h in DMEM. Particle suspension: (A,D) 20 ppm; (B,E) 50 ppm; (C,F) 70 ppm.

The results indicated up-regulation of p53, caspase 3, bax, bad and c-myc genes (indicated by upward arrow) and down-regulation of the bcl-2 and bcl-xl genes (indicated by downward arrow) in treated cells compared with untreated cells **(Fig. 7.17 (A) and (B))**. The expression of β-actin remained the same. It is already known that the bcl-2 (B-cell lymphoma 2) family controls mitochondrial outer membrane permeabilization and could lead to pro-apoptotic (bax, bad) or anti-apoptotic effects (bcl-2, bcl-xl) by altering the inner mitochondrial membrane permeability transition pore. The anti-apoptotic potential of bcl-xl (basal cell lymphoma-extra large) prevents the cell from entering into p53-mediated apoptosis. Further, the destabilization of the mitochondrial membrane by cytotoxic agents has been associated with caspase activation (Chao et al., 1998). Up-regulation of the p53 gene was observed, which indicated the start of the p53-mediated apoptotic pathway. Up-regulation of bax and bad, together with the down-regulation of bcl-2 and bcl-xl expression, was also observed in cells treated with CD-Ag@ZnO NC, which made the outer mitochondrial membrane more permeable. In addition, p53 is known to up-regulate bax, which is translocated to the mitochondria and changes its membrane permeability (Wolter et al., 1997). This allows the secretion of cytochrome c into the cytosol, leading to up-regulation of caspase 3 in treated cells, as observed here (Yang et al., 1997 and Kluck et al., 1997).

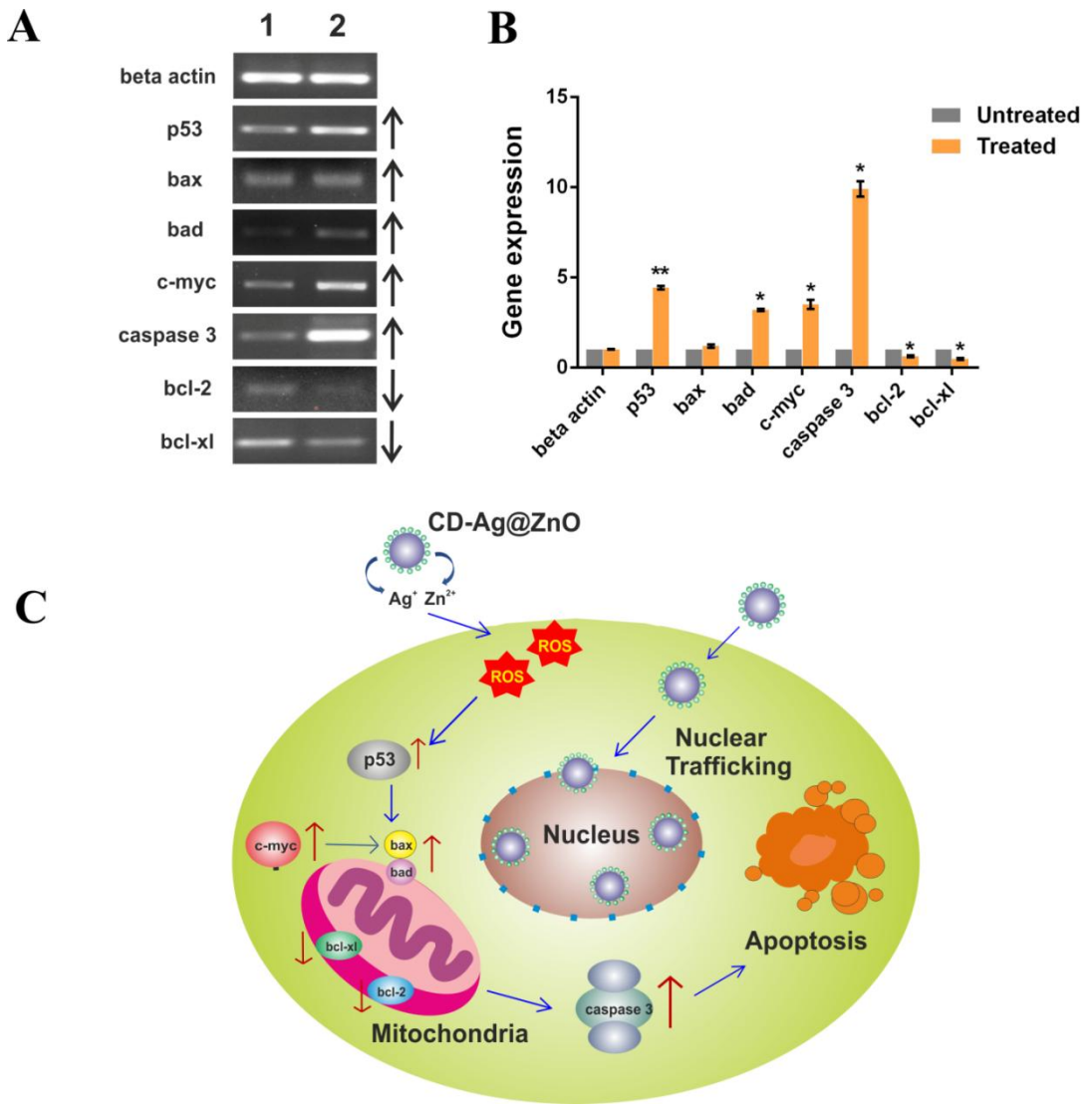

Figure 7.17 (A) Semi-quantitative RT-PCR analysis of apoptotic signalling genes. Lane 1 and 2: untreated and CD-Ag@ZnO NC treated MCF-7 cells (50 µg mL^{-1}) respectively. (B) Fold difference in gene expression in treated MCF-7 cells as compared to untreated MCF-7 cells. Data is represented as mean ± SD of two individual experiments. Statistical significance between groups is denoted by * *($p < 0.05$)* and ** *($p < 0.001$)*. (C) Schematic illustration of cellular uptake and apoptosis induction by CD-Ag@ZnO NC.

These observations corroborate well with previous reports (Gopinath et al., 2010, Sanpui et al., 2011, Akhtar et al., 2012, Sharma et al., 2012 and Wahab et al., 2014). In succession, the up-regulation of c-myc, a pro-apoptotic gene, was also seen, which in turn plays a significant part in down-regulating the anti-apoptotic genes bcl-2 and bcl-xl. This is evident by the increase in expression of c-myc, together with the decrease in expression of the bcl-2 and bcl-xl genes. Overall the sequence of events leading to apoptosis in CD-Ag@ZnO NC treated cells was illustrated. First, the NC attached and damaged the integrity of the cell membrane. On cellular uptake, the NC induced oxidative stress by evoking ROS and triggered the p53-mediated apoptotic pathway through which most of the chemotherapeutic drugs induce apoptosis **(Fig. 7.17 (C))**.

In summary, a dual-functional CD-Ag@ZnO NC was synthesized for simultaneous evaluation of cellular uptake and apoptosis induction. CD-Ag@ZnO NC exhibited enhanced antiproliferative effects against MCF-7 breast cancer cells compared to A549 lung cancer cells in a dose-dependent manner. Despite this potency, the CD-Ag@ZnO NC was less cytotoxic to normal lung L-132 cells than cancer cells in the same concentration range. Green fluorescence emission of CDs in CD-Ag@ZnO NC aided in tracking the intracellular distribution as well as in distinguishing between non-apoptotic and apoptotic cells under fluorescence microscopy based on the fluorescence staining pattern. Quantitative cellular uptake analysis of CD-Ag@ZnO NC indicated the accumulation of Ag^{+} and Zn^{2+} inside the cells in a concentration dependent manner. Subsequently, a detailed apoptotic mechanism was elucidated upon induction of CD-Ag@ZnO NC.

CHAPTER 8

Formulation of C-dots Integrated Polymeric Hydrogels as a Nanocarrier for Delivery of Chemotherapeutic drug for Cancer Theranostic Applications

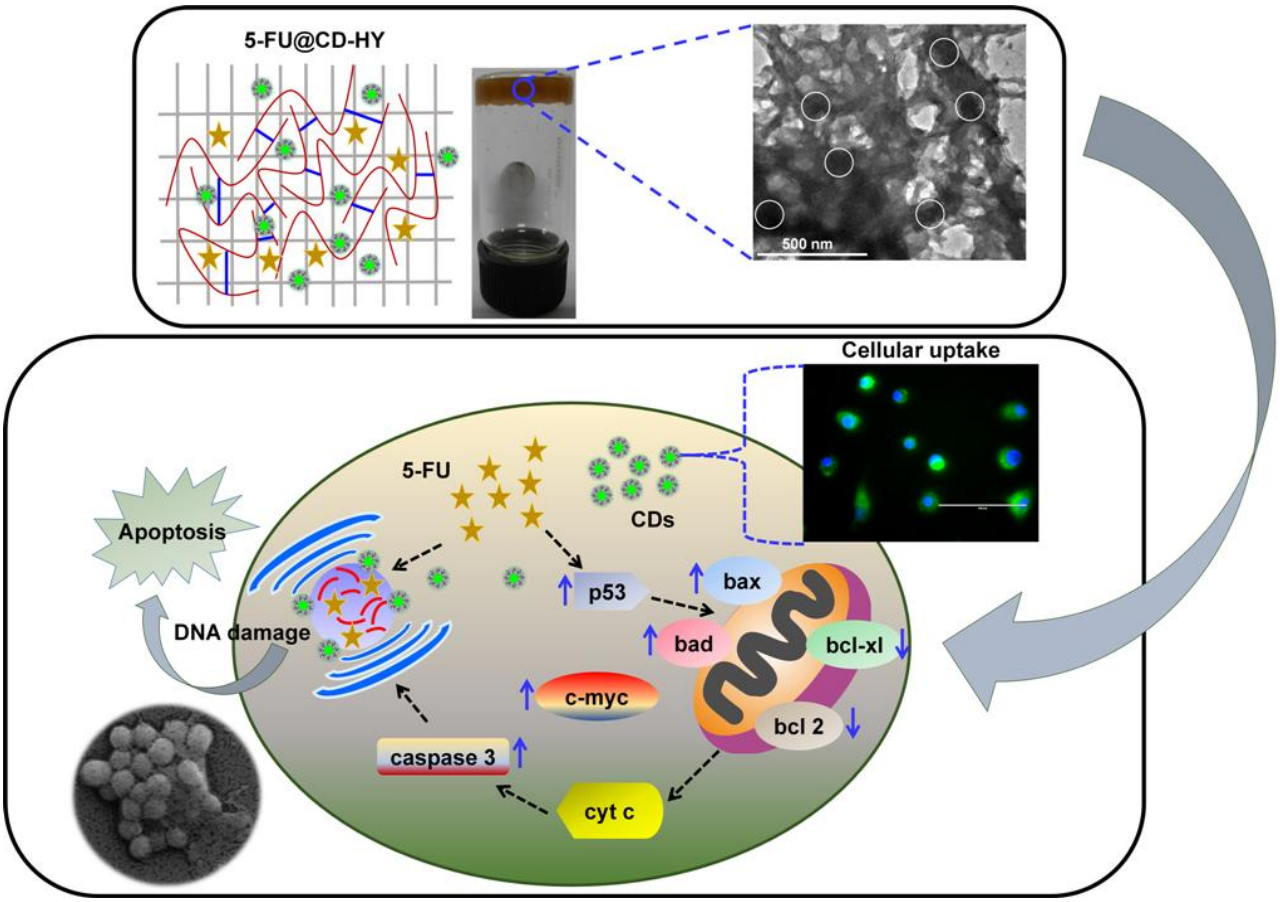

CHAPTER 8

FORMULATION OF C-DOTS INTEGRATED POLYMERIC HYDROGELS AS A NANOCARRIER FOR DELIVERY OF CHEMOTHERAPEUTIC DRUG FOR CANCER THERANOSTIC APPLICATIONS

8.1 Overview

Design and synthesis of polymeric nanocarriers with imaging and therapeutic modalities has been of prime significance for cancer nanotheranostics, circumventing the drawbacks associated with conventional cancer diagnosis and treatment (Janib et al., 2010 and Gopinath et al., 2015). In this context, hydrogels could also serve as an ideal system for simultaneous loading of imaging agents and anticancer drugs (Goncalves et al., 2014 and Li et al., 2015a). Chitosan-based hydrogels have been explored as anticancer drug delivery carriers due to their inherent properties of stimuli responsiveness, biocompatibility and biodegradability (Shu et al., 2001, Kumar et al., 2004 and Zhou et al., 2015). Over the past decade, C-dots have been the subject of intense research for bioimaging applications. An important parameter that influences the practicality of C-dots as bioimaging agents in multifunctional systems is their stability in composite form. Recent reports highlight the possibility of combining C-dots with metal nanocomposites as well as polymeric nanocarriers without compromising their fluorescence (Wang et al., 2013a, Liu et al., 2012a, Matai et al., 2015 and Sachdev et al., 2015b). This strategy provides new avenues for designing similar multifunctional platforms and opens a new area for the application of C-dots. There have been quite a few reports on the incorporation of C-dots in hydrogels for various bio-medical applications (Huang et al., 2013a, Gogoi et al., 2015 and Konwar et al., 2015). Conversely, the approach to combine C-dots based chitosan hydrogels with chemotherapeutic drugs for cancer theranostics is yet to be explored. A proficient approach involving chitosan-PEI combination has been followed for producing green fluorescent C-dots in a single step. Moreover, the model chemotherapeutic drug, 5-Fluorouracil (5-FU) used in the study has been proven effective against a variety of cancers including skin,

colorectal, liver, breast, pancreatic and lung cancers with a known mechanism of action. Following the above line of thoughts, herein multifunctional chitosan hydrogels synthesized by ionic cross-linking reactions have been reported. Creation of such formulations involves the inclusion of pre synthesized C-dots and 5-FU to form a dual-functional hybrid assembly (5-FU@CD-HY). In order to attain higher loading capacities, CDs and 5-FU were added during the formation of hydrogels. In the ensuing work, non-covalent pathway pursued for fostering the hybrid assembly has several benefits: (i) ionic interactions mediated integration of CDs with the ability to retain fluorescence properties, (ii) physical entrapment utilizing hydrophobic interactions for loading of 5-FU without any loss of activity inside hydrogel matrices and (iii) robust hybrid materials for biological applications (*vide infra*) (Yokoyama et al., 1998 and Datta et al., 2014). As a proof of concept, *in vitro* evaluation of bioimaging and therapeutic potential of 5-FU@CD-HY was done on A549 (human lung adenocarcinoma) cells. The purpose of incorporating CDs was, on one hand, to evaluate the cellular uptake of 5-FU@CD-HY and, on the other hand, to furnish the morphological changes induced by the action of 5-FU. To the best of our knowledge, this is the first instance where the CDs based hydrogel formulations have been used for cellular examinations in cancer cells. Finally, apoptosis evoking ability of released 5-FU was elucidated by carrying out various biochemical, morphological and molecular studies. Hence, this work envisions 5-FU@CD-HY as a versatile means for synchronized bioimaging and controlled drug release in cancer theranostic applications.

8.2 RESULTS AND DISCUSSION

8.2.1 Synthesis and characterization

Chitosan hydrogel (HY) was synthesized by cross-linking chitosan polymeric chains with glycerol. C-dots were synthesized by hydrothermal carbonization of chitosan, using polyethyleneimine (PEI) as an amine passivating agent which is known to effectively enhance the fluorescence properties (Sachdev et al., 2014). CD-HY preparation involves blending of C-dots with chitosan–glycerol solution. This method is based on ionic interaction and hydrogen bonding between amino groups of chitosan and C-dots with hydroxyl groups of glycerol, followed by the precipitation with NaOH. In a similar manner, 5-FU was encapsulated inside CD-HY matrices through hydrophobic interactions to forge 5-FU@CD-HY formulation. Step-wise sequence of events leading to the formation of 5-FU@CD-HY has been pictorially represented in **Figure 8.0**. UV–vis absorption spectra of HY did not display any peak in the region 200-700 nm, while CD-HY depicted characteristic peaks of CDs at 273 and 343 nm (marked by arrows in **Fig. 8.1 (A)**) in the same absorption range. For 5-FU@CD-HY, the

absorption peak shifted to 263 nm, while the peak at 343 nm remained unchanged. The observed peak shift along with absorption enhancement for 5-FU@CD-HY was due to the interaction between the components of hydrogel (5-FU and CDs). The inset in **Fig. 8.1 (A)** shows the photograph of blank HY (white) and 5-FU@CD-HY (brown) in hydrated form. The transition in colour suggests the inclusion of CDs in the hydrogels. A key aspect to be considered is the incorporation of CDs with intact fluorescence properties in the hydrogel. To investigate the same, fluorescence emission spectrum of CD-HY and 5-FU@CD-HY was recorded **(Fig. 8.1 (B))**. Both the formulations had an emission maximum at 450 nm upon 360 nm excitation wavelength, thereby demonstrating optical property similar to free CDs, as reported previously (Sachdev et al., 2014). However, the fluorescence intensity decreased slightly upon the addition of 5-FU in 5-FU@CD-HY which was primarily due to charge transfer processes between functional groups of 5-FU and CDs (Jin et al., 2013a and Khan et al., 2015b). Eventually, the digital image of hydrated 5-FU@CD-HY exhibits bright green fluorescence upon irradiation with UV light, which also substantiates the stability of CDs in solid form **(inset in Fig. 8.1 (B))**. Internal structure of freeze-dried 5-FU@CD-HY was examined by FE-SEM micrograph **(Fig. 8.2 (A))**. The cross-sectional view revealed irregular, highly porous and interconnected networks, typical of hydrogels. CDs were too small to be visualized by FE-SEM. The existence of CDs in matrices of 5-FU@CDHY could be clearly discerned by TEM micrographs, wherein many dark tiny domains of CDs generated a clear contrast with the relatively gray hydrogel matrix **(Fig. 8.2 (B))**. A high-resolution TEM image further depicts uniform distribution of CDs within the hydrogel matrix **(Fig. 8.2 (C))**. The average hydrodynamic diameter of HY was 229 nm, whereas the same for CD-HY was found to be 287 nm. With the addition of 5-FU to CD-HY, the size of 5-FU@CD-HY further increased to 382 nm, thereby suggesting the entrapment of 5-FU drug molecules **(Fig. 8.2 (D))**. Further, EDAX analysis confirmed the presence of distinctive element pertaining to 5-FU (fluorine) in 5-FU@CD-HY **(Fig. 8.3)**. FTIR spectroscopy was performed for studying the formation of HY and 5-FU@CD-HY **(Fig. 8.4 (A))**. Characteristic peaks of chitosan at 3437, 1644 and 1580 cm^{-1} represented O-H absorption band, amide I (C=O) stretching vibration and amide II (N-H) bending vibration. Other significant peaks in the chitosan spectra at 1412 and 1321 cm^{-1} corresponded to C-H vibrations, while peak at 1269 cm^{-1} was due to C-N bond stretching.

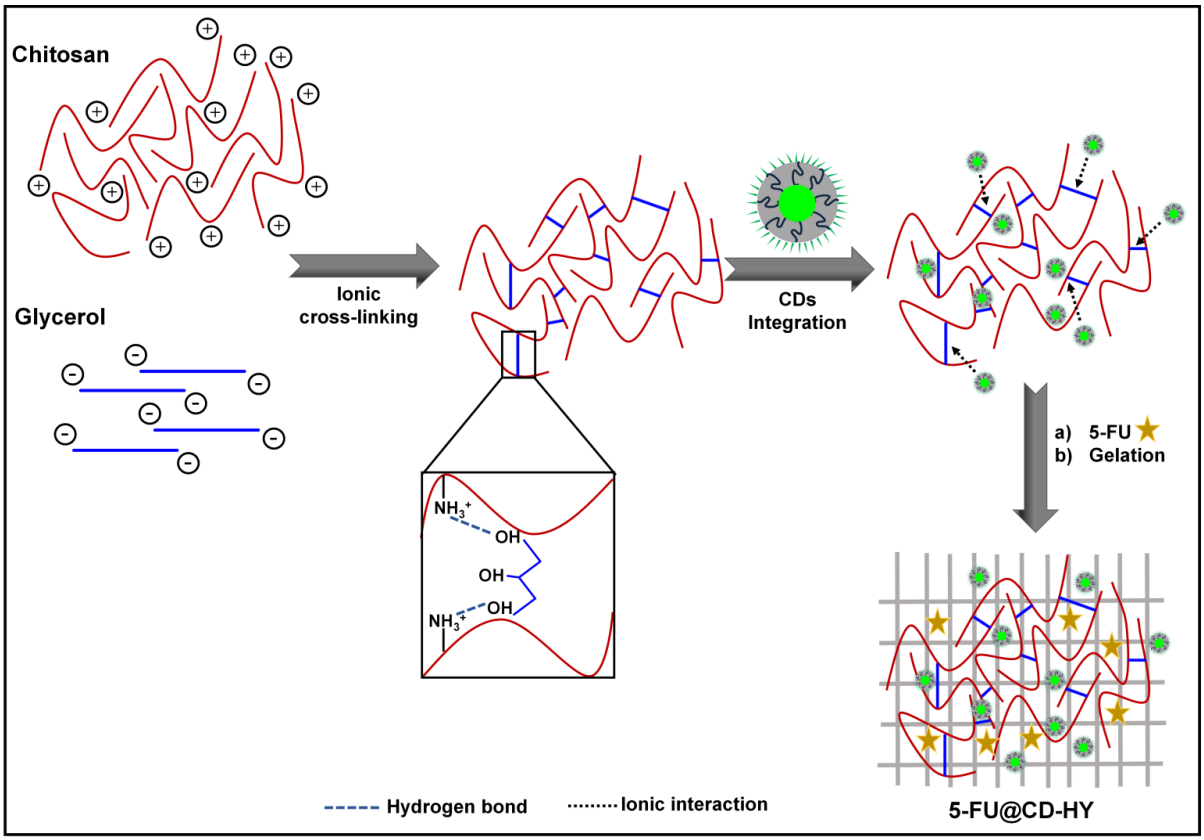

Figure 8.0 Schematic illustration for synthesis of 5-FU@CD-HY.

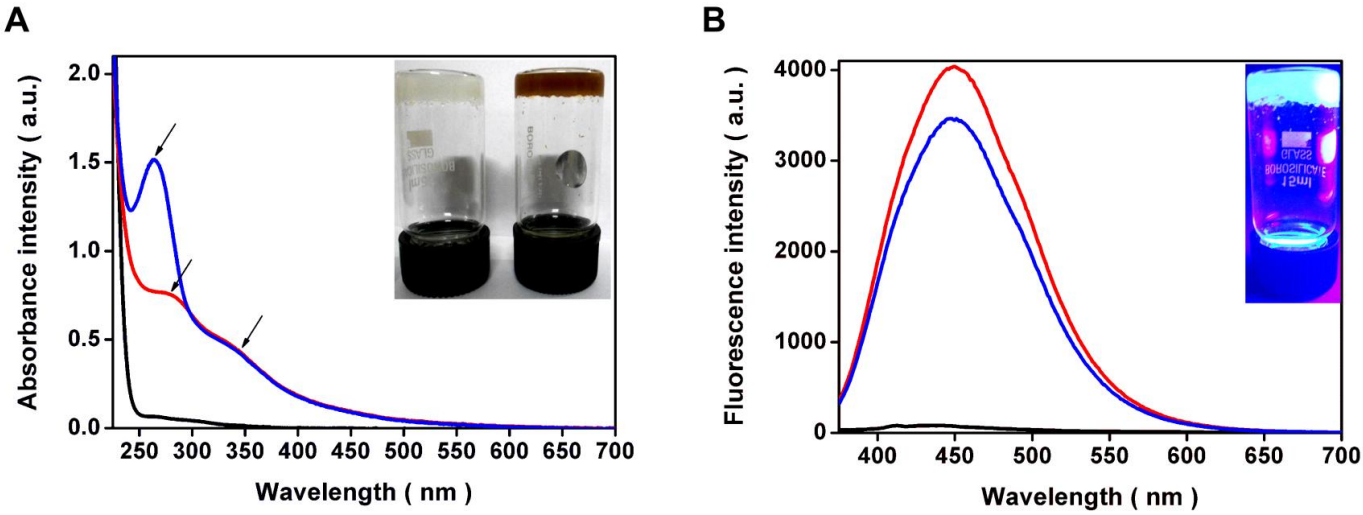

Figure 8.1 (A) UV-vis absorption spectra and (B) Fluorescence emission spectra of HY (black), CD-HY (red) and 5-FU@CD-HY (blue). Insets in Fig. 1(A) are the photographs of HY (left) and 5-FU@CD-HY (right) under daylight. Inset in Fig. 1(B) shows fluorescent 5-FU@CD-HY under UV light.

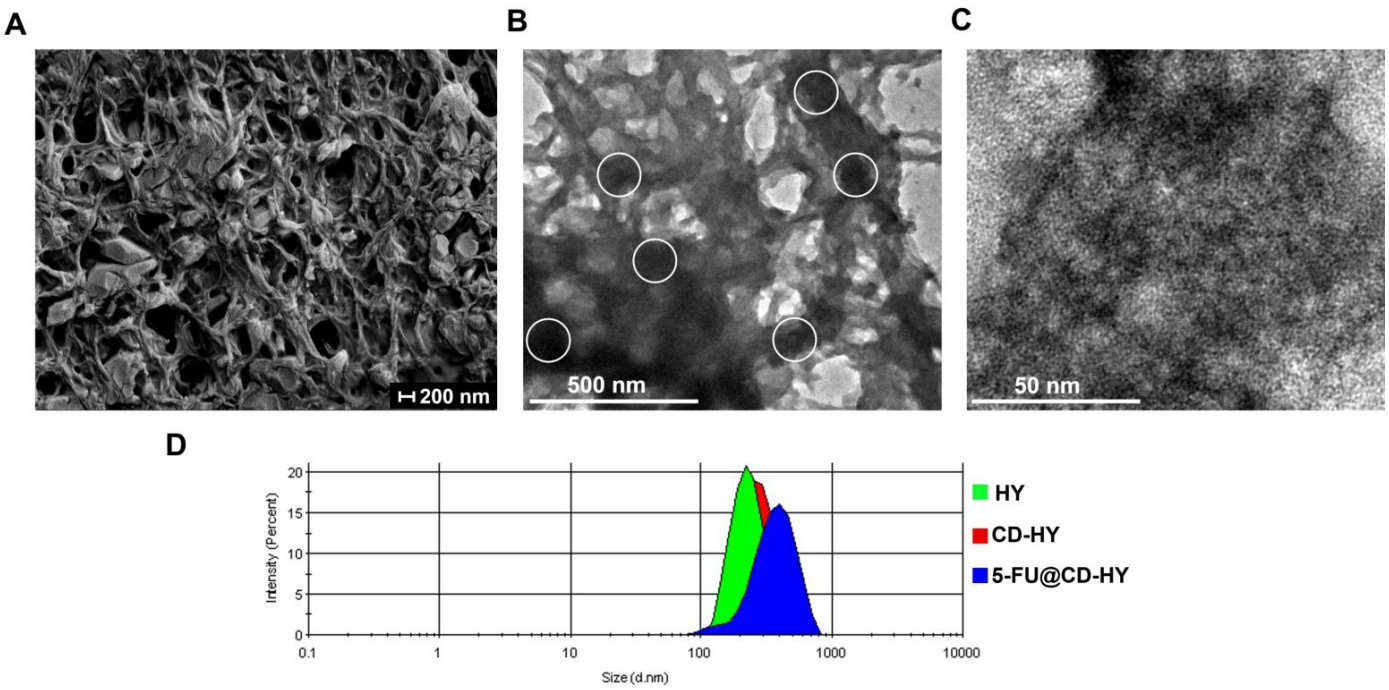

Figure 8.2 (A) FE-SEM (B) TEM (C) High resolution TEM image of freeze-dried 5-FU@CD-HY. (D) DLS based size distribution by intensity spectrum of HY, CD-HY and 5-FU@CD-HY.

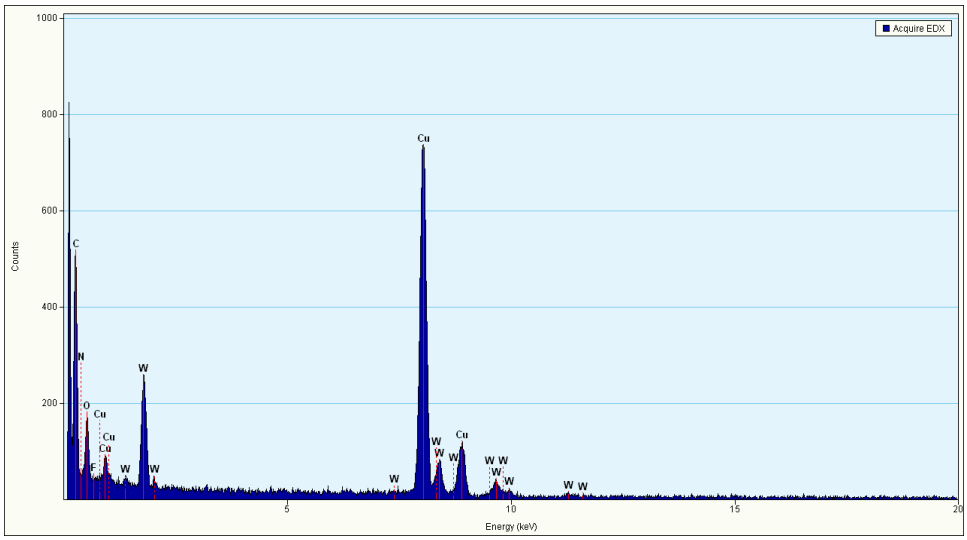

Figure 8.3 EDAX spectrum of 5-FU@CD-HY.

Additionally, small peaks at 1085 and 1015 cm^{-1} could be assigned to C-O stretching vibration. In case of HY, the characteristic peak at 1580 cm^{-1} in chitosan spectra was red-shifted to 1564 cm^{-1}, while the peak at 1269 cm^{-1} disappeared due to strong ionic interaction between N-H groups of chitosan and O-H groups of glycerol (Lawrie et al., 2007, Li et al., 2011b and Nagarwal et al., 2011). Furthermore, the peaks at 1412 and 1321 cm^{-1} became sharp and intense, which indicated increased interaction among chitosan monomers in the hydrogel networks. A relative increase in stretching vibration of C-O groups in HY was seen due to the cross-linking reaction. With regard to 5-FU@CD-HY, some additional peaks of 5-FU at 1280 (C-F), 1258 and 1221 cm^{-1} (aromatic ring structure), 759 cm^{-1} (CF=CH) were apparent which confirmed the encapsulation of 5-FU. In the present case, slight peak shift was seen for CF=CH bond in 5-FU due to effective interactions between 5-FU and hydrogel matrices, which is also supported by previous reports (Li et al., 2011b and Nagarwal et al., 2011). Moreover, in case of HY and 5-FU@CD-HY widening of peak at 3437 cm^{-1} was observed compared to chitosan owing to hydrogen bonding between chitosan, glycerol and CDs (Konwar etal., 2015). Changes in thermal stability of hydrogel formulations with the addition of 5-FU and CDs were studied by TGA **(Fig. 8.4 (B))**. Thermograms of HY, CD-HY and 5-FU@CD-HY showed negligible difference in the degradation pattern upto 100 °C. CD-HY and 5-FU@CD-HY followed multiple degradation steps along with higher weight depletion rates beyond 250 °C compared to HY. Consequently, beyond 400 °C significant difference in degradation profiles of the samples was documented. At 550 °C, about 53 % weight loss was observed for HY, which increased to 68 % and 69 % in case of 5-FU@CD-HY and CD-HY, respectively. Such lowering of thermal stability can be owed to integration of CDs and 5-FU and its interference with the hydrogel matrix formation. Zeta potential measurements were conducted to elucidate the surface charge and interactions among the components of 5-FU@CD-HY **(Fig. 8.5)**. Zeta potential of HY and CD-HY was found to be +45.2 and +39.3 mV, respectively. Due to anionic nature of 5-FU, zeta potential of 5-FU@CD-HY decreased (+34.9 mV) indicating encapsulation of 5-FU. Evidently, electrostatic interactions between 5-FU and chitosan chains as well as physical entrapment effect were the driving force for the loading of drug inside 5-FU@CD-HY during the gelation process (Zhu et al., 2013a). The amount of 5-FU in 5-FU@CD-HY was determined by concentration-absorption curve of 5-FU. Further, the encapsulation efficiency of 5-FU@CD-HY was estimated to be 54.56 ± 2.03 %. Swelling studies were performed to examine the water absorption and cross-linking density in hydrogel formulations (Ruiz et al., 2001 and Peng et al., 2007). From these experiments, % degree of swelling (w/w) for HY, CD-HY and 5-FU@CD-HY was estimated to be 30, 47 and 49 %, respectively.

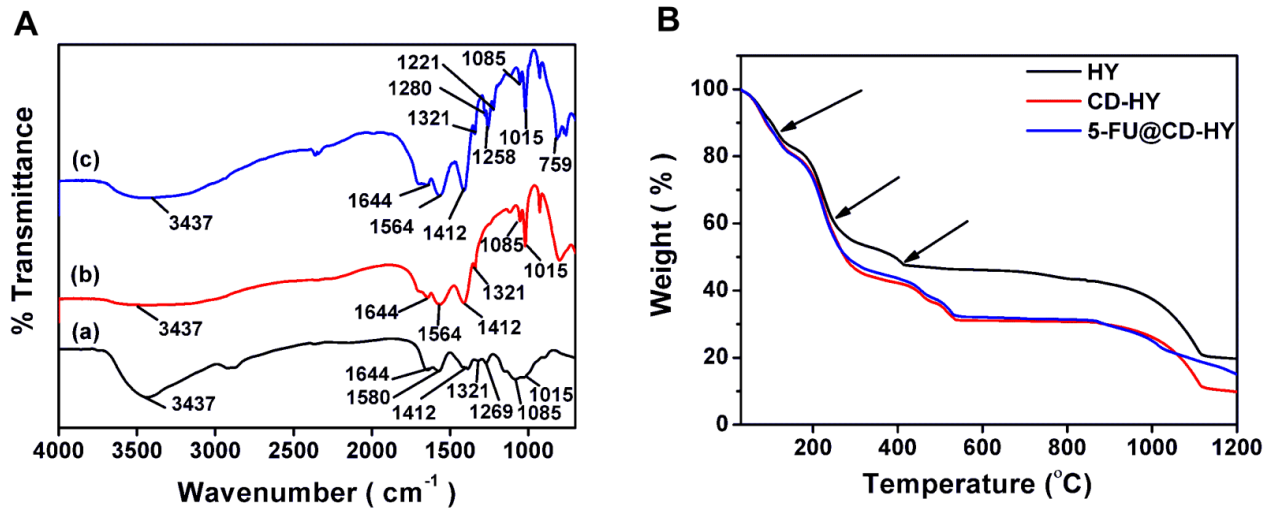

Figure 8.4 (A) Comparison of FTIR spectrum of (a) Chitosan, (b) HY and (c) 5-FU@CD-HY. (B) TG analysis of hydrogel formulations.

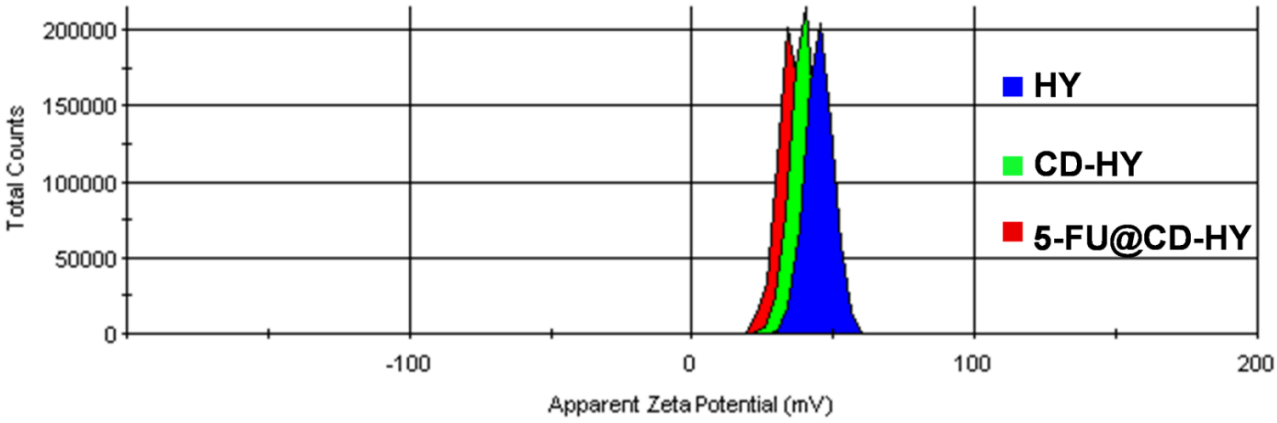

Figure 8.5 Zeta potential determination of various hydrogel formulations.

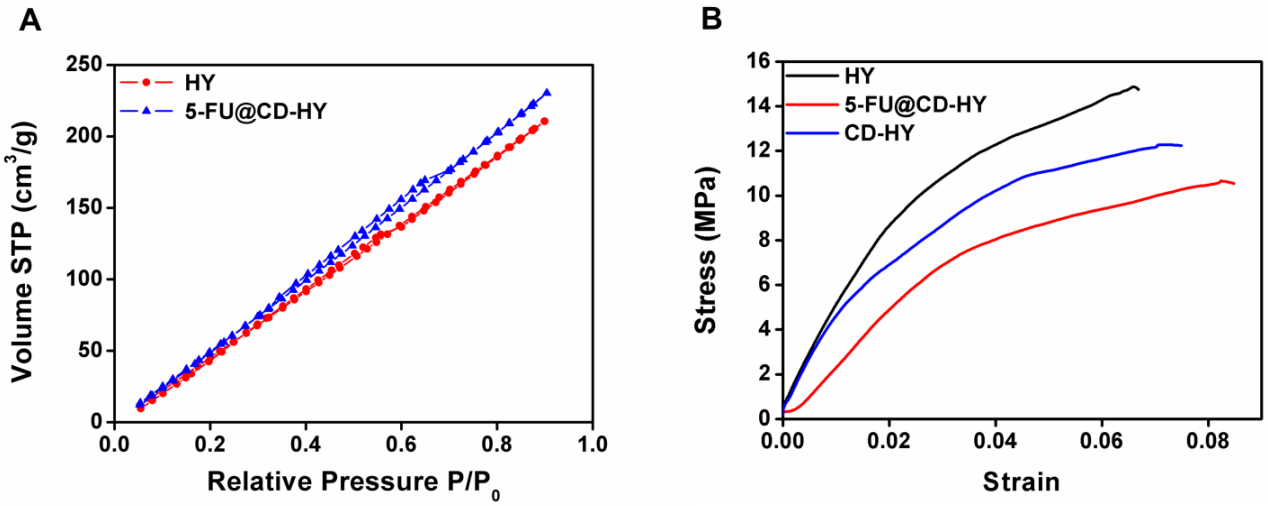

Figure 8.6 (A) N_2 adsorption-desorption isotherms (B) Tensile testing curves of hydrogel formulations, as labelled.

Generally, an increase in degree of polymer cross-linking results in a rigid, less porous structure due to which the swelling decreases (Xing et al., 2014 and Kumar et al., 2014). Likewise, increased swelling in case of CD-HY and 5-FU@CD-HY was attributed to decrease in degree of cross-linking due to the presence of CDs and 5-FU. Alternatively, optimum degree of cross-linking in HY lead to minimal water uptake. N_2 adsorption–desorption isotherms were recorded to establish the porous nature of hydrogels **(Fig. 8.6 (A))**. Compared to HY, the adsorbed volume of N_2 increased in case of 5-FU@CD-HY. Calculations based on the isotherms using the BET method were used for the determination of specific surface area and pore volume **(Table 8.1)**. Increase in surface area (182.55 $m^2\ g^{-1}$) and pore volume (0.07581 $cm^3\ g^{-1}$) was observed upon the integration of CDs and 5-FU. Thus, BET analysis predicted that 5-FU@CD-HY had more porosity compared to HY. This difference can be ascribed to the formation of lesser cross-links between chitosan chains during gelation due to the introduction of 5-FU and CDs. The above observations corroborates well with the swelling studies.

Mechanical stability of hydrogels is one of the decisive factors in determining their applicability for biomedical purposes. Therefore, tensile tests were performed to evaluate the mechanical properties of hydrogels. Stress-strain plots for HY, CD-HY and 5-FU@CD-HY have been presented in **Fig. 8.6 (B)**. Tensile strength (TS) and percent elongation at break for the samples are summarized in **Table 8.2**. TS value of HY was calculated to be 14.86 MPa, which decreased upon the successive addition of payload (CDs and 5-FU) to the hydrogel. Lower cross-linking density in CD–HY and 5-FU@CD-HY resulted in reduced tensile strength as well as stiffness. The change in mechanical strength is consistent with the swelling behaviour and TGA analysis. Conversely, the percent elongation at break value was higher for CD-HY and 5-FU@CD-HY, which is inversely correlated with the tensile strength. This trend can be understood by the stronger interactions of CDs and 5-FU with the hydrogel matrix, thereby rendering more flexibility (Xu et al., 2006).

8.2.2 *In vitro* drug release studies

An important aspect of an efficient nanocarrier is its ability to release the encapsulated drug in a sustained manner. For this end, *in vitro* release studies of 5-FU@CD-HY were performed at pH 5.5 and 7.4, respectively. **Fig. 8.7** depicts time-dependent release profiles of 5-FU in a biphasic manner, exemplified by an initial burst release followed by a period of sustained release. From the figure, pH dependent release of 5-FU was evident at all time points.

Sample	Surface area (m^2 g^{-1})	Pore volume (cm^3 g^{-1})
HY	168.56	0.05197
5-FU@CD-HY	182.55	0.07581

Table 8.1 Estimation of surface area and pore volume of freeze-dried hydrogels through BET method.

Sample	Tensile strength (MPa)	Elongation at break (%)
HY	14.86	6.68
CD-HY	12.27	7.46
5-FU@CD-HY	10.65	8.52

Table 8.2 Mechanical properties of hydrogel formulations.

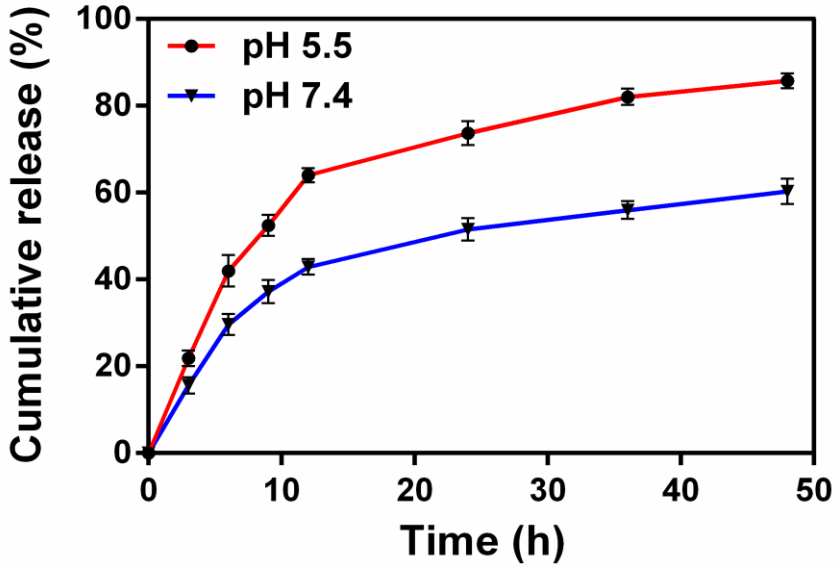

Figure 8.7 Time-dependent release profile of 5-FU from 5-FU@CD-HY. Experiments were performed at 37 °C in acetate buffer (pH 5.5) and phosphate buffer saline (pH 7.4).

Cumulative release rate of 5-FU increased from 60 % at pH 7.4 to about 85 % at pH 5.5 within 48 h. Acceleration of drug release under acidic conditions could be due to the weakening of interactions between 5-FU and hydrogel, owing to ionization of chitosan chains at low pH (Li et al., 2009 and Duan et al., 2011). In addition, other parameters like pH dependent swelling, cross-linking density and porosity of hydrogels can modulate the release of the drug under various conditions (Peppas et al., 2000a and Berger et al., 2004). Slow release of 5-FU at physiological conditions (pH 7.4) compared to acidic environment is advantageous since tumor cells have an acidic microenvironment. Hence, these hydrogels can be considered apposite candidates for anticancer drug delivery.

8.2.3 MTT Assay

To evaluate the utility of hydrogels as effective drug carriers, cell viability studies based on MTT assay were performed along with appropriate controls. Different formulations of hydrogels carrying different amounts of 5-FU and CDs were evaluated **(Fig. 8.8 (A))**. A549 cells treated with blank HY exhibited good cell viability at all the tested concentrations, satisfying the criteria for a biocompatible nanocarrier. On the other hand, CDs are already known to be biocompatible imaging agents, endorsed by our previous studies as well (Sachdev et al., 2014, 2015b). Similarly, CD-HY treated cells had appreciable cell viability (> 90 %) even at high concentrations of CDs. Nevertheless, with the addition of 5-FU to CD-HY a significant decline in cell viability was observed. More importantly, 5-FU@HY or 5-FU @CD-HY loaded with equivalent amount of 5-FU were able to inhibit the growth of A549 cells, with inhibition efficiency comparable to free 5-FU in a dose-dependent manner. For instance, at a 5-FU concentration of 3.2 μg mL^{-1}, cell viability reduced to almost 38 % with free 5-FU, whereas nearly equivalent cell viability (49 % and 46 %) was obtained after treatment with 5-FU@HY and 5-FU @CD-HY. With an increase in the concentration of 5-FU from 1.6 to 6.4 μg mL^{-1}, cell viability significantly decreased from 57 % to 27 % in 5-FU@CD-HY treated cells. Given the fact that HY did not affect the cell viability, the observed anti-proliferative effects were exclusively due to the loaded 5-FU drug. Essentially, the CDs did not contribute to the exhibited anti-proliferative action of 5-FU@CD-HY. Under similar treatment regime, the same set of hydrogel formulations displayed comparatively less cytotoxic effect on normal NIH3T3 cells **(Fig. 8.8 (B))**. In order to visualize the morphological changes in A549 cells upon incubation with HY, CD-HY, 5-FU@HY, 5-FU@CD-HY and free 5-FU, bright field images were taken after 48 h **(Fig. 8.9)**. Cells treated with HY, CD-HY retained a healthy morphology similar to control untreated cells (elongated spindle like shape and adhered to the matrix).

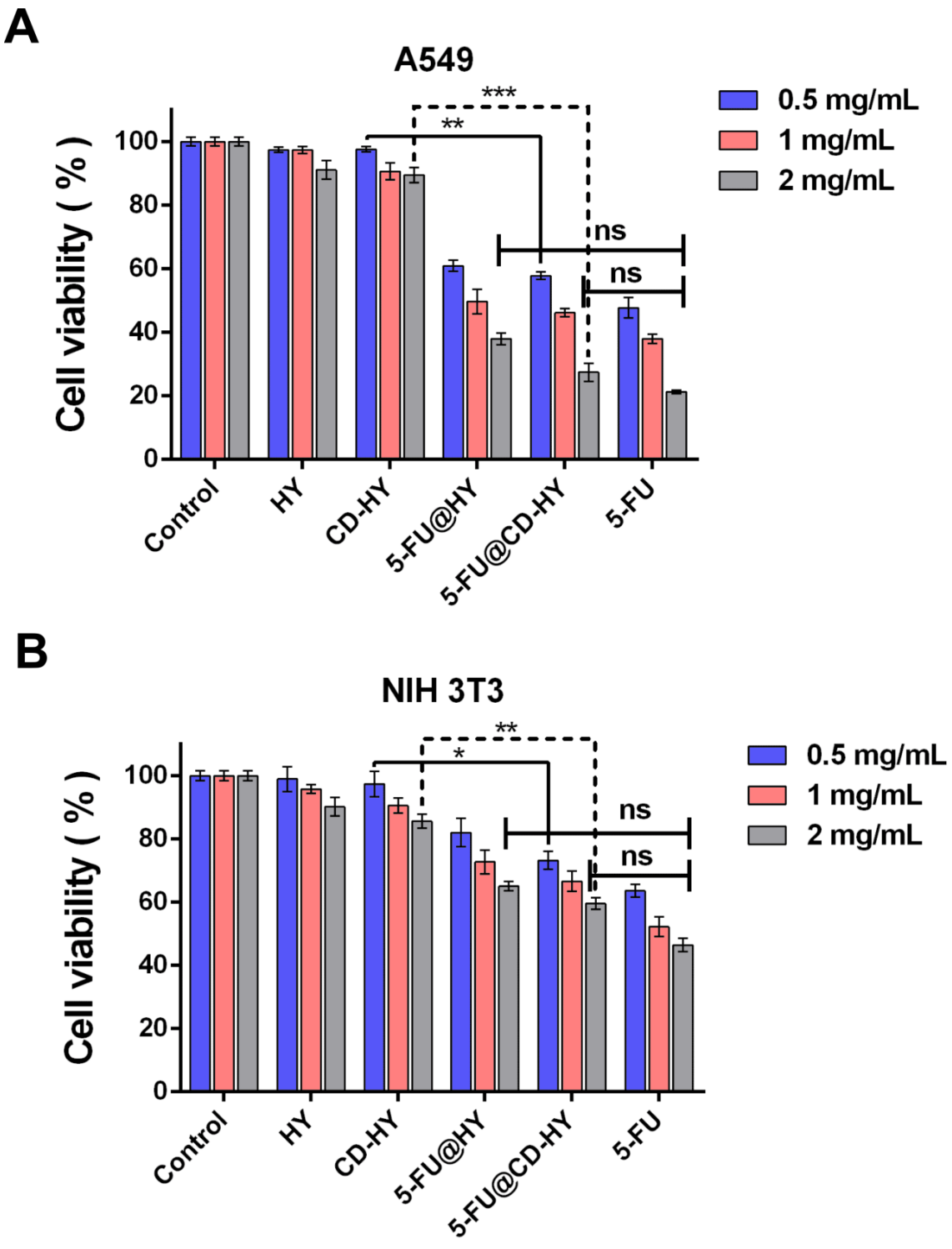

Figure 8.8 (A) Cell viability of A549 and (B) NIH3T3 cells estimated by MTT assay after 48 h treatment with HY, CD-HY, 5-FU@HY, 5-FU@CD-HY and free 5-FU. 0.5, 1 and 2 mg mL^{-1} of 5-FU@CD-HY correspond to 5-FU concentrations of 1.6, 3.2 and 6.4 µg mL^{-1}. 5-FU@HY and free 5-FU had equivalent concentrations of 5-FU. The error bars represent mean ± S.E.M. of three individual experiments. Statistical significance between various groups was denoted by *($p < 0.05$), **($p < 0.005$) and ***($p < 0.001$). Statistically insignificant data was represented by ns (non significant).

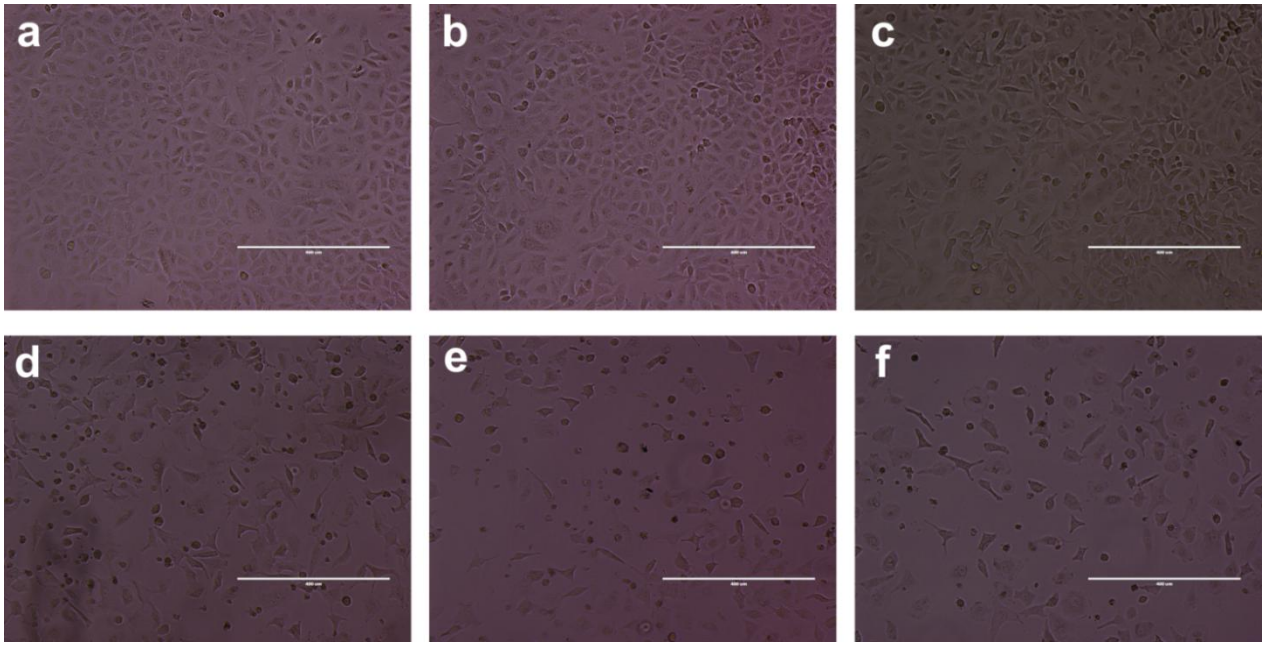

Figure 8.9 Bright field microscopic images depicting cell morphology (A549 cells) after 48 h treatment with (a) control, (b) HY, (c) CD-HY, (d) 5-FU@HY, (e) 5-FU@CD-HY and (f) 5-FU. Scale bar: 400 µm.

Contrastingly, more rounded (non-adherent) and fewer spindle like (adherent) cells existed in 5-FU@HY, 5-FU@CD-HY and free 5-FU treated cells, demonstrating similar cytotoxic effects. The cell morphological examinations are in accordance with the percentage cell viabilities estimated through MTT assay.

8.2.4 Cellular uptake

In general, a variety of fluorescent probes have been incorporated inside polymeric nanocarriers for monitoring their uptake and distribution in cells (Zhu et al., 2013a, Ghosh et al., 2015 and Matai et al., 2015). In view of this, the synthesized CDs were integrated with hydrogels (with and without 5-FU) for assessing the cellular uptake. A549 cells were incubated with different concentrations of CD-HY and 5-FU@CD-HY and their uptake was monitored qualitatively by fluorescence microscopy **(Fig. 8.10)**. Apparently, the green fluorescence (due to emission of CDs) and blue fluorescence (due to emission of Hoechst 33342) was observed in the cells for both hydrogel formulations. Increase in the green fluorescence inside the cells was seen with an increment in the concentration of CD-HY and 5-FU@CD-HY, illustrating concentration dependent effects. Usually, living cells are characterized by vacant fluorescence in the nucleus. Reduction in cell size, shift in fluorescence location from cytoplasm to nucleus and dense fluorescence of whole cells is symptomatic of apoptosis (Darzynkiewicz et al., 1997

and Liu et al., 2010). Accordingly, CD-HY treated cells did not reveal any change in the cell morphology and the fluorescence staining pattern. Green fluorescence emanating from cytoplasm further justifies their biocompatible nature of CD-HY. Differentially, 5-FU@CD-HY exhibited toxic effects which induced change in cell morphology and cell death. In these cells, cytoplasmic constriction led to lesser distribution of green fluorescence in the cytoplasm. Further, dense fluorescence in nucleus along with the observed co-localization of green and blue fluorescence (nuclear marker) suggested nuclear internalization (apoptotic cells). Hence, by tracking the fluorescence of CDs in 5-FU@CD-HY with respect to nucleus, living and apoptotic cancer cells could be distinguished. Also, the fluorescence of CDs could be used for quantitative evaluation of cellular uptake through flow cytometry. For this, A549 cells were separately incubated with CD-HY and 5-FU@CD-HY and percentage of cells expressing green fluorescence (due to CDs) with reference to control cells were determined by applying appropriate gating **(Fig. 8.11)**. Treated cells were monitored by green fluorescence in Ch02, whereas bright field and side scatter images were recorded in Ch01 and Ch06. Both CD-HY and 5-FU@CD-HY treated cells showed considerable shifts in the fluorescence intensity in Ch02 compared to untreated cells. For CD-HY, the percentage of fluorescent cells increased from 52.8 % to 94.1 % while the same increased from 55.2 % to 94.7 % in case of 5-FU@CD-HY with an increase in their concentration. This explains the equivalent uptake of CD-HY and 5-FU@CD-HY, which is in correlation with the fluorescence microscopic observation. Next, the localization of 5-FU@CD-HY in A549 cells was ascertained by using fluorescent tracer, Lysotracker red for fluorescence imaging of lysosomes. Following the uptake of 5-FU@CD-HY, green fluorescence was evident within the cells which increased in a time-dependent manner **(Fig. 8.12)**. On closer examination of the fluorescence micrographs, overlapping positions of bright green and red fluorescence spots were noticeable. The merged fluorescence microscopic images clearly suggest co-localization of 5-FU@CD-HY and lysosomes in A549 cells. These findings reveal lysosomes as the cellular target of 5-FU@CD-HY.

8.2.5 Cell cycle and apoptosis induction

Apoptosis has been one of the most widely studied mechanisms accounting for the anticancer action of 5-FU (Yoshikawa et al., 2001, Li et al., 2004, Liu et al., 2012b and Matai et al., 2015). Flow cytometry is the obvious choice for quantitative analysis of apoptosis. Thus, cell cycle analysis was pursued by staining the treated and untreated cells with PI and subsequently examined by flow cytometer.

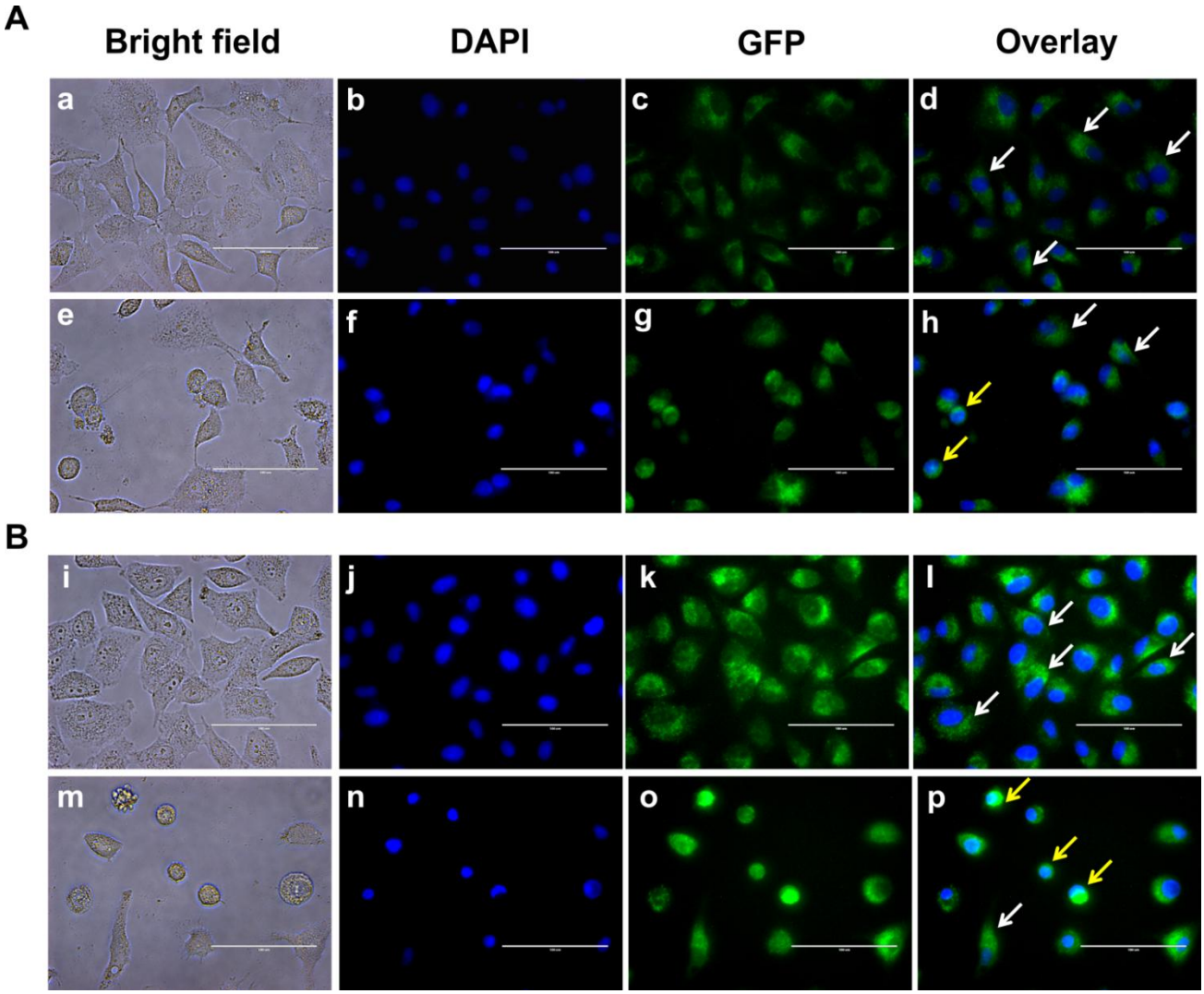

Figure 8.10 Fluorescence microscopic images of A549 cells treated with various concentrations of CD-HY and 5-FU@CD-HY after 48 h. (A) Cells treated with 0.5 mg mL^{-1} of CD-HY (a-d) and 5-FU@CD-HY (e-h).(B) Cells treated with 2 mg mL^{-1} of CD-HY (i-l) and 5-FU@CD-HY (m-p). White and yellow arrows represent live and apoptotic cells, respectively. The overlay images were generated using DAPI (for Hoechst 33342) and GFP (for CDs) filters. Scale bar: 100 µm.

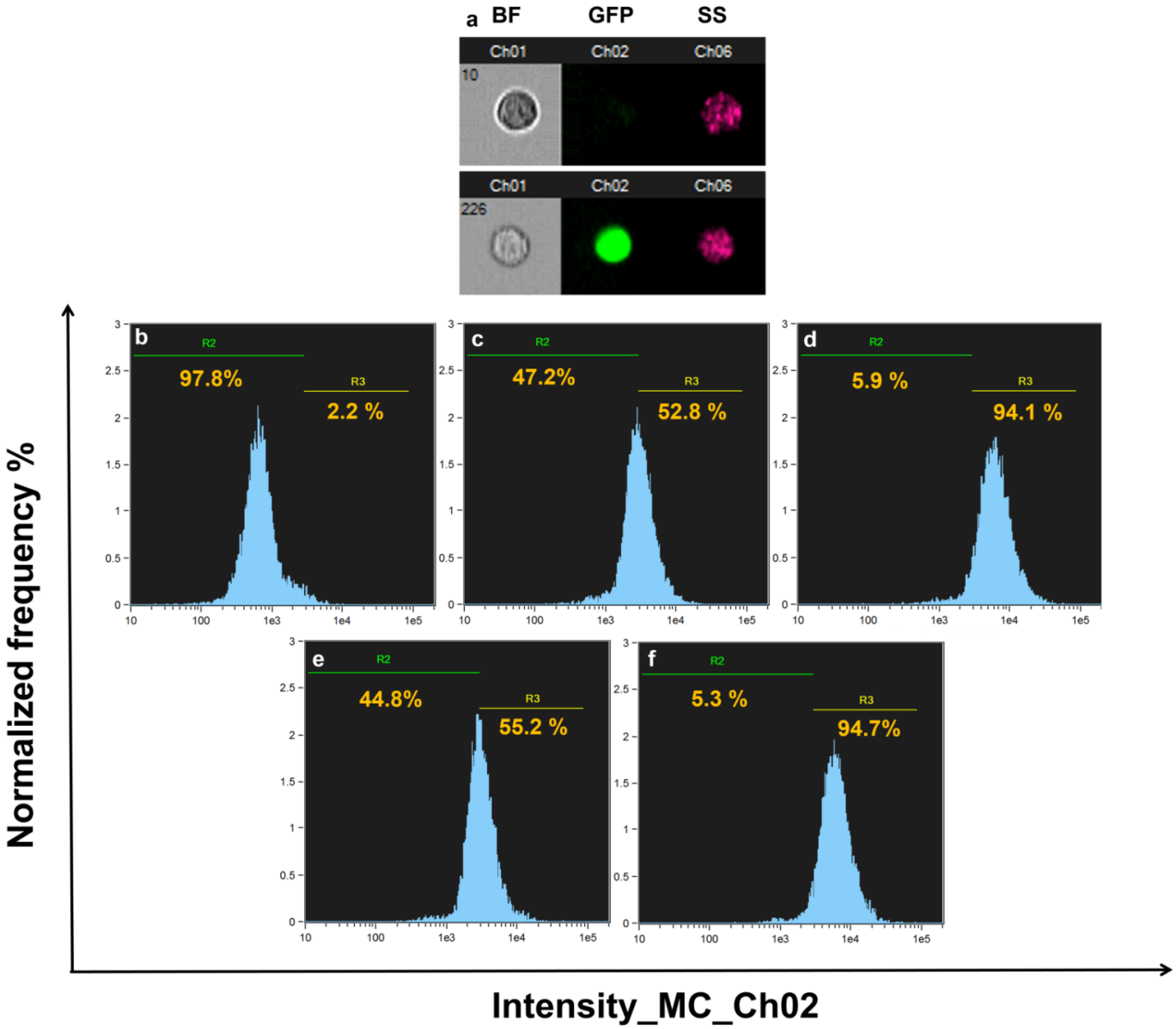

Figure 8.11 Flow cytometeric analysis for cellular uptake of CD-HY and 5-FU@CD-HY in A549 after 6 h. (a) Real-time images of untreated (upper) and treated (lower) cell acquired using the various flow cytometeric channels. Flow cytometeric histogram profiles of (b) untreated cells, (c,e) 0.5 mg mL^{-1} of CD-HY and 5-FU@CD-HY and (d,f) 2 mg mL^{-1} of CD-HY and 5-FU@CD-HY treated cells.

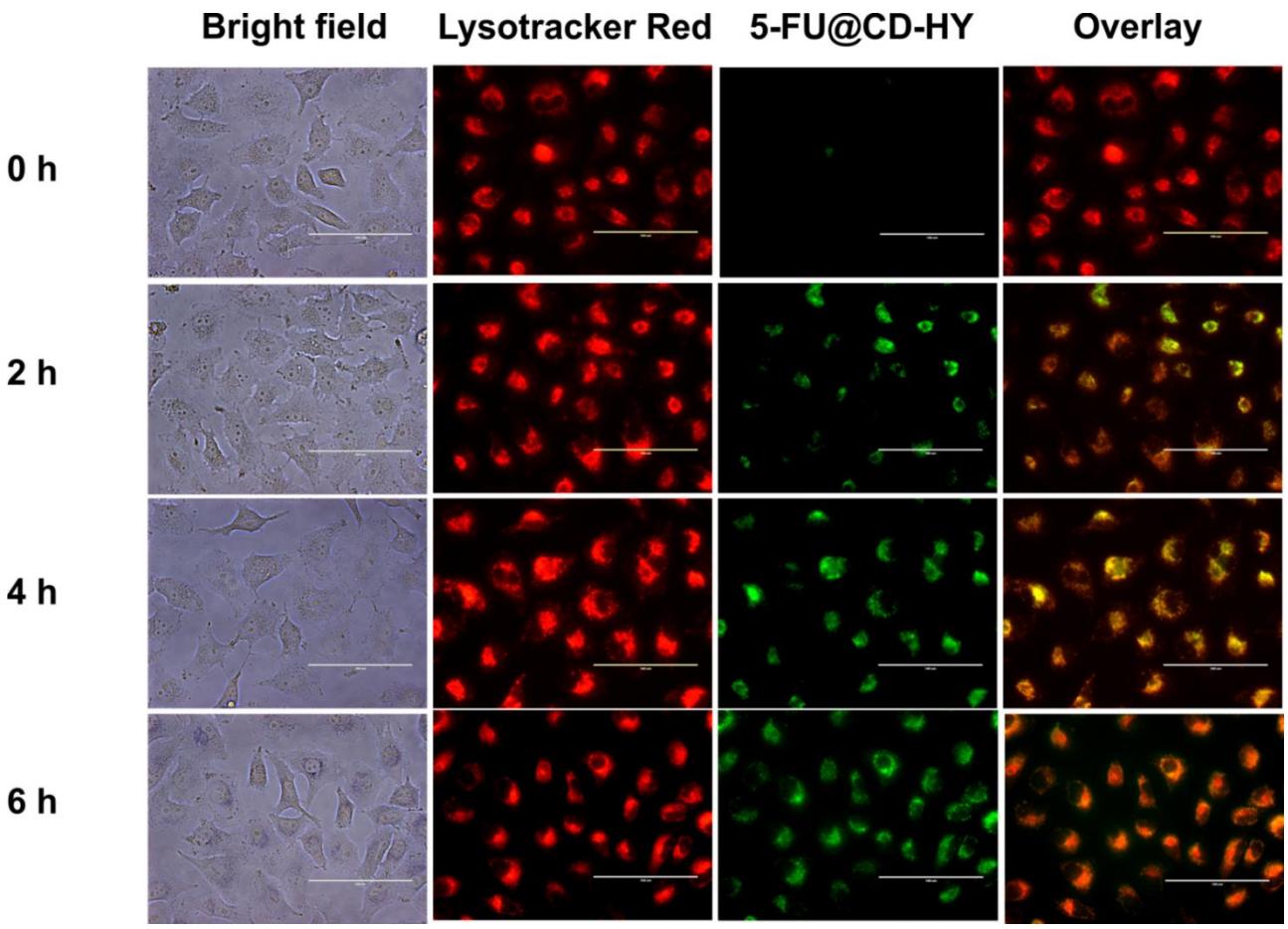

Figure 8.12 Co-localization of 5FU@CD-HY (green fluorescence) and lysosomes (red fluorescence) in A549 cells. The overlay images were generated using RFP (Lysotracker Red) and GFP (CDs) filters of fluorescence microscope. Scale bar: 100 μm.

The percentage distribution of cells in different stages of cell cycle for control and treated cells is presented in **Fig. 8.13 (A)**. CD-HY treatment did not cause any notable change in G0/G1, S and G2/M phases of cell cycle in comparison to untreated cells. In contrast, exposure of cells to 5-FU@CD-HYand free 5-FU led to an increase in the population of apoptotic cells, as determined by increased Sub-G1 population accompanied by a corresponding decline in cell numbers in G0/G1, S and G2/M phases. In the representative set of data, the proportion of apoptotic cells in 5-FU@CD-HY and free 5-FU treated cells increased to 23.66 % and 39.2 %, respectively. Nonetheless, cells treated with 5-FU@CD-HY accounted for lower apoptotic population compared to free 5-FU at similar dosage. This is for the reason that the actual concentration of released 5-FU from 5-FU@CD-HY was lower than free 5-FU due to sustained release behaviour of the hydrogels, thus explaining the difference in apoptotic population. These findings corroborate well with the release studies and cytotoxicity data. Manifestation of apoptosis in 5-FU@CD-HY treated A549 cells was ratified by FE-SEM morphological examinations **(Fig. 8.13 (B))**. Treated cells underwent shape change and drastic shrinkage in contrast to untreated cells. Contrarily, treated cells had disrupted cellular extensions with less spreading patterns. Apart from this, shedding of apoptotic bodies from dying cells and membrane blebbing authenticate the occurrence of apoptosis in treated cells (Darzynkiewicz et al., 1997). In order to ascertain the apoptotic gene signalling pathway, semi-quantitative RT-PCR analysis was performed to estimate the gene expression profiles of pro-apoptotic (p53, bax, bad, c-myc and caspase 3) and anti-apoptotic genes (bcl 2, bcl-xl) in control and treated cells **(Fig. 8.14 (A))**. Accordingly, cells treated with CD–HY, 5-FU@CD-HY and free 5-FU were analyzed for the expression of apoptosis related gene and fold change in gene expression was computed **(Fig. 8.14 (B))**. Negligible difference in the expression of pro-apoptotic and anti-apoptotic genes in CD-HY treated cells with respect to control. This finding is also supported by cell viability assay and cell cycle analysis. On the other hand, 5-FU@CD-HY and free 5-FU treated cells exhibited up-regulation of pro-apoptotic genes with consequent down-regulation of anti-apoptotic genes. The expression of housekeeping gene β-actin remained unchanged. Following treatment with 5-FU (5-FU@CD-HY and free 5-FU), p53 expression levels increased significantly. Pre-existing literature suggests the activation of p53 mediated pathway leading to apoptosis in cancer cells (Wolter et al., 1997, Yoshikawa et al., 2001 and Matai et al., 2015). B-cell lymphoma 2 (bcl 2) family exerts pro-apoptotic (bax, bad) or anti-apoptotic effects (bcl 2, bcl-xl) by altering the mitochondrial membrane permeability. Further, p53 is also known to enhance bax (bcl 2 associated X protein) and bad (bcl 2 associated death promoter) levels (Chao et al., 1998).

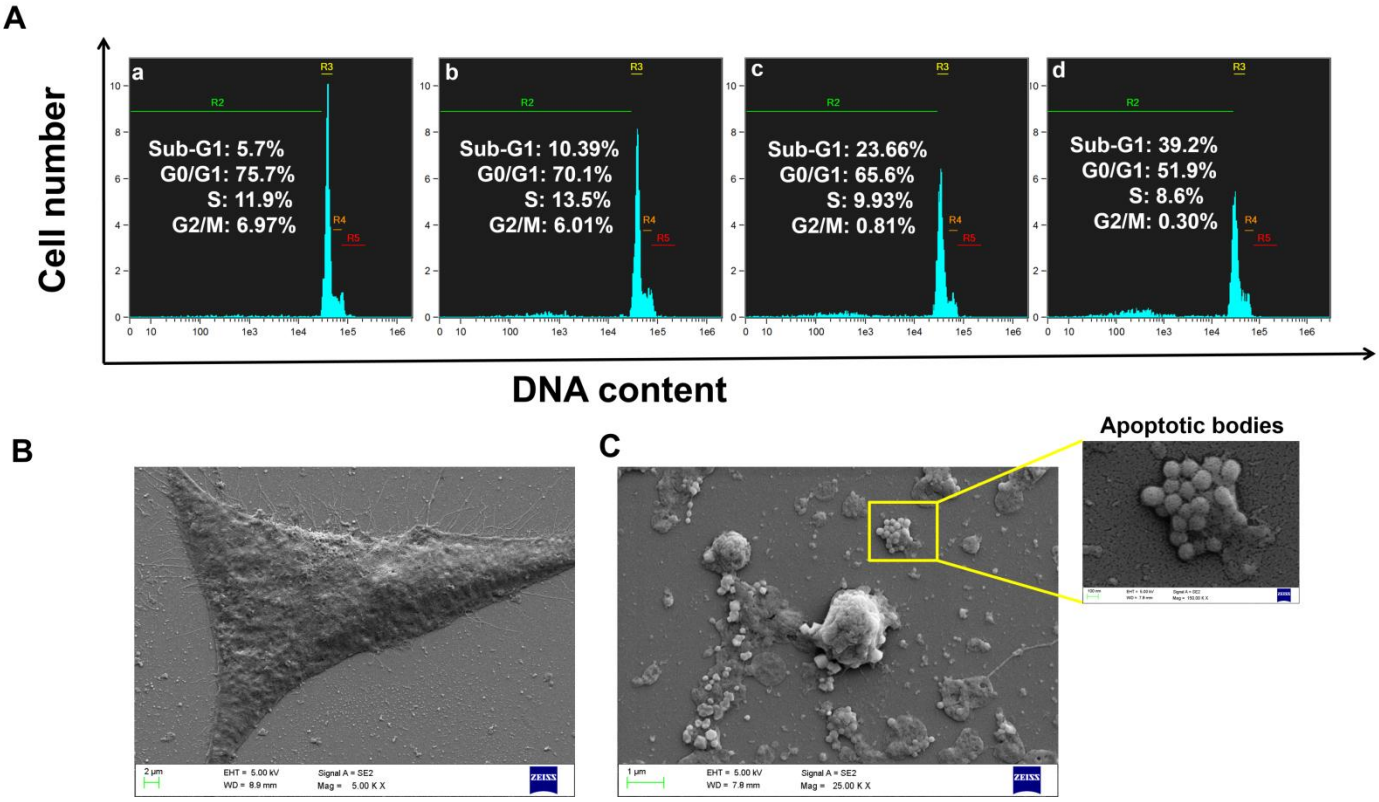

Figure 8.13 (A) Determination of cell cycle distribution profiles by flow cytometeric analysis of PI-stained samples. (a) untreated, (b) CD-HY, (c) 5-FU@CD-HY and free 5-FU (equivalent concentration) treated cells. Representative FE-SEM micrographs of (B) untreated and (C) 5-FU@CD-HY treated A549 cells after 48 h incubation.

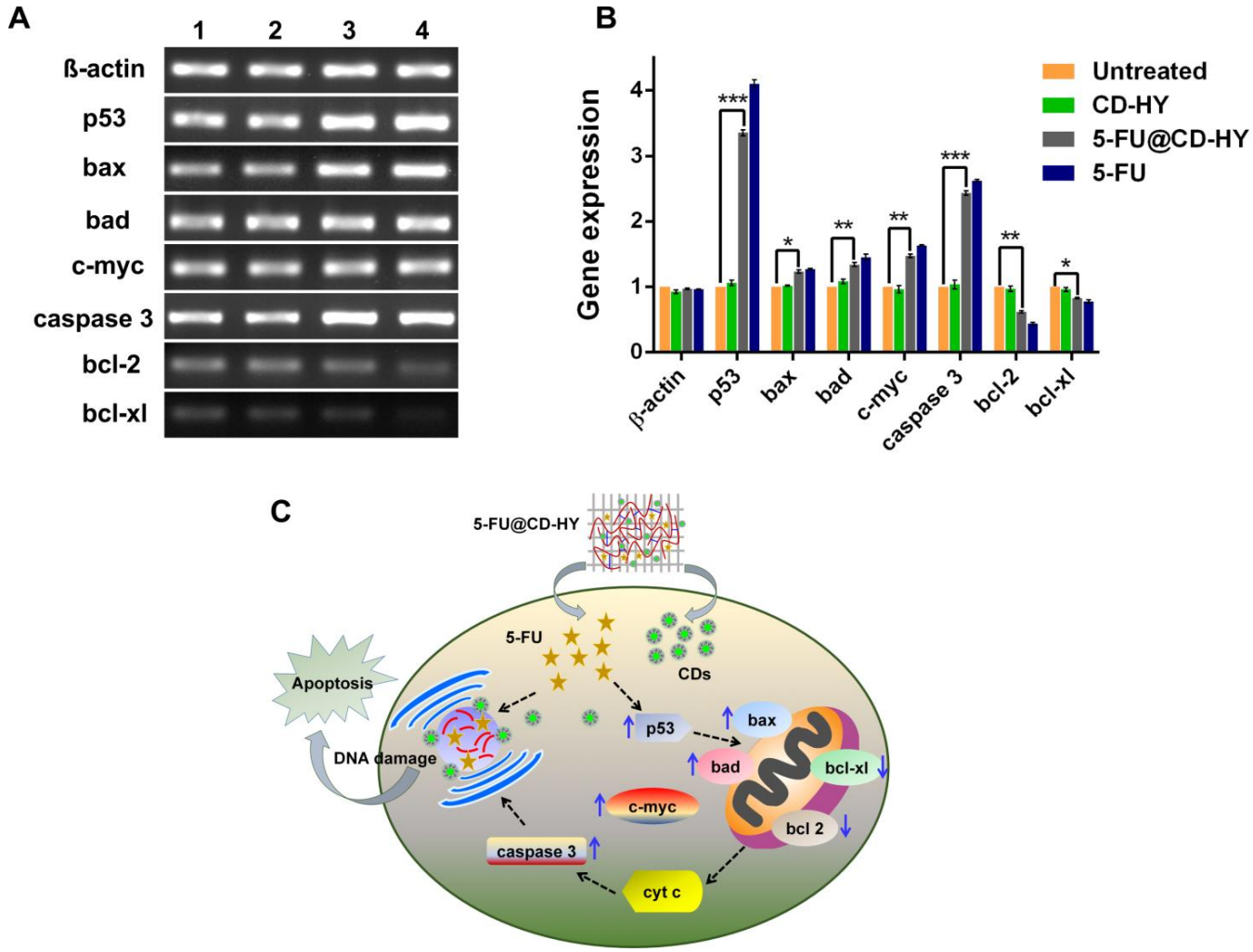

Figure 8.14 (A) Semi-quantitative RT-PCR analysis of pro-apoptotic and anti-apoptotic signaling genes in A549 cells. Lane1: untreated cells, Lane 2: CD-HY, Lane 3: 5-FU@CD-HY and Lane 4: free 5-FU treated cells. (B) Computed fold difference in gene expression in untreated and treated cells. Statistical significance between untreated and 5-FU@CD-HY treated A549 cells was designated by *($p < 0.05$), **($p < 0.005$) and ***($p < 0.001$). (C) Schematic representation of cellular uptake and subsequent activation of apoptotic gene signalling cascade upon 5-FU@CD-HY treatment.

Accordingly in our studies, down-regulation of bcl 2 and bcl-xl (basal cell lymphoma-extra large) along with up-regulation of bax, bad was observed, which marked the onset of apoptosis. Translocation of bax from mitochondria to cytosol leads to formation of pores in the mitochondrial membrane, leading to release of cyt c (cytochrome c) from mitochondria into the cytosol (Yang et al., 1997, Kluck et al., 1997 and Gopinath et al., 2010). The released cyt c further activates caspase 3, leading to nuclear genome fragmentation in apoptotic cells. Hence, enhanced expression of caspase 3 in treated cells transpires DNA damage and formation of apoptotic bodies, as observed here. Additionally, we observed increased c-myc expression in 5-FU treated cells which caused the down regulation of anti-apoptotic genes bcl 2 and bcl-xl. Thus, the activation of apoptotic gene signalling cascade is interplay of multiple pathways. Such events cause mitochondrial dysfunction and DNA damage ultimately leading to apoptotic mode of cell death in 5-FU@CD-HY treated cells **(Fig. 8.14 (C))**.

In summary, fluorescent C-dots based chitosan hydrogels loaded with 5-FU were synthesized to serve as multifunctional platform for cancer theranostic applications. In this way, it was possible to combine the merits of both CDs and 5-FU on a common platform through hydrogels. The formation of 5-FU@CD-HY was validated through various microscopic and optical characterization tools. The interactions between the encapsulated drug and the hydrogels allowed a sustained release of drug for 48 h along with a slow release of 5-FU under physiological conditions compared to acidic environment, enabling selectivity in action. Accordingly, the 5-FU loaded hydrogels were able to significantly inhibit the growth of A549 cells in a dose-dependent manner in contrast to non drug loaded counterparts. By tracking the green fluorescence of CDs in 5-FU@CD-HY with respect to nucleus, living and apoptotic cancer cells were distinguished. In case of non drug loaded hydrogels, the green fluorescence emanated from the cytoplasm of the cells. Differentially, 5-FU@CD-HY exhibited toxic effects which induced change in cell morphology. In these cells, cytoplasmic constriction led to lesser distribution of green fluorescence in the cytoplasm and dense fluorescence was seen inside the nucleus suggested nuclear internalization (apoptotic cells). In addition, the apoptotic effects induced by 5-FU released from the hydrogels were illustrated in detail. Hence, the multifunctional aspects of 5-FU@CD-HY in monitoring the cellular uptake (by CDs) and inflicting apoptosis (by 5-FU) through a cascade of events were successfully demonstrated.

CHAPTER 9

CONCLUDING REMARKS

In this chapter, concluding remarks and future scope of the present study has been discussed.

CHAPTER 9

CONCLUDING REMARKS

9.1 Conclusion

In this work, synthesis of C-dots was accomplished through innovative strategies that were simple and economical. The synthesized C-dots revealed excellent properties which made them amenable for a wide array of applications. Besides, C-dots were combined with drugs or nanoparticles to constitute multifunctional nanomaterials which demonstrated efficient competence for the intended biomedical applications under *in vitro* conditions. Based on the experimental findings, significant conclusions can be delineated.

A facile method for synthesizing intrinsically multicolour, fluorescent PEI and PEG passivated C-dots using chitosan as the starting material has been developed. The surface passivated C-dots demonstrated preeminent properties of tunable emission behaviour, pH sensitivity, small hydrodynamic size, abundant hydrophilic groups, together with resistance to photobleaching and changes in ionic strengths. Even though the carbon source remained the same, fluorescent properties of CD-PEI were amazingly good compared to CD-PEG in terms of strong fluorescence intensity, high quantum yield and longer lifetimes. Fluorescence microscopic and spectroscopic analysis predict CD-PEI as a superior bioimaging agent compared to CD-PEG, owing to its efficient fluorescent characteristics and tunable emission from blue to red under cell culture conditions. Interestingly, passivation polymer subjugated the physicochemical and bioimaging properties of C-dots. It is worthwhile to mention that the concentration of C-dots used for cell imaging did not pose any cytotoxicity. Regarding the surface of C-dots, selection of right polymer groups for surface functionalization can enhance the bioimaging efficiency.

Green synthetic approach for synthesizing self-passivated C-dots using coriander leaves as a herbal carbon source has been demonstrated for the first time, without using any additional passivating agent for surface modification. The as-synthesized green fluorescent C-dots had superior optical characteristics and demonstrated excitation, pH along with solvent dependent emission behaviour. These C-dots had inherent antioxidant potency, apart from having selective ion detection capability. Quenching of fluorescence of C-dots in the presence

of Fe^{3+} ions provides a platform for their quantitative sensing by monitoring the fluorescence emission intensity. C-dots were effectively taken up by normal as well as cancer cells and localized mainly in the cytoplasm without exerting any cytotoxic effects, highlighting their immense potential as bioimaging probes. Hence, the C-dots derived from coriander leaves exhibited a myriad of practical applications.

The grafting of CDs on CeO_2 nanoparticles was achieved through a facile *in situ* hydrothermal approach to generate CDs-CeO_2 NC. Various characterization tools, namely microscopic, spectroscopic, and XRD techniques, all confirmed the presence of CDs and CeO_2 phases in the as-synthesized NC. In addition, dual-modal properties of CDs-CeO_2 NC were intact and equally promising compared with their constituent materials as desired for biological applications. Nonetheless, the treatment of cells with CDs-CeO_2 NC did not cause any undesirable effects on cellular viability at any of the tested concentrations. Cellular uptake studies further revealed that the cells internalized CDs-CeO_2 NC in a time-dependent manner, which is imperative for their therapeutic response. Apart from this, the fluorescence of CDs was sensitive to H_2O_2, which could be used as a reference signal for evaluating the H_2O_2 mediated oxidative stress in cells. The study also verified the utility of CDs-CeO_2 NC for intracellular ROS scavenging and prevention of H_2O_2 induced oxidative stress.

The designing of CD-Ag@ZnO NC was based on the electrostatic interactions between oppositely charged CDs and Ag@ZnO. Various characterization techniques (TEM, DLS and SEM) unanimously indicated that the CDs had successfully decorated the surface of the Ag@ZnO to form a dual-modality hybrid assembly. The study provided sound evidence about the use of CD-Ag@ZnO NC to induce apoptosis in cancer cells in conjugation with imaging. These NCs clearly demonstrated antiproliferative effects against both MCF-7 and A549 cancer cells in a dose-dependent manner. Direct fluorescence monitoring of cellular uptake and the intracellular localization of NC inside the cancer cells was also studied using the fluorescence emission of CDs. Qualitative and quantitative analyses predicted marked differences in cellular uptake between MCF-7 and A549 cells. A preliminary investigation of NC treated cancer cells revealed characteristic apoptotic features such as changes in the morphology, cell shrinkage and cytoplasmic constriction. In addition, a dramatic increase in ROS along with an increase in the ratio of pro-apoptotic to anti-apoptotic expression was observed in cancer cells treated with CD-Ag@ZnO NC. From these results, it could be inferred that CD-Ag@ZnO NC provoked ROS-mediated activation of the apoptotic gene signalling cascade. Taken together, the

implication of these findings seems to be promising for the possible application of fluorescent C-dots for theranostic purposes.

In situ gelling CDs integrated chitosan hydrogels were prepared via ionic cross-linking method and further loaded with 5-FU to mediate anticancer effects. Moreover, these hydrogels demonstrated excellent functional features in terms of high surface area, good mechanical strength, swelling behaviour together with pH dependent drug release. Cytotoxicity studies explained that the concentration dependent anti-proliferative effects of 5-FU@CD-HY on A549 cells, solely due to the released 5-FU. Fluorescence of CDs in 5-FU@CD-HY was used to monitor the intracellular distribution as well as for flow cytometeric analysis. Apart from this, the fluorescence labelling pattern of CDs could clearly distinguish between live and apoptotic cells under fluorescence microscope, transcending the use of conventional dyes. Substantial increase in Sub-G1 phase with a concomitant reduction in S phase provided striking evidence about the apoptotic mode of cell death. Therefore, cell cycle investigations implicated DNA damage by 5-FU. In addition, morphological hallmarks of apoptotic cells such as surface blebbing and cytoplasm constriction were evident in FE-SEM imaging. An increase in the ratio of pro-apoptotic to anti-apoptotic gene expression upon 5-FU@CD-HY treatment suggested the triggering of apoptotic signalling pathway involving mitochondria. Hence, the study testifies the ability of 5-FU@CD-HY for simultaneous induction and imaging of apoptosis in cancer cells. Taken together, the above findings signify the application of hydrogels for combining therapeutic and bioimaging modalities on a single platform, making them prospective candidates for cancer theranostics.

9.2 Future scope of work

Considering the bright future of C-dots for various biomedical and analytical applications, suitable strategies can be evolved for improving their functional characteristics. Some of the thrust areas that can be explored have been enlisted below:

- New methods can be devised for producing C-dots in higher yields with higher quantum yields so as to pursue their *in vivo* studies. Doping with heteroatoms can enhance the fluorescence quantum yield of C-dots considerably.
- Fine-tuning the fluorescence emission of C-dots with excitation in red/near-IR spectral region to reduce the background fluorescence and enhance tissue penetration to make them more efficient for *in vivo* imaging.
- C-dots synthesized from coriander leaves can be evaluated for Fe^{3+} sensing ability in biological systems and river water samples.

- Surface functionalization of C-dots with specific molecular recognition elements can aid biosensing applications.
- Efficiency of C-dots-cerium oxide NCs in monitoring the intracellular distribution and ROS scavenging potential can be examined *in vivo*, where the environment is more complex.
- Nanocomplexes of C-dots with drugs or metal nanoparticles can be further functionalized with tumor recognition moieties to specifically target cancer cells to achieve enhanced therapeutic outcomes.
- C-dots-based hydrogels can be used as a nanocarrier for anticancer gene delivery with the ability to concurrently monitor the extent of transfection.

REFERENCES

1. Akhtar, M.J., Ahamed, M., Kumar, S., Khan, M.M., Ahmad, J. and Alrokayan, S.A., Zinc oxide nanoparticles selectively induce apoptosis in human cancer cells through reactive oxygen species. *Int. J. Nanomed.*, 7, 845-857 (2012).
2. Apostolova, N., Rovira-Llopis, S., Baldov´, H.G., Navalon, S., Asiri, A.M., Victor, V.M., Garcia, H. and Herance, J.R., Ceria nanoparticles with rhodamine B as a powerful theranostic agent against intracellular oxidative stress. *RSC Adv.*, 5, 79423-79432 (2015).
3. Asati, A., Santra, S., Kaittanis, C., Nath, S. and Perez, J.M., Oxidase-like activity of polymer-coated cerium oxide nanoparticles. *Angew Chem. Int. Ed.*, 48, 2308-2312 (2009).
4. AshaRani, P.V., Low Kah Mun, G., Hande, M.P. and Valiyaveettil, S., Cytotoxicity and genotoxicity of silver nanoparticles in human cells. *ACS Nano.*, 3, 279-290 (2009).
5. Babu, S., Cho, J.H., Dowding, J.M., Heckert, E., Komanski, C., Das, S., Colon, J., Baker, C.H., Bass, M., Self, W.T. and Seal, S., Multicolored redox active upconverter cerium oxide nanoparticles for bio-imaging and therapeutics. *Chem. Commun.*, 46, 6915-6917 (2010).
6. Baker, S.N. and Baker, G.A., Luminescent carbon nanodots: emergent nanolights. *Angew. Chem. Int. Ed.*, 49, 6726- 6744 (2010).
7. Bao, X., Shi, J., Nie, X., Zhou, B., Wang, X., Zhang, L., Liao, H. and Pang, T., A new Rhodamine B-based 'on-off' chemical sensor with high selectivity and sensitivity toward Fe(3+) and its imaging in living cells. *Bioorg. Med. Chem.*, 22, 4826-4835 (2014).
8. Barati, A., Shamsipur, M., Arkan, E., Hosseinzadeh, L. and Abdollahi, H., Synthesis of biocompatible and highly photoluminescent nitrogen doped carbon dots from lime: analytical applications and optimization using response surface methodology. *Mater. Sci. Eng. C*, 47, 325-332 (2015).
9. Baruah, U. and Devasish Chowdhury, D., Functionalized graphene oxide quantum dot-PVA hydrogel: a colorimetric sensor for Fe^{2+}, Co^{2+} and Cu^{2+} ions. *Nanotechnology*, 27, 145501 (2016).
10. Berger, J., Reist, M., Mayer, J.M., Felt, O., Peppas, N.A. and Gurny, R., Structure and interactions in covalently and ionically crosslinked chitosan hydrogels for biomedical applications. *Eur. J. Pharm. Biopharm.*, 57, 19-34 (2004).

11. Beyler, C.L. and Hirschler, M.M., *SFPE handbook of fire protection engineering, national fire protection association*, MA (1995).
12. Bhaisare, M. L., Wu, B.S., Wu, M.C., Khan, M.S., Tseng, M.H. and Wu. H.F., MALDI MS analysis, disk diffusion and optical density measurements for the antimicrobial effect of zinc oxide nanorods integrated in grapheme oxide nanostructures. *Biomater. Sci.*, 4, 183-194 (2016).
13. Bhardwaj, V., Ankola, D.D., Gupta, S.C., Schneider, M., Lehr, C.M. and Ravi Kumar, M.N., PLGA nanoparticles stabilized with cationic surfactant: Safety studies and application in oral delivery of paclitaxel to treat chemical induced breast cancer in rat. *Pharm Res.*, 26, 2495-2503 (2009).
14. Bhattarai, N., Gunn, J. and Zhang, M., Chitosan-based hydrogels for controlled, localized drug delivery. *Adv Drug Deliv Rev.*, 62, 83-99 (2010).
15. Bhunia, S.K., Maity, A.R., Nandi, S., Stepensky, D. and Jelinek, R., Imaging cancer cells expressing the folate receptor with carbon dots produced from folic Acid. *ChemBioChem*, 17, 614-619 (2016a).
16. Bhunia, S.K., Nandi, S., Shikler, R. and Jelinek, R., Tuneable light-emitting carbon-dot/polymer flexible films prepared through one-pot synthesis. *Nanoscale*, 8, 3400-3406 (2016b).
17. Bhunia, S.K., Saha, A., Maity, A.R., Ray, S.C. and Jana, N.R., Carbon nanoparticle-based fluorescent bioimaging probes. *Sci Rep.*, 3, 1473-1479 (2013).
18. Bhushan, B. and Gopinath, P., Antioxidant nanozyme: a facile synthesis and evaluation of the reactive oxygen species scavenging potential of nanoceria encapsulated albumin nanoparticles. *J. Mater. Chem. B*, 3, 4843-4852 (2015).
19. Bian, J., Huang, C., Wang, L., Hung, T., Daoud, W.A. and Zhang, R., Carbon dot loading and TiO_2 nanorod length dependence of photoelectrochemical properties in carbon dot/ TiO_2 nanorod array nanocomposites. *ACS Appl. Mater. Interfaces*, 6, 4883-4890 (2014).
20. Blum, C., Schleifenbaum, F., Stopel, M., Peter, S., Sackrow, M., Subramaniam, V. and Meixner, A.J., Room temperature excitation spectroscopy of single quantum dots. *Beilstein Journal of Nanotechnology*, 2, 516-524. (2011)
21. Bourlinos, A.B., Stassinopoulos, A., Anglos, D., Zboril, R., Georgakilas, V., and Giannelis, E.P., Photoluminescent carbogenic dots. *Chem. Mater.*, 20, 4539-4541 (2008).

22. Cadenas, E. and Davies, K.J.A., Mitochondrial free radical generation, oxidative stress, and aging. *Free Radic. Biol. Med.*, 29, 222-230 (2000).
23. Cao, L., Wang, X., Meziani, M.J., Lu, F., Wang, H., Luo, P.G., Lin, Y., Harruff, B.A., Veca, L.M., Murray, D., Xie, S.Y. and Sun, Y.P., Carbon dots for multiphoton bioimaging. *J. Am. Chem. Soc.*, 129, 11318-11319 (2007).
24. Cao, L., Yang, S.T., Wang, X., Luo, P.G., Liu, J.H., Sahu, S., Liu, Y. and Sun, Y.P., Competitive performance of carbon "quantum" dots in optical bioimaging. *Theranostics*, 2, 295-301 (2012).
25. Casettari, L., Vllasaliu, D., Mantovani, G., Howdle, S.M., Stolnik, S. and Illum, L., Effect of PEGylation on the toxicity and permeability enhancement of chitosan. *Biomacromolecules*, 11, 2854-2865 (2010).
26. Cassee, F.R., Van Balen, E.C., Singh, C., Green, D., Muijser, H., Weinstein, J. and Dreher, K., Exposure, health and ecological effects review of engineered nanoscale cerium and cerium oxide associated with its use as a fuel additive. *Crit. Rev. Toxicol.*, 41, 213-229 (2011).
27. Cedergren, J., Forslund, T., Sundqvist, T. and Skogh, T., Intracellular oxidative activation in synovial fluid neutrophils from patients with rheumatoid arthritis but not from other arthritis patients. *J. Rheumatol.*, 34, 2162-2170 (2007).
28. Celardo, I., De Nicola, M., Mandoli, C., Pedersen, J.Z., Traversa, E. and Ghibelli, L., Ce^{3+} ions determine redox-dependent anti-apoptotic effect of cerium oxide nanoparticles. .*ACS Nano*, 5, 4537-4549 (2011).
29. Chandra, S., Patra, P., Pathan, S.H., Roy, S., Mitra, S., Layek, A., Bhar, R., Pramanik, P. and Goswami, A., Luminescent S-doped carbon dots: an emergent architecture for multimodal applications. *J. Mater. Chem. B*, 1, 2375-2382 (2013).
30. Chao, D.T. and Korsmeyer, S.J., BCL-2 family: regulators of cell death. *Annu. Rev. Immunol.*, 16, 395-419 (1998).
31. Chaudhary, A., Dwivedi, C., Gupta, A. and Nandi, C.K., One pot synthesis of doxorubicin loaded gold nanoparticles for sustained drug release. *RSC Adv.*, 5, 97330-97334 (2015).
32. Chauhan, H., Kumar, Y. and Deka, S., New synthesis of two-dimensional CdSe/CdS core@shell dot-in-hexagonal platelet nanoheterostructures with interesting optical properties. *Nanoscale*, 6, 10347-10354 (2014).

33. Chen, F. and Gerion, D., Fluorescent CdSe/ZnS nanocrystal-peptide conjugates for long-term, nontoxic imaging and nuclear targeting in living cells. *Nano Lett.*, 4, 1827-1832 (2004).
34. Chen, N., He, Y., Su, Y., Li, X., Huang, Q., Wang, H., Zhang, X., Tai, R. and Fan, C., The cytotoxicity of cadmium-based quantum dots. *Biomaterials*, 33, 1238-1244 (2012b).
35. Chen, R., Chen, Q., Huo, D., Ding, Y., Hu, Y. and Jiang, X., *In situ* formation of chitosan-gold hybrid hydrogel and its application for drug delivery. *Colloids Surf B Biointerfaces*, 97, 132-137 (2012a).
36. Chetia, B. and Iyer, P.K., Selective fluoride anion sensing by simple benzimidazolyl based ligand. *Sensors and Actuators B*, 201, 191-195 (2014).
37. Choi, Y., Kim, S., Choi, M.H., Ryoo, S.R., Park, J., Min, D.H. and Kim, B.S., Highly biocompatible carbon nanodots for simultaneous bioimaging and targeted photodynamic therapy *in vitro* and *in vivo*. *Adv. Funct. Mater.*, 24, 5781-5789 (2014).
38. Chowdhury, D., Gogoi, N. and Majumdar, G., Fluorescent carbon dots obtained from chitosan gel. *RSC Adv.*, 2, 12156-12159 (2012).
39. Christensen, I.L., Sun, Y.P. and Juzenas, P., Carbon dots as antioxidants and prooxidants. *J. Biomed. Nanotechnol.*, 7, 667-676 (2011).
40. Corr, S.A., Rakovich, Y.P. and Gun'ko, Y.K., Multifunctional magnetic-fluorescent nanocomposites for biomedical applications. *Nanoscale Res. Lett.*, 3, 87-104 (2008).
41. Coyle, C.H., Martinez, L.J., Coleman, M.C., Spitz, D.R., Weintraub, N.L. and Kader, K.N., Mechanisms of H_2O_2-induced oxidative stress in endothelial cells. *Free Radic. Biol. Med.*, 40, 2206-2213 (2006).
42. Dankovich, T.A., Microwave-assisted incorporation of silver nanoparticles in paper for point-of-use water purification. *Environ. Sci.: Nano*, 1, 367-378 (2014).
43. Dar, A.A., Hussain, S., Dutta, D., Iyer, P.K. and Khan, A.T. One-pot synthesis of functionalized 4-hydroxy-3-thiomethylcoumarins: Detection and discrimination of Co^{2+} and Ni^{2+} ions. *RSC Adv.*, 5, 57749-57756 (2015).
44. Darzynkiewicz, Z., Juan, G., Li, X., Gorczyca, W., Murakami, T. and Traganos, F., Cytometry in cell necrobiology: Analysis of apoptosis and accidental cell death (Necrosis). *Cytometry*, 27, 1-20 (1997).
45. Das, B., Dadhich, P., Pal, P., Srivas, P.K., Bankoti, K. and Dhara, S., Carbon nanodots from date molasses: new nanolights for the *in vitro* scavenging of reactive oxygen species. *J. Mater. Chem. B*, 2, 6839-6847 (2014).

46. Das, D. and Pal, S., Modified biopolymer-dextrin based crosslinked hydrogels: application in controlled drug delivery. *RSC Adv.*, 5, 25014-25050 (2015).
47. Datta, K. K. R., Kozák, O., Ranc, V., Havrdová, M., Bourlinos, A.B., Šafářová, K., Holá, K., Tománková, K., Zoppellaro, G., Otyepka, M. and Zbořil, R., Quaternized carbon dots modified graphene oxide for selective cell labelling – controlled nucleus and cytoplasm imaging. *Chem. Commun.*, 50, 10782-10785 (2014).
48. De, B. and Karak, N., A green and facile approach for the synthesis of water soluble fluorescent carbon dots from banana juice. *RSC Adv.*, 3, 8286-8290 (2013).
49. Deka, M.J. and Chowdhury, D., Tuning electrical properties of graphene with different π-stacking organic molecules. *J. Phys. Chem. C*, 120, 4121-4129 (2016).
50. Deng, L., Li, Q., Yang, Y., Omar, H., Tang, N., Zhang, J. and Nie, Z., "Two-Step" raman imaging technique to guide chemo-photothermal cancer therapy. *Chem. Eur. J.*, 21, 17274-17281 (2015).
51. Deori, K., Gupta, D., Saha, B. and Deka, S., Design of 3-Dimensionally self-assembled CeO_2 nanocube as a breakthrough catalyst for efficient alkylarene oxidation in water. *ACS Catalysis*, 4, 3169-3179 (2014).
52. Deori, K., Gupta, D., Saha, B., Awasthi, S. and Deka, S., Introducing nanocrystalline CeO_2 as heterogeneous environmental friendly catalyst for the aerobic oxidation of para-xylene to terephthalic acid in water. *J. Mater. Chem. A*, 1, 7091-7099 (2013).
53. Deori, K., Kalita, C. and Deka, S., (100) surface-exposed CeO_2 nanocubes as an efficient heterogeneous catalyst in the tandem oxidation of benzyl alcohol, para-chlorobenzyl alcohol and toluene to the corresponding aldehydes selectively. *J. Mater. Chem. A*, 3, 6909-6920 (2015).
54. Ding, C., Zhu, A. and Tian, Y., Functional surface engineering of C-dots for fluorescent biosensing and *in vivo* bioimaging. *Acc. Chem Res.*, 47, 20-30 (2014).
55. Ding, H., Cheng, L.W., Ma, Y.Y., Kong, J.L. and Xiong, H.M., Luminescent carbon quantum dots and their application in cell imaging. *New J.Chem.*, 37, 2515-2520 (2013).
56. Ding, H., Yu, S.B., Wei, J.S. and Xiong, H.M., Full-color light-emitting carbon dots with a surface-state-controlled luminescence mechanism. *ACS Nano.*, 10, 484-491 (2016).
57. Dong, Y, Wang, R., Li, H., Shao, J., Chi, Y., Lin, X. and Chen, G., Polyamine-functionalized carbon quantum dots for chemical sensing. *Carbon*, 50, 2810-2815 (2012).

58. Dong, Y., Pang, H., Yang, H.B., Guo, C., Shao, J., Chi, Y., Li, C.M. and Yu, T., Carbon-based dots co-doped with nitrogen and sulfur for high quantum yield and excitation-independent emission. *Angew Chem. Int. Ed.*, 22, 7800-7804 (2013).
59. Du, F., Min, Y., Zeng, F., Yu, C. and Wu, S., A targeted and FRET-based ratiometric fluorescent nanoprobe for imaging mitochondrial hydrogen peroxide in living cells. *Small*, 10, 964-972 (2014).
60. Duan, C., Zhang, D., Wang, F., Zheng, D., Jia, L., Feng, F., Liu, Y., Wang, Y., Tian, K., Wang, F. and Zhang, Q., Chitosan-g-poly (N-isopropylacrylamide) based nanogels for tumor extracellular targeting. *Int. J. Pharm.*, 409, 252-259 (2011).
61. Dubertret, B., Skourides, P., Norris, D.J., Noireaux, V., Brivanlou, A.H. and Libchaber, A., *In vivo* imaging of quantum dots encapsulated in phospholipid micelles. *Science*, 298, 1759-1762 (2002).
62. Dubey, P., Matai, I., Kumar, S.U., Sachdev, A., Bhushan, B. and Gopinath, P., Perturbation of cellular mechanistic system by silver nanoparticle toxicity: Cytotoxic, genotoxic and epigenetic potentials. *Adv. Colloid Interface Sci.*, 221, 4-21 (2015).
63. Dwivedi, C., Gupta, A., Chaudhary, A. and Nandi, C.K., Gold nanoparticle chitosan composite hydrogel beads show efficient removal of methyl parathion from waste water. *RSC Adv.*, 4, 39830-39838 (2014).
64. Elbanowski, M. and Makowsaka, B., The lanthanides as luminescent probes in investigations of biochemical systems. *J. Photochem. Photobiol. A*, 99, 85-92 (1996).
65. En, D., Guo, Y., Chen, B.T., Dong, B. and Peng, M.J., Coumarin-derived Fe^{3+}-selective fluorescent turn-off chemosensors: synthesis, properties, and applications in living cells. *RSC Adv.*, 4, 248-253 (2014).
66. Fang, Y., Guo, S., Li, D., Zhu, C., Ren, W., Dong, S. and Wang, E., Easy synthesis and imaging applications of cross-linked green fluorescent hollow carbon nanoparticles. *ACS Nano.*, 6, 400-409 (2012).
67. Feynman, R., There's plenty of room at the bottom. *Science*, 254, 1300-1301 (1991).
68. Frasco, M.F. and Chaniotakis, N., Semiconductor quantum dots in chemical sensors and biosensors. *Sensors*, 9, 7266-7286 (2009).
69. Fu, M., Ehrat, F., Wang, Y., Milowska, K. Z., Reckmeier, C., Rogach, A. L., Stolarczyk, J. K., Urban, A. S. and Feldmann, J., Carbon dots: A unique fluorescent cocktail of polycyclic aromatic hydrocarbons. *Nano Lett.*, 15, 6030-6035 (2015).

70. Gangadharan, D., Harshvardan, K., Gnanasekar, G., Dixit, D., Popat, K.M. and Anand, P.S., Polymeric microspheres containing silver nanoparticles as a bactericidal agent for water disinfection. *Water Res.*, 44, 5481-5487 (2010).
71. Gao, H., Yang, Z., Zhang, S., Cao, S., Shen, S., Pang, Z. and Jiang, X., Ligand modified nanoparticles increases cell uptake, alters endocytosis and elevates glioma distribution and internalization. *Sci. Rep.*, 3, 2534-2541 (2013).
72. Gao, J., Gu, H. and Xu, B., Multifunctional magnetic nanoparticles: design, synthesis, and biomedical applications. *Acc. Chem Res.*, 42, 1097-1107 (2009).
73. Gao, X., Ding, C., Zhu, A. and Tian, Y., Carbon-dot-based ratiometric fluorescent probe for imaging and biosensing of superoxide anion in live cells. *Anal. Chem.*, 86, 7071-7078 (2014).
74. Gavvala, K., Satpathi, S., and Hazra, P., pH responsive translocation of an anticancer drug between cyclodextrin and DNA. *RSC Adv.*, 5, 98080-98086 (2015).
75. Gedd, G., Pandey, S., Bhaisare, M. L. and Wu, H.F., Carbon dots as nanoantennas for anti-inflammatory drug analysis using surface-assisted laser desorption/ionization time-of-flight mass spectrometry in serum. *RSC Adv.*, 4, 38027-38033 (2014).
76. Geng, T.M., Huang, R.Y. and Wu, D.Y., Turn-on fluorogenic and chromogenic detection of Fe^{3+} and Cr^{3+} in a completely water medium with polyacrylamide covalently bonding to rhodamine B using diethylenetriamine as a linker. *RSC Adv.*, 4, 46332-46339 (2014).
77. Ghosh, R., Goswami, U., Ghosh, S.S., Paul, A. and Chattopadhyay, A., Synergistic anticancer activity of fluorescent copper nanoclusters and cisplatin delivered through a hydrogel nanocarrier. *ACS Appl. Mater. Interfaces*, 7, 209-222 (2015).
78. Gill, R., Tian, L., Amerongen, H. and Subramaniam, V., Emission enhancement and lifetime modification of phosphorescence on silver nanoparticle aggregates. *Phys. Chem. Chem. Phys.*, 15, 15734-15739 (2013).
79. Gliga, A.R., Skoglund, S., Wallinder, I.O., Fadeel, B. And Karlsson, H.L., Size-dependent cytotoxicity of silver nanoparticles in human lung cells: the role of cellular uptake, agglomeration and Ag release. *Part. Fibre Toxicol.*, 11, 11-27 (2014).
80. Gogoi, N., Barooah, M., Majumdar, G. and Chowdhury, D., Carbon dots rooted agarose hydrogel hybrid platform for optical detection and separation of heavy metal ions. *ACS Appl. Mater. Interfaces*, 7, 3058-3067 (2015).

81. Goncalves, H., Jorge, P.A.S., Fernandes, J.R.A. and Esteves da Silva, J.C.G, Hg(II) sensing based on functionalized carbon dots obtained by direct laser ablation. *Sensors and Actuators B*, 145, 702-707 (2010).
82. Gonçalves, M., Maciel, D., Capelo, D., Xiao, S., Sun, W., Shi, X., Rodrigues, J., Tomás, H. and Li, Y., Dendrimer-assisted formation of fluorescent nanogels for drug delivery and intracellular imaging. *Biomacromolecules*, 15, 492-499 (2014).
83. Gong, X., Lu, W., Paau, M.C., Hu, Q., Wu, X., Shuang, S., Dong, C. and Choi, M.M., Facile synthesis of nitrogen-doped carbon dots for Fe^{3+} sensing and cellular imaging. *Anal. Chim. Acta*, 861, 74-84 (2015).
84. Gopinath, P., Gogoi, S.K., Sanpui, P., Paul, A., Chattopadhyay, A. and Ghosh, S.S., Signaling gene cascade in silver nanoparticle induced apoptosis. *Colloids Surf B Biointerfaces*, 77, 240-245 (2010).
85. Gopinath, P., Kumar, S. U., Matai, I., Bhushan, B., Malwal, D., Sachdev, A. and Dubey, P., Cancer Nanotheranostics. *Springer Briefs in Applied Science and Technology*, Springer, New York, http://dx.doi.org/10.1007/978-981-287-435-1, 1-93 (2015).
86. Goutam, P. J.and Iyer, P.K., Selective detection of resorcinol using abis(benzothiazol-2-yl)pyridine based ditopic receptor. *Sensors and Actuators B*, 211, 263-267 (2015).
87. Gupta, A., Chaudhary, A., Mehta, P., Dwivedi, C., Khan, S., Verma, N.C. and Nandi C.K. Nitrogen-doped, thiol-functionalized carbon dots for ultrasensitive Hg(II) detection. *Chem Commun (Camb).*, 51, 10750-10753 (2015).
88. Gupta, A., Verma, N.C., Khan, S. and Nandi, C.K., Carbon dots for naked eye colorimetric ultrasensitive arsenic and glutathione detection. *Biosens. Bioelectron.*, 82, 465-472 (2016a).
89. Gupta, A., Verma, N.C., Khan, S., Tiwari, S., Chaudhary, A. and Nandi, C.K. Paper strip based and live cell ultrasensitive lead sensor using carbon dots synthesized from biological media. *Sensors and Actuators B*, 232, 107-114 (2016b).
90. Hamidi, M., Azadi, A. and Rafiei, P., Hydrogel nanoparticles in drug delivery. *Adv. Drug Deliv. Rev.*, 60, 1638-1649 (2008).
91. Hanley, C., Layne, J., Punnoose, A., Reddy, K.M., Coombs, I., Coombs, A., Feris, K. and Wingett, D., Preferential killing of cancer cells and activated human T cells using zinc oxide nanoparticles. *Nanotechnology*, 19, 295103-295113 (2008).

92. Hardman, R., A toxicologic review of quantum dots: toxicity depends on physicochemical and environmental factors. *Environ Health Perspect.*, 114, 165-72 (2006).
93. Heckert, E.G., Karakoti, A.S., Seal, S. and Self, W.T., The role of cerium redox state in the SOD mimetic activity of nanoceria. *Biomaterials*, 29, 2705-2709 (2008).
94. Hennink, W.E. and Van Nostrum, C.F., Novel crosslinking methods to design hydrogels. *Adv. Drug Deliv. Rev.*, 54, 13-36 (2002).
95. Hoare, T.R. and Kohane, D. S., Hydrogels in drug delivery: progress and challenges. *Polymer*, 49, 1993-2007 (2008).
96. Hoffman, A.S., Hydrogels for biomedical applications. *Adv. Drug Deliv. Rev.*, 54, 3-12 (2002).
97. Hsiao, I.L. and Huang, Y.J., Titanium oxide shell coatings decrease the cytotoxicity of ZnO nanoparticles. *Chem. Res. Toxicol.*, 24, 303-313 (2011).
98. Hsu, P.C., Chen, P.O., Ou, C.M., Chang, H.Y. and Chang, H.T., Extremely high inhibition activity of photoluminescent carbon nanodots toward cancer cells. *J. Mater. Chem. B*, 1, 1774-1781 (2013).
99. Hsu, P.C., Shih, Z.Y., Lee, C.H. and Chang, H.T., Synthesis and analytical applications of photoluminescent carbon nanodots. *Green Chem.*, 14, 917-920 (2012).
100. Hu, L., Sun, Y., Li, S., Wang, X., Hu, K., Wang, L., Liang, X. and Wu, Y., Multifunctional carbon dots with high quantum yield for imaging and gene delivery *Carbon*, 67, 508-513 (2014).
101. Hu, S., Trinchi, A., Atkin, P. and Cole, I., Tunable photoluminescence across the entire visible spectrum from carbon dots excited by white light. *Angew. Chem., Int. Ed.*, 54, 2970-2974 (2015).
102. Hu, S.L., Liu, J., Yang, J.L., Wang, Y.Z. and Cao, S., Laser synthesis and size tailor of carbon quantum dots. *J. Nanopart. Res.*, 13, 7247-7252 (2011).
103. Huang, H., Xu, Y., Tang, C.J., Chen, J.R., Wang, A.J. and Feng, J.J., Facile and green synthesis of photoluminescent carbon nanoparticles for cellular imaging. *New J. Chem.*, 38, 784-789 (2014).
104. Huang, P., Lin, J., Wang, X., Wang, Z., Zhang, C., He, M., Wang, K., Chen, F., Li, Z., Shen, G., Cui, D. and Chen, X., Light-triggered theranostics based on photosensitizer-conjugated carbon dots for simultaneous enhanced-fluorescence imaging and photodynamic therapy. *Adv. Mater.*, 24, 5104-5110 (2012).

105. Huang, Q., Hu, S., Zhang, H., Chen, J., He, Y., Li, F., Weng, W., Ni, J., Bao, X. and Lin, Yi., Carbon dots and chitosan composite film based biosensor for the sensitive and selective determination of dopamine. *Analyst*, 138, 5417-5423 (2013a).
106. Huang, Y., He, L., Liu, W., Fan, C., Zheng, W., Wong, Y.S. and Chen, T., Selective cellular uptake and induction of apoptosis of cancer-targeted selenium nanoparticles. *Biomaterials*, 34, 7106-7016 (2013b).
107. Hussain, S., Al-Nsour, F., Rice, A. B., Marshburn, J., Yingling, B., Ji, Z. X., Zink, J. I., Walker, N. J. and Garantziotis, S., Cerium dioxide nanoparticles induce apoptosis and autophagy in human peripheral blood monocytes. *ACS Nano*, 6, 5820-5829 (2012).
108. Hussain, S., Malik, A H., Afroz, A.M. and Iyer, P.K. Ultrasensitive detection of nitro explosive-picric acid *via* conjugated polyelectrolyte in aqueous media and solid support. *Chem. Commun.*, 51, 7207-7210 (2015).
109. Huynh, D.P., Im, G.J., Chae, S.Y., Lee, K.C. and Lee, D.S., Controlled release of insulin from pH/temperature-sensitive injectable pentablock copolymer hydrogel. *J. Control. Release*, 137, 20-24 (2009).
110. Im, J.S., Bai, B.C., In, S.J. and Lee, Y.S., Improved photodegradation properties and kinetic models of a solar-light-responsive photocatalyst when incorporated into electrospun hydrogel fibers. *J. Colloid Interface Sci.*, 346, 216–221 (2010).
111. Jaiswal, A., Ghosh, S.S. and Chattopadhyay, A., One step synthesis of C-dots by microwave mediated caramelization of poly(ethylene glycol). *Chem. Commun.*, 48, 407-409 (2012).
112. Janib, S. M., Moses, A. S. and MacKay, J. A., Imaging and drug delivery using theranostic nanoparticles. *Adv. Drug Delivery Rev.*, 62, 1052-1063 (2010).
113. Jia, X., Li, J. and Wang, E., One-pot green synthesis of optically pH-sensitive carbon dots with upconversion luminescence. *Nanoscale*, 4, 5572-5575 (2012).
114. Jiang, H., Chen, F., Lagally, M.G. and Denes, F.S., New strategy for synthesis and functionalization of carbon nanoparticles. *Langmuir*, 26, 1991-1995 (2010).
115. Jin, S., Gu, J., Shi, Y., Shao, K., Yu, X. and Yue, G., Preparation and electrical sensitive behavior of poly (N-vinylpyrrolidone-co-acrylic acid) hydrogel with flexible chain nature. *Eur. Polym. J.*, 49, 1871-1880 (2013b).
116. Jin, S.H., Kim da, H., Jun, G.H., Hong, S.H. and Jeon, S., Tuning the photoluminescence of graphene quantum dots through the charge transfer effect of functional groups. *ACS Nano*, 2, 1239-1245 (2013a).

117. Kairdolf, B.A., Smith, A.M., Stokes, T.H., Wang, M.D., Young, A.N. and Nie, S., Semiconductor quantum dots for bioimaging and biodiagnostic applications. *Annu. Rev. Anal. Chem.*, 6, 143-162 (2013).

118. Kamali, K.Z., Pandikumar, A., Sivaraman, G., Lim, H.N., Wren, S.P., Sund, T. and Huang, N.M., Silver@graphene oxide nanocomposite-based optical sensor platform for biomolecules. *RSC Adv.*, 5, 17809-17816 (2015).

119. Karakoti, A.S., Monteiro-Riviere, N.A., Aggarwal, R., Davis, J.P., Narayan, R.J., Self, W.T., McGinnis, J. and Seal, S., Nanoceria as antioxidant: synthesis and biomedical applications. *JOM*, 60, 33-37 (2008).

120. Karthik, S., Saha, B., Ghosh, S.K. and Pradeep Singh, N.D., Photoresponsive quinoline tethered fluorescent carbon dots for regulated anticancer drug delivery. *Chem. Commun.*, 49, 10471-10473 (2013).

121. Kashyap, N., Viswanad, B., Sharma, G., Bhardwaj, V., Ramarao, P. and Ravi Kumar, M.N., Design and evaluation of biodegradable, biosensitive in situ gelling system for pulsatile delivery of insulin. *Biomaterials*, 28, 2051-2060 (2007).

122. Kelkar, S.S. and Reineke, T.M., Theranostics: combining imaging and therapy. *Bioconjug. Chem.*, 22, 1879-1903 (2011).

123. Khan, M. M., Ansari, S.A., Ansari, M.O., Min, B.K., Lee, J. and Cho, M.H., Biogenic fabrication of Au@CeO2 nanocomposite with enhanced visible light activity. *J. Phys. Chem. C*, 118, 9477-9484 (2014).

124. Khan, S., Gupta, A., Verma, N.C. and Nandi, C.K., Time-resolved emission reveals ensemble of emissive states as the origin of multicolor fluorescence in carbon dots. *Nano Lett.*, 15, 8300-8305 (2015a).

125. Khan, S., Verma, N.C., Gupta, A. and Nandi, C.K., Reversible photoswitching of carbon dots. *Sci Rep.*, 5, 11423 (2015b).

126. Khlebtsov, B.N., Khanadeyev, V.A. and Khlebtsov, N.G., Collective plasmon resonances in monolayers of metal nanoparticles and nanoshells. *Optics and Spectroscopy*, 104, 324-337 (2008).

127. Khlebtsov, B.N., Tuchina, E., Tuchin, V. and Khlebtsov, N.G., Multifunctional Au nanoclusters for targeted bioimaging and enhanced photodynamic inactivation of Staphylococcus aureus. *RSC Adv.*, 5, 61639-61649 (2015).

128. Kim, J., Park, J., Kim, H., Singha, K. and Kim, W.J., Transfection and intracellular trafficking properties of carbon dot-gold nanoparticle molecular assembly conjugated with PEI-pDNA. *Biomaterials*, 34, 7168-7180 (2013).

129. Kleinauskas, A., Rocha, S., Sahu, S., Sun, Y.P. and Juzenas, P., Carbon-core silver-shell nanodots as sensitizers for phototherapy and radiotherapy. *Nanotechnology*, 24, 325103 (2013).

130. Kluck, R.M., Wetzel-Bossy, E., Green, D.R. and Newmeyer, D.D., The release of cytochrome c from mitochondria: a primary site for Bcl-2 regulation of apoptosis. *Science*, 275, 1132-1136 (1997).

131. Komarneni, S., Nanophase materials by hydrothermal, microwave, hydrothermal and microwave-solvothermal methods. *Current Science*, 85, 1730-1734 (2003).

132. Kong, B., Zhu, A., Ding, C., Zhao, X., Li, B. and Tian, Y., Carbon dot-based inorganic-organic nanosystem for two-photon imaging and biosensing of pH variation in living cells and tissues. *Adv. Mater.*, 24, 5844-5848 (2012).

133. Kong, W., Liu, R., Li, H., Liu, J., Huang, H., Liu, Y. and Kang, Z., High-bright fluorescent carbon dots and their application in selective nucleoli staining. *J. Mater. Chem. B*, 2, 5077-5082 (2014).

134. Koninti, R.K., Sengupta, A., Gavvala, K., Ballav, N. and Hazra, P., Loading of an anti-cancer drug onto graphene oxide and subsequent release to DNA/RNA: a direct optical detection. *Nanoscale*, 6, 2937-2944 (2014).

135. Konwar, A., Gogoi, N., Majumdar, G. and Chowdhury, D., Green chitosan–carbon dots nanocomposite hydrogel film with superior properties. *Carbohydr. Polym*., 115, 238-245 (2015).

136. Korsvik, C., Patil, S., Seal, S. and Self, W.T., Superoxide dismutase mimetic properties exhibited by vacancy engineered ceria nanoparticles. *Chem. Commun. (Camb)*, 14, 1056-1058 (2007).

137. Kumar, A. and Gupta, S.K., 5′-Guanosine monophosphate mediated biocompatible porous hydrogel of β-FeOOH- viscoelastic behavior, loading, and release capabilities of freeze-dried gel. *J. Phys. Chem B*, 118, 10543-10551 (2014).

138. Kumar, B., Koul, S., Khandrika, L., Meacham, R.B. and Koul, H.K., Oxidative stress is inherent in prostate cancer cells and is required for aggressive phenotype. *Cancer Res.*, 68, 1777-1785 (2008).

139. Kumar, M.N., Muzzarelli, R.A., Muzzarelli, C., Sashiwa, H. and Domb, A.J., Chitosan chemistry and pharmaceutical perspectives. *Chem. Rev.*, 104, 6017-6084 (2004).

140. Kumar, S.U., Bhushan, B., Dubey, P., Matai, I., Sachdev, A. and Gopinath, P., Emerging applications of nanoparticles for lung cancer diagnosis and therapy. *Int. Nano Lett.*, 3, 45-53 (2013).

141. Kwon, W., Do, S., Kim, J.H., Seok Jeong, M.M. and Rhee, S.W., *Sci Rep.*, 5, 12604 (2015).

142. Lakowicz, J.R., Principles of fluorescence spectroscopy. *Springer*, Berlin (1999).

143. Lan, M., Di, Y., Zhu, X., Ng, T.W., Xia, J., Liu, W., Meng, X., Wang, P., Lee, C.S. and Zhang, W.A., A carbon dot-based fluorescence turn-on sensor for hydrogen peroxide with a photo-induced electron transfer mechanism. *Chem. Commun.*, 51, 15574-15577 (2015).

144. Lawrie, G., Keen, I., Drew, B., Chandler-Temple, A., Rintoul, L., Fredericks, P. and Grøndahl, L., Interactions between alginate and chitosan biopolymers characterized using FTIR and XPS. *Biomacromolecules*, 8, 2533-2541 (2007).

145. Lee, C.H., Rajendran, R., Jeong, M.Y., Ko, H.Y., Joo, J.Y., Cho, S., Chang, Y.K. and Kim, S., Bioimaging of targeting cancers using aptamer-conjugated carbon nanodots. *Chem. Commun*., 49, 6543-6345 (2013b).

146. Lee, S.S., Song, W., Cho, M., Puppala, H.L., Nguyen, P., Zhu, H., Segatori, L. and Colvin, V.L., Antioxidant properties of cerium oxide nanocrystals as a function of nanocrystal diameter and surface coating. *ACS Nano*, 7, 9693-9703 (2013a).

147. Li, C.L., Huang, C.C., Periasamy, A.P., Roy, P., Wu, W.C., Hsu, C.L. and Chang, H.T., Synthesis of photoluminescent carbon dots for the detection of cobalt ions. *RSC Adv.*, 5, 2285-2291 (2015b).

148. Li, C.L., Ou, C.M., Huang, C.C., Wu, W.C., Chen, Y.P., Lin, T.E., Ho, L.C., Wang, C.W., Shih, C.C., Zhou, H.C., Lee, Y.C., Tzeng, W.F., Chiou, T.Z., Chu, S.T., Cang, J. and Chang, H.T., Carbon dots prepared from ginger exhibiting efficient inhibition of human hepatocellular carcinoma cells. *J. Mater. Chem. B*, 2, 4564-4571 (2014a).

149. Li, F., Hong, W., Zhang, H., Li, F., Gu, C. and Yang, Q., Antitumor drug paclitaxel-loaded pH-sensitive nanoparticles targeting tumor extracellular pH. *Carbohydr. Polym.*, 77, 773-778 (2009).

150. Li, H., Kang, Z., Liu, Y. and Lee, S.T., Carbon nanodots: synthesis, properties and applications. *J. Mater. Chem.*, 22, 24230-24253 (2012a).

151. Li, H., Liu, J., Yang, M., Kong, W., Huang, H. and Liu, Y., Highly sensitive, stable, and precise detection of dopamine with carbon dots/tyrosinase hybrid as fluorescent probe. *RSC Adv.*, 4, 46437-46443 (2014b).

152. Li, H.L., Zhang, Y.W., Wang, L., Tian, J.Q. and Sun, X.P., Nucleic acid detection using carbon nanoparticles as a fluorescent sensing platform. *Chem. Commun*., 47, 961-963 (2011c).

153. Li, H.T., He, X.D., Kang, Z.H., Huang, H., Liu, Y., Liu, J.L., Lian, S.Y., Tsang, C. H. A., Yang, X.B. and Lee, S.T., Water-soluble fluorescent carbon quantum dots and photocatalyst design. *Angew. Chem., Int. Ed.*, 49, 4430-4434 (2010b).

154. Li, J., Zhang, B., Wang, F. and Liu, C.Y., Silver/carbon-quantum-dot plasmonic luminescent nanoparticles. *New J. Chem.,* 35, 554-557 (2011a).

155. Li, LL, Wu, G.H., Yang, G.H., Peng, J., Zhao, J.W. and Zhu, J.J., Focusing on luminescent graphene quantum dots: current status and future perspectives. *Nanoscale*, 5, 4015-4039 (2013c).

156. Li, M.H., Ito, D., Sanada, M., Odani, T., Hatori, M., Iwase, M. and Nagumo, M., Effect of 5-fluorouracil on G1 phase cell cycle regulation in oral cancer cell lines. *Oral Oncol.*, 40, 63-70 (2004).

157. Li, N, Liang, X., Wang, L., Li, Z., Li, P., Zhu, Y. and Song, J., Biodistribution study of carbogenic dots in cells and *in vivo* for optical imaging. *J. Nanopart. Res.*, 14, 1177-1185 (2012b).

158. Li, P., Wang, Y., Peng, Z., She, F. and Kong, L., Development of chitosan nanoparticles as drug delivery systems for 5-fluorouracil and leucovorin blends. *Carbohydr. Polym.*, 85, 698-704 (2011b).

159. Li, Q., Ohulchanskyy, T.Y., Liu, R., Koynov, K., Wu, D., Best, A., Kumar, R., Bonoiu, A. and Prasad, P.N., Photoluminescent carbon dots as biocompatible nanoprobes for targeting cancer cells *in vitro*. *J. Phys. Chem. C*, 114, 12062-12068 (2010a).

160. Li, W., Yue, Z., Wang, C., Zhang, W. and Liu, G., An absolutely green approach to fabricate carbon nanodots from soya bean grounds. *RSC Adv.*, 3, 20662-20665 (2013a).

161. Li, Z., Xu, W., Wang, Y., Shah, B.R., Zhang, C., Chen, Y., Li, Y. and Li, B., Quantum dots loaded nanogels for low cytotoxicity, pH-sensitive fluorescence, cell imaging and drug delivery. *Carbohydr. Polym.*, 121, 477-485 (2015a).

162. Liang, Q., Ma, W., Shi, Y., Li, Z. and Yang, X., Easy synthesis of highly fluorescent carbon quantum dots from gelatin and their luminescent properties and applications *Carbon*, 60, 421-428 (2013b).

163. Liang, Z., Zeng, L., Cao, X., Wang, Q., Wang, X. and Sun, R., Sustainable carbon quantum dots from forestry and agricultural biomass with amplified photoluminescence by simple NH_4OH passivation. *J. Mater. Chem. C*, 2, 9760-9766 (2014).

164. Lim, S. Y., Shen, W. and Gao, Z., Carbon quantum dots and their applications. *Chem. Soc. rev.*, 44, 362-381 (2015).

165. Lin, W. S., Huang, Y. W., Zhou, X. D. and Ma, Y.F., Toxicity of cerium oxide nanoparticles in human lung cancer cells. *Int. J. Toxicol.*, 25, 451-457 (2006).

166. Liu , C., Zhang, P., Zhai, X., Tian, F., Li, W., Yang, J., Liu, Y., Wang, H., Wang, W. and Liu, W, Nano-carrier for gene delivery and bioimaging based on carbon dots with PEI-passivation with enhanced fluorescence. *Biomaterials*, 33, 3604-3613 (2012a).

167. Liu, B., Sun, Z., Huang, P.J. and Liu, J., Hydrogen peroxide displacing DNA from nanoceria: mechanism and detection of glucose in serum. *J. Am. Chem. Soc.*, 137, 1290-1295 (2015a).

168. Liu, C. J., Zhang, P., Tian, F., Li, W.C., Li, F. and Liu, W.G., One-step synthesis of surface passivated carbon nanodots by microwave assisted pyrolysis for enhanced multicolor photoluminescence and bioimaging. *J. Mater. Chem.*, 21, 13163-13167 (2011).

169. Liu, H.P., Ye, T. and Mao, C.D., Preparation of fluorescent carbon nanoparticles from candle soot. *Angew. Chem., Int. Ed.*, 46, 6473-6475 (2007).

170. Liu, L., Yu, M., Duan, X. and Wang, S., Conjugated polymers as multifunctional biomedical platform: anticancer activity and apoptosis imaging. *J. Mater. Chem.*, 20, 6942-6947 (2010).

171. Liu, S., Tian, J., Wang, L., Zhang, Y., Qin, X., Luo, Y., Asiri, A.M., Al-Youbi, A.O. and Sun, X., Hydrothermal treatment of grass: A low-cost, green route to nitrogen-doped, carbon-rich, photoluminescent polymer nanodots as an effective fluorescent sensing platform for label-free detection of Cu(II) ions. *Adv. Mater.*, 24, 2037-2041 (2012d).

172. Liu, W., Li, X., Wong, Y.S., Zheng, W., Zhang, Y., Cao, W. and Chen, T., Selenium nanoparticles as a carrier of 5-fluorouracil to achieve anticancer synergism. *ACS Nano*, 6, 6578-6591 (2012b).

173. Liu, Y., Wu, H., Chong, Y., Wamer, W.G., Xia, Q., Cai, L., Nie, Z., Fu, P.P. and Yin, J.J., Platinum nanoparticles: Efficient and stable catechol oxidase mimetics. *ACS Appl. Mater. Interfaces*, 7, 19709-19717 (2015b).

174. Liu, Y., Yin, J.J. and Nie, Z., Harnessing the collective properties of nanoparticle ensembles for cancer theranostics. *Chem. Eur. J.*, 7, 1719-1730 (2014a).

175. Liu, M., Zhang, X., Yang, B., Deng, F., Huang, Z. and Yang, Y., Huang, Z., Zhang, X. and Wei, Y., Luminescence tunable fluorescent organic nanoparticles from polyethyleneimine and maltose: facile preparation and bioimaging applications. *RSC Adv.*, 4, 22294-22298 (2014b).

176. Liu, X., Wei, W., Yuan, Q., Zhang, X., Li, N., Du, Y., Ma, G., Yan, C. and Ma, D., Apoferritin–CeO_2 nano-truffle that has excellent artificial redox enzyme activity. *Chem. Commun.*, 48, 3155-3157 (2012c).

177. Lord, M.S., Jung, M., Teoh, W.Y., Gunawan, C., Vassie, J.A., Amal, R. and Whitelock, J.M., Cellular uptake and reactive oxygen species modulation of cerium oxide nanoparticles in human monocyte cell line U937. *Biomaterials*, 33, 7915-7924 (2012).

178. Lu, J., Yang, J., Wang, J., Lim, A., Wang, S. and Loh, K., One-pot synthesis of fluorescent carbon nanoribbons, nanoparticles, and graphene by the exfoliation of graphite in ionic liquids. *ACS Nano*, 3, 2367-2375 (2009).

179. Lu, W., Qin, X., Liu, S., Chang, G., Zhang, Y., Luo, Y., Asiri, A.M., Al-Youbi, A,O. and Sun, X., Economical, green synthesis of fluorescent carbon nanoparticles and their use as probes for sensitive and selective detection of mercury(II) ions. *Anal Chem.*, 84, 5351-5357 (2012).

180. Luo, P. G., Sahu, S., Yang, S.T., Sonkar, S.K., Wang, J., Wang, H., LeCroy, G. E., Cao L. and Y.P. Sun, Carbon "quantum" dots for optical bioimaging. *J. Mater. Chem. B*, 1, 2116-2127 (2013).

181. Luo, P., Li, C. and Shi, G., Synthesis of gold@carbon dots composite nanoparticles for surface enhanced Raman scattering. *Phys. Chem. Chem. Phys.*, 14, 7360-7366 (2012).

182. Ma, Z., Ming, H., Huang, H., Liu, Y. and Kang, Z., One-step ultrasonic synthesis of fluorescent N-doped carbon dots from glucose and their visible-light sensitive photocatalytic ability. *New J. Chem.*, 36, 861-864 (2012).

183. Maksimova, I.L., Akchurin, G.G., Terentyuk, G.S., Khlebtsov, B.N., Akchurin G.G. Jr., Ermolaev, I.A., Skaptsov, A.A., Revzina, E.M., Tuchin, V.V. and Khlebtsov N.G., Laser photothermolysis of biological tissues by using plasmon-resonance particles. *Quantum Electronics*, 38, 536-542 (2008).

184. Malik, A.H., Hussain, S., Tanwar, A., Layek, S., Trivedi, V. and Iyer, P.K., Anionic conjugated polymer as a multi-action sensor for the sensitive detection of Cu^{2+}, PPi, real-time ALP assaying and cell imaging. *Analyst*, 140, 4388-4392 (2015).

185. Mao, G.Y., Yang, W.J., Bu, F.X., Jiang, D.M., Zhao, Z.J., Zhang, Q.H., Fang, Q.C. and Jiang, J.S., One-step hydrothermal synthesis of Fe_3O_4@C nanoparticles with great performance in biomedicine. *J. Mater. Chem. B*, 2, 4481-4488 (2014).

186. Matai, I., Sachdev, A. and Gopinath, P., Multicomponent 5- fluorouracil loaded PAMAM stabilized-silver nanocomposites synergistically induce apoptosis in human cancer cells. *Biomater. Sci.*, 3, 457-468 (2015).

187. Matai, I., Sachdev, A., Dubey, P., Kumar, S.U., Bhushan, B. and Gopinath, P., Antibacterial activity and mechanism of Ag–ZnO nanocomposite on *S. aureus* and GFP-expressing antibiotic resistant *E. coli*. *Colloids Surf B Biointerfaces*, 115, 359-367 (2014).

188. Matai, I., Sachdev, A. and Gopinath, P., Self-assembled hybrids of fluorescent carbon dots and PAMAM dendrimers for epirubicin delivery and intracellular imaging. *ACS Appl. Mater. Interfaces*, 21, 11423-11435 (2015).

189. Mazurak, V.C., Burrell, R.E., Tredget, E.E., Clandinin, M.T. and Field, C.J., The effect of treating infected skin grafts with Acticoat on immune cells. *Burns*, 33, 52-58 (2007).

190. Mehta, V.N., Jha, S., Singhal, R.K. and Kailasa, S.K., Preparation of multicolor emitting carbon dots for HeLa cell imaging. *New J. Chem.*, 38, 6152-6160 (2014).

191. Mewada, A., Pandey, S., Shinde, S., Mishra, N., Oza, G., Thakur, M., Sharon, M. and Sharon, M., Green synthesis of biocompatible carbon dots using aqueous extract of Trapa bispinosa peel. *Mater. Sci. Eng. C*, 33, 2914-2917 (2013).

192. Mewada, A., Pandey, S., Thakur, M., Jadhav, D. and Sharon, M., Swarming carbon dots for folic acid mediated delivery of doxorubicin and biological imaging. *J. Mater. Chem. B*, 2, 698-705 (2014).

193. Mitra, S., Chandra, S., Pathan, S.H., Sikdar, N., Pramanik, P. and Goswami, A., Room temperature and solvothermal green synthesis of self passivated carbon quantum dots. *RSC Adv.*, 3, 3189-3193 (2013).

194. Mody, V.V., Siwale, R., Singh, A. and Mody, H.R., Introduction to metallic nanoparticles. *J. Pharm. Bioallied. Sci.*, 2, 282–289 (2010).

195. Mondal, P., Ghosal, K., Bhattacharyya, S.K., Das, M., Bera, A., Ganguly, D., Kumar, P., Dwivedi, J., Gupta, R. K., Martí, A.A., Gupta, B.K. and Maiti, S., Formation of gold-carbon dot nanocomposite with superior catalytic ability towards reduction of aromatic nitro group in water. *RSC Adv.*, 4, 25863-25866 (2014).

196. Monteiro, O.A.C. and Airoldi, C., Some studies of crosslinking chitosan-glutaraldehyde interaction in a homogeneous system, *Int. J. Biol.Macromol.*, 26, 119-128 (1999).

197. Moos, P.J., Chung, K., Woessner, D., Honeggar, M., Cutler, N.S. and Veranth, J.M., ZnO particulate matter requires cell contact for toxicity in human colon cancer cells. *Chem. Res. Toxicol.*, 23, 733-739 (2010).

198. Moura, M.J., Gil, M.H. and Figueiredo, M.M., Delivery of cisplatin from thermosensitive co-cross-linked chitosan hydrogels. *Eur. Polym. J.*, 49, 2504-2510 (2013).

199. Moura, M.J., Faneca, H., Lima, M.P., Gil, M.H. and Figueiredo, M.M., *In situ* forming chitosan hydrogels prepared via ionic/covalent co-cross-linking. *Biomacromolecules*, 12, 3275-3284 (2011).

200. Mukherjee, S., Chowdhury, D., Kotcherlakota, R., Patra, S., Vinothkumar, B., Bhadra, M.P., Sreedhar, B. and Patra, C.R., Potential theranostics application of bio-synthesized silver nanoparticles (4-in-1 System). *Theranostics*, 4, 316-335 (2014).

201. Muzzarelli, R.A.A., Human enzymatic activities related to the therapeutic administration of chitin derivatives. *Cell. Mol. Life Sci.*, 53, 131-140 (1997).

202. Nagarwal, R.C., Singh, P.N., Kant, S., Maiti, P. and Pandit, J.K., Chitosan nanoparticles of 5-Fluorouracil for ophthalmic delivery: characterization, *in vitro* and *in vivo* study. *Chem. Pharm. Bull (Tokyo)*, 59, 272-280 (2011).

203. Nair, S., Sasidharan, A., Divya Rani, V.V., Menon, D., Nair, S., Manzoor, K., Raina, S., Role of size scale of ZnO nanoparticles and microparticles on toxicity toward bacteria and osteoblast cancer cells. *J. Mater. Sci. Mater. Med.*, 20, 235-241 (2009).

204. Nandi, S., Ritenberg, M and Jelinek, R., Bacterial detection with amphiphilic carbon dots. *Analyst*, 140, 4232-4237 (2015).

205. Nie, H., Li, M., Li, Q., Liang, S., Tan, Y., Sheng, L., Shi, W. And Zhang, S. X.A., Carbon dots with continuously tunable full-color emission and their application in ratiometric pH sensing. *Chem.Mater.*, 26, 3104-3112 (2014).

206. Ornatska, M., Sharpe, E., Andreescu, D. and Andreescu, S., Paper bioassay based on ceria nanoparticles as colorimetric probes. *Anal. Chem.*, 83, 4273-4280 (2011).

207. Pan, D.Y., Zhang, J.C., Li, Z. and Wu, M.H., Hydrothermal route for cutting graphene sheets into blue-luminescent graphene quantum dots. *Adv Mater*., 22, 734-738 (2010).

208. Pandey, S., Thakur, M., Mewada, A., Anjarlekar, D., Mishra, N. and Sharon**,** M., Carbon dots functionalized gold nanorod mediated delivery of doxorubicin: tri-functional nano-worms for drug delivery, photothermal therapy and bioimaging. *J . Mater. Chem. B*, 1, 4972-4982 (2013).

209. Panfilova, E., Shirokov, A., Khlebtsov, B.N., Matora, L. and Khlebtsov, N.G., Multiplexed dot immunoassay using Ag nanocubes, Au/Ag alloy nanoparticles, and Au/Ag nanocages. *NanoRes.*, 5, 124-134 (2012).

210. Park, E. J., Choi, J., Park, Y. K. and Park, K., Oxidative stress induced by cerium oxide nanoparticles in cultured BEAS-2B cells. *Toxicology*, 245, 90-100 (2008).
211. Park, S.Y., Lee, H.U., Park, E.S., Lee, S.C., Lee, J.W., Jeong, S.W., Kim, C.H., Lee, Y.C., Huh, Y.S. and Lee, J., Photoluminescent green carbon nanodots from food-waste derived sources: large-scale synthesis, properties and biomedical applications. *ACS Appl. Mater. Interfaces*, 6, 3365-3370 (2014).
212. Park, Y., Yoo, J., Lim, B., Kwon, W. and Rhee, S.W. Improving the functionality of carbon nanodots: doping and surface functionalization. *J. Mater. Chem. A*, 4, 11582-11603 (2016).
213. Parveen, S., Misra, R. and Sahoo, S.K., Nanoparticles: a boon to drug delivery, therapeutics, diagnostics and imaging. *Nanomedicine*, 8, 147-166 (2012).
214. Payne, G.F. and Raghavan, S.R., Chitosan: a soft interconnect for hierarchical assembly of nano-scale components. *Soft Matter*, 3, 521-527 (2007).
215. Peng, H. and Travas-Sejdic, J., A simple aqueous solution route to luminescent carbogenic dots from carbohydrates. *Chem. Mater.*, 21, 5563-5565 (2009).
216. Peng, H. T., Martineau, L. and Shek, P. N., Hydrogel-elastomer composite biomaterials: Preparation of interpenetrating polymer networks and *in vitro* characterization of swelling stability and mechanical properties. *J. Mater. Sci.-Mater. Med.*, 18, 975-986 (2007).
217. Peppas N.A. and Merrill, E.W., Differential scanning calorimetry of crystallized PVA hydrogels. *J. Appl. Polym. Sci.*, 20, 1457-1465 (1976).
218. Peppas, N.A. and Sahlin, J.J., Hydrogels as mucoadhesive and bioadhesive materials: a review. *Biomaterials*, 17, 1553-1561 (1996).
219. Peppas, N.A., Bures, P., Leobandung, W. and Ichikawa, H., Hydrogels in pharmaceutical formulations. *Eur. J. Pharm. Biopharm.*, 50, 27-46 (2000b).
220. Peppas, N.A., Huang, Y., Torres-Lugo, M., Ward, J.H and Zhang, J., Physicochemical foundations and structural design of hydrogels in medicine and biology. *Annu. Rev. Biomed. Eng.*, 2, 9-29 (2000a).
221. Perez, J.M., Asati, A., Nath, S. and Kaittanis, C., Synthesis of biocompatible dextran-coated nanoceria with pH-dependent antioxidant properties. *Small*, 4, 552-556 (2008).
222. Petryayeva, E., Algar, W.R. and Medintz, I.L., Quantum dots in bioanalysis: a review of applications across various platforms for fluorescence spectroscopy and imaging. *Appl. Spectrosc.*, 67, 215-252 (2013).

223. Pierrat, P., Wang, R., Kereselidze, D., Lux, M., Didier, P., Kichler, A., Pons, F. and Lebeau, L., Efficient *in vitro* and *in vivo* pulmonary delivery of nucleic acid by carbon dot-based nanocarriers. *Biomaterials*, 51, 290-302 (2015).

224. Pirmohamed, T., Dowding, J.M., Singh, S., Wasserman, B., Heckert, E., Karakoti, A.S., King, J.E., Seal, S. and Self, W.T., Nanoceria exhibit redox state-dependent catalase mimetic activity. *Chem. Commun.*, 46, 2736-2738 (2010).

225. Ponomarenko, L.A., Schedin, F., Katsnelson, M.I., Yang, R., Hill, E.W., Novoselov, K.S. and Geim, A.K., Chaotic dirac billiard in graphene quantum dots. *Science*, 320, 356-358 (2008).

226. Premanathan, M., Karthikeyan, K., Jeyasubramanian,K. and Manivannan, G., Selective toxicity of ZnO nanoparticles toward gram-positive bacteria and cancer cells by apoptosis through lipid peroxidation. *Nanomed. Nanotechnol. Biol. Med.*, 7, 184-192 (2011).

227. Purkayastha, M.D., Manhar, A.K., Das, V.K., Borah, A., Mandal, M., Thakur, A.J. and Mahanta, C.L., Antioxidative, hemocompatible, fluorescent carbon nanodots from an "end-of-pipe" agricultural waste: exploring its new horizon in the food-packaging domain. *J Agric Food Chem.*, 62, 4509-4520 (2014).

228. Pylaev, T.E., Khanadeev, V.A., Khlebtsov, B.N., Dykman, L.A., Bogatyrev, V.A. and Khlebtsov, N.G., Colorimetric and dynamic light scattering detection of DNA sequences by using positively charged gold nanospheres: a comparative study with gold nanorods. *Nanotechnology*, 22, 285501-285511 (2011).

229. Pyrzynska, K. and Pekal, A., Application of free radical diphenylpicrylhydrazyl (DPPH) to estimate the antioxidant capacity of food samples. *Anal. Methods*, 5, 4288-4295 (2013).

230. Qin, X.Y., Lu, W.B., Asiri, A.M., Al-Youbi, A.O. and Sun, X.P., Green, low-cost synthesis of photoluminescent carbon dots by hydrothermal treatment of willow bark and their application as an effective photocatalyst for fabricating Au nanoparticles–reduced graphene oxide nanocomposites for glucose detection, *Catal. Sci.Technol.*, 3, 1027-1035 (2013a).

231. Qin, X.Y., Lu, W.B., Asiri, A.M., Al-Youbi, A.O. and Sun, X.P., Microwave-assisted rapid green synthesis of photoluminescent carbon nanodots from flour and their applications for sensitive and selective detection of mercury(II) ions. *Sensors and Actuators B*, 184, 156-162 (2013b).

232. Qu, S., Zhou, D., Li, D., Ji, W., Jing, P., Han, D., Liu, L., Zeng, H. and Shen, D. Toward efficient orange emissive carbon nanodots through conjugated sp(2) -domain controlling and surface charges engineering. *Adv Mater.*, 28, 3516-3521 (2016).

233. Rasmussen, J.W., Martinez, E., Louka, P. and Wingett, D.G., Zinc oxide nanoparticles for selective destruction of tumor cells and potential for drug delivery applications. *Expert Opin Drug Deliv.*, 7, 1063-1077 (2010).

234. Ratnam, D.V., Ankola, D.D., Bhardwaj, V., Sahana, D.K. and Ravi Kumar, M.N., Role of antioxidants in prophylaxis and therapy: A pharmaceutical perspective. *J. Control Release.*, 113, 189-207 (2006).

235. Ravibabu, V., Hussain, S., Iyer, P.K., Pugazhenthi, G. and Katiyar, V., Non-isothermal crystallization kinetics of sucrose palmitate reinforced poly(lactic acid) bionanocomposites. *Polym. Bull.*, 73, 21-38 (2016).

236. Ray, P.D., Huang, B.W. and Tsuji, Y., Reactive oxygen species (ROS) homeostasis and redox regulation in cellular signaling. *Cell Signal*, 24, 981-990 (2012).

237. Ray, S. C., Saha, A., Jana, N.R. and Sarkar, R., Fluorescent carbon nanoparticles: synthesis, characterization, and bioimaging application. *J. Phys. Chem. C*, 113, 18546-18551 (2009).

238. Reddy, K.M., Feris, K., Bell, J., Wingett, D.G., Hanley, C. and Punnoose, A., Selective toxicity of zinc oxide nanoparticles to prokaryotic and eukaryotic systems. *Appl. Phys.Lett.*, 90, 213902-213903 (2007).

239. Ritenberg, M., Nandi, S., Kolusheva, S., Dandela, R., Meijlerand, M.M. and Jelinek, R., Imaging pseudomonas aeruginosa biofilm extracellular polymer scaffolds with amphiphilic carbon dots. *ACS Chem. Biol.*, doi: 10.1021/acschembio.5b01000 (2016).

240. Ruan, S., Qian, J., Shen, S., Chen, J., Zhu, J., Jiang, X., He, Q., Yang, W. and Gao, H., Fluorescent carbonaceous nanodots for noninvasive glioma imaging after angiopep-2 decoration. *Bioconjug. Chem.*, 25, 2252-2259 (2014).

241. Ruedas-Rama, M.J., Walters, J.D., Orte, A. and Hall, E.A., Fluorescent nanoparticles for intracellular sensing: a review. *Anal. Chim. Acta.*, 751, 1-23 (2012).

242. Ruel-Gariépy, E., Shive, M., Bichara, A., Berrada, M., Le Garrec, D., Chenite, A. and Leroux J.C., A thermosensitive chitosan-based hydrogel for the local delivery of paclitaxel. *Eur. J. Pharm. Biopharm.*, 57, 53-63 (2004).

243. Ruiz, J., Mantecon, A. and Cadiz, V., Synthesis and properties of hydrogels from poly(vinyl alcohol) and ethylenediaminetetraacetic dianhydride. *Polymer*, 42, 6347-6354 (2001).

244. Rurup, W.F., Verbij, F., Koay, M.S.T., Blum, C., Subramaniam, V. and Cornelissen, J.J.L.M., Predicting the loading of virus-like particles with fluorescent proteins. *Biomacromolecules*, 15, 558-563. (2014).

245. Sachdev, A. and Gopinath, P., Green synthesis of multifunctional carbon dots from coriander leaves and their potential application as antioxidants, sensors and bioimaging agents. *Analyst*, 140, 4260-4269 (2015a).

246. Sachdev, A., Matai, I. and Gopinath, P., Dual-functional carbon dots–silver@zinc oxide nanocomposite: *In vitro* evaluation of cellular uptake and induction of apoptosis. *J. Mater. Chem. B*, 3, 1217-1229 (2015b).

247. Sachdev, A., Matai, I. and Gopinath, P., Implications of surface passivation on physicochemical and bioimaging properties of carbon dots. *RSC Adv.*, 4, 20915-20921 (2014).

248. Sachdev, A., Matai, I., Kumar, S.U., Bhushan, B., Dubey P. and Gopinath, P., A novel one-step synthesis of PEG passivated multicolour fluorescent carbon dots for potential biolabeling application. *RSC Adv.*, 3, 16958-16961 (2013).

249. Saha, T., Sengupta A., Hazra, P. and Talukdar, P., *In vitro* sensing of Cu^{+} through a green fluorescence rise of pyranine. *Photochem. Photobiol. Sci.*, 13, 1427-1433 (2014).

250. Sahu, S., Behera, B., Maiti, T.K. and Mohapatra, S., Simple one-step synthesis of highly luminescent carbon dots from orange juice: application as excellent bio-imaging agents. *Chem. Commun.*, 48, 8835-8837 (2012).

251. Salata, O.V., Applications of nanoparticles in biology and medicine. *J Nanobiotechnology*, 2, 3 (2004).

252. Sanpui, P., Chattopadhyay, A. and Ghosh, S.S., Induction of apoptosis in cancer cells at low silver nanoparticle concentrations using chitosan nanocarrier. *ACS Appl. Mater. Interfaces*, 3, 218-228 (2011).

253. Schilling, K., Bradford, B., Castelli, D., Dufour, E., Nash, J.F., Pape, W., Schulte, S., Tooley, I., Van den Bosch, J. and Schellauf, F., Human safety review of ‘‘nano’’ titanium dioxide and zinc oxide. *Photochem. Photobiol. Sci.*, 9, 495-509 (2010).

254. Schmid, G., Baumle, M., Geerkens, M., Heim, I., Osemann, C. and Sawitowski, T., Current and future applications of nanoclusters. *Chem. Soc. Rev.*, 28, 179-185 (1999).

255. Schütz, C.A., Juillerat-Jeanneret, L., Käuper, P. and Wandrey, C., Cell response to the exposure to chitosan-TPP//alginate nanogels. *Biomacromolecules*, 12, 4153-4161.

256. Shan, X., Chai, L., Ma, J., Qian, Z., Chen, J. and Feng, H., B-doped carbon quantum dots as a sensitive fluorescence probe for hydrogen peroxide and glucose detection. *Analyst*, 139, 2322-2325 (2014).

257. Sharma, S., Chockalingam, S., Sanpui, P., Chattopadhyay, A. and Ghosh, S.S., Silver nanoparticles impregnated alginate–chitosan blended nanocarrier induces apoptosis in human glioblastoma cells. *Adv. Healthcare Mater.*, 3, 106-114 (2014).

258. Sharma, V., Anderson, D. and Dhawan, A., Zinc oxide nanoparticles induce oxidative DNA damage and ROS-triggered mitochondria mediated apoptosis in human liver cells (HepG2). *Apoptosis*, 17, 852-870 (2012).

259. Shen, P. and Xia, Y., Synthesis-modification integration: one-step fabrication of boronic acid functionalized carbon dots for fluorescent blood sugar sensing. *Anal. Chem.*, 86, 5323-5329 (2014).

260. Shi, L., Li, X., Li, Y., Wen, X., Li, J., Choi, M.M., Dong, C. and Shuang, S., Naked oats-derived dual-emission carbon nanodots for ratiometric sensing and cellular imaging. *Sensors and Actuators B*, 210, 533-541 (2015).

261. Shimomura, O., Johnson, F.H. and Saiga, Y., Extraction, purification and properties of aequorin, a bioluminescent protein from the luminous hydromedusan, aequorea. *J. Cell. Comp. Physiol.* 59, 223-239 (1962).

262. Shu, X.Z., Zhu, K.J. and Song, W., Novel pH-sensitive citrate cross-linked chitosan film for drug controlled release. *Int. J. Pharm.*, 212, 19-28 (2001).

263. Silva, G.A., Introduction to nanotechnology and its applications to medicine. *Surg. Neurol.*, 61, 216-220 (2004).

264. Sirelkhatim, A., Mahmud, S., Seeni, A., Kaus, N.M.K., Ann, L.C., Bakhori, S.K.M., Hasan, H. and Mohamad, D., Review on zinc oxide nanoparticles: antibacterial activity and toxicity mechanism. *Nano-Micro Lett.*, 7, 219-242 (2015).

265. Sivaraman, G. and Chellappa, D., Rhodamine based sensor for naked-eye detection and live cell imaging of fluoride ions. *J. Mater. Chem. B*, 1, 5768-5772 (2013).

266. Sivaraman, G., Anand, T. and Chellappa, D., A fluorescence switch for the detection of nitric oxide and histidine and its application in live cell imaging. *ChemPlusChem*, 79, 1761-1766 (2014a).

267. Sivaraman, G., Anand, T. and Chellappa, D., Turn-on fluorescent chemosensor for Zn (II) via ring opening of rhodamine spirolactam and their live cell imaging. *Analyst*, 137, 5881-5884 (2012).

268. Sivaraman, G., Sathiyaraja, V. and Chellappa, D., Turn-on fluorogenic and chromogenic detection of Fe (III) and its application in living cell imaging. *J. Luminescence*, 145, 480-485 (2014b).

269. Sk, M.P., Jaiswal, A., Paul, A., Ghosh, S.S. and Chattopadhyay, A., Presence of amorphous carbon nanoparticles in food caramels. *Sci. Rep.*, 2, 383 (2012).

270. Smijs, T.G. and Pavel, S., Titanium dioxide and zinc oxide nanoparticles in sunscreens: focus on their safety and effectiveness. *Nanotechnology, Science and Applications*, 4, 95-112 (2011).

271. Song, Y., Shi, W., Chen, W., Li, X. and Ma, H., Fluorescent carbon nanodots conjugated with folic acid for distinguishing folate-receptor-positive cancer cells from normal cells. *J. Mater. Chem.*, 22, 12568-12573 (2012).

272. Srivastava, M., Das, A. K., Khanra, P., Uddin, M.E., Kim, N.H. and Lee, J.H., Characterizations of *in situ* grown ceria nanoparticles on reduced graphene oxide as a catalyst for the electrooxidation of hydrazine. *J. Mater. Chem. A*, 1, 9792-9801 (2013).

273. Stern, R. and Jedrzejas, M.J., Carbohydrate polymers at the center of life's origins: The importance of molecular processivity. *Chem. Rev.*, 108, 5061-5085 (2008).

274. Stopel, M.W.H., Prangsma, J.C., Blum, C. and Subramaniam, V., Blinking statistics of colloidal quantum dots at different excitation wavelengths. *RSC Adv.*, 3, 17440-17445 (2013).

275. Sun, D., Ban, R., Zhang, P.H., Wu, G.H., Zhang, J.R. and Zhu, J.J. Hair fiber as a precursor for synthesizing of sulfur- and nitrogen-co-doped carbon dots with tunable luminescence properties. *Carbon*, 64, 424-434 (2013).

276. Sun, Y.P., Zhou, B., Lin, Y., Wang, W., Fernando, K. A. S., Pathak, P., Meziani, M. J., Harruff, B.A., Wang, X., Wang, H.F., Luo, P.J.G., Yang, H., Kose, M.E., Chen, B. L., Veca, L.M. and Xie, S.Y., Quantum-sized carbon dots for bright and colorful photoluminescence. *J. Am. Chem. Soc.*, 128, 7756-7757 (2006).

277. Sung, H.W., Huang, R.N., Huang, L.L.H. and Tsai, C.C., *In vitro* evaluation of cytotoxicity of a naturally occurring cross-linking reagent for biological tissue fixation. *J. Biomater. Sci. Polym. Ed.*, 10, 63-78 (1999).

278. Ta, H.T., Dass, C.R., Larson, I., Choong, P.F. and Dunstan, D.E., A chitosan-dipotassium orthophosphate hydrogel for the delivery of doxorubicin in the treatment of osteosarcoma. *Biomaterials*, 30, 3605-3613 (2009).

279. Tagit, O., Tomczak, N., Benetti, E.M., Cesa, Y., Blum, C., Subramaniam, V., Herek, J.L. and Vancso, G., Temperature-modulated quenching of quantum dots covalently

coupled to chain ends of poly(N-isopropyl acrylamide) brushes on gold. *Nanotechnology*, 20, 185501 (2009).

280. Tang, L., Ji, R., Cao, X., Lin, J., Jiang, H., Li, X., Teng, K.S., Luk, C.M., Zeng, S., Hao, J. and Lau, S.P., Deep ultraviolet photoluminescence of water-soluble self-passivated graphene quantum dots. *ACS Nano*, 6, 5102-5110 (2012).
281. Tang, Y., Heaysman, C.L., Willis, S. and Lewis, A.L., Physical hydrogels with self-assembled nanostructures as drug delivery systems. *Expert Opin. Drug Deliv.*, 8, 1141-1159 (2011).
282. Tao, H., Yang, K., Ma, Z., Wan, J., Zhang, Y., Kang, Z. and Liu, Z., *In vivo* NIR fluorescence imaging, biodistribution, and toxicology of photoluminescent carbon dots produced from carbon nanotubes and graphite. *Small*, *8*, 281-290 (2012).
283. Tao, W., Zeng, X., Zhang, J., Zhu, H., Chang, D., Zhang, X., Gao, Y., Tang, J., Huang, L. and Mei, L., Synthesis of cholic acid-core poly(ε-caprolactoneran-lactide)-b-poly(ethylene glycol) 1000 random copolymer as a chemotherapeutic nanocarrier for liver cancer treatment. *Biomater. Sci.*, 2, 1262-1274 (2014).
284. Teng, X., Ma, C., Ge, C., Yan, M., Yang, J., Zhang, Y., Morais, P.C. and Bi, H., Green synthesis of nitrogen-doped carbon dots from konjac flour with "off–on" fluorescence by Fe^{3+} and L-lysine for bioimaging. *J. Mater. Chem. B*, 2, 4631-4639 (2014).
285. Tian, L., Ghosh, D., Chen, W., Pradhan, S., Chang, X. and Chen, S., Nanosized carbon particles from natural gas soot. *Chem. Mater.*, 21, 2803-2809 (2009).
286. Ting, S.R., Whitelock, J.M., Tomic, R., Gunawan, C., Teoh, W.Y., Amal, R. and Lord, M.S., Cellular uptake and activity of heparin functionalised cerium oxide nanoparticles in monocytes. *Biomaterials*, 34, 4377-4386 (2013).
287. Tripathi, K.M., Sonker, A.K., Sonkar, S.K. and Sarkar, S., Pollutant soot of diesel engine exhaust transformed to carbon dots for multicoloured imaging of *E. coli* and sensing cholesterol. *RSC Adv.*, 4, 30100-30107 (2014).
288. Turney, T.W., Duriska, M.B., Jayaratne, V., Elbaz, A., O'Keefe, S.J., Hastings, A.S., Piva, T.J., Wright, P.F. and Feltis, B.N., Formation of zinc-containing nanoparticles from Zn^{2+} ions in cell culture media: implications for the nanotoxicology of ZnO. *Chem. Res. Toxicol.*, 25, 2057-2066 (2012).
289. Ueno, T. and Nagano, T., Fluorescent probes for sensing and imaging. *Nat. Methods*, 8, 642-645 (2011).
290. Vashist, A., Vashist, A., Gupta, Y.K. and Ahmad, S., Recent advances in hydrogel based drug delivery systems for the human body. *J. Mater. Chem. B*, 2, 147-166 (2014).

291. Wahab, R., Siddiqui, M.A., Saquib, Q., Dwivedi, S., Ahmad, J., Musarrat, J., Al-Khedhairy, A. A. and Shin, H.S., ZnO nanoparticles induced oxidative stress and apoptosis in HepG2 and MCF-7 cancer cells and their antibacterial activity. *Colloids Surf B Biointerfaces*, 117, 267-276 (2014).
292. Wang, C., Xu, Z., Lin, H., Huang, Y. and Zhang, C., Large scale synthesis of highly stable fluorescent carbon dots using silica spheres as carriers for targeted bioimaging of cancer cells. *Part. Part. Syst. Charact.*, 32, 944-951 (2015).
293. Wang, F., Tan, W.B., Zhang, Y., Fan, X. and Wang, M., Luminescent nanomaterials for biological labelling. *Nanotechnology*, 17, R1-R13 (2006).
294. Wang, J., Peng, F., Lu, Y., Zhong, Y., Wang, S., Xu, M., Ji, X., Su, Y., Liao, L. and He, Y., Large-scale green synthesis of fluorescent carbon nanodots and their use in optics applications. *Adv. Optical Mater.*, 3, 103-111 (2014a).
295. Wang, J., Song, K., Wang, L., Liu, Y., Liu, B., Zhu, J., Xie, X. and Nie, Z., Formation of hybrid core-shell microgels induced by autonomous unidirectional migration of nanoparticles. *Mater. Horiz.*, 3, 78-82 (2016a).
296. Wang, J., Zhang, Z., Zha, S., Zhu, Y., Wu, P., Ehrenberg, B. and Chen, J.Y., Carbon nanodots featuring efficient FRET for two-photon photodynamic cancer therapy with a low fs laser power density. *Biomaterials*, 35, 9372-9381 (2014g).
297. Wang, L. and Zhou, H.S., Green synthesis of luminescent nitrogen-doped carbon dots from milk and its imaging application. *Anal. Chem.*, 86, 8902-8905 (2014b).
298. Wang, L., Li, B., Xu, F., Shi, X., Feng, D., Wei, D., Li, Y., Feng, Y., Wang, Y., Jia, D. and Zhou, Y., High-yield synthesis of strong photoluminescent N-doped carbon nanodots derived from hydrosoluble chitosan for mercury ion sensing via smartphone APP. *Biosens. Bioelectron.*, 79, 1-8 (2016b).
299. Wang, L., Zhu, S.J., Wang, H.Y., Qu, S.N., Zhang, Y.L., Zhang, J.H., Chen, Q.D., Xu, H.L., Han, W., Yang, B. and Sun, H.B., Common origin of green luminescence in carbon nanodots and graphene quantum dots. *ACS Nano.*, 8, 2541-2547 (2014f).
300. Wang, M.Z. Fang, Y. and Hu, D.D., Preparation and properties of chitosan-poly(N-isopropylacrylamide) full-IPN hydrogels. *React.Funct. Polym.*, 48, 215-221 (2001).
301. Wang, Q., Huang, X., Long, Y., Wang, X., Zhang, H., Zhu, R., Liang, L., Teng, P. and Zheng, H., Hollow luminescent carbon dots for drug delivery. *Carbon*, 59, 192-199 (2013a).

302. Wang, Q., Liu, X., Zhang, L.C. and Lv, Y., Microwave assisted synthesis of carbon nanodots through an eggshell membrane and their fluorescent application. *Analyst*, 137, 5392-5397 (2012).

303. Wang, Q., Song, H., Hu, Y., Su, Y. and. Lv, Y., Accelerated reducing synthesis of Ag@CDs composite and simultaneous determination of glucose during the synthetic process. *RSC Adv.*, 4, 3992-3997 (2014c).

304. Wang, R., Li, G., Dong, Y., Chi, Y. and Chen, G., Carbon quantum dot-functionalized aerogels for NO_2 gas sensing. *Anal. Chem.*, 85, 8065-8069 (2013b).

305. Wang, W., Li, Y., Cheng, L., Cao, Z. and Liu, W., Water-soluble and phosphorus-containing carbon dots with strong green fluorescence for cell labeling. *J. Mater. Chem. B*, 2, 46-48 (2014d).

306. Wang, X., Qu, K., Xu, B., Rena, J. and Qu, X., Microwave assisted one-step green synthesis of cell-permeable multicolor photoluminescent carbon dots without surface passivation reagents. *J. Mater. Chem*., 21, 2445–2450 (2011).

307. Wang, Y. and Hu, A., Carbon quantum dots: synthesis, properties and applications. *J. Mater. Chem. C*, 2, 6921-6939 (2014e).

308. Warner, J.H., Hoshino, A., Yamamoto, K. and Tilley, R.D., Water-soluble photoluminescent silicon quantum dots. *Angew Chem. Int. Ed.*, 117, 4626-4630 (2005).

309. Wee, S.S., Ng, Y.H. and Ng, S.M., Synthesis of fluorescent carbon dots via simple acid hydrolysis of bovine serum albumin and its potential as sensitive sensing probe for lead (II) ions. *Talanta*, 116, 71-76 (2013).

310. Wei, J., Ren, J., Liu, J., Meng, X., Ren, X., Chen, Z. and Tang, F., An eco-friendly, simple, and sensitive fluorescence biosensor for the detection of choline and acetylcholine based on c-dots and the fenton reaction. *Biosens. Bioelectron.*, 52, 304-309 (2014).

311. Whitesides, G.M., Nanoscience, nanotechnology, and chemistry. *Small*, 1, 172-179 (2005).

312. WHO, World Health Organization Switzerland, 4, 226 (2011).

313. Wichterle O. and Lim, D., Hydrophilic gels for biological use. *Nature*, 185, 117-118 (1960).

314. Wijeratne, S.S., Cuppett, S.L. and Schlegel, V., Hydrogen peroxide induced oxidative stress damage and antioxidant enzyme response in Caco-2 human colon cells. *J. Agric. Food Chem.*, 53, 8768-8774 (2005).

315. Wolfbeis, O.S., An overview of nanoparticles commonly used in fluorescent bioimaging. *Chem. Soc. Rev.*, 44, 4743-4768 (2015).

316. Wolter, K.G., Hsu, Y., Smith, C.L., Nechushtan, A., Xi, X. and Youle, R.J.J., Movement of Bax from the cytosol to mitochondria during apoptosis. *Cell Biol.*, 139, 1281-1292 (1997).

317. Wu, H.Y., Mi, C.C., Huang, H.Q., Han, B.F., Li, J.and Xu, S.K., Solvothermal synthesis of green-fluorescent carbon nanoparticles and their application. *J. Lumin.*, 132, 1603-1607 (2012).

318. Wu, J., Wang, X., Keum, J.K., Zhou, H., Gelfer, M., Avila-Orta, C.A., Pan, H., Chen, W., Chiao, S.M., Hsiao, B.S. and Chu, B., Water soluble complexes of chitosan-*g*-MPEG and hyaluronic acid. *J Biomed Mater Res A.*, 80, 800-812 (2007).

319. Xing, Q., Yates, K., Vogt, C., Qian, Z., Frost, M.C. and Zhao, F., Increasing mechanical strength of gelatin hydrogels by divalent metal ion removal. *Sci Rep.*, 4, 4706 (2014).

320. Xu, C. and Qu, X., Cerium oxide nanoparticle: a remarkably versatile rare earth nanomaterial for biological applications. *NPG Asia Materials*, 6, 90 (2014).

321. Xu, X., Ray, R., Gu, Y., Ploehn, H. J., Gearheart, L., Raker, K. and Scrivens, W.A., Electrophoretic analysis and purification of fluorescent single-walled carbon nanotube fragments. *J. Am. Chem. Soc.*,126, 12736-12737 (2004).

322. Xu, Y., Ren, X. and Hanna M.A., Chitosan/clay nanocomposite film preparation and characterization. *J. Appl. Polym. Sci.*, 99, 1684-1691, (2006).

323. Yan, F., Zou, Y., Wang, M., Mu, X., Yang, N. and Chen, L., Highly photoluminescent carbon dots-based fluorescent chemosensors for sensitive and selective detection of mercury ions and application of imaging in living cells. *Sensors and Actuators B*, 192, 488-495 (2014).

324. Yan, Y., Sun, J., Zhang, K., Zhu, H., Yu, H., Sun, M., Huang, D. and Wang, S., Visualizing gaseous nitrogen dioxide by ratiometric fluorescence of carbon nanodots-quantum dots hybrid. *Anal. Chem.*, 87, 2087-2093 (2015).

325. Yang, C., Deng, W., Liu, H., Ge, S. and Yan, M., Turn-on fluorescence sensor for glutathione in aqueous solutions using carbon dots–MnO_2 nanocomposites. *Sensors and Actuators B*, 216, 286-292 (2015).

326. Yang, J., Liu, X., Bhalla, K., Kim, C.N., Ibrado, A.M., Cai, J., Peng, T.I., Jones, D.P. and Wang, X., Prevention of apoptosis by Bcl-2: release of cytochrome c from mitochondria blocked. *Science*, 275, 1129-1132 (1997).

327. Yang, S.T., Cao, L., Luo, P.G., Lu, F., Wang, X., Wang, H., Meziani, M.J., Liu, Y., Qi, G. and Sun, Y.P., Carbon dots for optical imaging *in vivo*. *J. Am. Chem. Soc.*, 131, 11308-11309 (2009a).

328. Yang, S.T., Wang, X., Wang, H., Lu, F., Luo, P.G., Cao, L., Meziani, M.J., Liu, J.H., Liu, Y., Chen, M., Huang, Y. and Sun, Y.P., Carbon dots as nontoxic and high-performance fluorescence imaging agents. *J. Phys. Chem.C*, 113, 18110-18114 (2009b).

329. Yang, X., Zhuo, Y., Zhu, S., Luo, Y., Feng, Y. and Dou, Y., Novel and green synthesis of high-fluorescent carbon dots originated from honey for sensing and imaging. *Biosens. Bioelectron.*, 60, 292-298 (2014b).

330. Yang, Y. H., Cui, J.H., Zheng, M.T., Hu, C.F., Tan, S.Z., Xiao, Y., Yang, Q. and Liu, Y. L., One-step synthesis of amino-functionalized fluorescent carbon nanoparticles by hydrothermal carbonization of chitosan. *Chem. Commun.*, 48, 380-382 (2012).

331. Yang, Z., Xu, M., Liu, Y., He, F., Gao, F., Su, Y., Wei, H. and Zhang, Y., Nitrogen-doped, carbon-rich, highly photoluminescent carbon dots from ammonium citrate. *Nanoscale*, 6, 1890-1895 (2014a).

332. Yang, Z.C. Wang, M., Yong, A.M., Wong, S.Y., Zhang, X.H., Tan, H., Chang, A.Y., Li, X. and Wang, J., Intrinsically fluorescent carbon dots with tunable emission derived from hydrothermal treatment of glucose in the presence of monopotassium phosphate. *Chem. Commun.*, 47, 11615-11617 (2011).

333. Yazid, S.N.A.M., Chin, S.F., Pang, S.C. and Ng, S.M., Detection of Sn (II) ions via quenching of the fluorescence of carbon nanodots. *Microchim. Acta*, 180, 137-143 (2013).

334. Yi, H., Ghosh, D., Ham, M.H., Qi, J., Barone, P.W., Strano, M.S. and Belcher, A.M. M13 Phage-functionalized single-walled carbon nanotubes as nanoprobes for second near-infrared window fluorescence imaging of targeted tumors. *Nano Lett.*, 12, 1176-1183 (2012).

335. Yin, J.Y., Liu, H.J., Jiang, S., Chen, Y. and Yao, Y., Hyperbranched polymer functionalized carbon dots with multistimuli-responsive property. *ACS Macro Lett.*, 2, 1033-1037 (2013).

336. Yin, Y.J., Zhao, F., Song, X.F., Yao, K.D., Lu, W.W. and Leong, J.C., Preparation and characterization of hydroxyapatite/chitosan-gelatin network composite. *J. Appl. Polym. Sci.*, 77, 2929-2938 (2000).

337. Yokoyama, M., Fukushima, S., Uehara, R., Okamoto, K., Kataoka, K., Sakurai, Y. and Okano, T., Characterization of physical entrapment and chemical conjugation of

adriamycin in polymeric micelles and their design for *in vivo* delivery to a solid tumor. *J. Control Release*, 50, 79-92 (1998).

338. Yong, K.T., Law, W.C., Hu, R., Ye, L., Liu, L., Swihart, M.T. and Prasad, P.N., Nanotoxicity assessment of quantum dots: from cellular to primate studies. *Chem Soc Rev.*, 42, 1236-1250 (2013).
339. Yoshikawa, R., Kusunoki, M., Yanagi, H., Noda, M., Furuyama, JI. Yamamura, T, and Hashimoto-Tamaoki, T., Dual antitumor effects of 5-fluorouracil on the cell cycle in colorectal carcinoma cells: A novel target mechanism concept for pharmacokinetic modulating chemotherapy. *Cancer Res.*, 6, 1029-1037 (2001).
340. Yu, B., Li, X., Zheng, W., Feng, Y., Wong, Y.S. and Chen, T., pH-responsive cancer-targeted selenium nanoparyicles: A transformable drug carrier with enhanced theranostic effects. *J. Mater. Chem. B*, 2, 5409-5418 (2014).
341. Yu, C., Wu, Y., Zeng, F. and Wu, S., A fluorescent ratiometric nanosensor for detecting NO in aqueous media and imaging exogenous and endogenous NO in live cells. *J. Mater. Chem. B*, 1, 4152-4159 (2013).
342. Yu, H., Chao, J., Patek, D., Mujumdar, R., Mujumdar, S. and Waggoner, A.S., Cyanine dye dUTP analogs for enzymatic labeling of DNA probes. *Nucleic Acids Res.* 22, 3226-3232 (1994).
343. Yu, H., Zhang, H., Huang, H., Liu, Y., Li, H., Ming, H. and Kang, Z., ZnO/carbon quantum dots nanocomposites: one-step fabrication and superior photocatalytic ability for toxic gas degradation under visible light at room temperature. *New J. Chem.*, 36, 1031-1035 (2012).
344. Zhai, X., Zhang, P., Liu, C., Bai, T., Li, W., Dai, L. and Liu. W., Highly luminescent carbon nanodots by microwave-assisted pyrolysis. *Chem. Commun.*, 48, 7955-7957 (2012).
345. Zhai, Y., Zhu, Z., Zhu, C., Ren, J., Wang, E. and Dong, S., Multifunctional water-soluble luminescent carbon dots for imaging and Hg^{2+} sensing. *J. Mater. Chem. B*, 2, 6995-6999 (2014).
346. Zhang, H., Chen, Y., Liang, M., Xu, L., Qi, S., Chen, H. and Chen, X., Solid-phase synthesis of highly fluorescent nitrogen-doped carbon dots for sensitive and selective probing ferric ions in living cells. *Anal. Chem.*, 86, 9846-9852 (2014a).
347. Zhang, J. and Yu, S.H., Carbon dots: large-scale synthesis, sensing and bioimaging. *Mater. Today*, doi:10.1016/j.mattod.2015.11.008 (2015).

348. Zhang, J., Shen, W., Pan, D., Zhang, Z., Fang, Y. and Wu, M., Controlled synthesis of green and blue luminescent carbon nanoparticles with high yields by the carbonization of sucrose. *New J. Chem.*, 34, 591-593 (2010).

349. Zhang, X., Zhang, X., Tao, L., Chi, Z., Xu, J. and Wei, Y., Aggregation induced emission-based fluorescent nanoparticles: fabrication methodologies and biomedical applications. *J. Mater. Chem. B*, 2, 4398-4414 (2014b).

350. Zhang, Y.Y., Wu, M., Wang, Y.Q., He, X.W., Li, W.Y. and Feng, X.Z., A new hydrothermal refluxing route to strong fluorescent carbon dots and its application as fluorescent imaging agent. *Talanta*, 117, 196-202 (2013).

351. Zhang, Z., Hao, J., Zhang, J., Zhang, B. and Tang, J., Protein as the source for synthesizing fluorescent carbon dots by a one-pot hydrothermal route. *RSC Adv.*, 2, 8599-8601 (2012).

352. Zhao, M.X., Zeng, E.Z., Li, Y. and Wang, C.J., A study on effects of naphthalimide derivative-capped quantum dots on the cellular internalization, proliferation, and apoptosis ability. *J. Mater. Chem. B*, 2, 7351-7359 (2014).

353. Zheng, L.Y., Chi, Y.W., Dong, Y.Q., Lin, J.P. and Wang, B.B., Electroluminescence of water-soluble nanocrystals released electrochemically from graphite. *J. Am.Chem. Soc.*, 131, 4564-4565 (2009).

354. Zheng, M., Liu, S., Li, J., Qu, D., Zhao, H., Guan, X., Hu, X., Xie, Z., Jing, X. and Sun, Z., Integrating oxaliplatin with highly luminescent carbon dots: an unprecedented theranostic agent for personalized medicine. *Adv. Mater.*, 26, 3554-3560 (2014).

355. Zheng, M., Xie, Z., Qu, D., Li, D., Du, P., Jing, X. and Sun, Z. On-off-on fluorescent carbon dot nanosensor for recognition of chromium(VI) and ascorbic acid based on the inner filter effect. *ACS Appl. Mater. Interfaces*, 5, 13242-13247 (2013).

356. Zholobak, N.M., Shcherbakov, A.B., Vitukova, E.O., Yegorova, A.V., Scripinets, Y.V., Leonenko, I.I., Baranchikov, A.Y., Antonovich, V.P. and Ivanov, V.K., Direct monitoring of the interaction between ROS and cerium dioxide nanoparticles in living cells. *RSC Adv.*, 4, 51703-51710 (2014).

357. Zhou, H.Y., Jiang, L.J., Cao, P.P., Li, J.B. and Chen, X.G., Glycerophosphate-based chitosan thermosensitive hydrogels and their biomedical applications. *Carbohydr. Polym.*, 117, 524-536 (2015).

358. Zhou, J., Sheng,Z., Han, H., Zou, M. and Li, C., Facile synthesis of fluorescent carbon dots using watermelon peel as a carbon source. *Mater. Lett.*, 66, 222-224 (2012).

359. Zhou, J.G., Booker, C., Li, R.Y., Zhou, X.T., Sham, T.K., Sun, X.L. and Ding, Z.F., An electrochemical avenue to blue luminescent nanocrystals from multiwalled carbon nanotubes (MWCNTs). *J. Am. Chem. Soc.*, 129, 744-745 (2007).

360. Zhou, L., Li, Z., Liu, Z., Ren J. and Qu, X., Luminescent carbon dot-gated nanovehicles for pH-triggered intracellular controlled release and imaging. *Langmuir*, 29, 6396-6403 (2013a).

361. Zhou, J., Liu, H., Jin, B., Liu, X., Fu, H. and Shangguan, D., A guanidine derivative of naphthalimide with excited-state deprotonation coupled intramolecular charge transfer properties and its application. *J. Mater. Chem. C*, 1, 4427-4436 (2013b).

362. Zhu, C., Zhai, J. and Dong, S., Bifunctional fluorescent carbon nanodots: green synthesis *via* soy milk and application as metal-free electrocatalysts for oxygen reduction. *Chem. Commun.*, 2012, 48, 9367-9369 (2012).

363. Zhu, H., Wang, X. L., Li, Y. L., Wang, Z. J., Yang F. and Yang, X. R., Microwave synthesis of fluorescent carbon nanoparticles with electrochemiluminescence properties, *Chem. Commun.*, 5118-5120 (2009).

364. Zhu, K., Ye, T., Liu, J., Peng, Z., Xu, S., Lei, J., Deng, H. and Li, B., Nanogels fabricated by lysozyme and sodium carboxymethyl cellulose for 5-Fluorouracil controlled release. *J. Int. Pharm.*, 441, 721-727 (2013a).

365. Zhu, L., Yin, Y., Wang, C.F. and Chen, S., Plant leaf-derived fluorescent carbon dots for sensing, patterning and coding. *J. Mater. Chem. C*, 1, 4925-4932 (2013b).

366. Zhu, S., Meng, Q., Wang, L., Zhang, J., Song, Y., Jin, H., Zhang, K., Sun, H., Wang, H. and Yang, B., Highly photoluminescent carbon dots for multicolor patterning, sensors, and bioimaging. *Angew. Chem. Int. Ed.*, 52, 3953-3957 (2013c).

367. Zong, J., Yang, X., Trinchi, A., Hardin, S., Cole, I., Zhu, Y., Li, C., Muster, T. and Wei, G., Carbon dots as fluorescent probes for "off-on" detection of Cu^{2+} and L-cysteine in aqueous solution. *Biosens. Bioelectron.*, 51, 330-335 (2014).

368. Zrazhevskiy, P., Sena, M. and Gao, X., Designing multifunctional quantum dots for bioimaging, detection, and drug delivery. *Chem. Soc. Rev.*, 39, 4326-4354 (2010).

369. Zuo, P., Lu, X., Sun, Z., Guo, Y. and He, H., A review on syntheses, properties, characterization and bioanalytical applications of fluorescent carbon dots. *Microchim. Acta*, 183, 519-542 (2016).